Laser Induced Plasma Studies on W, Mo and alloys of Cu in air via Time and Space Resolved LIBS and application in Single Line Calibration Free -LIBS

DOCTOR OF PHILOSOPHY

by

ESHITA MAL

DEPARTMENT OF PHYSICS

INDIAN INSTITUTE OF TECHNOLOGY GUWAHATI

GUWAHATI -781039, INDIA

SEPTEMBER 2019

Laser Induced Plasma Studies on W, Mo and alloys of Cu in air via Time and Space Resolved LIBS and application in Single Line Calibration Free -LIBS

A Thesis submitted in partial fulfillment of the requirements for the award of the degree of

DOCTOR OF PHILOSOPHY

by

ESHITA MAL

DEPARTMENT OF PHYSICS

INDIAN INSTITUTE OF TECHNOLOGY GUWAHATI

GUWAHATI -781039, INDIA

SEPTEMBER 2019

Dedicated to my Parents

Eshita Mal
Registration No. 136121022
Department of Physics
Indian Institute of Technology Guwahati
Guwahati-781039, Assam, India

Statement

I hereby declare that the matter embodied in this thesis is the result of investigations carried out by me at the Department of Physics, Indian Institute of Technology Guwahati, Guwahati, India, under the supervision of **Prof. Alika Khare**. This thesis has not been submitted to any university, institute or elsewhere for the award of the any degree, diploma or associate-ship.

Date: ……. **Eshita Mal**

भारतीय प्रौद्योगिकी संस्थान गुवाहाटी

Indian Institute of Technology Guwahati
Department of Physics
Guwahati-781039, Assam State, INDIA
Phone: +91 361 2582705, 2582701, 2690321 to 328 (extn. 2705),
Fax: +91 361 2582749
Dr. Alika Khare
Professor
E-mail: alika@iitg.ac.in, k_alika@yahoo.com

Date: Sept. , 2019

Certificate

This is to certify that work contained in the thesis entitled '**Laser Induced Plasma Studies on W, Mo and alloys of Cu in air via Time and Space Resolved LIBS and application in Single Line Calibration Free -LIBS**' by **Ms Eshita Mal** (Roll no 136121022), a student of Department of Physics, Indian Institute of Technology Guwahati, for the award of degree of Doctor of Philosophy, has been carried out under my supervision and the same has not been submitted elsewhere for the award of any other degree.

(Alika Khare)

Acknowledgement

I would like to thank all the people who help me in some way to complete this thesis. First and foremost I would like to express my sincere gratitude to my thesis supervisor Prof. Alika Khare for the patient guidance, encouragement, advices and constant support she has provided during my PhD work. I would like to acknowledge her, for investing valuable time in all the discussions and ideas in my research work.

I sincerely thankful to Dr. Manoj Kumar Gundawar from Advanced Centre of Research in High Energy Materials (ACRHEM), University of Hyderabad, for collaborative research work, allowing me to perform part of the experiment related to my thesis work and all the useful discussions during my staying in ACRHEM.

I am indebted to doctoral committee members, Prof. Saurabh Basu, Prof. Amarendra Kumar Sarma and Prof. Anugrah Singh for their critical reviews and valuable suggestions to improve my thesis work. I am also thankful to Dr. Ashwini Kumar Sharma for all the valuable discussions and suggestions.

I would like to extend my gratitude to the present and former Head and staff members of the Department of Physics and Central Instrument Facility of IIT Guwahati. I would like to thank IIT Guwahati and MHRD, GATE and Equal Opportunity Cum Special Reservation Cell fellowship to provide financial support during my Ph.D tenure.

I am thankful to Department of Physics, IIT Guwahati and Central Instrument Facility (CIF), IIT Guwahati for providing me the necessary facilities to fulfill my PhD thesis objectives.

I would like to thank my lab seniors, Dr. Indrajeet, Dr. Shanta, Dr. Partha, Dr. Gyan. Rahul, and Prahlad. I am specially thankful to my juniors Gobinda, Sasmita, Sumit and Nagendra for their love and support in all difficult situations during my Ph.D. My special thanks goes to Rajendhar for helping me in LIBS experiment and all the useful discussions. I would like to thank to Rashmi and Sundarlal for surface profilometer analysis. I am thankful to Kamal and Juhi for FESEM analysis. I would like thank to all my friends from ACRHEM, Dr. Konda Srinivas, Dr. Manikantha, Dr. Narshimha, Dr. Abdul, Nagaraju, Chandu and Arun for providing me friendly environment to carry out the experiment and all the necessary help to

stay in the campus. I would like to thank my batch mates and juniors, Dr. Debanad, Dr.Subhadeep. Dr. Sanjib, Dr. Susmita, Dr. Priyadarshini, Sunayana, Monika, Ramyani, Ruma and Srijita for listening to me and support me in my tough days in IIT Guwahati.

I would convey my very special thanks to my childhood friends Ankita, Afrin, Bandhusree, and Paramita for their selfless support, advice, suggestions and encouragement in every phase of life.

I would like to thank Prasanta for his support, encouragement, understanding and friendship in my life.

I want to express my special gratitude to my family members. I would to like thank my mother Mrs. Kabita Mal, father, Mr. Balai Chandra Mal for their unconditional love, blessing, providing the help, support and courage to lead the battle field of life. I would like thank my little sister Aditi to support me in every situations and making my life joyful.

Eshita Mal

Abstract

Laser induced breakdown spectroscopy (LIBS) is an optical emission based spectrochemical analytical method. LIBS is capable of both, the qualitative and quantitative analysis of any kind of sample irrespective of its physical state. In LIBS, a high power pulsed laser is focused on to the target surface to generate the laser induced plasma (LIP). LIP expands into the ambient and cools down to emit radiation. The LIP is extremely transient and inhomogeneous in nature. So the temporal and spatial characterization of LIP is considered as one of the initial points for the LIBS technique. Therefore, in the present thesis work, time and space resolved LIBS studies are performed on tungsten, molybdenum and three different types of copper alloys as a function of incident laser energy in air. From the temporal studies, the emission from the LIP is recorded in the delay time range of 0.5-5 μs. From the LIP spectra, several atomic and ionic transitions are identified. The suitable identified transitions are analyzed to estimate the plasma temperature and electron density. In the space resolved studies, keeping the delay fixed at 2 μs, the emission from LIP is recorded as a function of distance from the target. From the space-resolved studies, it is evident that plasma emission intensity, SNR and plasma parameters increase up to a certain distance away from the target surface, attain the maximum value and fall down with further increase in separation from the target. The Mc-Whirter criteria is applied to test the validity of local thermodynamic equilibrium (LTE) for temporal as well as space-resolved studies. The relaxation time and diffusion length are estimated to take care of the transient and inhomogeneous nature of the LIP. The optical thin condition of LIP is verified by employing branching ratio method. From the temporal and space resolved studies, an optimized temporal window of 2-4 μs and spatial window of 0.8-2.8 mm is identified where the SNR is large and LTE and optical thin plasma conditions are satisfied. As an application of the LIBS, single line calibration free LIBS (CF-LIBS) technique is employed on three different types copper alloys to estimate the percentage composition of the constituent elements as a function delay time and axial position. From these studies, an optimized temporal and spatial window is identified for enhanced accuracy of CF-LIBS technique. The surface characterization of laser ablated region is also under taken via optical microscope, surface profilometer, FESEM and Raman spectroscopy for the three different targets to understand the surface modification during LIP formation and dependency on laser energy and plasma parameters.

Contents

List of Figures

List of Tables

Abbreviation

a.u.	Arbitrary unit
CF-LIBS	Calibration Free-laser induced breakdown spectroscopy
DG	Delay generator
DSO	Digital storage oscilloscope
EUV	Extreme Ultraviolet
EDX	Energy dispersive X-ray
FESEM	Field Emission scanning electron microscope
Fig.	Figure
FWHM	Full width at half maximum
IB	Inverse bremsstrahlung
ICCD	Intensified charge coupled device
LA-ICP-MS	Laser-ablation inductively coupled-plasma mass spectrometry
LIB	Laser-induced breakdown
LIBS	Laser-induced breakdown spectroscopy
LIP	Laser induced plasma
LTE	Local thermodynamic equilibrium
LSAW	Laser supported absorption waves
LSC	Laser supported combustion wave
LSD	Laser supported detonation wave
LSR	Laser supported radiation wave
Nd:YAG	Neodymium yttrium aluminum garnet
PLD	Pulsed laser deposition
PFC	Plasma facing component
PI	Photon ionization
SNR	Signal to noise ratio
UV	Ultraviolet
w.r.t	With respect to

Symbol

~	Approximately
A_{nm}	Transition Probability
Al	Aluminium
AlI	Atomic Aluminium
c	Speed of light
cm	Centimeter
Cu	Copper
CuI	Atomic Copper
D	Diffusion Coefficient
E_0	Energy of the free electron
E_n	Energy of Upper state
eV	Electron Volt
fs	Femtosecond
f_{nm}	Oscillator Strength
F	Experimental factor
Fe	Iron
FeI	Atomic Iron
<*g*>	Gaunt Factor
g_n	Degeneracy
h	Planck Constant
Hz	Hertz
I	Laser Intensity
I_{nm}	Intensity of Transition from *n* to *m*
J	Joule
K	Kelvin
Kg	Kilogram
k_B	Boltzmann constant
L_{diff}	Diffusion Length
m_e	Mass of the electron
M_A	Atomic mass
mm	Millimetre
mJ	Mili Joule
$\dot{m}$	Mass ablation rate
Mo	Molybdenum
MoI	Atomic Molybdenum
MoII	Singly ionized Molybdenum
N	Total number density
N_n	Population number density in n state
N^z	Population number density in z^{th} ionization state
Ni	Nickel
Ni	Atomic Nickel
N_D	Number of particle in Debye sphere
N_e	Electron Density
Pb	Lead
PbI	Atomic Lead
ps	Picosecond

s	Second
Sn	Tin
SnI	Atomic Tin
T_e	Plasma Temperature
U	Partition Function
w	Electron impact width parameter
W	Watt
W	Tungsten
WI	Atomic tungsten
WII	Singly ionized tungsten
W(v)	Photon energy distribution in black body radiation
Zn	Zinc
ZnI	Atomic transition from Zinc
α_{IB}	Absorption coefficient
$\Delta_{\lambda D}$	Doppler Broadening width
ΔE_{nm}	Energy difference between n and m sate
χ	Ionization Energy
ν_l	Laser frequency
λ_l	Laser wavelength
μm	Micrometer
μg	Microgram
μs	Microsecond
ν_p	Plasma frequency
τ_{rel}	Relaxation time
$\Delta\lambda_{1/2}$	Stark-broadening Width
λ_{nm}	Wavelength of transition from upper state n to lower state m

Chapter 1 Introduction

The focusing of a high-power pulsed laser beam onto a material results in to the removal of material from the focal volume region and produce a hot luminous plasma on to the target surface, known as laser induced plasma (LIP) [1-3]. LIP comprises of ions, electrons, neutrals, and excited particles. LIP emits radiation in the visible, ultraviolet (UV), extreme UV, and x-ray regions of the electromagnetic spectrum [4]. LIP has been the focus of extensive basic scientific research due to many fold applications in various field including pulsed laser deposition (PLD) [5, 6], elemental characterization using laser-induced breakdown spectroscopy (LIBS) [4, 7], laser-ablation inductively coupled-plasma mass spectrometry (LA-ICP-MS) [8], nano-particles synthesis [9-11], micromachining [12, 13], generation of ion source [14-16], lithography [17-19], plasma diagnostics, laser shock penning [20], higher harmonic generation [21, 22], production of X-rays and EUV [23], laboratory simulation of astrophysical plasmas [24, 25], inertial confinement of fusion [26] and many more.

As soon as LIP is generated on the surface of a material, it starts expanding into the surrounding medium. During the expansion of LIP, it cools down and emits characteristic line radiation of the constituent elements. By analyzing the line radiation from each of the constituent element in a sample, it is possible to identify the constituent elements. This optical emission spectroscopic technique is known as laser-induced breakdown spectroscopy (LIBS) [7, 27, 28]. One of the foremost application of LIBS is towards qualitative as well as quantitative analysis of any kind of material. In 1962, two years after the invention of first ruby laser, Brech and Cross [29] demonstrated the viability of powerful lasers as excitation sources in atomic emission spectroscopy for the first time. The first analytical use of LIP for spectrochemical

analysis of surface is reported in France in 1963, which is considered as the "birth" of the LIBS technique [30]. However, for a quite some time, LIP and LIBS are continued to merely a topic of scientific research. The research work remained devoted more towards the fundamental characteristics of LIP rather than to its analytical capabilities. Starting in the early 1980s, there have been renewed interest in LIBS. The fast developments of LIBS as an analytical technique can be traced back to the work of Radziemski and Cremers and their co-workers at Los Alamos National Laboratory and this group first coined the acronym LIBS for laser-induced breakdown spectroscopy [27]. Since 1990s, LIBS has undergone a drastic progress towards becoming a viable technique for both laboratory and field analysis [27, 31-34]. In 2004, in the review article by Winefordner et al., LIBS has been described as "a future super star"[35]. LIBS is receiving immense interest as a spectrochemical analytical technique in the present era due to its some inherent capabilities and advantages over other analytical tools as listed below [4, 7, 31, 36]

- **Applicable to any sample:** LIBS is capable of analyzing any kind of samples irrespective of its physical state (i.e. solid, liquid or gaseous) over all the element present in the periodic table and their composites.
- **Devoid of any sample preparation:** LIBS technique doesn't require any sample preparation and thus contamination free.
- **Non-destructive:** In LIBS, laser is focused to a very small size and thus the mass of the ablated material is hardly few nano gram. Thus it is nearly nondestructive technique.
- **Multi-elemental detection:** Detection of multiple elements in any matrix of sample is possible.

- **Ease of detection:** In LIBS, normally the emitted radiation is confined from UV-visible to IR regions, therefore the radiation can be detected in the air even from the remote location.
- **Independent of ambient:** This technique can be applied to any ambient conditions, in air, vacuum, low or high pressure of any gas, inside water, low or high temperature and also in hazardous environment.
- **Non-contact and Stand-off detection:** The LIBS technique requires only optical access to the focusing laser and the emitted plasma radiation from the sample thus making it non-contact technique and can be implemented in standoff detection mode.
- **Quick measurement and analysis:** The development of high speed array photo detectors making it feasible for single shot analysis.
- **Simple, low cost and portable:** LIBS experimental setup is simple for implementation and overall cost is expected to be low compared to other well established analytical technique. All the components required in LIBS experiment can be assembled or transported easily at the location of investigation. Thus making it possible as a portable tool.
- **Surface analytical tool:** LIBS is also foreseen as surface analytical tool for 3D mapping of the sample.
- **Compatible with other method:** LIBS technique can be suitably combined with others technique, such as Raman spectroscopy or laser induced fluorescence for simultaneous detection of multi molecular surface of any heterogeneous material.

Due to several salient features as listed above, LIBS is finding its application in almost every sector of scientific investigation [33, 37]. It is being implemented in industry for production

control and on line monitoring as well as offline quality assessment [38], environmental monitoring (air pollution, smoke monitoring, assessment of contamination in water or soil) [39, 40], space exploration [41], biomedical [42, 43] and pharmaceutical research [44], cultural heritage conservation (e.g. frescoes, historical buildings, objects located in museums, laser cleaning etc.) [45-48], for security purpose (i.e. finger print mapping, chemical and biological warfare agent materials) [49-51], measurements in hostile environments of high temperatures and pressure, radiation hazardous zone, or explosive etc. [52-54].

1.1 Processes involved in laser induced breakdown

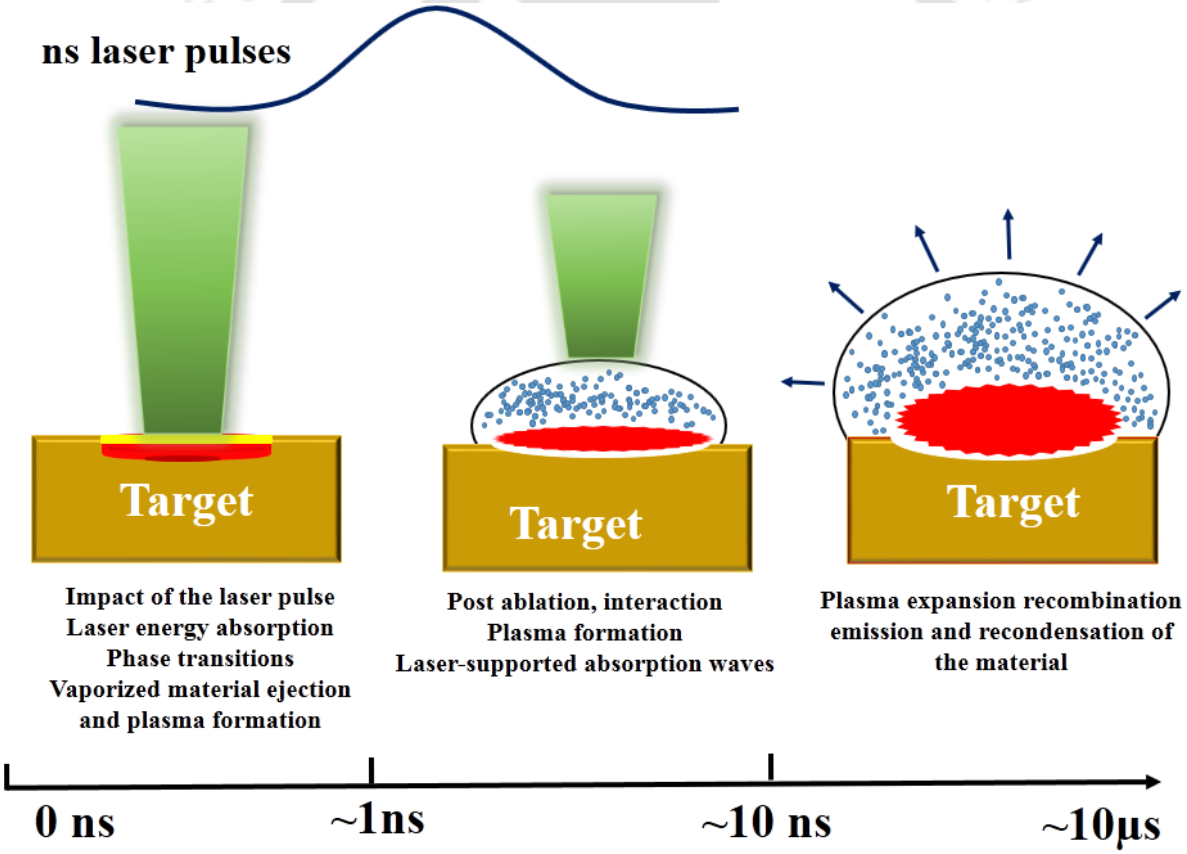

Figure 1.1 Sequential processes in the generation and evolution of a plasma in a nanosecond laser pulse with a typical time scale.

The understanding of LIBS technique and its good analytical performance lies in the proper understanding of the various processes occurring in LIP. The successive processes involved in the formation of LIP through the laser ablation are bond breaking and plasma formation of the under investigation, plasma expansion cooling, radiation emission and particulate formation [7]. The pictorial view of all these processes occurring in laser induced breakdown (LIB) of a sample in case of nanosecond laser pulse are depicted in Fig 1.1 along with a flow chart Fig.1.2.

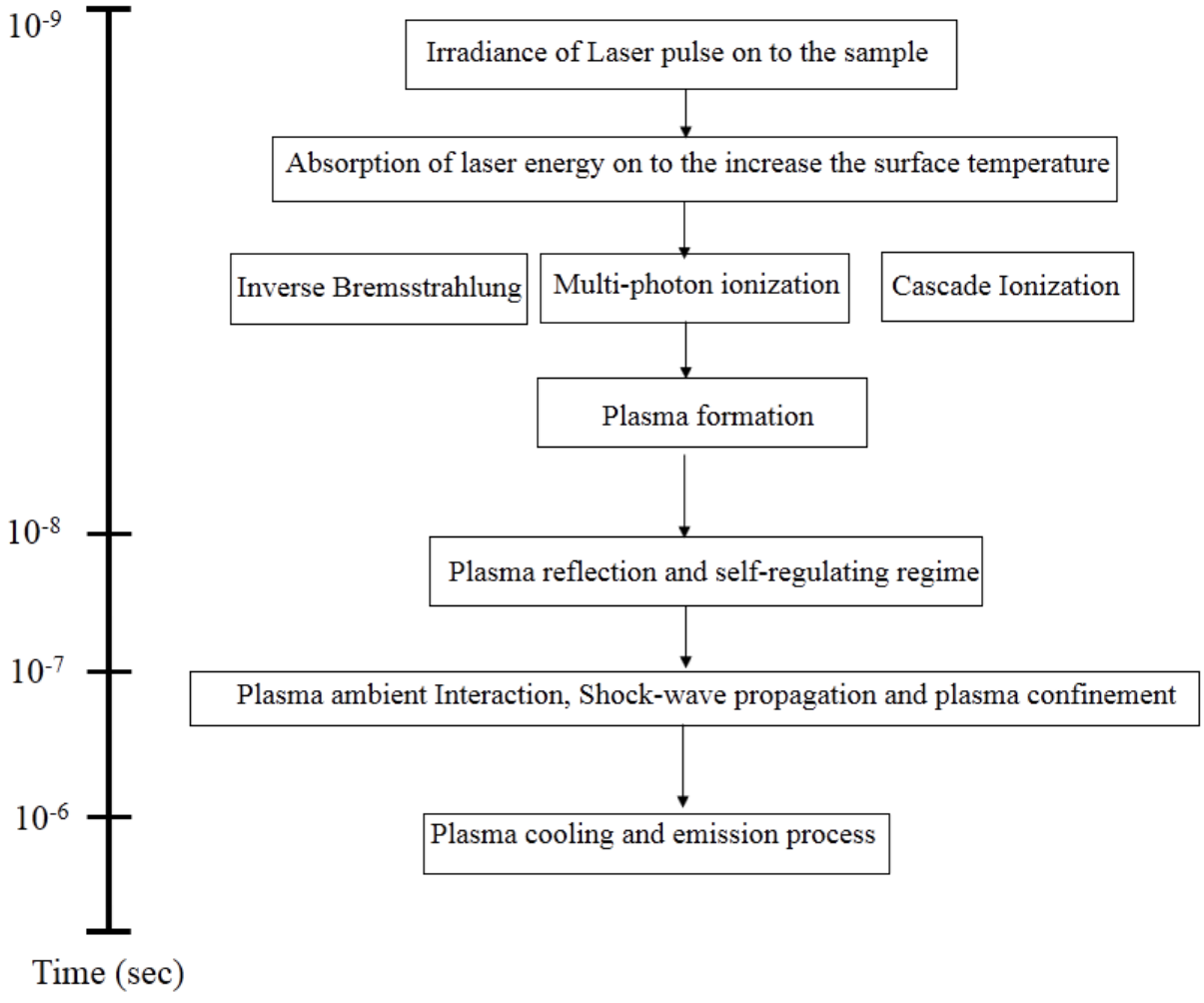

Figure 1.2 Flow chart of all the process involved in LIB for a solid in case of nanosecond laser pulse.

As soon laser pulse is focused on to the sample surface, having energy above the breakdown threshold of the sample, the ablation process occurs through a variety of nonlinear processes spread over different time scale. As depicted in the Fig1.1 and 1.2 [55], due to the irradiance of laser pulse on the sample surface, the laser energy is absorbed by the target surface due to the focal heating. This results in to increase in temperature and thermal vaporization. The vaporized material is comprised of electron, ions, molecules, cluster and particles. The vaporized material absorb energy from the laser pulse through inverse bremsstrahlung (IB), multi-photon ionization (PI) and cascade ionization and generate the plasma in the time scale of 10^{-9} to 10^{-8} sec. For a nanosecond laser pulse, the trailing part of the laser pulse is absorbed by the LIP. After the commencement of LIP, it starts expanding in to the surrounding medium. During the expansion in to the ambient gas, LIP compresses the surrounding gas, produces a shock wave and due to the expansion it loses its kinetic energy and cools down to emit radiation due to recombination. At the last stage of LIP evolution, plasma condensation occurs and particulate formation takes place. So the entire process of LIB can be divide into four stages: (i) laser matter interaction and plasma generation, (ii) laser-plasma interaction (iii) plume expansion, cooling and emission of radiation and (iv) formation of nanoparticles. These are described in details in the following subsections.

1.1.1 Laser matter interaction and plasma formation

Whenever the laser energy, impinging on the sample, exceeds the ablation breakdown threshold, its plasma formation is initiated and a flash of visible light is produced with the popping sound [56]. In case of nanosecond laser, the predominant mechanism for absorption of laser in the material is IB absorption [57]. Initially, it is a free-free absorption or electron-neutral absorption process, occurring in the femtosecond (fs) timescale [58]. This results into

the energy transfer from free electrons to neighboring atoms and ions and dominant absorption mechanism switches from electron-neutral to electron-ion IB process. Approximately 100 ps after laser energy deposition, melting and evaporation of the material begins on the sample surface within the focal region. This is followed by ablation and plasma formation [59]. The IB absorption coefficient, α_{IB} is given by the following equation

$$\alpha_{IB}\,(cm^{-1}) = 1.37 \times 10^{-35}\,\lambda_l^{3} N_e^{2} T_e^{1/2} \tag{1.1}$$

where λ_l is the wavelength of the laser photons in μm, N_e and T_e are the electron density and plasma temperature in the unit of cm^{-3} and eV respectively.

Another mechanism through which laser absorption occurs is photoionization [60]. For photoionization, laser photon energy, $h\nu_l$, where h is the Planck constant and ν_l is the frequency of laser photon, must be greater than ionization energy of the atom. In most of the cases, ionization energy of the atom is greater than laser photon energy as it is in the visible and IR region and negating the possibility of single photo ionization. Multi-photon ionization and photoionization of the excited state can contribute to this process, if the laser intensity is high and laser wavelength is short. The absorption coefficient due to multi-photon ionization is given by following equation [60],

$$\alpha_{PI}\,(cm^{-1}) = \sum_{n} 7.9 \times 10^{18} \left(\frac{E_n}{h\nu_l}\right)^{3} \left(\frac{\chi}{E_n}\right)^{1/2} N_n \tag{1.2}$$

where E_n and N_n are the energy and number density of the excited state n, and χ is ionization potential of the atom.

1.1.2 Plasma expansion

After the formation of LIP over the target surface, it expands from a large value of solid density in the surrounding ambient of relatively much lower density, normal to the target surface, at

a supersonic speed. The expansion of high pressure LIP compresses the surrounding gas and produce a shock wave. Also during the expansion, energy is transferred to ambient gas by the combination of thermal conduction, radiative transfer and heating by shock wave [7]. The initial part of laser contributes to generate the plasma while rest of the laser energy in the later part is absorbed by the plasma and the shocked gas. This accelerates the plasma expansion in the surrounding colder environment which generates the waves known as laser supported absorption waves (LSAW) [7] [61]. There are three different types of LSAW reported in literature, namely [7, 62] (i) laser supported combustion wave (LSC), (ii) laser supported detonation wave (LSD) and (iii) laser supported radiation wave (LSR). This classification is mainly based on velocity, pressure, and on the effect of radial expansion of LIP during the subsequent to plasma evolution, which is strongly dependent on incident laser fluence. Relatively at lower fluence (10^{6}Wcm^{-2}), the LSC waves are occurring during plasma expansion. In this case there will be precursor shock wave ahead of plasma and absorption zone. The shocked gas remain transparent so that the plasma can absorb the laser energy and propagate into the shocked gas which results in to the LSC wave. This shock wave increases the ambient gas density, pressure and temperature. The radiative transfer from the hot plasma to the high pressure cold shocked gas is the main mechanism for the LSC wave formation. As the laser fluence increases, at intermediate fluence ($10^{10\text{-}11}$ Wcm^{-2}), the shocked gas is hot enough to absorb the laser radiation itself without further getting heated from the plasma radiation. In this case, there is no demarcation boundaries between plasma, absorption zone and the shocked gas. The pressure, temperature and the density continuously vary between the plasma absorption zone and the shocked gas and these move with the same velocity too. The propagation of the LSD wave is driven by the absorption of laser energy by the shocked gas.

The velocity of shocked gas is found to be higher in the LSD regime than LSC. At very high laser fluence, the plasma is generated with a very high temperature and the ambient gas also acquires high temperature directly via absorption of laser radiation, before the arrival of shockwave it is able to absorb the laser radiation. In absolute LSR domain without any change in pressure and density, the ambient gas can absorb laser energy directly and get ionized. The absorption wave propagates with the very high velocity in LSR compared to those of LSC and LSD mode.

1.1.3 Plasma cooling and emission of radiation

During the expansion of LIP in the ambient gas, plasma cools down by various processes and emits radiation [63]. LIP radiation comprising of continuum as well as discrete lines of atomic and ionic emissions of the constituent elements of the target. In the initial phase of plasma evolution, the plasma emission is dominated by the continuum emission [64]. The continuum radiation is emitted by the plasmas as a result of free-free and free-bound transitions [56]. Free-free transitions (Bremsstrahlung emission) is emitted when a charged particle is deflected in the vicinity of the coulomb field of another charged particle. Free-bound transitions occurs when a free electron recombines into the bound states of an ion. If E_0 is the energy of the free electron ($1/2mv^2$) and χ_i is the ionization potential of the i^{th} level of the ion, the energy of the emitted photon is given by $h\nu = E_0 - \chi_i$,. Since the kinetic energy of the free electron follows the continuous distributions, the recombination radiation spectrum is also continuous.

The line radiation is emitted in LIP as a result of recombination of ions and electrons and subsequent relaxation of these via line emission. These transitions occur between two bound states of atom or ion, hence this transition is referred to bound-bound transition. Various processes through which line radiation emitted are following:

Three body recombination: This process occurs when the two free electrons enter at the same time into the region of plasma containing ion and one of the electron is captured in bound state, while the other takes up the extra energy (equation (1.3)). This leads the atom (or lower ionization state ion) in the excited sate which decays to the lower energy level releasing the photon

$$\begin{aligned} A^{+} + e + e &\rightarrow A^{*} + e \\ A* &\rightarrow A + h\nu \end{aligned} \tag{1.3}$$

Radiative recombination: when a free electron passing in the vicinity of a positive ion recombines to an excited state resulting in to the radiative transition known radiative recombination

$$A^{+} + e \rightarrow A^{*} \rightarrow A + h\nu \tag{1.4}$$

Dielectric recombination: In this process, a free electron recombines into an excited state of the ion and the extra energy is taken up by one of the highly excited bound state of the atom, which then decay via cascade process to suitable lower states and the chain of line radiation is emitted.

$$\begin{aligned} A^{+} + e+ &\rightarrow A^{**} \\ A^{**} &\rightarrow A^{*} + h\nu_1 \\ A^{*} &\rightarrow A + h\nu_2 \end{aligned} \tag{1.5}$$

Charge exchange recombination: In this process, ion A^{+} picks an electron from atom B, and recombine to form excited atom A^{*}, leaving B ionized. The excited atom decays to lower states by emitting the radiation.

$$A^{+} + B+ \rightarrow A^{*} + B^{+}$$
$$A^{*} \rightarrow A + h\nu \quad (1.6)$$

Electron impact excitation and de-excitation: In electron impact excitation, a free electron that moves near to an ion loses energy by exciting a bound electron from a lower state into higher state of the atom later of which decays releasing the photon.

$$A + e \rightarrow A^{*} + e$$
$$A^{*} \rightarrow A + h\nu \quad (1.7)$$

For electron impact de-excitation, an electron moving near an excited ion induces a downward ionic transition from an upper state to a lower ionic state.

$$A^{*+} + e \leftrightarrow A^{+} + e + h\nu \quad (1.8)$$

1.1.4 Particulate formation

The last stage of plasma expansion is condensation of plasma and particle formation. LIP cools down after expansion/traversing certain distance from the target experiencing the fall in plasma temperature below the boiling point of the sample material and thus atoms molecules begin to condense and form micro/nano-particles. The size of particles are determined by the cooling time, and the density of the plasma plume [65, 66] etc. Thus the LIB is also being viewed as an efficient technique for the synthesis of various kinds of nanoparticles.

1.2 Laser induced breakdown spectroscopy

LIBS is an optical emission based spectrochemical analytical technique where the emission lines from LIP are analyzed for the qualitative as well as quantitative studies of the sample.

The qualitative and quantitative studies of LIP through LIBS technique relies on the accurate determination of plasma temperature and electron density. The determination of these plasma parameters depend on the validity of local thermodynamic equilibrium (LTE) and emission of optically thin lines from LIP. But these criteria are not always possible to be maintained inside LIP, due to its highly transient and inhomogeneous nature. These plasma parameters varies both in time and space. The LIB is a complex phenomenon and strongly dependent on the experimental parameters in turn influencing the LIBS technique [67].These experimental parameters include laser parameters [68] (i.e. wavelength, energy, pulse duration), physical and chemical properties of the target material, the geometry of laser focusing for plasma production, the surrounding ambient conditions (gas species, pressure) which effect the laser material coupling and the morphology of the plasma. All these parameters effect the LIB processes altogether, so it is not possible to study, the effect of any individual parameter without considering the indulgent of the other. An overall studies on how each of these parameters influence on LIBS behavior is presented in this section.

1.2.1 Influence of laser parameters on LIBS

The initial breakdown of the target material depends on laser wavelength, its pulse width and the energy incident on the target. The wavelength of the laser plays a significant role in the ablation. The mass ablation rate is given by the following equation [69],

$$\dot{m} = 110 \left(\frac{I^{1/3}}{10^{14}} \right) \lambda_l^{-4/3} \tag{1.9}$$

where the mass ablation rate is denoted as $\dot{m}$ (kg/s cm^2), laser wavelength (λ_l), and the absorbed laser intensity I (W/cm^2). The equation (1.9) clearly indicates that the mass ablation rate

increases at shorter wavelength. At shorter wavelength, laser energy is more effectively couple to material and it is favorable for LIBS signal as it will give high signal to noise ratio (SNR). The formation LIP on the surface of a target primarily occurs due to the absorption of laser energy by two different photo absorption processes (i) IB and (ii) photoionization of excited or ground sate atom. The IB absorption coefficient varies approximately λ^3 equation (1.1) and thus for longer wavelength this process is highly dominant [70-72]. Hoffman et al. [73] estimated the ratio between absorption coefficients for the ablation of carbon target at 1064, 532, and 355 nm and the reported ratio of ablation is approximately 9:2:1. So in general it is due to the dominance of IB absorption at longer wavelength the temperature and lifetime of LIP will increase.

The effect of laser pulse width on the LIP is also documented in the literature [74-77]. It has been observed that plasma emission intensity, continuum radiation and plasma temperature increases with increases of laser pulse width. The reason behind this is, that the trailing part of laser pulse in case of nanosecond laser will further heats the plasma there by increase in its parameters as compared to that of the picosecond and femtosecond laser, the later of which are too short duration to interact with the plasma after its formation [75].

During the laser ablation processes; (i.e. melting, fusion, sublimation, erosion, explosion etc.) are strongly depended on the laser energy [78]. For the given pulse duration, and the laser spot size on sample, mass ablation increases with the laser energy there by results in to the higher emission intensity, plasma temperature and electron density [79]. This increase in plasma parameters with the laser energy will be up to a certain energy range only beyond which there is no further increment in the plasma parameters with laser energy. This situation known as plasma shielding [80, 81]. In case of plasma shielding, the electron density becomes very high

to the extent that the plasma frequency $\nu_p=8.9\times10^3N_e^{0.5}$exceeds the laser frequency and reflects the laser energy in the trailing edge of the laser pulse and prevent the laser beam from falling on to the target thus curtailing the further ablation. According to Harilal et al. [82], the saturation in plasma parameters at higher incident laser energy is not possible to explain only by two laser energy absorption mechanisms of IB and photoionization process. For this, the 'self-regulating regime' is derive to take care the saturation effect in plasma parameters. If the absorption energy by the plasma becomes higher due to high plasma density, the ablation from the target is curtailed, which in turn decreases density of the charged species. This consequently increases the absorption of the laser energy by the target which in turn increases the temperature of the plasma. Otherwise, when the absorption of the laser energy is less the process is reversed with similar results. The whole process continues and the situation is known self-regulating regime.

1.2.2 Effect of the surrounding medium

The LIP expands away from the target and normal to the target in the surrounding environment. The LIP coming out from a solid is having particle number density of the order of 10^{22} cm^{-3} and evolves in the surrounding air medium of particle number density of the order of 10^{19} cm^{-3}. Due to this large difference in particle number density, there is a pressure gradient between LIP and surrounding air medium and to counter the pressure gradient, LIP expands away from the target at supersonic speed. Thus the plasma dynamics, plasma plume morphology and plasma emission are strongly affected by surrounding ambient gas. The affect of the presence of various types of gas and the pressure of the ambient gas on the plasma parameters and LIBS studies have been reported by several research groups [83]. Majority of the reports on LIBS are performed in air, O_2 and inert gas (Ar, He, N_2, Co_2). Bashir et al. [84] investigated the LIP

of Cd in air, Ar, and He by focusing a 1064 nm laser in the pressure range of vacuum to atmospheric pressure. It is found that the plasma temperature, Ar>Air>He at all the gas pressure. The mass of the background gas, ionization energy and thermal conductivity all together affect the LIP parameters. The lower values of the ratio of ionization energy to mass is more favorable for the process. The higher the conductivity of the surrounding gas, LIP loses energy easily and thus there is a faster decay of plasma parameters. The energy loss from LIP is inversely proportional to the mass of background gas.

In many of LIBS studies, gas pressure is varied from vacuum to very high atmospheric pressure. Most of the studies showed that as the gas pressure increases from vacuum to atmospheric pressure there is an increase in plasma emission intensity as well as plasma parameters [78, 85]. At higher ambient pressure, confinement of the plasma and collisional heating are responsible for this increment [86],

1.2.3 Target characteristics and geometry

The breakdown threshold of a material, the plasma formation and plasma properties are dependent on the physical and mechanical properties of target (thermal properties, optical absorption coefficient, surface reflectivity, melting and boiling points, latent heat of fusion and evaporation and ionization potential) [87]. The simulation studies presented by Bleiner et al[88], confirm that plasma temperature follow the trend Cu> Zn> Mn >Fe > Mo> Al. Higher absorption coefficient, thermal conductivity and boiling temperature produces more high temperature plasma. There are several studies on the influence of sample hardness on plasma properties [89]. In general it is found that the lower thermal conductivity of the sample, the generated plasma attains to higher temperature.

The formation of cavity on the sample surface confine the plasma, so with the higher cavity ratio (depth/diameter values) will contribute to higher temperature of the plasma [90].The optical alignment geometry for generation and collection of signal from the plasma influence the LIBS accuracy [91]. In the air medium, for LIBS the air breakdown is to be avoided in front of the sample, so the focal length of the lens as well as separation between target and lens are to be adjusted carefully [92-94]. In case of liquid in order to protect the optics from the splashing liquid, focus of the laser beam directed on the surface should be oriented optimally [95].

1.3 Objective of the present work

The LIP as well as its emitted radiation are highly exuberant in nature and its parameters vary drastically with distance from the target surface both along the plume expansion direction (axial) and orthogonal to plume expansion directions (radial) and as well as with the time immediately after the onset of LIP [96]. So the elemental analysis of a sample (identification of the constituent elements and percentage composition) and estimation of plasma parameters through the LIBS is a very challenging task. The analysis of data from LIBS are dependent on the LTE and optical thin condition of plasma. For the quantitative analysis, the calibration free LIBS (CF-LIBS) technique is being viewed as a relatively handy tool for the elemental compositional analysis [97]. The analytical performance of quantitative analysis aspect of LIBS technique i.e. limit of detection, accuracy and reproducibility using CF-LLIBS is not up to the mark at present compared to that of the other well developed analytical techniques [31]. This is due to the complex nature of laser-material and the laser plasma interaction along with highly transient and inhomogeneous nature of LIP which depends on various parameters as discussed in previous sections. Therefore the present work is aimed towards the time and space

resolved LIBS analysis of LIP to identify the optimum time and space window where all the conditions of LTE and optical thin plasma are applicable for qualitative as well as quantitative analysis through the CF-LIBS. In the present thesis work LIBS is performed on tungsten (W), molybdenum (Mo) and three different alloys of copper (Cu-alloy).

Tungsten, Molybdenum, their alloys and multilayers with other elements like Rh, Cu, and C etc. have been proved to be one major surface material for future tokamak diverter and first wall plasma-facing components (PFC) [98-102] in ITER and fusion reactor because of their favorable good physical–chemical properties such as high melting point, low activation, superior thermo-mechanical properties, low sputtering erosion and low tritium retention and co-deposition [103-106]. Further the nanostructures of compound elements of tungsten, WO_3, WS_2, WSe_2 and that of molybdenum MoO_3, MoS_2, $MoSe_2$ etc. have distinctive properties of electrochromism, photochromism, gas sensing, photo catalysis, photoluminescence which is useful various application in optoelectronics devices [107-109]. The LIBS technique is also being thought of as means to measure the basic atomic parameters i.e. Einstein coefficient of spontaneous emission and electron impact parameters. There are very few reports on the LIP of tungsten and molybdenum [71, 105, 110-115] and as well as scarcity in available atomic data for the transitions lines required for the LIBS studies.

Therefore, these two elements are considered as target material under LIBS study. The third sample, Cu alloys, is extensively used in cultural heritage and industry and its properties are highly influenced by its composition. There is a requirement for quick and online analysis of copper based alloys, i.e. brass, in art restoration as well as in industrial production. The quantitative analysis of Cu-alloys by LIBS is of great challenge because there is a considerable difference in the melting and vaporization temperature of the constituent elements which can

result in nonstoichiometric ablation [58, 116-118]. Therefore, copper alloys are subjected to single line CF-LIBS measurement as an application of LIP in the present thesis work. The entire thesis work is distributed in following eight chapters.

Chapter 1: The first chapter on **'Introduction'** gives a brief introduction to LIP and background review of LIBS as a spectrochemical analytical tool for various applications. The basics of laser-matter interaction, laser ablation and laser plasma interaction for the nanosecond laser pulse is described. The essential influencing parameters for the laser ablation and LIBS studies are discussed and a detailed literature survey is provided to get insight of LIBS technique.

Chapter 2: The second chapter is on **'Characterization of Laser Induced Plasma using LIBS'** describes the methodology of analyzing the LIBS data. In the first section of the chapter, the necessary assumptions for estimation of plasma parameters using LIBS are described. The next section describes the method for estimation plasma temperature and electron density from LIBS signal.

Chapter 3: The details of the experimental setup used in the present thesis work to record the time and space resolved spectra from LIP in air as a function of incident laser energy are described in this chapter on **'Experimental Details'**.

Chapter 4: In this chapter, **'Time and Space-Resolved Studies on Laser Induced Plasma of Tungsten in air'** the LIP of tungsten plasma is studied in detail using time and space resolved LIBS. The time and space evolution of the plasma emission, signal to noise ratio (SNR), plasma temperature and electron density are reported as a function of laser energy.

From these studies, optimize temporal and spatial window are identified for LIBS studies where the condition of LTE, optical thin condition of plasma are verified having large SNR.

Chapter 5: This chapter, **'Time and Space-Resolved Studies on laser induced plasma of Molybdenum in air via LIBS**' represents the time and space resolved studies on molybdenum plasma in air at various laser energy in the same manner similar to that of the chapter 4.

Chapter 6: The CF-LIBS technique is applied to three different Cu-alloys to estimate elemental composition of the constituent elements. The aim of work presented in this chapter on **'Single-Line Calibration Free LIBS Technique on Cu-alloys for Compositional Analyses'** is to study the effect of delay time and axial distance from the target sample surface on the analytical performance of CF-LIBS technique. To do this, single line CF-LIBS algorithm is applied and concentration of the percentage composition of the constituent elements are estimated as a function of delay time and axial positions at various incident laser energies. This study reveals that there is a need to optimize the temporal and spatial window to meet all the necessary requirements of CF-LIBS for higher accuracy.

Chapter 7: Due to the laser ablation and plasma formation there is a formation of crater and re-deposition on sample its surface in the focal region. In this chapter, '**Surface Morphological Characterization of Laser Ablated Sample',** these craters are studied using optical microscope. The depth profile of the crater is measured using surface profilometer and mass ablation rate as a function of laser energy is reported. The FESEM images of crater surface provide the information about the micro and nano-structured re-deposited materials. The Raman spectra identified molecular formation of the micro and nano structure.

Chapter 8: The conclusions drawn from the present studies and some of the directions for future work on the subject matter are listed in the **'Conclusion and Future Scope'** chapter.

Chapter 2 Characterization of Laser Induced Plasma using LIBS

The high power pulsed laser induced plasma (LIP) is highly transient in nature as well as very complicated due to the occurrence of various processes simultaneously in it. It is characterized by time and space resolved evolution of its plasma temperature and electron density. There are several plasma characterization techniques for measurement of plasma parameters in LIP. Some of these are laser induced breakdown spectroscopy (LIBS) [96] [119], Langmuir probe [120], microwave and laser interferometry [121], Thomson scattering [122], fast imaging technique [123] [82] etc. Among these, LIBS is a non-contact diagnostic tool capable of delivering time and space resolved plasma parameters. In the present thesis work, LIBS is employed for the characterization of LIP in air. In next section, section 2.1 describes the LIBS technique in brief and the necessary assumptions of local thermodynamic equilibrium (LTE) and optical thin plasma condition for the determination of the plasma temperature and electron density. In section 2.2, Boltzmann plot method is described for the estimation of plasma temperature and the stark-broadened method to estimate the electron density.

2.1 Laser induced breakdown spectroscopy

Among various diagnostic technique the most important diagnostic tool for characterizing LIP properties is LIBS. When a high power pulsed laser is focused onto the surface of a material, it ablates a small amount within the focal region and produces a transient inhomogeneous laser induced plasma (LIP). The LIP expands in the surrounding medium and cools down, emitting characteristic radiation comprised of atomic and ionic lines of constituent elements present in the sample under investigation. Thus by exploiting the optical emission, LIP can be easily

characterized as well as constituent elements in the sample can be identified. This technique is known as laser induced breakdown spectroscopy (LIBS). It is a non-invasive technique having benefit of remote measurement without perturbing the plasma during its formation and evolution. It provides the important information regarding the neutral and ionic species within the plasma, as well as instantaneous information concerning the plasma density, temperature and degree of ionization. LIP characterization is based on mainly two assumption (i) local thermodynamic equilibrium (LTE) and (ii) optical thin condition of plasma [78, 96]. In the following sections, the validity of LTE and optical thin conditions along with the Boltzmann plot method and stark-broadened profile measurement are described for the estimation of plasma temperature and electron density respectively.

2.1.1 Local thermodynamic equilibrium (LTE)

LIP is highly transient and inhomogeneous in nature. The various processes involved inside expanding LIP are collision ionization, photo-ionization, radiative and three-body recombination, collisional excitation and de-excitation, photo-excitation, Bremsstrahlung etc. [78]. To obtain the kinetic information about LIP, there is a need to solve a complex set of simultaneous equations describing all of these processes assuming the system is in thermodynamic equilibrium. In case of complete thermodynamic equilibrium (TE) all processes in LIP will be in equilibrium with each other. This is possible when the rate of each process is same as that of the inverse processes, known as principle of detail balance [78]. In TE, the entire LIP system, comprised of different species, is described by a single temperature and the state of the whole system made up of different species are described by a series of equilibrium distribution function of energy [124]. Under TE conditions, the Boltzmann

distribution law gives the relative population of excited levels of an atom or ion, given by following equation [78, 96, 124],

$$N_n = N \frac{g_n \exp\left(\frac{-E_n}{k_B T_e}\right)}{U(T_e)} \tag{2.1}$$

where N_n stands for the population of certain quantum level n, g_n the degeneracy of that level, E_n the corresponding energy of that n level, N the total number density of the species under consideration, k_B the Boltzmann constant, T_e and $U(T_e)$ are the temperature and the partition function. The number densities of any particular species in different ionization stages can be described by the Saha–Eggert equation [78, 125, 126]

$$\frac{N_e N^{z+1}}{N^z} = 2\frac{U^{z+1}}{U_Z}\left(\frac{2\pi m_e k_B T_e}{h^2}\right)^{3/2} \exp\left(\frac{-E_z + E_{z+1} - \chi}{k_B T_e}\right) \tag{2.2}$$

where N_e represents the electron number density, N_z the number density of z^{th} ionization state, N_{z+1} the number density of next lower ionization stage, m_e the mass of the electron, χ the first ionization energy for an isolated system. Finally, in case of TE, the radiation within it also has a well-defined distribution of energy that depends on temperature. The spectral energy density of a photon in vacuum $W(\nu)$ at temperature T_e is given by following equation [78, 96, 124],

$$W(\nu) = \frac{8\pi h \nu^3}{c^3}\left(\frac{1}{e^{\frac{h\nu}{k_B T_e}} - 1}\right) \tag{2.3}$$

In real situation in LIP, TE can never be possible due to its highly transient and inhomogeneous nature. In LIP , the radiative energy is decoupled from the other forms of energy and radiative equilibrium requires the plasma to be optically thick for all the emitted radiation (black body) [78, 124]. Obviously it is not the situation in LIP because photons escape from the plasma and

their energy distribution will no longer follow the Planck distribution function equation (2.3) and this will automatically disturb the principle of detail balance. Still if the energy released in the case of photons is smaller than that involved in the other processes for other species, the Saha–Boltzmann and Maxwell distributions are still a valid description of the LIP system and thus, a new equilibrium local thermodynamic equilibrium (LTE), condition is derived [78, 127]. LTE means that equilibration is maintained in a small region of space, although it may be different from one region to other. The LTE condition is a crucial and extremely necessary concept for plasma characterization and for the quantitative analysis using Calibration Free-LIBS (CF-LIBS). Though the accomplishment of LTE in LIP is not automatic and involves some special conditions. In the following sub sections, the conditions for the validity of the LTE in LIP are described for three different cases [128] where plasma is (i) stationary and homogeneous, (ii) transient and homogeneous and (iii) stationary but inhomogeneous.

In first case, the LIP is assumed to be stationary and homogeneous and to maintain the LTE criteria inside the plasma, collisional processes should be dominated over the radiative processes. This requires the electron number density in plasma should exceeds certain critical value given by Mc Whirter criterion [78, 129] ,

$$N_e\left(cm^{-3}\right) \geq 1.6 \times 10^{12} T_e^{1/2} \left(\Delta E_{nm}\right)^3 \qquad (2.4)$$

where ΔE_{nm} is energy the gap between the adjacent energy levels. The condition of LTE, equation (2.4) has to be fulfill for the maximum value of ΔE involved in the system. It usually corresponds to the energy differences between the ground state and the first excited state of an atom (or an ion).

The LIP is transient and inhomogeneous and therefore the McWhirter criterion is not a sufficient condition for LTE. Therefore in the second case, the LIP is assumed to be homogeneous but transient to take into account the additional requirement of the transient nature of the plasma. In this situation, the relaxation time τ_{rel} i.e. the time taken for the establishment of excitation and ionization equilibrium should be much shorter than that of variation in thermodynamic parameters: plasma temperature and electron density is expressed by the flowing inequalities [128, 130, 131].

$$\frac{T_e(t+\tau_{rel}) - T_e(t)}{T_e(t)} << 1 \tag{2.5}$$

$$\frac{N_e(t+\tau_{rel}) - N_e(t)}{N_e(t)} << 1 \tag{2.6}$$

If this condition is not fulfilled, the evolution of the plasma will be so fast that the electrons and atoms/ions do not get enough time to attain thermodynamic equilibrium. In order to check these criterion, equations (2.5) and (2.6), the thermodynamic relaxation time τ_{rel} is to be estimated. The τ_{rel} between the ground state and the first excited level is in general is the longest compared to that of the rest of the pair of the energy levels and can be estimated by [128, 131],

$$\tau_{rel} = \frac{6.3 \times 10^{4}}{N_e f_{mn} \langle g \rangle} \Delta E_{nm} (kT_e)^{1/2} \exp\left(\frac{\Delta E_{nm}}{kT_e}\right) \tag{2.7}$$

where f_{nm} represents transition oscillator strength of the line, $<g>$ is the effective gaunt factor [132]. The third case is the spatial domain, where the LIP is assumed to be stationary but inhomogeneous. In this case, the diffusion length of atoms or ions during the relaxation time should be shorter than the scale length (variation length) of the temperature as well as that of the electron number density in the plasma and is expressed by the following [128, 130, 131]

$$\frac{T_e(z + L_{dif}) - T_e(z)}{T_e(t)} << 1 \tag{2.8}$$

$$\frac{N_e(z + L_{dif}) - N_e(z)}{N_e(z)} << 1 \tag{2.9}$$

where z is the local position and L_{dif} is the diffusion length during the relaxation time. The estimation of diffusion length L_{dif} of atoms and ions is quite tedious as it requires the implementation of cross sections of collision processes occurring in the plasma and the absolute atom and ion number densities. Therefore for a rough estimation of the order of magnitude of L_{dif}, some approximations have to be used. Generally, the diffusion length of atoms is typically larger than those of ions. Therefore for the establishment of LTE, only diffusion length of atoms is to be considered. Under these assumptions, the diffusion length can be expressed as [128]

$$L_{dif} = (D.\tau_{rel})^{1/2} = 1.4 \times 10^{12} \frac{(kT)^{3/4}}{N_e} \left(\frac{\Delta E_{nm}}{M_A f_{nm}} \right)^{1/2} \exp\left(\frac{\Delta E_{nm}}{2kT_e} \right) \tag{2.10}$$

where D (cm^2s^{-1}) is the diffusion coefficient, M_A is the relative mass of the species under consideration and k_BT_e and ΔE_{nm} are expressed in eV. Thus LTE condition will be satisfied if the plasma dimension is significantly larger than the diffusion length i.e. at least ten times larger than this diffusion length [62].

2.1.2 Optical thin condition of plasma

The plasma is considered to be optically thin if the emitted radiation traverse and escapes from the plasma without undergoing any significant absorption or scattering [27] and thus the line profile is undistorted. If the plasma is optically thick then the self-absorption and self-reversal

leads to the distorted line profile [78, 96]. Fig. 2.1 illustrate the effect of self-absorption on the line profile [27]. As an example, one of the line radiation emitted from the LIP is depicted in Fig. 2.1 (a). The outer layer of the plasma is comprised of cooler species than those radiating from the core of LIP. The cooler species absorb the radiation emitted from the core of the plasma. This absorption profile from the same line is depicted in Fig. 2.1 (b). Then the observed line profile is given by the convolution of both these profiles, Fig. 2.1(a) and (b), leading to the appearance of dip around the central wavelength as shown in Fig. 2.1(c). This may lead to the confusion of having two closely spaced emission lines rather than the one single line. Self-absorption is more susceptible for the emission lines where the lower energy level of the transition is the ground state sometimes termed as resonant transition [128, 133].

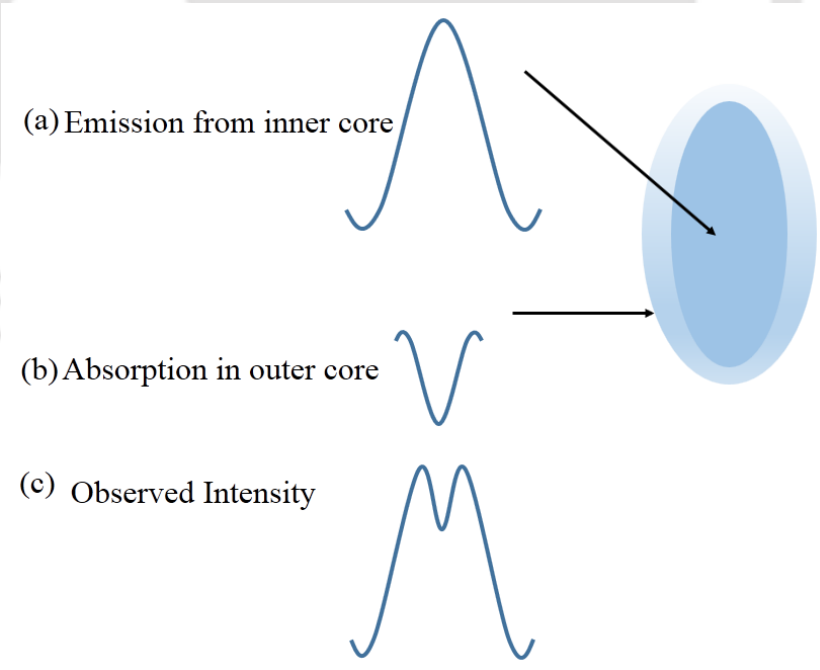

Figure 2.1 Illustration of Self-absorption phenomena in LIP.

In this case, the effective radiative population rate of the ground state is reduced by a certain factor which is of the order of the ratio of the actual intensity observed to the corresponding intensity in the absence of any self-absorption. This results in an enormous error in the estimation of plasma temperature and electron density via LIBS as described in the next section. Therefore, it is extremely crucial to have the optically thin plasma emission lines for the determination of plasma parameters and also towards the application of CF-LIBS for the spectrochemical analyses of multicomponent with high degree of accuracy. The optically thin condition of plasma can be verified by branching ratio method. It is the intensity ratio of two atomic lines of an element having the same upper level energy and is given by following equation [134, 135],

$$\frac{I'_{n'm'}}{I_{nm}} = \frac{g_{n'}A_{n'm'}\lambda_{nm}}{g_n A_{nm} \lambda_{n'm'}} \tag{2.11}$$

where I_{nm}, g_n, A_{nm}, and λ_{nm} are the line intensity, statistical weight, transition possibility, and wavelength of the emitted lines in LIP respectively and the primes refers to two different transitions under consideration. If experimental intensity ratio matches that of the theoretically observed value from equation (2.11) then the plasma can be considered to be optically thin.

2.2 Plasma parameters

Plasma temperature and electron density are the most important parameters for its characterization. Measurement of both these parameters employing LIBS are described in the following sections.

2.2.1 Plasma temperature

For an optically thin plasma under LTE condition, the excited levels of any given ionization state or neutral atoms are populated according to the Boltzmann distribution and successive

ionization states are populated according to the Saha–Boltzmann equilibrium equation (2.2). Under these conditions, the measured integrated spectral line intensity for a transition I_{nm} (J s^{-1} m^{-1} sr^{-1} nm^{-1}) from an upper level n to a lower level m is related to the energy of the upper state, E_n , and is given by the following equation [136-140]

$$I_{nm} = \frac{FNA_{nm} g_n}{\lambda_{nm} U(T_e)} \exp\left(-\frac{E_n}{k_B T_e}\right) \tag{2.12}$$

From equation (2.12) the intensities of two lines is given by following equation [78, 141],

$$\frac{I'_{n'm'}}{I_{nm}} = \frac{g_{n'} A_{n'm'} \lambda_{nm}}{g_n A_{nm} \lambda_{n'm'}} \exp\left(-\frac{|E'_n - E_n|}{k_B T_e}\right) \tag{2.13}$$

The intensity and wavelength are measured from the experimentally obtained LIP spectrum while other spectroscopic parameters involved in equation (2.13) are obtained from literature and thus making it possible to determine the plasma temperature using the intensity ratio of any two lines only. The advantage of this two-line Boltzmann method is its simplicity and quick way to assess plasma temperature particularly in the situation where just a very few transitions are recorded. The Accuracy of temperature estimation from the Boltzmann equation may be improved by involving a large number of different lines having upper energy sates widely apart. Taking the logarithm of the equation (2.12) and after rearranging it can be written as [136]

$$\ln\left(\frac{I_{nm}\lambda_{nm}}{g_n A_{nm}}\right) = -\frac{1}{k_B T_e} E_n + \ln\left(\frac{FN}{U(T_e)}\right) \tag{2.14}$$

The plot of the LHS of equation (2.13) against E_n for several number of transitions is a straight line. The temperature of the species can be thus be obtained from the slope, $-1/k_B T_e$, of the equation (2.14) without any knowledge of the partition function [126, 142, 143].

2.2.2 Electron density via stark-broadened profile

Electron density is another important plasma parameter required to be estimated with good accuracy. In LIBS, the electron density can be estimated from the stark-broadened profile of the emitted lines [96]. There are a number of broadening mechanisms that can affect the shape and width of a spectral line in LIP. These include natural, Doppler, collisional and stark-broadening. The minimum width of a spectral transition is its inherent natural line width which is due to the finite lifetime of species (atom/ion) in its excited states. Doppler broadening is due to the Doppler-effect caused by a distribution of velocity of atoms, ions or molecules [7]. In this case, the broadening depends on the frequency (wavelength) of the spectral line, the mass of the particles emitting the line radiation and plasma temperature. The full width half maximum (FWHM) of the Doppler broadened profile in LIP is given by [31]

$$\Delta\lambda_D = 7.16 \times \lambda_{nm} \times 10^{-7} \sqrt{\frac{T_e}{M_A}} \tag{2.15}$$

where $\Delta\lambda_D$ is the Doppler Broadening contribution in nm, and M_A is the atomic mass in a.m.u. and T_e is the plasma temperature in K. In LIP the, contribution of the Doppler broadening is very small in comparison to that of the stark-broadening. The emitting species (atoms or ions) in plasma are under the influence of electric fields by fast-moving electrons and relatively slow-moving ions. This perturbing electric field acts on atoms or ions and shift the energy levels, which cause broadening of the emission lines and is known Stark broadening. The broadening due to stark-effect is proportional to the electron density and FWHM of Stark-broadened line $\Delta\lambda_{1/2}$ is given by the following relation [96],

$$\Delta\lambda_{1/2} = 2w\left(\frac{N_e}{10^{16}}\right) + 3.5A\left(\frac{N_e}{10^{16}}\right)^{1/4}\left[1 - 1.2N_D^{-1/3}\right]w\left(\frac{N_e}{10^{16}}\right) \tag{2.16}$$

where N_e is the electron number density (cm^{-3}), w is the electron impact width parameter and A is the ion broadening parameter. Both w and A are weak functions of temperature and can be obtained from the literature. N_D is the number of particles in the Debye sphere and can be calculated by the following relation [133]

$$N_D = 1.72 \times 10^9 \frac{T_e^{3/2}}{N_e^{1/2}} \tag{2.17}$$

The first term in equation (2.16) refers to the electron broadening and the second term is the contribution from ion broadening, which is very small in the present case and can be neglected, thus equation (2.16) reduces to [96]

$$\Delta\lambda_{1/2} = 2w\left(\frac{N_e}{10^{16}}\right) \tag{2.18}$$

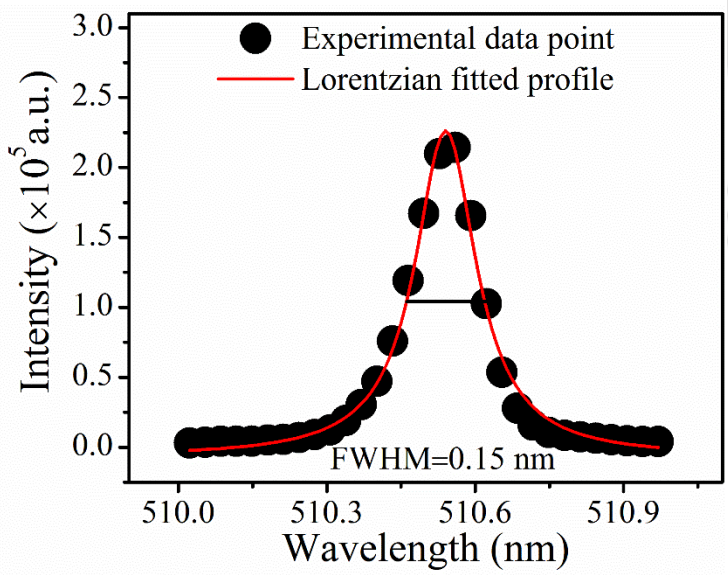

Figure 2.2 CuI-510.5 nm Stark-broadened profile fitted to Lorentzian function.

Thus by measuring the FWHM of well separated transition and taking the *w* value from the literature the electron density can be estimated from equation (2.18). The stark-broadened profile (the data point shown by full circle) of CuI-510.5 nm line recorded in LIP of one of the Cu-alloy and fitted to lorentzian profile (the solid curve line) is shown in Fig.2.2 as an example.

2.3 Conclusion

In the present chapter characterization of LIP via LIBS technique is discussed. The discussion mainly focuses on the measurement of plasma temperature and electron density. The measurement of these plasma parameters are based on the validity of LTE and optical thin condition of plasma. The LTE is discussed in three different situation of LIP i.e. (i) stationary and homogeneous, (ii) transient and homogeneous and (iii) stationary but inhomogeneous. The applicability of branching ratio method is mentioned for the assessment of the optical thin condition in LIP. The Boltzmann plot method to estimate the plasma temperature is described. Among various line broadening mechanism, the stark-broadened line profile is the dominant and is used to estimate the electron density inside the LIP and thus can be used to estimate the plasma density.

Chapter 3 Experimental Details

The laser induced plasma (LIP) have been studied in wide perspective. The LIP of large number single element as well as composite solid targets have been studied under vacuum or in low pressure gas for various applications i.e. as source of x-ray generation [23], pulsed laser deposition (PLD) [144] etc. The spotlight is also on the studies of LIP in liquid and laser target-liquid interaction not only to unveil the understanding of basic processes [145, 146] but also to numerous applications and generation of nano particles [147, 148] etc. In the present thesis temporal and spatial evolution of LIP of tungsten, molybdenum and alloys of copper have been studied via LIBS and CF-LIBS is applied to unveil the composition of various alloys of copper. In this chapter, the experimental setup to study the time and space resolved LIP spectrum as a function of laser energy is described.

3.1 Experimental set up for time-resolved LIBS studies

The schematic of the experimental set up to record the temporal evolution of LIP spectrum is shown in Fig. 3.1. The experimental system consists of 2nd harmonic of a Q-switched Nd: YAG laser (INNOLAS Split light 1200), pulse duration~7 ns, repetition rate 1Hz and capable of delivering the maximum energy of 600 mJ/pulse. The laser beam is steered suitably by a set of mirrors (in the schematic only one mirror is shown for the simplicity) and focused on to the targets. The target is mounted on to an X-Y linear translational stage (Newport ESP300) in order to move it across the laser beam so as to provide the fresh surface for each and every laser shots and avoid the formation of deep crater in order to ensure the reproducibility on shot to shot basis. On focusing of the laser beam, highly intense and luminous plasma is generated. This plasma radiation is collected at 45° with the incident laser beam by a system of collection

optics as shown in Fig. 3.1 and transmitted through an optical fiber of core diameter 600 µm which is coupled to the entrance of an echelle spectrometer (Andor Mechelle ME5000).

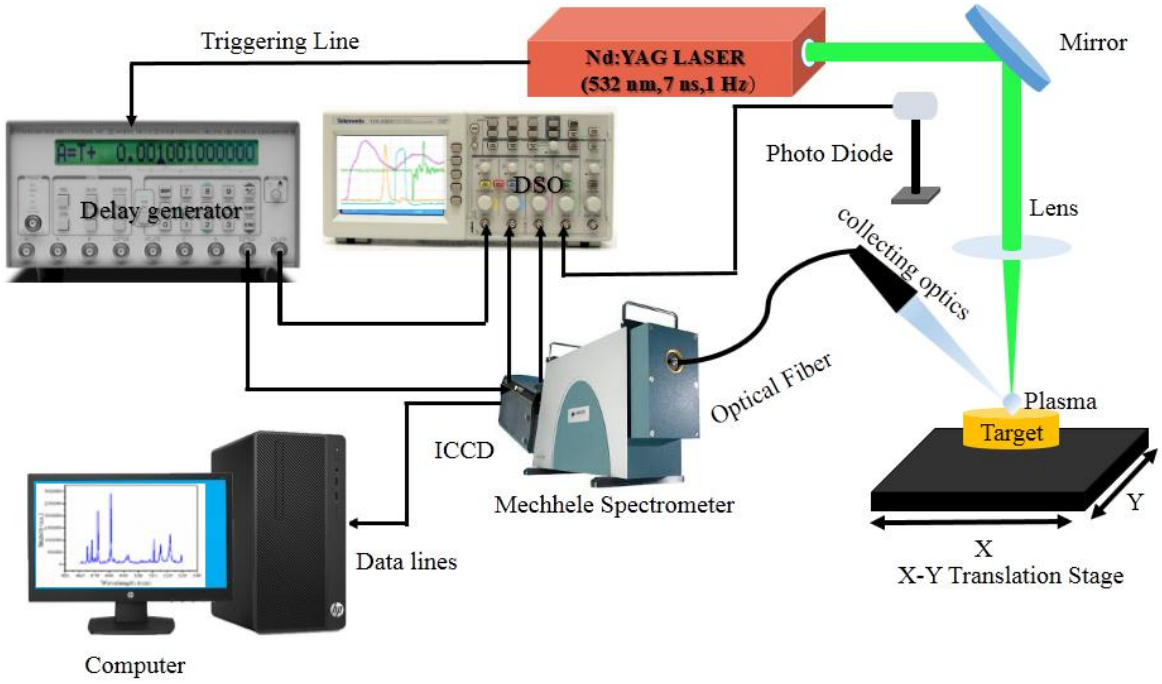

Figure 3.1 Schematic of the experimental set up in air for recording time-resolved spectra.

The Mechelle spectrometer is calibrated by using two standard calibration lamps namely the mercury-argon calibration lamp for wavelength and the deuterium halogen calibration source for intensity. The spectrometer is equipped with intensified charge coupled capacitor (ICCD) and interfaced to the computer, enabling the recording of the spectrum over a wide spectral range of 200–850 nm in a single shot acquisition. The schematic of laser pulse and the emitted radiation from the LIP as a function of time is shown in Fig. 3.2. Thus in order to record the temporal evolution of LIP spectrum ICCD is to be operated in gated mode. For this, a delay generator (Stanford Research Systems DG545) is triggered with the Pockels cell output of the laser and a desirable delayed TTL (0–5 V) pulse is generated from the delay generator to trigger

the ICCD. To monitor the arrival of laser pulse and opening of ICCD, a part of the laser beam is detected by a photodiode and is displayed on one of a four channel of a on digital storage oscilloscope (DSO) (Tektronix TDS 2024B) along with the ICCD gate delay on other channel simultaneously. On the third channel of DSO, delayed pulse is displayed and the ICCD gate opening pulse is fed to the fourth channel (this is also in Fig. 3.3 screenshot). The oscilloscope displaying all these four pulses are shown in Fig. 3.3. For the clarity saved data is plotted in Fig. 3.4. In order to avoid high intense continuum radiation in the initial stage of plasma formation, the spectra are acquired starting with a delay of 0.5 and recoded up to delay time of 5 µs in step of 0.5 µs. The gate width of the ICCD is maintained at 0.5 µs throughout the experiment. In order to improve both the signal-to-noise ratio (SNR) and the reproducibility, the spectra are recorded for each and every delay for 10 consecutive laser pulses and integrated automatically by built in software of ICCD. In this way ten distinct spectra are recorded for each and every delay and analyzed independently.

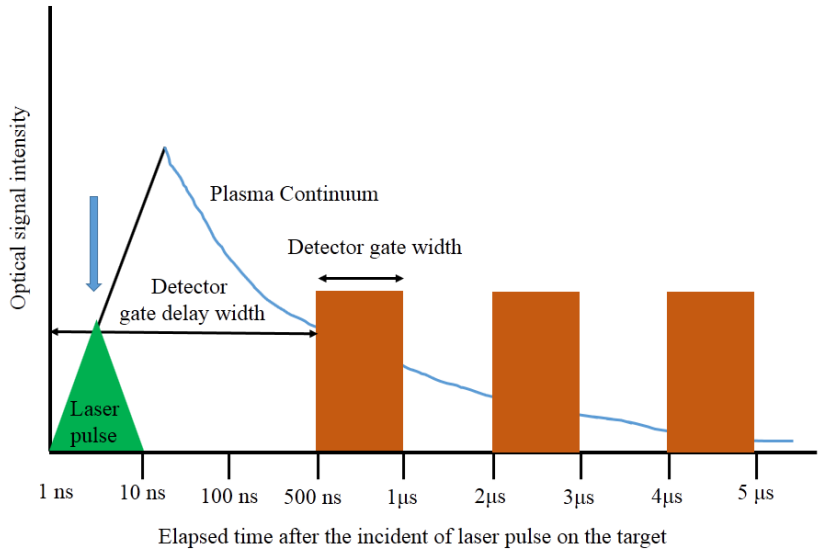

Figure 3.2 Schematic of overview of the temporal evolution of LIP in LIBS studies.

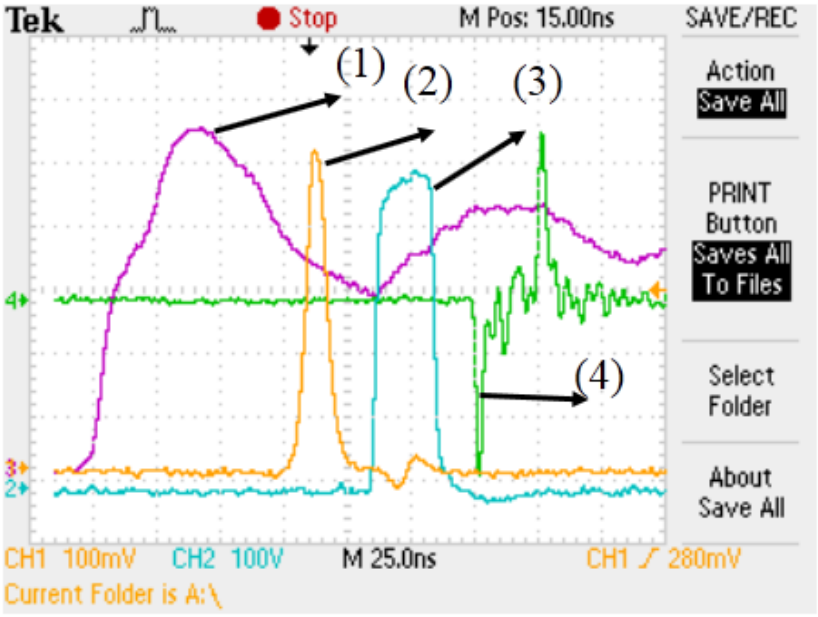

Figure 3.3 Oscilloscope trace (1) pockel cell, (2) laser pulse (3) delay generator pulse and (4) ICCD gate opening pulse.

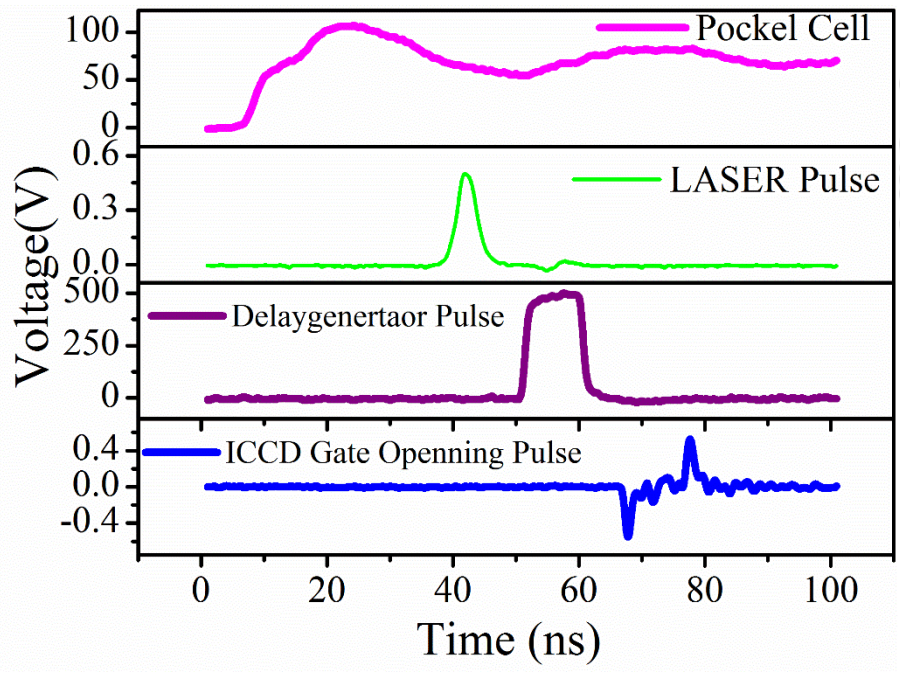

Figure 3.4 Timing scheme diagram for triggering ICCD detector for recording Time-resolved spectra.

3.2 Experimental set up for space-resolved LIBS studies

The experimental setup used for space-resolved spectroscopic analysis of the plasma plume is sketched in Fig. 3.5 and is similar to that of the temporal evolution with the difference in the collection optics.

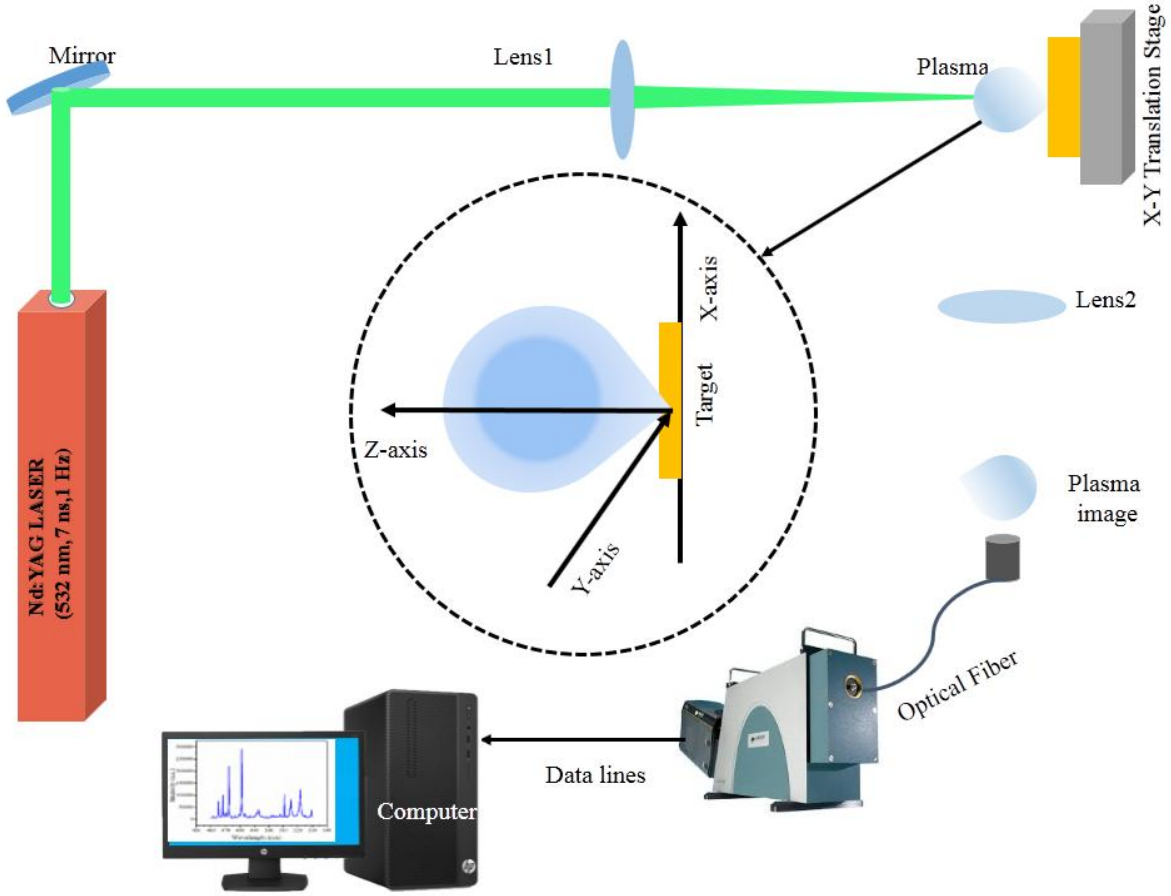

Figure 3.5 Schematic experimental setup in air for recording space-resolved spectra.

In this, a lens of focal length of 10 cm is used in one to one the configuration to form an inverted image of the plasma with a magnification of unity. The laser beam is assumed be along z-axis, the plasma emission is collected using an optical fiber of 400 μm core diameter positioned in the image plane (x-z plane) as shown in Fig. 3.5. The fiber is positioned on a

motorized linear-translational stage. The movement of this stage along the z axis enables the collection of radiation from the various slices of the LIP along the direction of plasma expansion. The scanning step is maintained at 0.4 mm to match the diameter of the optical. These space-resolved signals are transmitted through the optical fiber fed to the echelle spectrometer. In space-resolved studies, the ICCD gate delay is kept fixed at 2 μs w.r.t laser pulse as this is within the range of optimum temporal window where the LTE and optical thin condition of plasma are satisfied. The acquisition time is maintained at 10 μs.

In the present thesis work, the incident laser energy is varied from 25 -100 mJ by controlling the voltage of the flash lamp. The laser beam focused by a lens of focal length of 15 cm on to the samples at normal incidence in air. The diameter of the beam spot size on the targets are measured by optical microscope (OLYMPUS BX51M) and found to be 230 μm .There is no change in the focused area with the incident laser energy. The images of single shot laser on to the three targets, tungsten, molybdenum and one of the Cu-alloy (commercial brass) is shown in Fig. 3.6 at a laser energy of 25 mJ as an example. From this, the laser fluence (=Energy/Area) as well as intensity (Power/Area) onto the target surface is estimated and is listed in Table 3.1.

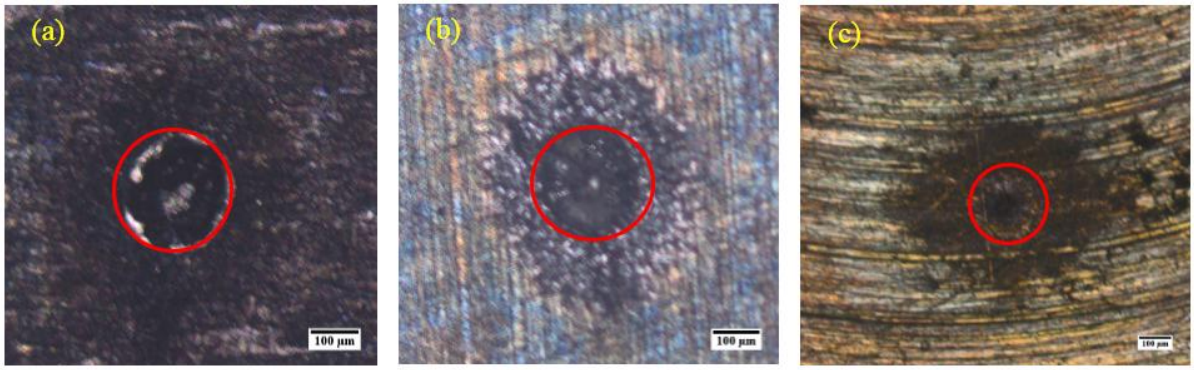

Figure 3.6 Laser focused spot from single shot laser ablation on (a) tungsten, (b) molybdenum and (c) copper alloys target for incident laser energy of 25 mJ.

Table 3.1 The laser energy, fluence and intensity in the present work.

Laser Energy (mJ)	Fluence (J cm^{-2})	Intensity ($\times 10^9$ W cm^{-2})
25	60	8.60
50	120	17.20
75	240	25.80
100	360	34.4

3.3 Conclusion

In this chapter, the experimental set up employed for the recording of time and space resolved emission from the LIP is described. In LIBS experiment, the three main required component i.e. (i) high power laser focusing optics, (ii) collection of emitted radiation from the LIP and (iii) the time sequence to record the spectrum w.r.t laser pulse for the studies on the temporal evolution of plasma. For the temporal evolution studies, the plasma emission is recorded as function of delay time w.r.t laser pulse over temporal window of 0.5-5 μs in a step of 0.5 μs. In case of space evolution studies of LIP, the delay time is kept fixed in the optimum temporal range and the emission spectra are recorded from the different location of the plasma. Both the studies are performed at four different incident laser energies.

भारतीय प्रौद्योगिकी संस्थान गुवाहाटी
Indian Institute of Technology Guwahati

Chapter 4 Time and Space-Resolved Studies on Laser Induced Plasma of Tungsten in air

Tungsten is being considered as one of the important materials used in-vessel components of thermonuclear reactors [149]. Its various properties, such as high thermal conductivity and melting point [150], low tritium retention [151, 152], sputtering yield [153], erosion rate [98] and high neutron load capacity [154] make this metal a suitable candidate for plasma-facing components (PFC) in the fusion reactor [155, 156]. During the operating condition inside the fusion vessel, several kinds of complex phenomenon take place between the plasma and inner walls of the vessel [157, 158]. Due to interaction of plasma, the PFC undergoes erosion and deposition [104].The deposited layer enhances the fuel retention of PFC and alter its properties which in turn deteriorate the performance of the fusion reactor. The deposited amount should be within below certain limit so as not to affect its performance [159]. To maintain the high performance and safety of fusion reactor, there is an active need of monitoring deposited materials on PFC and in order to implement its appropriate cleaning. At present, offline method is employed to study the thickness of the deposited material and its composition but this method is limited due to time integrated effect [159]. For the online monitoring , Laser-induced breakdown spectroscopy (LIBS) is being considered to be suitable for analysis of composition and quantification of the PFC depositant [160]. Apart from its utility in nuclear reactor, laser ablation of tungsten using high power pulsed laser is finding its various applications such as the deposition of high quality thin films [161, 162] and fabrication of micro/nanostructures of compound elements of tungsten (WO_3, WS_2 etc.) which are used for sensor and optoelectronics devices [163, 164]. All these applications are strongly dependent on LIP dynamics and plasma

parameters. So the detailed knowledge about LIP evolution to understand the mechanism involved in laser-target and laser-plasma interaction is very much required for optimizing experimental parameters for cost-effective implementation. But there is a scarcity of the reported literature on tungsten and lack of database on atomic parameters for the transitions of tungsten.

Therefore, in this chapter, the time and space evolution of the LIP of tungsten is reported as a function of incident laser energy in air. The plasma parameters are measured in both the studies via LIBS. The optical thin radiation and LTE condition of LIP are explicitly studied for transient and inhomogeneous LIP. These studies provide the optimum temporal and spatial window for studying LIP of tungsten in air for various application i.e. measurement of transition probability [101, 165], CF-LIBS [157]etc.

4.1 Time-resolved studies on LIP of tungsten

The temporal evolution of LIP of tungsten in air is studied by recording the emission spectrum in the delay time range of 0.5-5 μs w.r.t incident laser pulse using the experimental set up described in section 3.1 and shown in Fig. 3.1. The spectra are recorded at four different incident laser energy of 25, 50, 75 and 100 mJ. In the following sections the experimental results are presented for the temporal variation of the plasma emission intensity, plasma temperature and electron density. The optical thin condition of LIP and LTE criteria, the two essentials condition are verified in the present case for plasma characterization to assess the suitable temporal window.

4.1.1 Time-resolved emitted intensity of WI and WII transitions in LIP of tungsten

The time-resolved spectra recorded at four different laser energies i.e. 25, 50, 75 and 100 mJ in delay time range of 0.5-5 μs are shown in Fig. 4.1 (a), (b), (c) and (d) respectively. The spectra are analyzed and several atomic and ionic transitions of tungsten are identified using NIST [166] and Kurucz database [167] respectively. The expanded view of the temporal variation of the spectra in the range of 266-278 nm and 429-431 nm is shown in Fig. 4.2 (a) and (b) respectively at a laser energy of 25 mJ. As an example, the lines of WII at 265.8, 270.2 and 276.4 nm are marked in the Fig. 4.2 (a) and that of the neutral atomic lines, WI, at 429.4, 430.2 and 430.7 nm in the Fig. 4.2 (b).

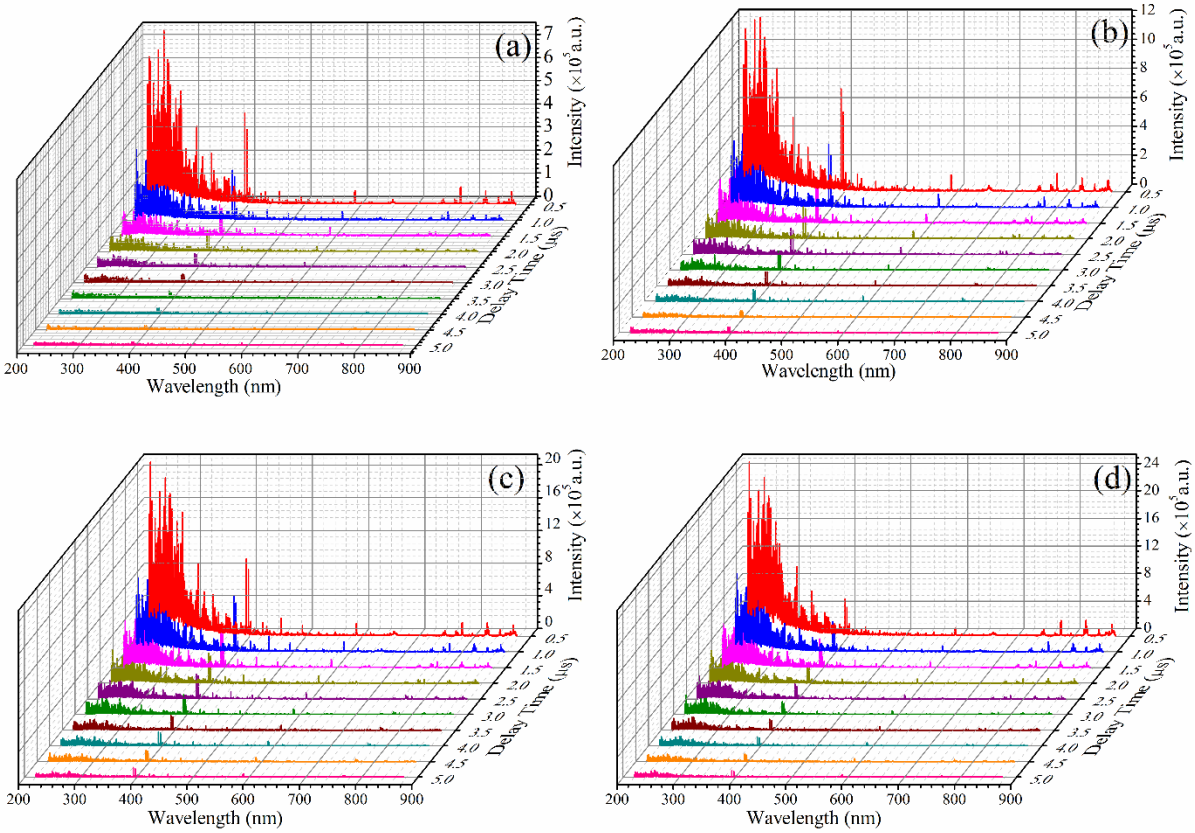

Figure 4.1 Temporal evolution of plasma emission from LIP of tungsten at (a) 25, (b) 50, (c) 75 and (d) 100 mJ of incident laser energy.

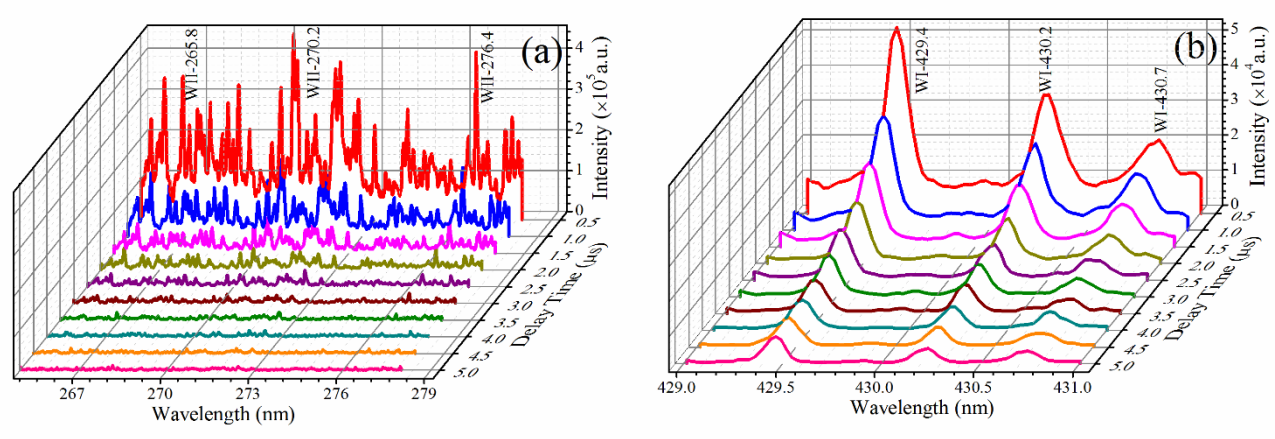

Figure 4.2 Expanded view of the spectrum in the range of (a) 266-278 nm (b) 429-431 nm for the incident laser energy of 25 mJ.

In the UV spectral range of 200-300 nm, the spectra is dominated by ionic transitions whereas in the visible range, 300-850 nm, the emitted spectral lines are attributed to mainly atomic transitions. The variation of decay profile for ionic and atomic transitions as a function of incident laser energy are shown in Fig. 4.3 (a) and (b) respectively. The decay time of ionic and atomic lines is the time over which the initial intensity fall down to 1/e factor. The decay time is estimated from these temporal profile by fitting the exponential data points to exponential decay. The variation of the decay time of ionic and atomic lines are shown in Fig. 4.3(c) as a function of incident laser energy. From this, Fig. 4.3(c), it is observed that decay time for ionic line is 0.60 (±0.02), 0.84 (±0.04), 1.06 (±0.03) and 1.02 (±0.04) μs and that of the atomic line is 1.26 (±0.03), 1.63 (±0.09), 1.65 (±0.01) and 1.59 (±0.09) μs at four incident laser energy of 25, 50, 75 and 100 mJ respectively. The decay time for atomic as well as for ionic lines increases with the increase in laser energy up to 75 mJ and then there is marginal fall in it. This is due to the plasma shielding at higher laser energy [60, 72] .

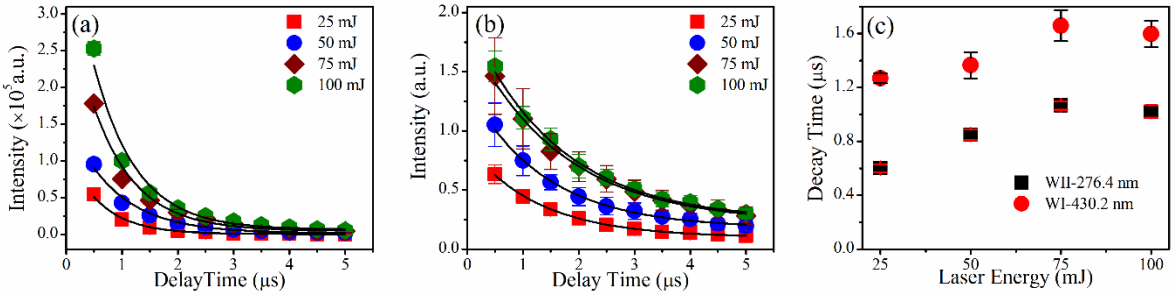

Figure 4.3 Decay of (a) WII-276.4 nm (b) WI-430.2 nm and (c) variation of ionic and atomic lines decay time as function of incident laser energy.

The signal to noise ratio (SNR) of the spectra is estimated using WI-430.2 and WI-505.3 nm transition by the following equation [168, 169],

$$SNR = \frac{I_{max} - I_{background}}{\sigma_{background}} \tag{4.1}$$

where I_{Max} is the integrated peak intensity, $I_{Background}$, is the averaged background intensity in the neighborhood of the line under consideration, and $\sigma_{bacground}$ is the standard deviation in the background intensity. The temporal evolution of the SNR is also studied as a function of incident laser energy to identify the most suitable window for recording the spectra with optimum SNR. The temporal variation of the SNR of the spectra using WI-430.2 nm and WI-505.3 nm at four incident laser energies is shown in Fig. 4.4 (a) and (b) respectively. It is observed that SNR increases with the delay time up to 3.5 μs for all the laser energy and then starts falling down, similar behavior is found for the other lines too. In the initial phase as well as towards the trailing end of LIP, the SNR is very crucial as in the former, there is a large contribution of continuum emission and in the later part the signal intensity goes down

drastically. This confirms that for LIBS detection there is a need to record the spectrum within an appropriate temporal window where the SNR is sufficiently large.

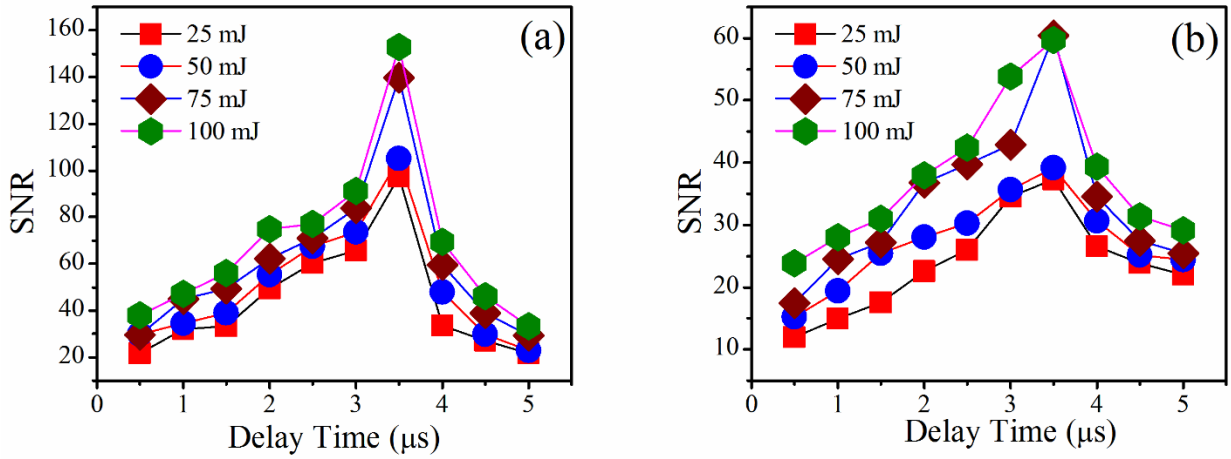

Figure 4.4 Temporal variation of SNR of the spectra as function of incident laser energy from (a) WI-430.2 nm and (b) WI-505.3 nm lines.

4.1.2 Temporal evolution of plasma temperature in LIP of Tungsten

The plasma temperature is an important parameter to be estimated, as many of kinetic processes are dependent on it. The well-known Boltzmann plot method, discussed in section 2.2.1, equation (2.14), is employed to estimate the plasma temperature. Accuracy of temperature measurement from Boltzmann plot method depends on the selection of the lines under following criteria, (1) the line's transition probability should not be high to avoid self-absorption, (2) the lines should not be a resonant line (terminating to the ground state) and (3) spread in upper energy level as much large as possible. The six atomic lines at 430.7, 449.4, 468.0, 484.3, 505.3 and 524.2 nm and that of the three ionic lines at 251.0, 227.9 and 357.2 nm are selected for the estimation of plasma temperature based on these criteria .The upper energy levels of all these selected lines for Boltzmann plot are widely apart as well as they possess low values of transition probability and also non-resonant line in order to ensure the

accuracy of the plasma temperature. The spectroscopic parameters required for these atomic and ionic transactions are taken from NIST [166] database and Kurucz database [167] are listed in Table 1 and 2 respectively.

Table 4.1 Spectroscopic parameters for WI lines for Boltzmann plot.

Wavelength (λ_{nm}) (nm)	**A_{nm} ($10^6 s^1$)**	**Lower Level Energy E_m (eV)**	**Upper Level Energy E_n (eV)**	**Lower Level Conf.**	**Upper Level Conf.**	**g_m**	**g_n**
430.7	5.40	2.458	5.335	$5d^46s^2$	-	11	11
449.4	3.00	2.387	5.145	$5d^5(^4G)6s$	-	9	7
468.0	1.40	0.598	3.247	$5d^46s^2$	$5d^46s(^6D)6p$	7	7
484.3	1.90	0.421	2.971	$5d^46s^2$	$5d^46s(^6D)6p$	5	5
505.3	1.90	0.207	2.659	$5d^46s^2$	$5d^46s(^6D)6p$	3	3
524.2	1.10	2.037	4.401	$5d^46s^2$	-	9	7

Table 4.2 Spectroscopic parameters for WII lines for Boltzmann plot.

Wavelength (λ_{nm}) (nm)	**A_{nm} ($10^7 s^1$)**	**Lower Level Energy E_m (eV)**	**Upper Level Energy E_n (eV)**	**Lower Level Conf.**	**Upper Level Conf.**	**g_m**	**g_n**
251.0	4.219	2.634	7.301	$5d^54G$	-	10	12
272.9	4.272	1.095	5.635	6sa4P	5d4(5D)6p	2	2
357.2	2.207	1.313	4.728	6sa4P	6pz2S	4	2

The partial energy level diagram for these atomic and ionic transitions are drawn in Fig. 4.5 and Fig. 4.6 respectively.

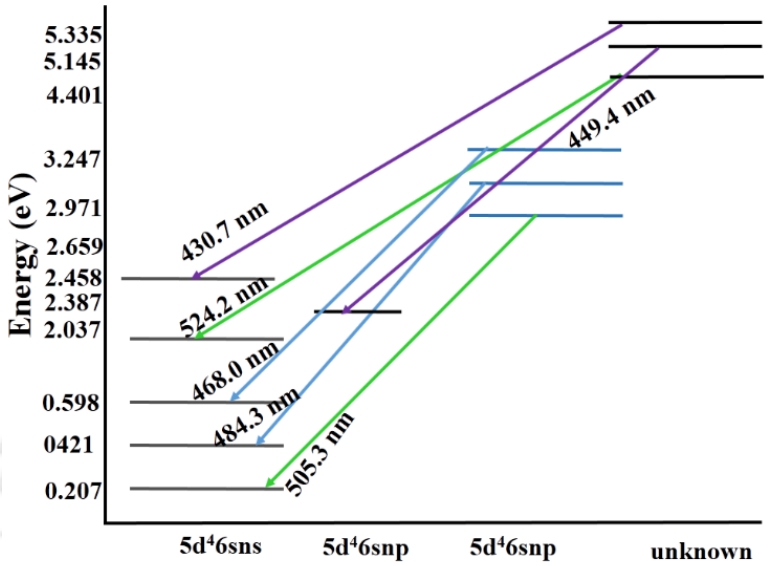

Figure 4.5 Partial energy level diagram of WI lines.

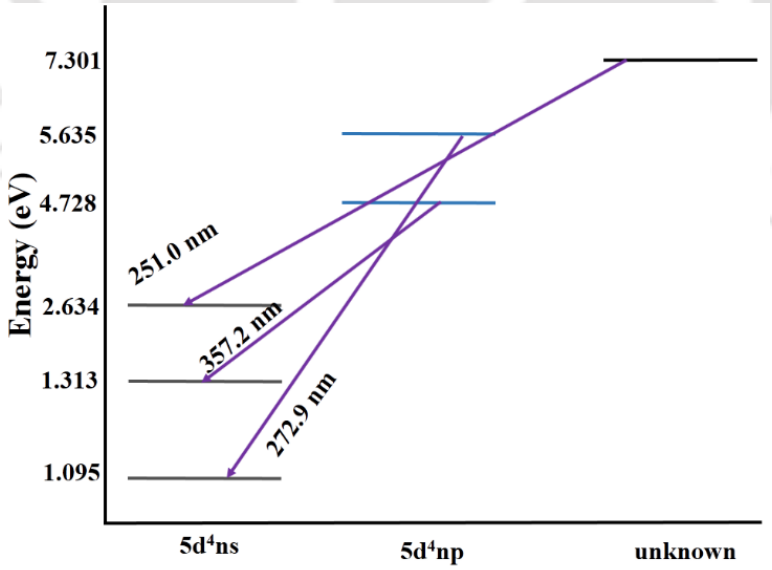

Figure 4.6 Partial energy level diagram of WII lines.

The Boltzmann plot for WII at a delay time of 0.5, 3.0 and 5.0 μs for the laser energy of 25 mJ are shown in Fig. 4.7 (a), (b), (c) and that of for the WI lines shown in Fig. 4.8 (a), (b) and (c) respectively as an example. The experimental data points fit well to straight line having correlation coefficient of 0.98-99.

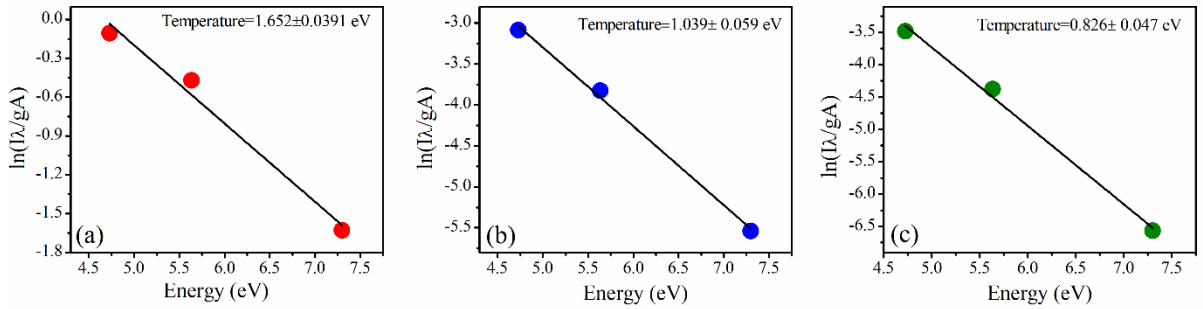

Figure 4.7 Boltzmann plot from ionic lines at (a) 0.5 (b) 3.0 and (c) 5.0 μs for the incident laser energy of 25 mJ.

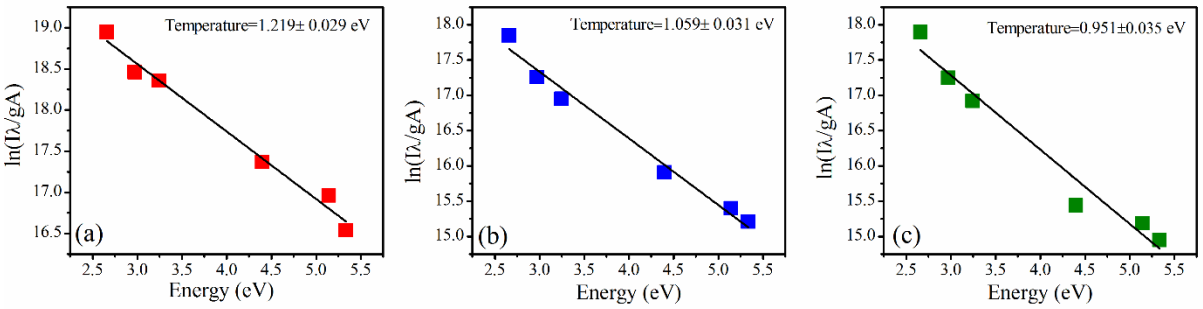

Figure 4.8 Boltzmann plot from atomic lines at (a) 0.5 (b) 3.0 and (c) 5.0 μs for the incident laser energy of 25 mJ.

The variation in plasma temperature as a function of delay time for all the four laser energies estimated from atomic and ionic transitions are shown in Fig. 4.9 (a) and (b) respectively. It is observed that with the delay time, the plasma temperature decreases but increases with the increase of incident laser energy in both the cases. It is found that the plasma temperature from WII lines are higher than that of WI lines in the delay time range of 0.5-1 μs but at later time

and in the temporal window of 1.5-4.0 μs both the temperatures are nearly same indicating the coexistence of thermal equilibrium among tungsten atoms and ions.

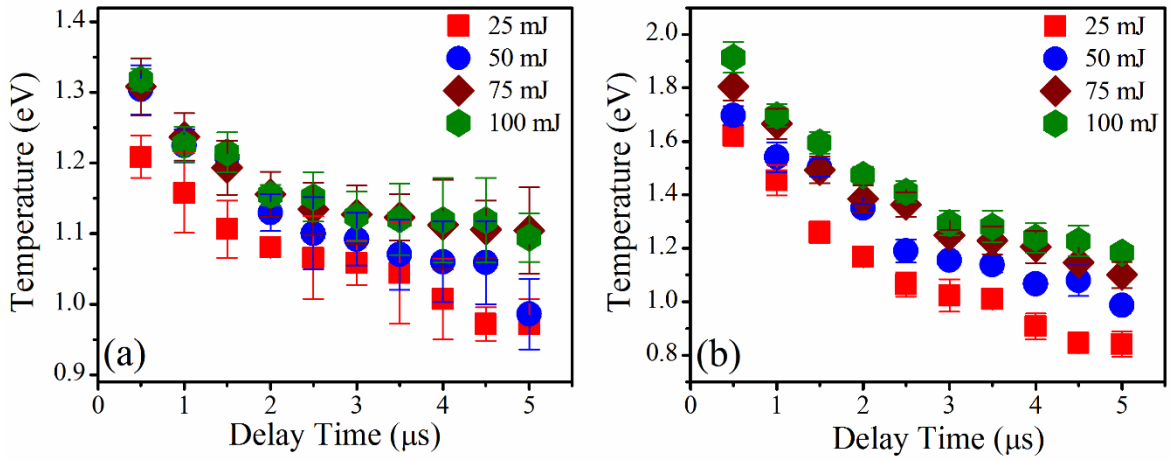

Figure 4.9 Temporal variation of plasma temperature from (a) atomic lines and (b) ionic lines as a function of incident laser energy.

The initial higher value of temperature for ionic lines is due to the fact that it requires higher temperature and thus there is the nonexistence of local thermodynamic equilibrium (LTE) among tungsten atoms and ions [170]. It is found that plasma temperature from WII lines varies in the range of 1.622-0.840 (±0.034), 1.696-0.985 (±0.033), 1.805-1.001 (±0.045), and 1.913-1.182 (±0.044) eV and that for WI lines from 1.208-0.971(±0.042), 1.304-0.985 (±0.041), 1.308-1.104 (±0.042) and 1.312-1.094 (±0.035) eV as the delay time increases from 0.5 to 5 μs for four incident laser energies of 25, 50, 75 and 100 mJ respectively.

4.1.3 Time-resolved studies on electron density of tungsten LIP

In the present study, electron density is determined using stark broadened profile from the atomic tungsten transition at 430.2 nm using the equation (2.18). The value of electron impact parameter for this line is obtained from the literature [171]. The maximum value of Doppler

broadening, from equation (2.15), for the atomic transition at 430.2 nm is 0.006 nm which is much less than instrumental resolution and thus is neglected in the present case.

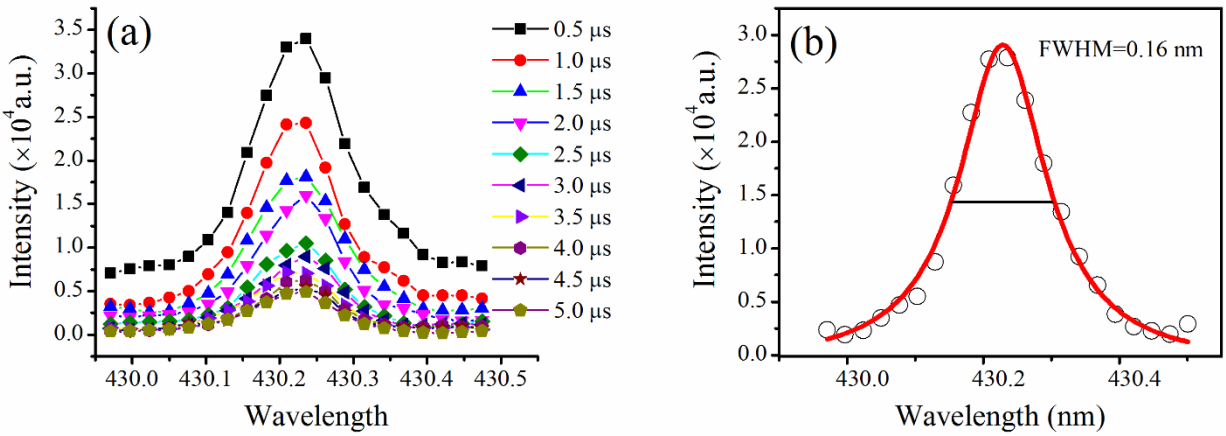

Figure 4.10 (a) Temporal variation of line profile of WI-430.2 nm and (b) Lorentzian fitted profile for the incident laser energy of 25 mJ.

The time evolution of the line profile of WI-430.2 nm at 25 mJ laser energy and the lorentzian fitted profile on it at a delay of 0.5 µs for are shown in Fig. 4.10(a) and (b) respectively. The correlation coefficients for the lorentzian fitting is observed to be in the range of 0.98-99 indicating good fitting without any distortion in the line. The decay in electron density in the delay range of 0.5-5 µs as a function of incident laser energy is shown in Fig. 4.11. The electron density is varying from 2.40-1.70 (±0.15), 2.33-1.76 (±0.13), 2.44-1.84 (±0.16) and 2.54-1.82 (±0.07) $\times 10^{17} cm^{-3}$ as the delay time increases from 0.5 to 5 µs respectively in the increasing order of laser energy .

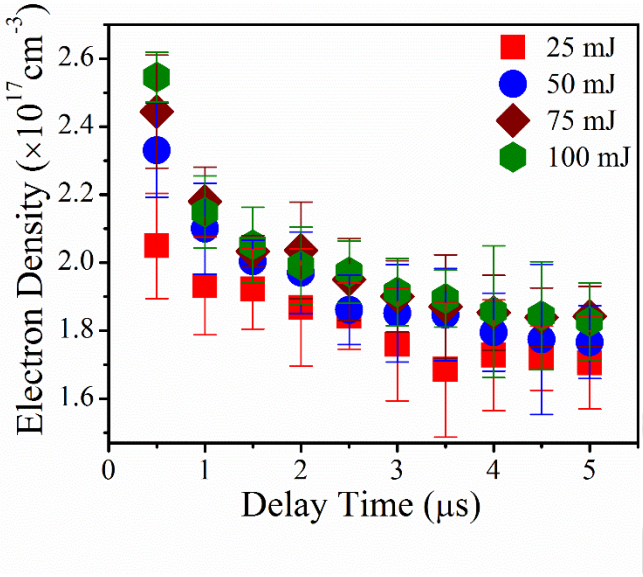

Figure 4.11 Temporal variation of electron density as a function of incident laser energy.

It is observed from the Fig. 4.3, 4.9 and 4.11 that intensity of the spectral lines, plasma temperature and electron density are falling down w.r.t delay time and increase with the increase of laser energy. The plasma temperature and electron density is found to be maximum at 0.5 μs delay (initial recording time) at each of the incident laser energy. Immediately after the commencement of the LIP, it starts expanding into the surrounding medium and loses its energy. The overall process of laser induced breakdown (LIB) can be divided into mainly three stages, first one, is the initial laser target interaction to form plasma, second one is plasma laser interaction and the last stage is plasma cooling and particulates formation. The rising part of the laser pulse generates the plasma while the trailing part heats the plasma [7]. During the laser pulse, the plasma expands isothermally but after the termination of the laser pulse, its expansion is adiabatic as there is no means to supplement the energy further to the plasma. Thus it loses its energy due to thermal conduction to the ambient and target sample, the conversion of the thermal energy to the kinetic energy via work done by the expanding plasma

and the various radiative as well as non-radiative processes involved in it along with the collisional mechanism. Due to all these energy dissipative processes with the time, the temperature and electron density fall down. The emission of radiation from plasma is interrelated with the plasma temperature and electron density, and exhibited the similar trend in temporal behavior as that of plasma parameters (Fig. 4.3, 4.9 and 4.11). The drop in plasma parameters is faster during 0.5- 1.5 μs as compared to that of the later time of 2-5 μs. The possible reasons behind this are three body recombination and the effect of surrounding atmosphere particularly at later stage. In three body recombination process, the energy is released due to the recombination of ions and electrons which compensate the energy loss due to plasma expansion.

The LIP radiation and plasma parameters are strongly influenced by the laser energy. The target absorbs the energy mainly from the initial rising part of the laser pulse and this absorption increases with the increase in the laser energy thus furnishing the higher plasma temperature and electron density. However, at the laser energy above the plasma shielding effect [60], the absorption of energy by the target is curtailed and thus the plasma parameters exhibits hardly any variation with the impinging laser energy. Fig. 4.3, 4.9 and 4.11 clearly indicate that the variation in the intensity of the spectral lines, plasma temperature and the electron density with the laser energy is more prominent up to 75 mJ and beyond this energy, there is not much significant difference in the plasma characteristics with further increase in laser energy.

4.1.4 Validity of optical thin condition of transient LIP of tungsten

The estimation of plasma parameters i.e. plasma temperature and electron density rely on the fulfillment of the condition of optical thin radiation from LIP. The optical thick LIP reabsorbs

its own radiation that results into the distorted line profile and width. This will induce error in the estimation of plasma temperature and electron density via the Boltzmann plot and stark-broadening method respectively. In the present experimental condition the visible range of the spectrum is employed for the estimation of plasma temperature and electron density. So a pair of line in the visible region i.e. WI at 468.0 nm and 500.6 nm having the same upper level energy i.e. 3.247 eV is selected for verification of optical thin condition of LIP a function of time through the branching ratio relation.

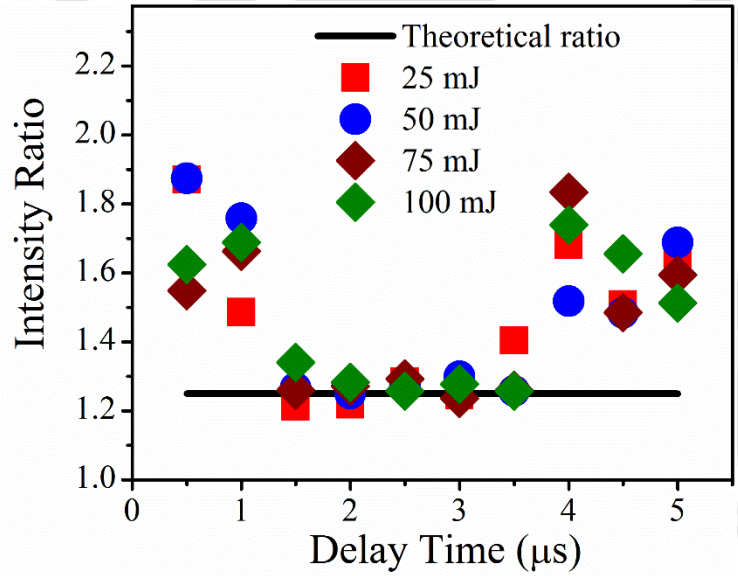

Figure 4.12 Temporal variation of branching ratio of WI-468.0/WI-505.3 as a function of incident laser energy.

The theoretical branching ratio from equation (2.11) for these lines is 1.26. The experimental values of branching ratio are varying from 1.25-1.40, 1.26-1.25, 1.25-1.25 and 1.34-1.25 within the time range of 1-3.5 μs at 25, 50, 75 and 100 mJ of laser energy respectively as shown in Fig. 4.12. The temporal evolution of branching ratio shows that the deviation in experimental

values is minimum in the delay range of 1-3.5 μs but for 0.5-1 μs and 4-5 μs, there is a large deviation from the theoretical value. Thus the optimum temporal window in which the plasma can be assumed to optically thin is 1-3.5 μs.

4.1.5 Evaluation of LTE condition for transient LIP of tungsten

For the time-resolved study, the LTE condition is verified under two conditions (i) in the first case, plasma is assumed to be stationary and homogeneous and (ii) the second case the plasma is assumed to be transient but homogeneous [128]. For the first case, the Mc-Whirter criteria, the equation (2.4) is employed to estimate the required minimum electron density necessary for the collisional processes to dominate over the radiative processes in order to maintain the LTE in LIP. The lower limit for electron density in the present case has been estimated using the WI-498.2 nm transition between the ground level and first excited level of WI [128], having energy gap ΔE_{nm}=2.487 eV. The variation of minimum required electron density as a function of delay time is shown in Fig. 4.13 (a) which varies from 2.91-1.61, 3.02-2.63, 3.03-2.78 and 3.04-2.77×10^{15} cm^{-3} for the incident laser energy of 25, 50, 75 and 100 mJ respectively and this range of minimum electron density is nearly similar for all the laser energies. On comparing the Fig. 4.11 and Fig. 4.13 (a), it is obvious that the required minimum electron density as per equation (2.4) is less than that of the experimentally estimated for all the four laser energies thus confirming the LTE for LIP of tungsten in the present case. In the second case, the relaxation time is estimated from the equation (2.7) to check whether the temporal evolution of the plasma parameters are sufficiently slow in order to allow the plasma enough time to reach the thermodynamic equilibrium. The variation of the relaxation time from equation (2.7) as a function of delay time w.r.t laser pulse is shown in Fig. 4.13 (b). The relaxation time [128] in the present experimental conditions is found to be of the order of 10^{-9}

s which is much smaller than decay time of plasma parameters, estimated to be of the order of microsecond, Fig. 4.3, thus satisfying the second criteria for LTE condition.

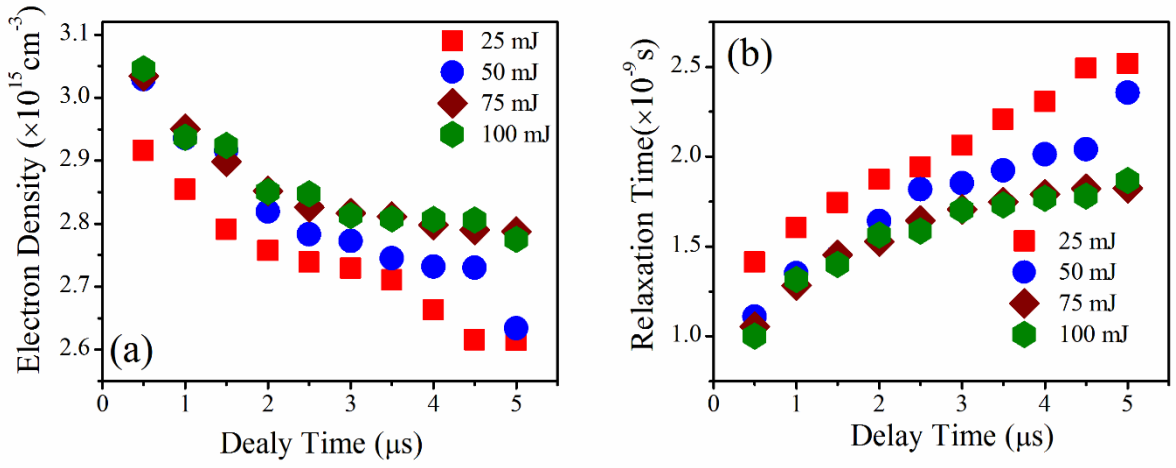

Figure 4.13 Assessment of LTE at various delay time as a function of incident laser energy (a) Mc-Whirter criteria and (b) relaxation time.

4.2 Space-resolved studies on LIP of tungsten

The LIP expands both along axial as well radial direction simultaneously with time evolution thus plasma parameters change inhomogeneously as a function of space. In the second part, of the present study on LIP of tungsten, the spatial characterization of LIP of tungsten is performed in air at delay of 2 s w.r.t laser pulse, as it lies within the optimum temporal window. The emission intensity, plasma temperature and electron density are measured at different axial locations of the plasma as is described in section 3.2 and shown in Fig. 3.5. The essential optical thin condition of plasma and LTE is verified in order to assess the optimum spatial window for the analysis of LIP.

4.2.1 Spatial distribution of plasma emission intensity of tungsten

The experimental set up described in section 3.2 is implemented to record the spatial profile of emitted spectrum from LIP of tungsten at various incident laser energy. The spatial distribution of emission intensity in the spectral range of 220-890 nm for the four incident laser energy is shown in Fig. 4.14 (a), (b), (c) and (d). The expanded view of the spatial evolution of the spectrum in the spectral range 266-278 nm and 429-432 nm are shown in Fig. 4.15 (a) and (b) respectively at laser energy of 25 mJ. The same WII lines at, 265.8, 270.2 and 276.4 nm and WI transitions are WI, at 429.4, 430.2 and 430.7 are marked in the Fig. 4.15 (a) and (b) respectively as in the time evolution studies.

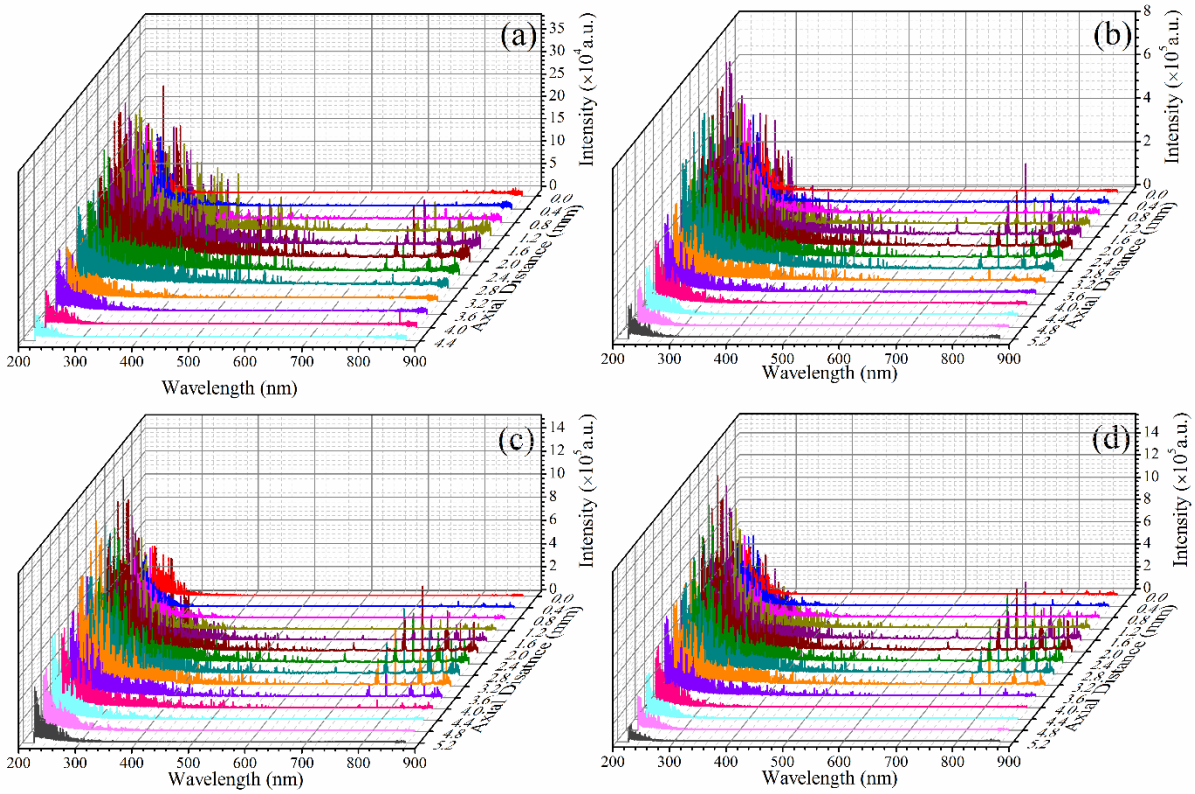

Figure 4.14 Spatial evolution of emission spectrum from LIP of tungsten in air at (a) 25 , (b) 50 , (c) 75 and (d) 100 mJ of laser energy.

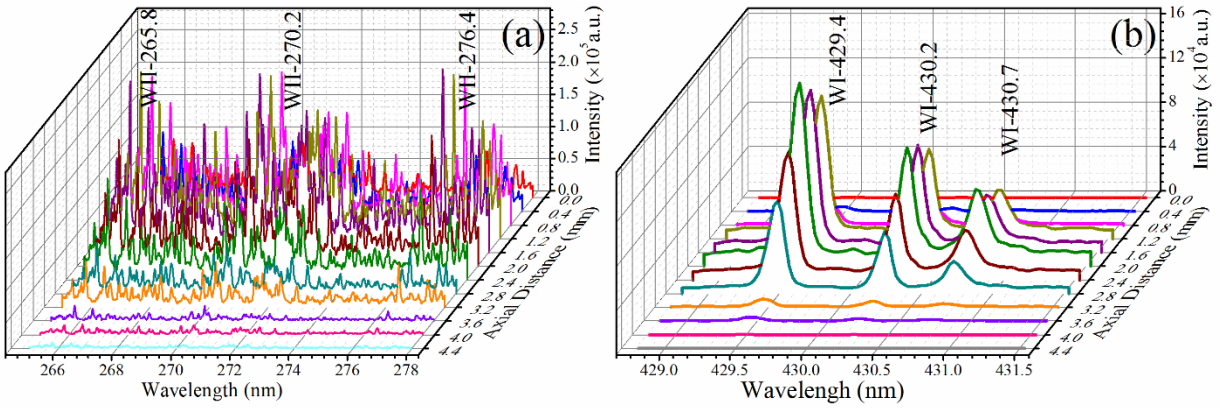

Figure 4.15 Expanded view of the spectral emission in spectral region of (a) 265-278 nm and (b) 429-432 nm.

The spatial evolution of the ionic and atomic transitions at 276.4 and 430.2 nm are shown Fig. 4.16 (a) and (b) respectively as a function of incident laser energy.

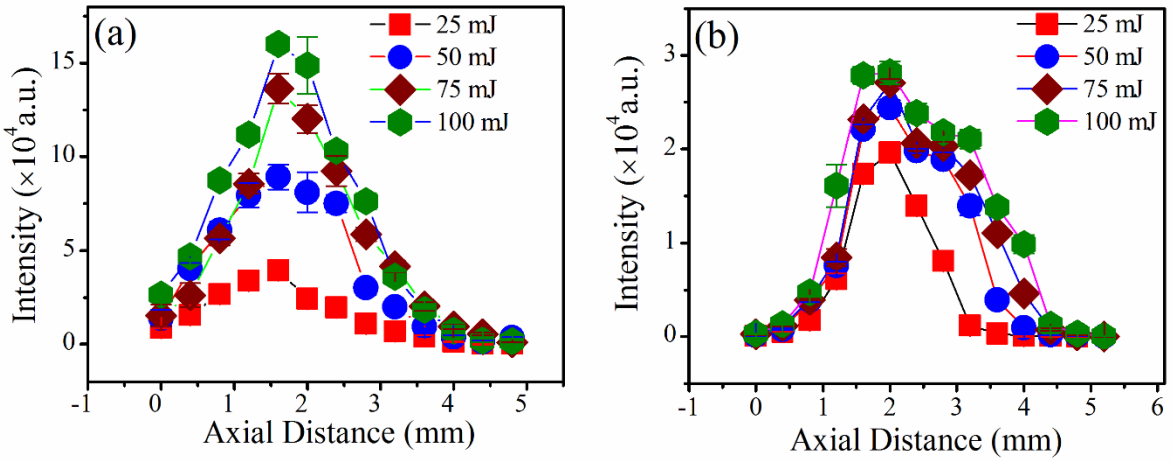

Figure 4.16 Axial intensity distribution of (a) WII-276.4 nm and (b) WI-430.2 nm as a function of incident laser energy.

It is observed from axial distribution of intensity of expanding plasma, the intensity of atomic and ionic transitions increase upto a certain distance and then start falling down. The WII-276.4 nm line attained maximum intensity at 1.6 mm distance away from the target surface while that of WI-430.2 at 2.0 mm. The ionic lines appear close to the target surafce as compared to that of the atomic lines. It is also observed that with the increse in incident laser energy, the intensity of both the tansitions increses up to a certain distanc and then fall down which is similar to that of documented in literature [79, 172-174]. The separation between the position of maximum intensity of atoms and ions is due to their velocity diffrence. Ions posses higher kintic energy as well velocity than the atoms. It is also seen from the temporal studies that the persistent time of ionic line is smaller than atomic lines. So with the higher velocity and less persistent time ions will decay nearer to the target surafce than the atoms. The intensity of WII-276.4 nm lines increases with the laser energy and after attaining a maxima there is a sharp decrease in the intensity. In contarst, WI-430.2 nm line, the intensity variation with the laser energy is not prominent but intensity extends to higher axial distance for higher energy. This is due to the fact that with higher incident laser energy, the plasma plume length increases and the emission from higher stages of ionization results from the hot inner core of the LIP while emission from neutral or lower stages of ionization occur from outer part of the LIP. Thus the atomic transitions attain maximum at later distance as compared to the ionic transition [175]. The spatial variation of the SNR for WI-430.2 nm and 505.3 nm at all the four laser energies estimated from eqution (4.1) are shown in Fig. 4.17(a) and (b) respectively. It is concluded from the observation that SNR increases up to 2 mm and then start to decrease. This is similar to the observation has been reported in literature [176].

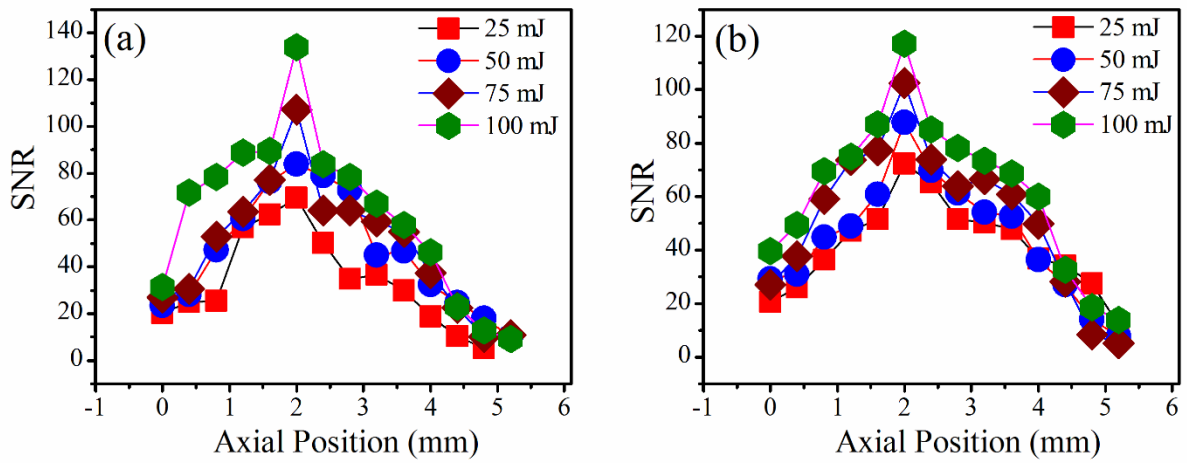

Figure 4.17 Spatial variation of SNR as a function of incident laser energy from WI at (a) 430.2 nm and (b) 505.3 nm.

4.2.2 Spatial distribution of plasma temperature LIP of tungsten

The same six WI transitions are used in equation (2.14) for study spatial profile of plasma temperature as in time-resolved studies section 4.1.2. The spatial variation of plasma temperature as a function of incident laser energy is shown in Fig. 4.18. It indicates a maximum value of the plasma temperature at a certain distance from the target surface and decreases at both, close to target surface and plasma edges away from the target surface. Similar observation are reported in the literature on the Cu target [177]. The plasma temperature changes from 0.838 (±0.040)-0.630 (±0.046), 0.866 (±0.048)-0.654 (±0.067), 0.914 (±0.026)-0.751 (±0.028) and 1.021 (±0.038)-0.812 (±0.039) eV in the spatial extent from the surface of the target to 4.4 mm away from it with the increasing laser energy. For the incident laser energy of 25 mJ, the maximum value of electron temperature is 0.932 (±0.007) eV, is observed at a distance of 1.6 mm away from the target surface but for other energy it is around 2 mm distance. The maximum value of the temperatures are 1.077 (±0.0.009) eV, 1.095 (±0.0.016) eV and 1.177 (±0.028) eV for the incident laser energy of 50, 75 and 100 mJ respectively. It is concluded that with the increase of incident laser energy, the plasma temperature increases similar to that of the

temporal studies of previous section. The fall in the plasma temperature close to the surface for the atomic transitions is due to the fact that neutral are emitted directly due to the thermal heating of laser. Whereas away from the target neutrals are dominated by that of the recombination of ions with the electrons, than later of which are at higher temperature. This is also consistent with the spatial evolution of the line emission from the atomic transition of Al and steel [79, 178].

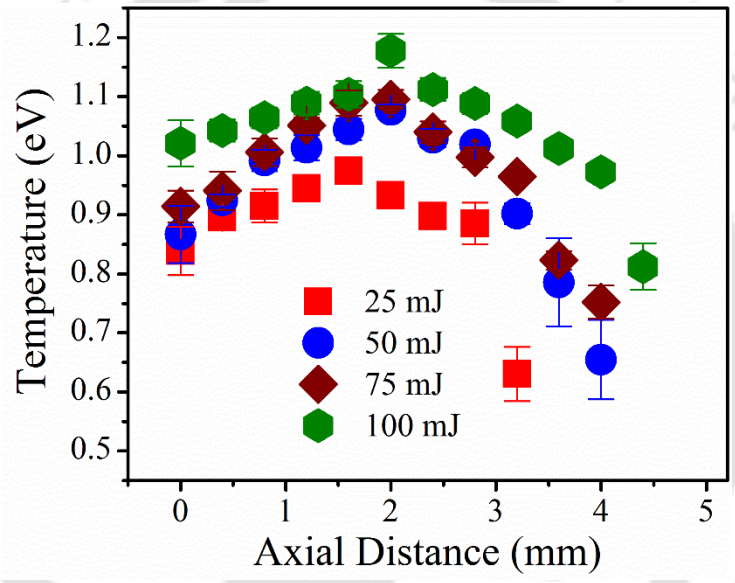

Figure 4.18 Spatial distribution of plasma temperature as a function of incident laser energy.

4.2.3 Spatial distribution of electron density LIP of tungsten

The axial distribution of electron density as measured from WI-430.2 nm line as a function of incident laser energy is shown in Fig. 4.19. The variation of electron density in the range of 0-4.4 mm distance from the target are 1.32 (±0.04)-1.03(±0.06), 1.35 (±0.01)-1.18 (±0.01), 1.46 (±0.08)-1.39 (±0.67) and 1.48 (±0.14)-1.58 (±0.06) $\times 10^{17} cm^{-3}$. It attains a maximum value of electron density of 1.71 (±0.19), 1.73 (±0.25), 1.78 (±0.05) and 1.84 (±0.05) $\times 10^{17} cm^{-3}$ at 2.0 mm distance for incident laser energy of 25, 50, 75 and 100 mJ.

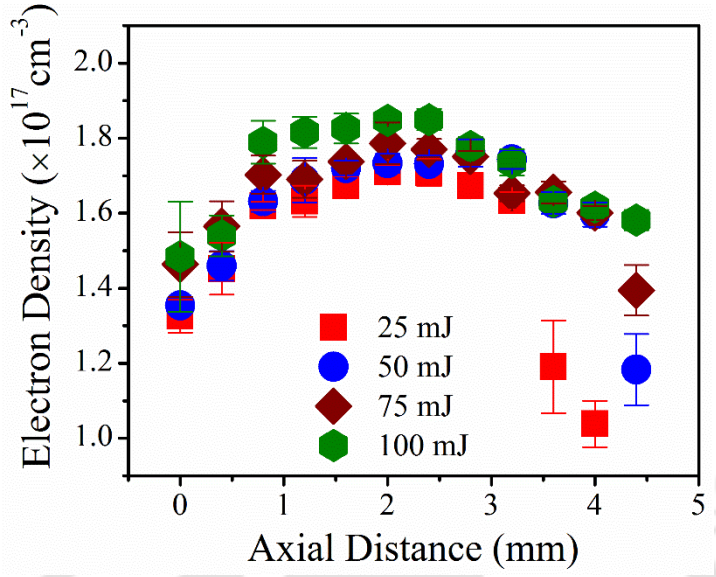

Figure 4.19 Axial distribution of electron density as a function of incident laser energy.

From Fig. 4.19, it is evident that the electron density reaches a maximum value at distance of 2 mm away from the target surface. This is in contrast to that of the documented in literature as generally the electron density decreases on moving away from the target surface. In the present case the experiments is performed at a fixed delay of 2 μs (in the optimized temporal window), the LIP is already expanded in air. The maxima of the electron density is lying in the core of the plasma. The peripheral region is comprised of neutral species (due to the recombination of ion with the electrons) [175, 179].

4.2.4 Analysis of optical thin condition for inhomogeneous LIP of tungsten

The variation in the branching ratio of WI transitions at 468.0 nm and 500.6 nm, having the same upper level energy, is applied in equation (2.11), is shown in Fig. 4.20 as a function of distance from the target surface along with its theoretical value of 1.26.

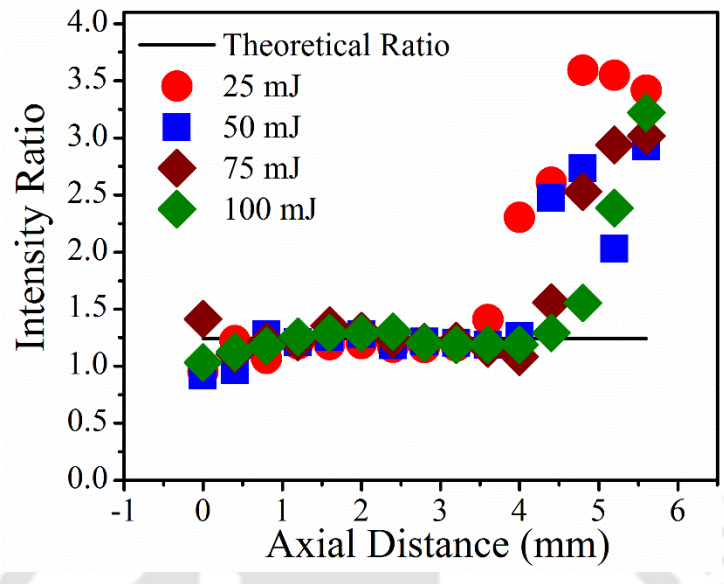

Figure 4.20 Spatial variation of experimental branching ratio as a function of incident laser energy.

The close proximity of the experimentally obtained value of branching ratio with that of its theoretical value is in the range of 0.8-3.2 mm, confirms that the plasma can be treated under optically thin condition. Outside this range it is not optically thin. Thus the optimum spatial window in which the plasma can be assumed to optically thin is 0.8-3.2 mm.

4.2.5 Validity of LTE criteria for inhomogeneous LIP of tungsten

In the space resolve study, the LTE criteria is evaluated in two case: (i) the LIP is considered to be stationary and homogeneous and (ii) LIP is regarded as stationary but inhomogeneous. The Mc-Whirter criteria is applied for the first situation to evaluate the minimum electron density required to maintain the LTE at different locations of LIP. The spatial variation of minimum electron density at four incident laser energies is shown in Fig. 4.21(a). On Comparing the Fig. 4.19 and Fig. 4.21(a), it is evident that experimentally obtained electron

density is greater than the required electron density by two order of magnitude validating the LTE in LIP.

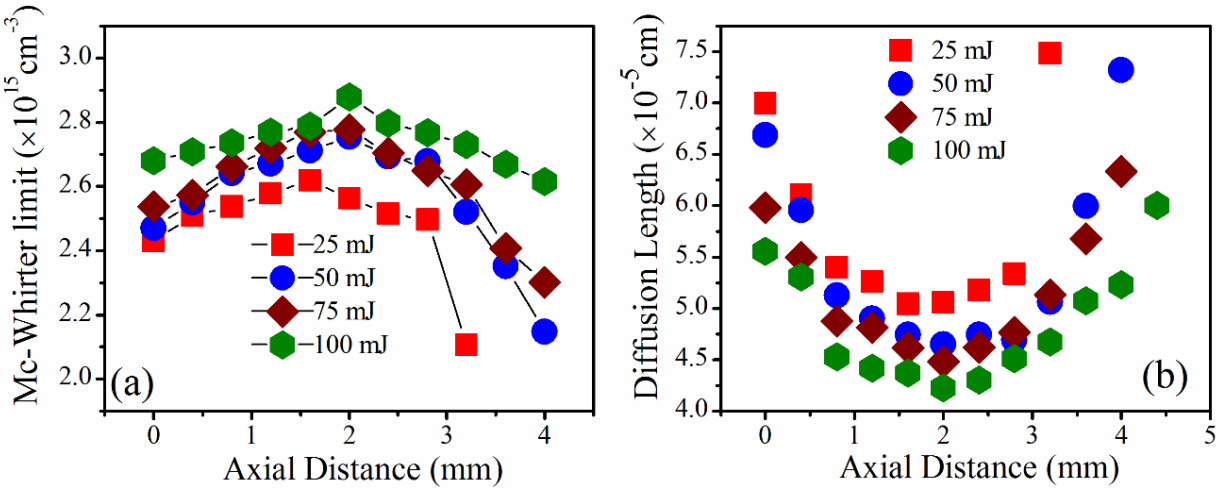

Figure 4.21 Assessment of LTE at various axial position as a function of incident laser energy (a) Mc-Whirter criteria and (b) diffusion length.

In the second situation, in order to consider the inhomogeneity of LIP, the diffusion length of plasma species is estimated. The diffusion length as a function of target separation is estimated using equation (2.10) and shown in Fig. 4.21 (b). The diffusion length LIP considering the atomic transition at WI-498.2 nm and is of the order of 10^{-4} mm which is less than plasma dimension (of the order of few mm) that confirming the validity of LTE in LIP. In the close proximity to the target surface and towards edge of the plasma (far away the target) the diffusion length is increasing , indicating the tendency of deviation of LTE [179]. Thus LTE is maintained for axial position of 0.8-3.2 mm w.r.t target.

4.3 Conclusion

The LIP of tungsten in air is studied using both time and space-resolved LIBS technique. In the first part of the present work, the line emission intensity of LIP of tungsten in air, its plasma

temperature, and electron number density are examined at different delay time in the time range of 0.5-5 μs and in the second part same parameters are studied at different axial locations of LIP at various incident laser energies. In both the cases, optical thin plasma and LTE conditions are scrutinized to justify the application of LIBS technique for transient and inhomogeneous nature of LIP. The temporal evolution of plasma emission intensity reveals the presence of several atomic and ionic transitions of tungsten which decay exponentially with the time. The persistence time of ionic line is smaller than that of atomic lines. The temporal evolution of SNR at four different energy reveals that it increases with the laser energy in the temporal window of 0.5- 3.5 μs, but beyond this window it falls down. The plasma temperature is estimated using several atomic and ionic transitions of tungsten through the Boltzmann plot method. The ionic lines are offering higher value of plasma temperature in the initial time of 0.5-1 μs as compared to that of the obtained from neutral atomic lines, while at later time both these temperatures possess nearly same values indicating the coexistence of thermodynamic equilibrium among tungsten ions and atoms in temporal window of 1.5-4 μs. The stark-broadened profile of WI line at 430.2 nm is exploited for the estimation of electron densities of LIP of tungsten. The plasma parameters increases with the increase of incident laser energy from 25-75 mJ but at higher energy of 100 mJ its start to saturate due the plasma shielding effect. The lower limit of electron densities to maintain the LTE inside the plasma at different delay time as a function of incident laser energy is estimated using McWhirter criterion as well relaxation time is also measured to take into account the transient nature of the plasma. The relaxation time is found to be of the order few nanosecond which is much less than plasma evolution time of the order of 10^{-6} s. Confirming the prevalence of LTE in the present case of transient LIP. The branching ratio method is applied for the estimation of optical thin condition

of LIP. It is found that in temporal window of 1-3.5 μs, the LIP is fulfilling the optical thin condition of plasma. All these indicates that the temporal window of 1-3.5 μs where the optical thin condition as well as LTE conditions are satisfied is the optimum temporal window for the characterization of LIP via LIBS.

In the second part of the work, the spatial distribution of intensity of atomic, ionic, electron temperature and density are studied at different incident laser energy in the expanding plasma at delay of 2 μs, the optimum temporal range. These quantities are found to reach maximum value away from the target surface. The maximum of ionic line intensity appears close to the target surface than that of the atomic transition. The SNR of plasma emission intensity increases up to 2 mm from the target surface but then begins to fall. Plasma emission intensity as well as plasma parameters increases up to certain distance from the target surface, after attaining the maximum value start fall down. The thermal conduction from the plasma towards the solid target and the radiative cooling of the plasma, as well as conversion of thermal energy to kinetic energy are responsible for this behavior. The LIP is observed to be in LTE up to a distance of 4.0 mm from the target beyond this it starts to depart from LTE. It is observed that close to the target surface and away from the target surface after the distance 3.2 mm the experimental intensity ratio of the suitable lines deviate more from theoretical intensity ratio (branching ratio). This confirm that LIP is optical thin in the range of 0.8-3.2 mm. Thus in order to implement the LIBS technique along with the optimum temporal window, the optimized spatial window, which under present experimental configuration lies in the range of 0.8-3.2 mm, is required to be explored.

Chapter 5 Time and Space-Resolved Studies on Laser Induced Plasma of Molybdenum in air via LIBS

The molybdenum is a promising candidate in nuclear fusion reactor as it possesses high melting point, low sputtering yield and high reflectivity for broad range of wavelengths and thus it is suitable for the first mirror (FM) in ITER [180-182]. Inside fusion reactor in harsh environment, the bombarding of high energy particles, exposure to highly intense electromagnetic radiation and deposition on the mirror, degrade the FM and thus reduces its lifetime. To maintain and improve the quality of the FM, there is an active need of online cleaning and monitoring. For this purpose, due to the inherent salient features of LIBS technique, it is suitable for the analysis of plasma facing component (PFC). Besides the application of Mo in fusion reactor, it has many other applications, such as the nanostructures of compound elements of Mo like MoO_3, MoS_2 etc. are beneficial in sensing and optoelectronic devices, deposition of high quantity thin films via pulsed laser deposition (PLD), micro structuring through laser ablation etc. on it [164]. There are a very few studies on LIP of Mo via the LIBS technique [182]. Moreover also there is scarcity of atomic data base for Mo transitions which is essential for LIP characterization using LIBS. The time and space-resolved LIBS for various incident laser energies on Mo target is reported in the present chapter. The suitable temporal as well as spatial window are identified for the validity of LTE and optical thin condition of the LIP. The branching ratio method is employed for the assessment of optical thin condition of LIP. The experimental set up employed for LIBS for Mo have already been stated in chapter 3, section 3.1 and 3.2, Fig. 3.1 and Fig. 3.5.

5.1 Studies on the temporal evolution of LIP of molybdenum

The emission spectra from LIP of Mo in air at four different incident laser energies are recorded. Several atomic and ionic lines are identified in the spectra of LIP using NIST [166] and Kurucz [167] database. The identified MoI and MoII transitions are separately employed in Boltzmann plot method [78] to estimate the plasma temperatures. The MoI-312.3 nm lines used for estimation of plasma electron density. The temporal evolution of both these plasma parameters are studied as function of incident laser energy. The validity of the LTE and optical thin conditions are the essential criteria for employing plasma diagnostic technique. So these conditions are verified considering the transient nature of the LIP.

5.1.1 Temporal variation of plasma emission intensity of molybdenum

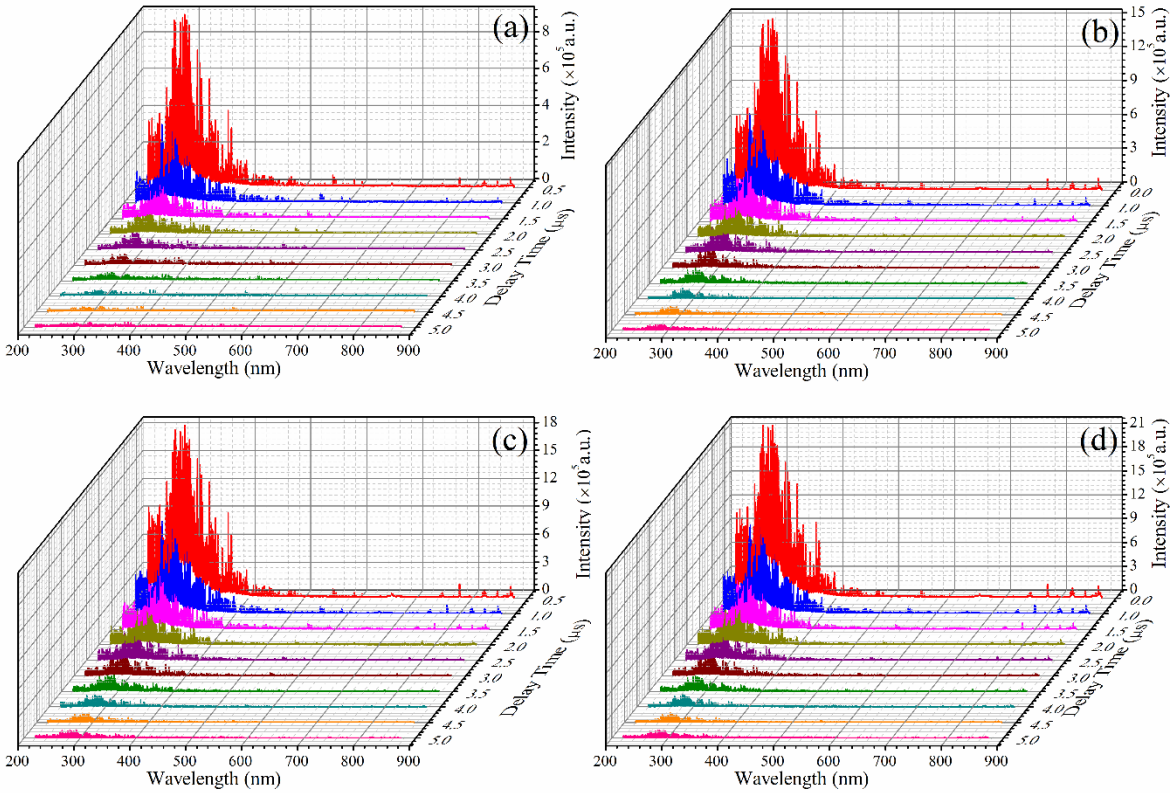

Figure 5.1 Temporal evolution of plasma emission from LIP of molybdenum at (a) 25, (b) 50, (c) 75 and (d) 100 mJ of incident laser energy.

The experimental setup described in section 3.1 is utilized to record the time evolution of the LIP of Mo in the time range of 0.5-5 μs at four different incident laser energies. The temporal evolution of LIP spectra of Mo recorded at all the four laser energies of 25, 50, 75 and 100 mJ in the spectral range of 220-850 nm are shown in Fig. 5.1. The expanded view in the range of 277-288 and 550-570 nm are shown in Fig. 5.2 (a) and (b) respectively.

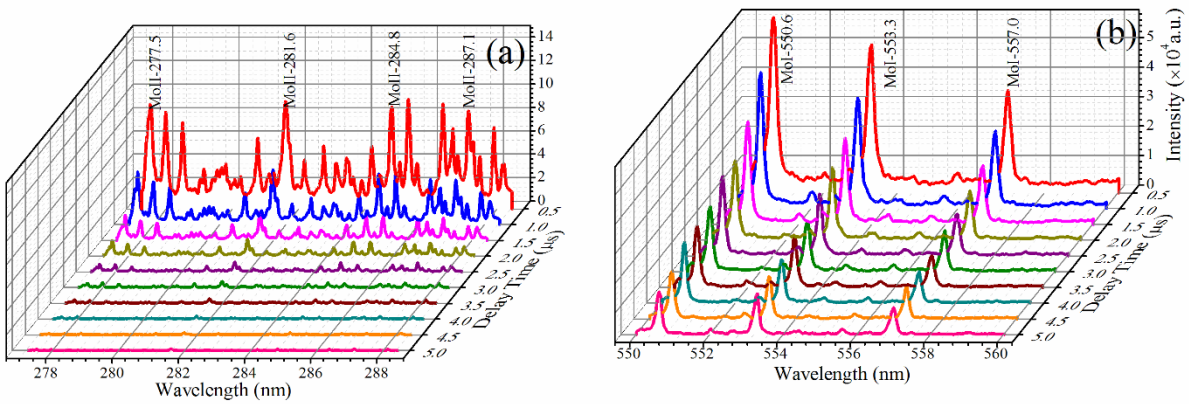

Figure 5.2 Expanded view of the temporal variation of (a) Ionic lines in the spectral range 277-288 (b) atomic lines in the spectral range 550-570 nm.

The spectral range of 287-288 nm is comprised of predominantly ionic lines of Mo while that of the 550-570 nm is attributed to atomic lines. The temporal variation of MoII-248.8 nm and MoI-550.6 nm lines at four laser energies are shown in Fig. 5.3(a) and (b) respectively.

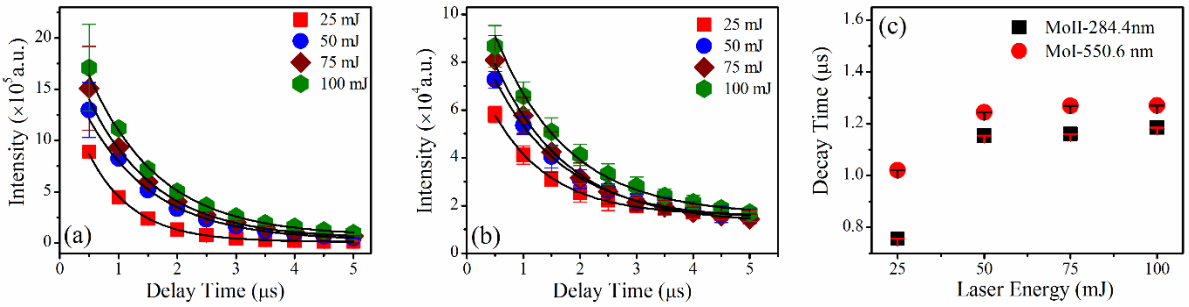

Figure 5.3 Variation of intensity as function of time (a) MoII-284.8 and (b) MoI-550.6 nm transition and (c) decay time as a function of incident laser energy.

These intensities are fitted using the exponential decay function to estimate the decay time and are shown by solid lines in Fig. 5.3 (a) and (b).The variation of decay time with respect to the incident laser energies for MoII-284.8 and MoI-550.6 nm are shown in Fig. 5.3(c). It is observed that the decay of ionic lines are faster than the atomic lines. The decay time of MoII-284.8 nm line is 0.75 (±0.01), 1.15 (±0.04), 1.16 (±0.03) and 1.18 (±0.04) μs and that of the MoI-550.6 nm lines is 1.02 (±0.04), 1.24 (±0.4), 1.26 (±0.03) and 1.27 (±0.01) μs for the incident laser energies of 25, 50, 75 and 100 mJ respectively. Due to the higher energy, ionic lines decay faster than that of the atoms. In both the cases, decay time increases with the increase in the incident laser energy to a certain extent beyond that there is hardly any change.

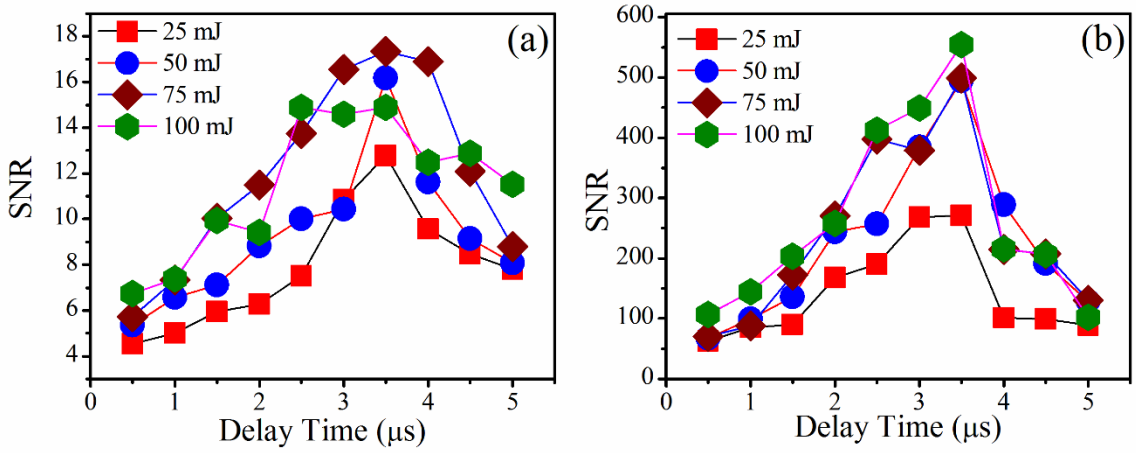

Figure 5.4 Temporal variation of SNR of the spectra as function of incident laser energy from (a) MoI-357.0 nm and (b) MoI-557.0 nm.

The temporal variation of signal to noise ratio (SNR) from equation (4.1) for MoI-357.0 nm and MoI-557.0 nm line is shown in Fig. 5.4 (a) and (b) respectively. It is observed that the SNR increases up to 3.5 μs for each incident laser energy and beyond this it falls down with time delay. This trend is similar for all other lines. This gives an indication that for the detection of spectra with large SNR, LIP emission spectrum should be recorded around this range of optimized temporal window. Similar range of optimized window is observed for all the spectral lines in the present case.

5.1.2 Temporal variation of plasma temperature of molybdenum

Considering the LIP of Mo in LTE and emitting optically thin emission of radiation, the Boltzmann plot method is applied to estimate the plasma temperature already described in section 2.2.1, equation (2.14). Ten numbers of atomic transitions at 357.0, 406.9, 423.2, 438.1, 453.6, 476.0, 550.6, 553.3, 557.0 and 592.8 nm and five ionic transitions 230.4, 269.2, 283.1, 363.5 and 374.2 nm are used in Boltzmann plot separately to estimate the plasma temperature for neutral and singly ionized Mo. The necessary atomic parameters for estimation of plasma temperature for MoI and MoII are taken from NIST [166] and Kurucz database [167] and are listed in table 1 and 2 respectively. While selecting these lines it is kept in mind that these possess maximum energy spread in the upper level of the considered transitions which enhance the accuracy of the estimation of plasma temperature. The simplified partial energy diagram for these MoI and MoII lines used in Boltzmann plot are shown in Fig. 5.5 and Fig. 5.6 respectively.

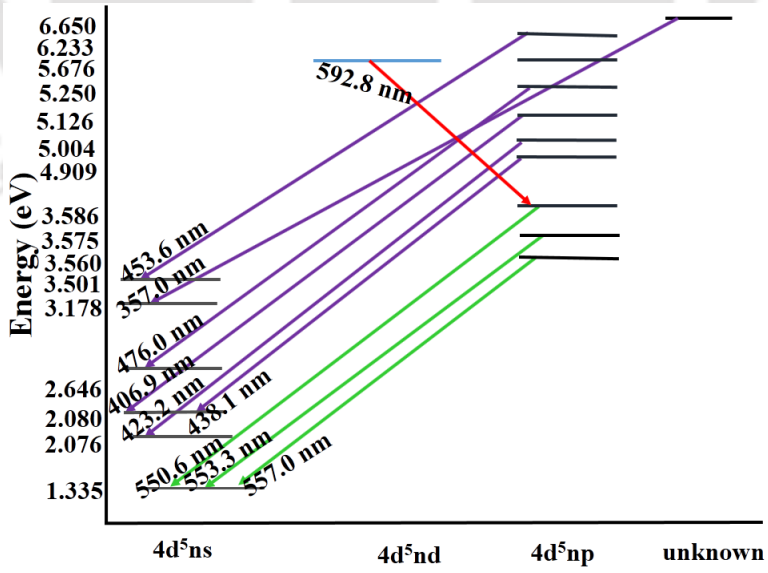

Figure 5.5 Partial energy level diagram for MoI lines.

Table 5.1 Spectroscopic data of MoI lines for Boltzmann plot.

Wavelength (λ_{nm}) (nm)	A_{nm} ($10^7 s^1$)	Lower Level Energy E_m (eV)	Upper Level Energy E_n (eV)	Lower Level Conf.	Upper Level Conf.	g_m	g_n
357.0	7.2	3.178	6.650	$4d^5(^2I)5s$		15	15
406.9	3.25	2.080	5.126	$4d^5(^4G)5s$	$4d^5(^4G)5p$	13	11
423.2	3.17	2.076	5.004	$4d^5(^4G)5s$	$4d^5(^4G)5p$	9	11
438.1	2.93	2.080	4.909	$4d^5(^4G)5s$	$4d^5(^4G)5p$	13	13
453.6	5.00	3.501	6.233	$4d^5(^2I)5s$	$4d^5(^2I)5p$	13	15
476.0	4.67	2.646	5.250	$4d^5(^4G)5s$	$4d^5(^4G)5p$	11	13
550.6	3.61	1.335	3.586	$4d^5(^4D)5s$	$4d^45s(^4D)5p$	5	7
553.3	3.72	1.335	3.575	$4d^5(^6S)5s$	$4d^5(^6S)5p$	5	5
557.0	3.30	1.335	3.560	$4d^5(^6S)5s$	$4d^5(^6S)5p$	5	3
592.8	5.30	3.586	5.676	$4d^5(^6S)5p$	$4d^5(^6S)5d$	7	9

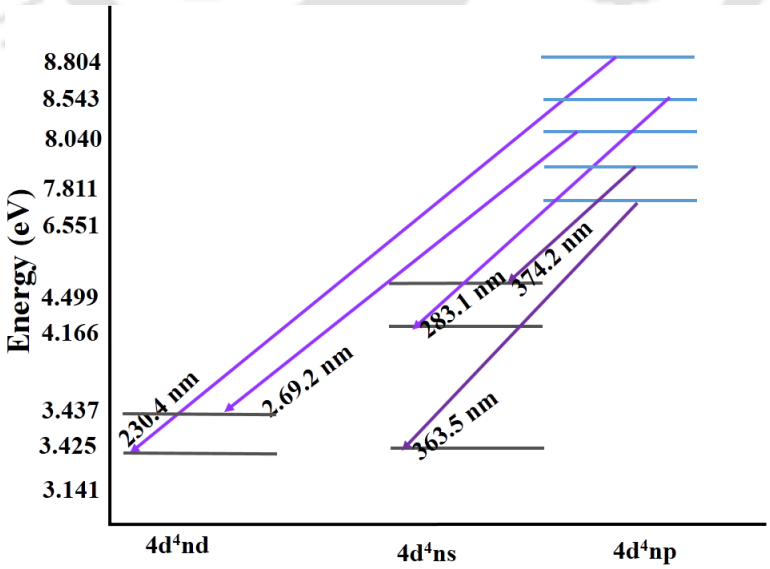

Figure 5.6 Partial energy level diagram for MoII lines.

Table 5.2 Spectroscopic data of MoII lines for Boltzmann plot.

Wavelength (λ_{nm})	A_{nm} ($10^7 s^1$)	Lower Level Energy E_m (eV)	Upper Level Energy E_n (eV)	Lower Level Conf.	Upper Level Conf.	g_m	g_n
230.4	1.609	3.425	8.804	4d5 a2H	5p w2G	12	10
269.2	1.382	3.437	8.040	4d5 a2H	5p y2G	10	8
283.1	1.132	4.166	8.543	5s a6D	5p z6F	12	13
363.5	0.5531	3.141	6.551	5s b4D	5p z4F	8	10
374.2	1.90	4.499	7.811	5s c2F	5p y4F	6	4

The Boltzmann plot for atomic and ionic lines at delay time of 0.5, 3.0 and 5.0 μs for the incident laser energy of 25 mJ are shown in Fig. 5.7 (a)-(c) and 5.8 (a)-(c) respectively as an example. The temperature is estimated from the slope ($-1/k_B T_e$) of these plots.

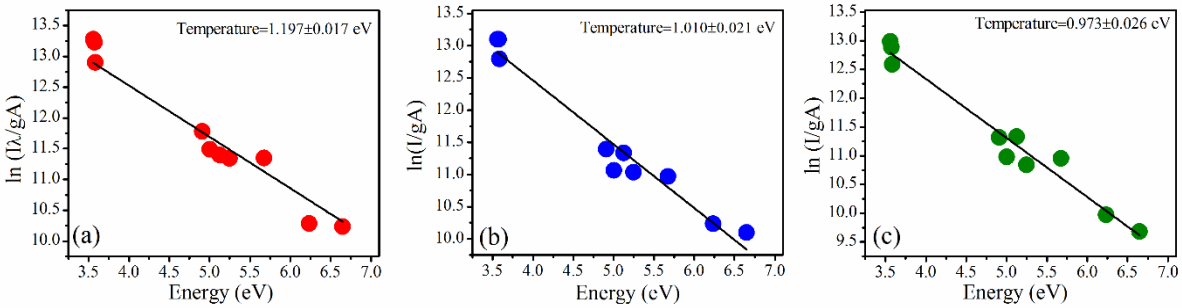

Figure 5.7 Boltzmann plot for atomic lines at delay time of (a) 0.5 (b) 3.0 and 5.0 μs.

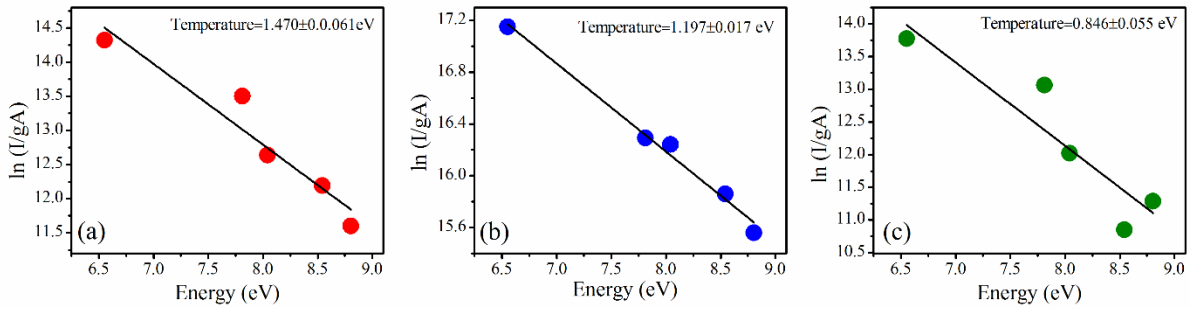

Figure 5.8 Boltzmann plot for ionic lines at delay time of (a) 0.5 (b) 3.0 and 5.0 μs.

The temporal variation of plasma temperature as a function of incident laser energy for MoI and Mo II lines are shown in Fig. 5.9 (a) and (b) respectively. It is observed from the temporal evolution of the plasma temperature that it is decreasing as the delay time increases, in both the cases, MoI and MoII lines, but increases with the increase in incident laser energy. The plasma temperature shows variation as a function of delay from 1.203 (±0.17)-0.783 (±0.026), 1.301 (±0.16)-0.997 (±0.021), 1.376 (±0.028)-1.052 (±0.037) and 1.413 (±0.029)-1.027 (±0.034) eV for MoI lines while with that for MoII lines from 1.435 (±0.061)-0.783 (±.057), 1.636 (±0.044)-0.916 (±0.083), 1.679 (±0.031)-0.927 (±0.067) and 1.897 (±0.049)-1.004 (±0.065) eV at the laser energy of 25, 50, 75 and 100 mJ respectively. In the initial delay range of 0.5-1.0 μs the range of temperature is higher for MoII than that of the MoI but at later time range of 1.5-5 μs the temperature in both the cases possess similar values. The difference in the temperature is due to the non-coexistence of equilibrium of atomic and ionic species among themselves at the initial stage of the formation of plasma [170]. But in the later time scale there is a co-existence of the thermal equilibrium among Mo atoms and ions.

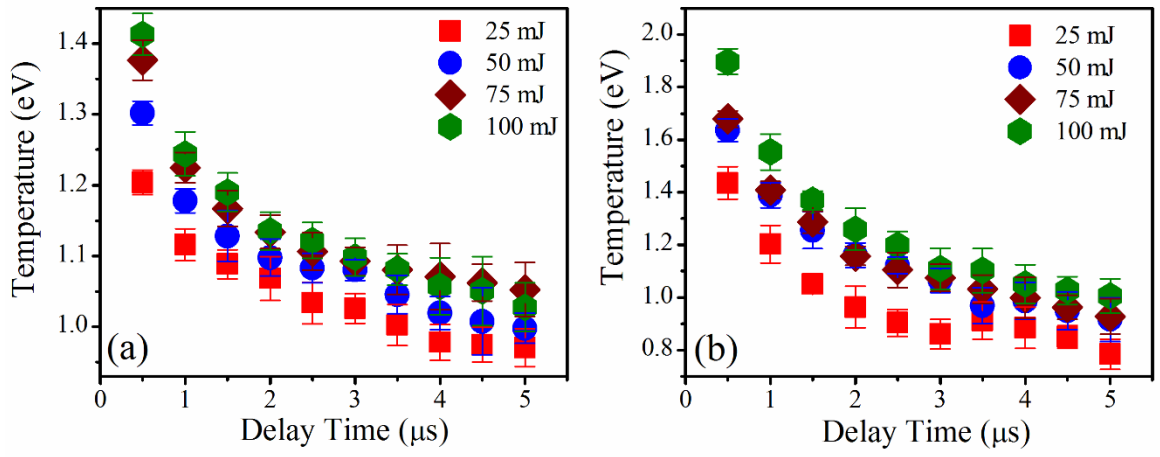

Figure 5.9 Temporal variation from plasma temperature from (a) atomic and (b) ionic lines as a function of laser energy.

5.1.3 Temporal variation of electron density from the stark-broadened profile of molybdenum

Electron density is an important parameter to describe the plasma environment and is also crucial for establishing thermodynamic equilibrium. One of the most powerful spectroscopic techniques to determine the electron number density with reasonable accuracy is via measurements of the Stark-broadened line profile of an isolated atom or singly charged ion. In the present case, the electron density in LIP of Mo is estimated using the stark-broadened profile of MoI-313.2 nm line using equation (2.18) in chapter 2 section 2.2.2. The electron impact width parameters are obtained from the literature [114]. The temporal variation of line profile as a function of incident laser energy of 25 mJ is shown in Fig.5.10 (a). The line profile of MoI-313.2 nm fitted to Lorentzian function at a delay time of 0.5 μs is shown in Fig 5.10 (b) along with the FWHM marked on it.

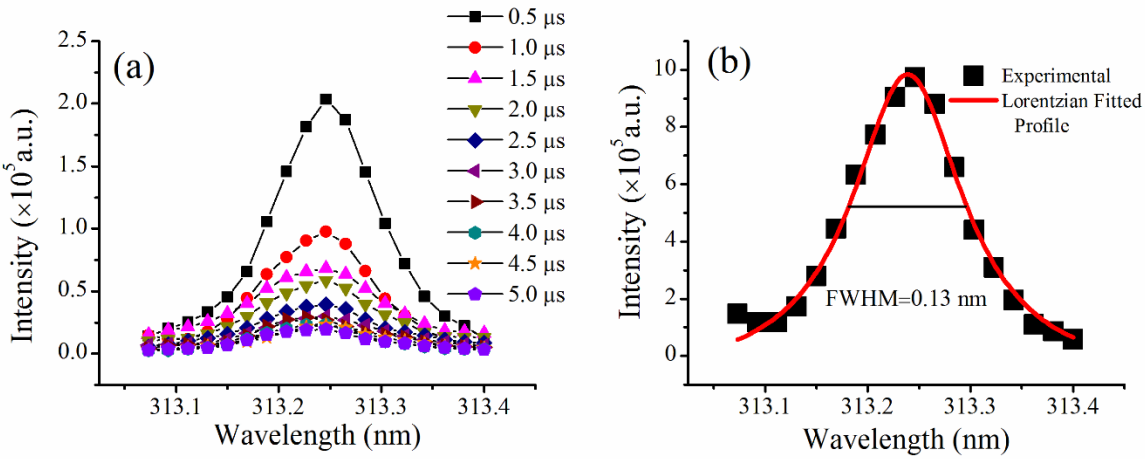

Figure 5.10 (a) Temporal variation of line profile of MoI-313.2 nm and (b) lorentzian fitted profile for the incident laser energy of 25 mJ.

The temporal variation of electron density as a function of incident laser energies from equation (2.18) are shown in Fig. 5.11. As the delay time increases from 0.5 μs to 5.0 μs, the electron density changes from 5.97 (±0.34)-3.75 (±0.23), 8.51 (±0.31)-4.06 (±0.18), 10.28 (±0.09)-

3.80 (±0.09) and 13.93 (±0.23)-4.45 (±0.15) $\times 10^{16}$ cm^{-3} for the incident laser energies of 25, 50, 75 and 100 mJ respectively. The variation in the electron density with the incident laser energy is more prominent in the initial temporal window of 0.5-1.5 μs as compared to that of the later delay time.

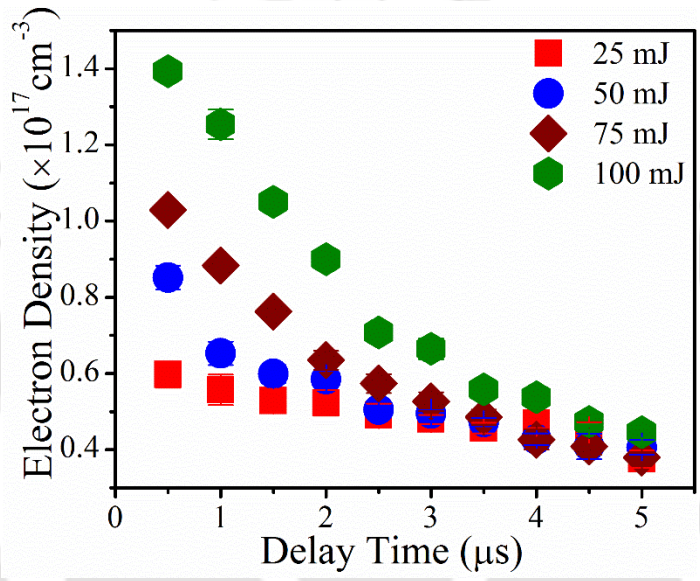

Figure 5.11 Temporal variation of electron density as a function of laser energy.

From the Fig. 5.4, 5.9 and 5.11 it is evident that the plasma emission intensity of MoI and MoII lines, plasma temperatures and electron density decrease with the increase in delay time but increase with the increase of the incident laser energy. The decrease in plasma emission intensity, electron density and plasma temperature with the delay time after the termination of laser pulse is due to the three mechanisms i.e. thermal conduction, expansion and radiative cooling. This is due to the fact that with the incident of laser on to the target, plasma is generated by the initial part of laser pulse while its trailing part heats the plasma. During the laser pulse, plasma expands isothermally but after the end of the laser pulse there is no external

source of energy available for the plasma. So LIP expands adiabatically in the surrounding air and loses its energy which results into the decrease in plasma emission intensity as well plasma temperature and electron density. The increase in incident laser energy results into higher mass ablation and the plasma emission intensity and plasma parameters increases for the incident laser energy of 25-75 mJ but at higher energy of 100 mJ the increment is not significant due to the plasma shielding [60].

5.1.4 Assessment of optical thin condition in transient LIP of molybdenum

The plasma parameters can be estimated with good accuracy provided emitted radiation in LIP is optically thin. The Branching ratio method equation (2.11), is applied for the evaluation of optical thin condition of LIP at different as a function of delay time and incident laser energy. The theoretical value of intensity ratios of MoI-585.8 /MoI-572.2 and MoI-568.9/MoI-579.1 are 2.98 and 1.16 respectively. The variation in the experimentally obtained intensity ratios for MoI-572.2/MoI-585.8 in delay time range of 0.5-5.0 μs is shown in Fig.5.12 (a) and is varying from 3.81-2.36, 2.81-2.50, 2.66-2.77and 2.32-3.17. The intensity ratio 568.9/MoI-579.1 is shown in Fig.5.12 (b) and is varying from 1.41-1.23, 1.58-1.26, 1.62-1.17 and 1.61-1.29 for the incident laser energies of 25, 50, 75 and 100 mJ respectively. The close proximity of these values of branching ratio obtained experimentally with that of the theoretical value is observed in the range of 1.5-5 μs confirming the optical thin condition in the LIP of Mo for this particular temporal window.

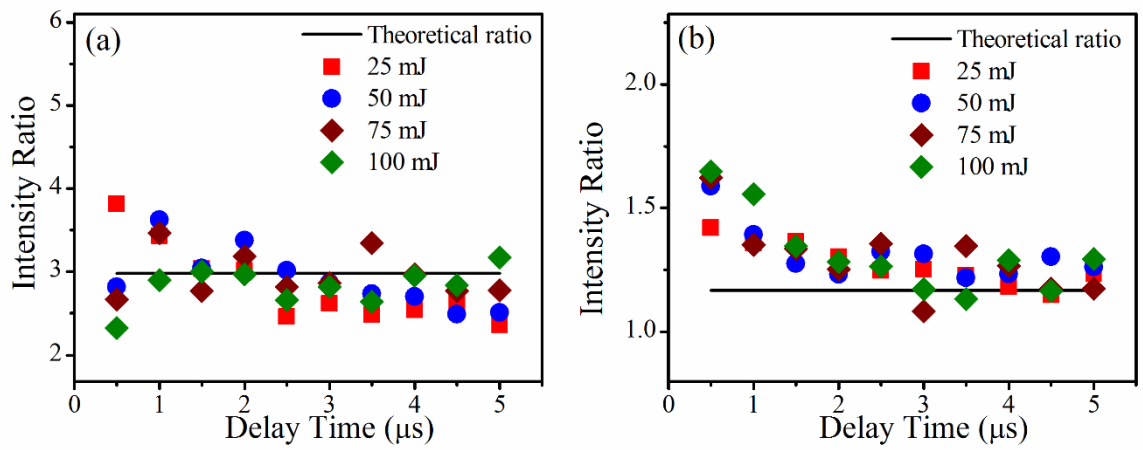

Figure 5.12 Temporal variation of intensity ratio of (a) MoI-572.2/585.8 and (b) MoI-568.9/579.1.

5.1.5 Validity of LTE condition in transient LIP of molybdenum

The validity of LTE is another essential criteria inside the plasma to obtain plasma parameters. In the present study, the LTE condition is verified by employing Mc-Whirter equation (2.4) where plasma is assumed to be homogeneous and stationary [96]. The relaxation time is estimated to take into the transient nature of the LIP. To estimate the minimum required electron density in order the collisional process to dominate over the radiation processes by Mc-Whirter equation, the MoI-390.2 nm transitions is used. It is the first resonance line having the energy difference between ground and upper state, ΔE_{nm}=3.175 eV. The relaxation time is also estimated using this transition. The temporal variation of required minimum electron density and relaxation time as a function of incident laser energy is shown in Fig. 5.13 (a) and (b) respectively. From the figure it is observed that required minimum electron density is of the order of 10^{15} while the estimated electron density is of the order of 10^{16} confirming the validity of LTE through the Mc-Whirter equation. The estimated relaxation time is of the order

of 10^{-10} s which is much less than the decay time of LIP as measured in the present experimental found to be of the order 10^{-6} s, confirm the validity of LTE in transient situation.

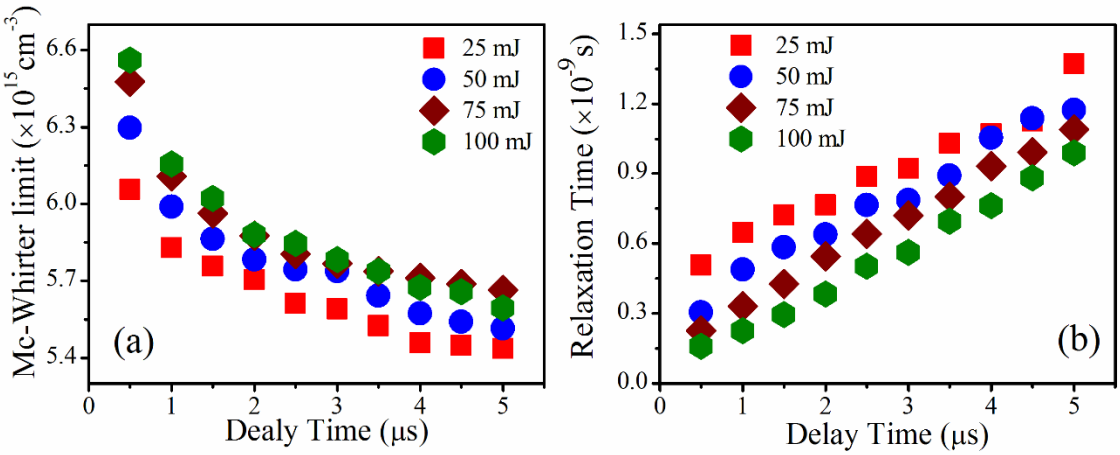

Figure 5.13 Temporal evolution of (a) minimum electron density for LTE and (b) relaxation time at different laser energies.

5.2 Studies on the spatial evolution of LIP of molybdenum

To study the spatial evolution of LIP, the emission spectra of Mo are recorded at different locations along the plasma axial expansion direction (Fig. 3.5) as a function of incident laser energy. In this part of the experiment, spectra are recorded at a delay of 2 μs which is falling in the optimum range of temporal window as shown in previous section where the condition of LTE and optical thin plasma prevails. In the following sections the spatial evolution of plasma parameters i.e. plasma temperature and electron density as a function of incident laser energy is presented. The LTE condition verified during the spatial evolution of plasma by taking into account the inhomogeneous nature of the plasma. The optical thin condition of plasma is also assed to obtain the spatial window for its validity.

5.2.1 Spatial variation of plasma emission intensity of molybdenum

The LIP emission spectra recorded at different locations along the axial expansion direction (*z* axis) of the LIP of Mo using experimental set up, Fig. 3.5, as a function of laser energy is shown in Fig. 5.14.

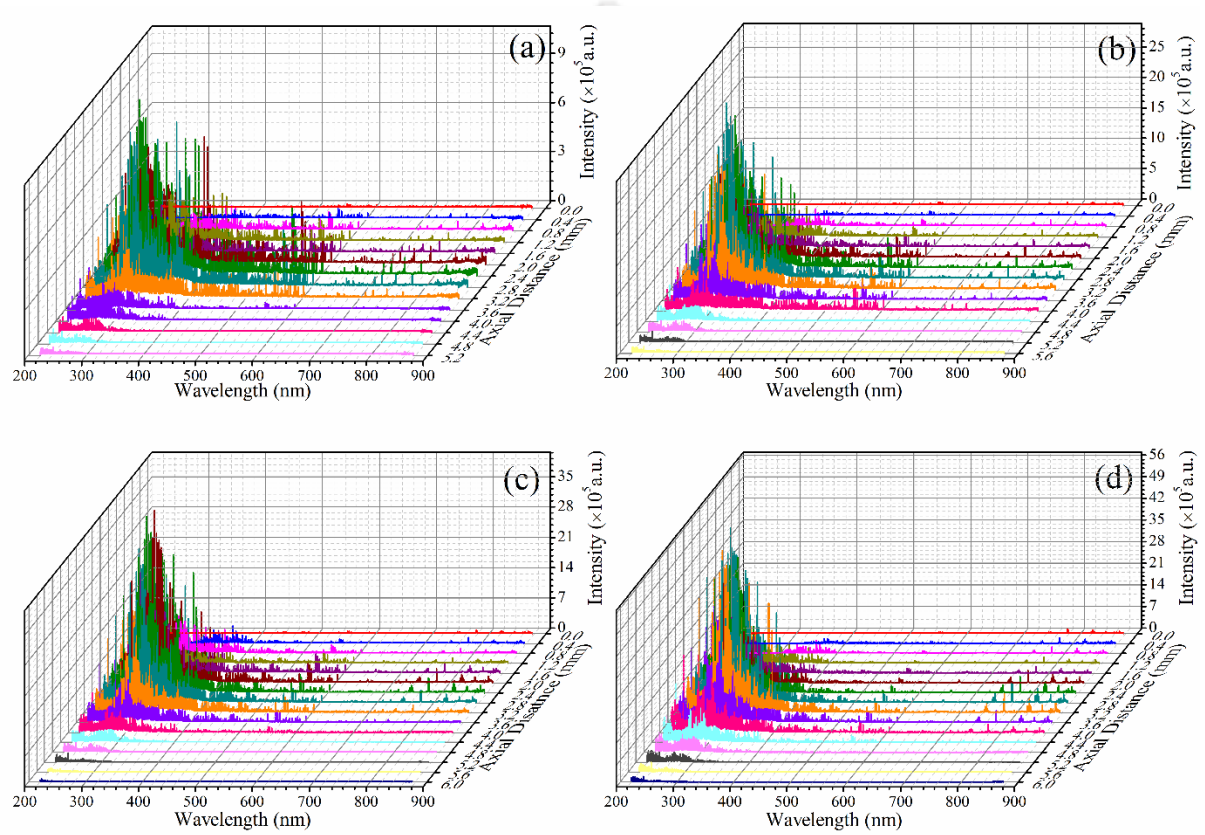

Figure 5.14 Spatial evolution of plasma emission from LIP of molybdenum at (a) 25, (b) 50, (c) 75 and (d) 100 mJ of incident laser energy.

The axial variation in the intensity of LIP in the spectral range of 277-288 nm and 550-570 nm for the incident laser energies at 25 mJ are shown in Fig. 5.15 (a) and (b) respectively. The intensity profile along the axial direction of the plasma plume for the MoII-284.8 and MoI-550.6 nm lines at various laser energies are shown in Fig. 5.16 (a) and (b) respectively. From the axial distribution of plasma emission intensity, it is observed that the maximum in emission

intensity for ionic lines appear nearer to the target surface than that of the atomic lines slightly away from the target. The ionic transition reaches a maximum at a distance of 1.6 mm from the target surface for the laser energy of 25 mJ and other higher laser energy at 2.0. The atomic transition attains maximum intensity at 2.4 mm distance away from the target for the incident laser energy of 25-75 mJ but for 100 mJ the distance is 3.2 mm. Similar trend has been reported in the literature. [62, 175].

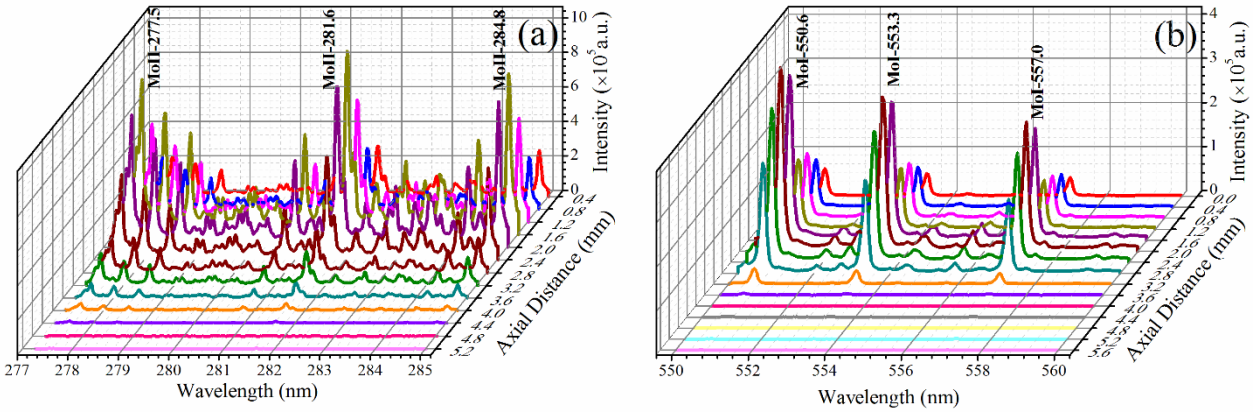

Figure 5.15 Axial variation of (a) ionic lines in the spectral range of 277-285 nm and (b) atomic lines in the spectral range of 550-570 nm for laser energy of 25 mJ.

The velocities of ions and atoms are different in the LIP and possess different persistent time as seen from temporal studies section 5.1.1. The persistence time of ions are less than that of the atoms and the velocities of ions are higher than the atoms, thus maxima in the ionic intensity appears close to the target surface than that of the atomic transition. At higher incident laser energy, the plasma plume length increases and the emission from ionic stages results from the hot inner core of the LIP while emission from neutral atom or lower stages occurs in the outer part of the LIP, so the atomic transition reaches maximum towards the extended location as compared to that of ionic transition. It is concluded that intensity for both the MoI and MoII

transitions increases up to certain distance and after attaining the maximum intensity these start to decreases due to the various energy loss mechanisms [79, 172, 177] .

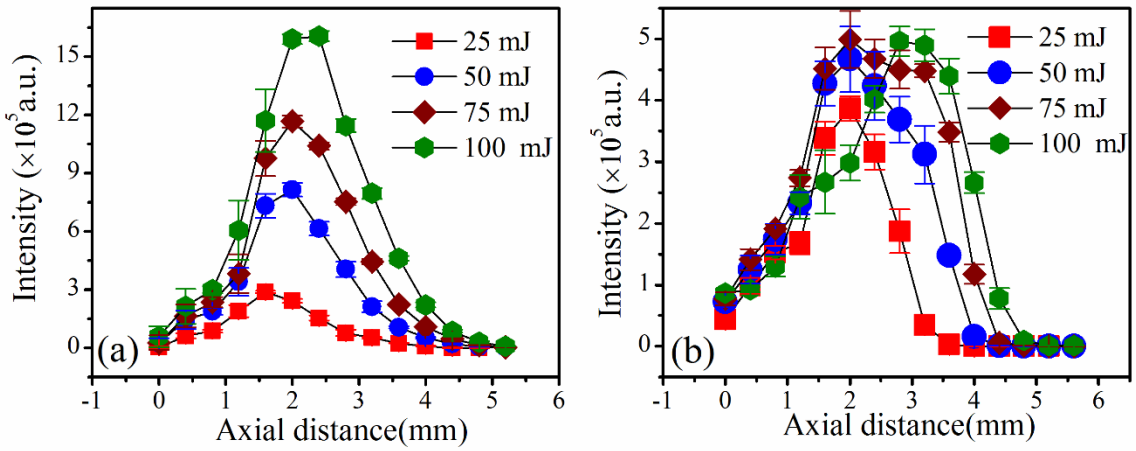

Figure 5.16 Intensity variation of (a) MoII-284.8 nm and (b) MoI-550.6 nm along the axial expansion direction of the plasma as function of incident laser energy.

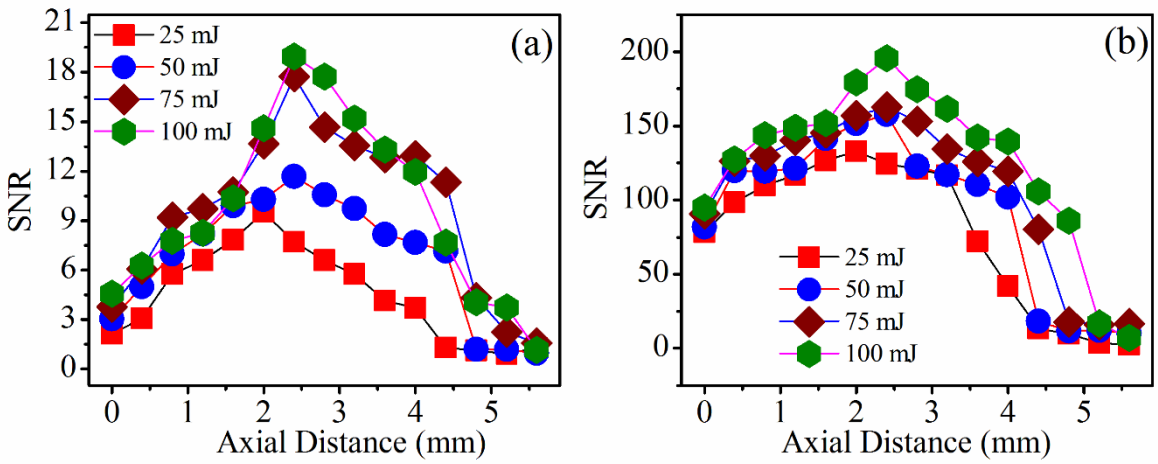

Figure 5.17 Spatial variation of SNR of the spectra as function of incident laser energy from (a) MoI-357.0 nm and (b) MoI-557.0 nm.

The spatial variation of SNR as function of energy as obtained equation (4.1) for MoI-357.0 nm and MoI-557.0 nm line is shown in Fig. 5.17(a) and (b) respectively. The value of SNR

increases from the target surface up to a distance of 2.4 mm, and then there is a decrease in the SNR value beyond this distance.

5.2.2 Spatial variation of plasma temperature of molybdenum

Assuming LTE is prevailing in LIP of Mo and emitting optical thin emission of radiation, the atomic transitions are used to measure the plasma temperature at various axial positions. The spatial variation in plasma temperature (from the Boltzmann plot) is shown in Fig. 5.18. It follows the similar trend as that of the intensity profile of MoI line, the temperature approaches a maximum value at a position of 2 mm distance from the target surface for the incident laser energy of 25 mJ and for other higher laser energies it is 2.4 mm from the target surface and then it falls down. This is in agreement with that of the reported in literature [62, 79, 172, 175, 177, 178, 183].

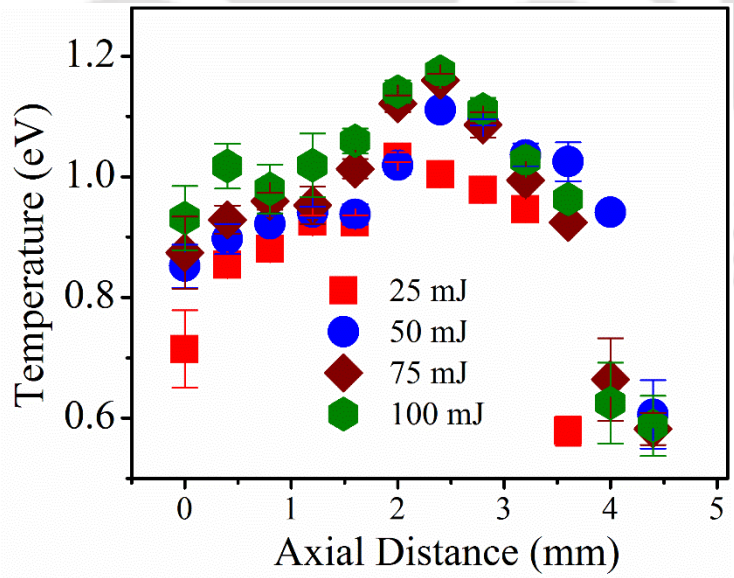

Figure 5.18 Temperature variation along the axial direction of the plasma at different laser energies.

The value of the temperature is increasing with incident laser energy. The temperature values change from 0.714-0.578, 0.851-0.606, 0.874-0.582 and 0.931-0.587 eV as the axial distance increases from 0-4 mm in a step of 0.4 mm while attaining through the maximum value of 1.032, 1.110, 1.121 and 1.174 eV for the incident laser energy of 25, 50, 75 and 100 mJ respectively. After the 4 mm distance from the target, it is not possible the estimate the plasma temperature correctly as the intensity is extremely low.

5.2.3 Spatial variation of electron density of molybdenum

From the Fig. 5.19, it is evident that the electron density reaches a maximum value at distance of 2 mm away from the target. Normally it is expected that the electron density decreases away from the target surface but in the present study, spatial profile is recorded at a fixed delay of 2 μs, at which the LIP is already detached from the target and moving away from the target while expanding simultaneously.

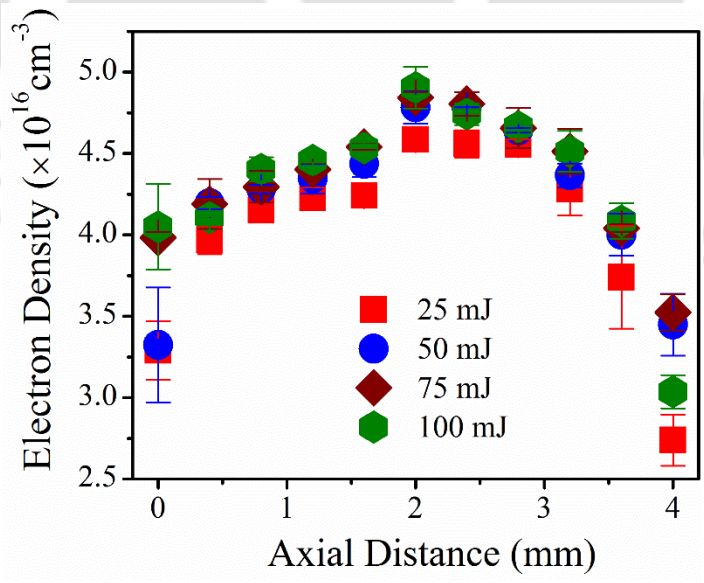

Figure 5.19 Variation of the electron density along the plasma axial direction at different laser energies.

The maxima of the electron density is always within its core. Thus the electron density attains the maximum value at a certain distance away w.r.t the target at later time scale. Electron density changes from 3.28 (±0.18)-2.73 (±0.15), 3.32 (±0.35)-3.44(±0.18), 3.94 (±0.03)-3.52 (±0.11) and 4.05 (±0.26)-3.03 (±0.10)×10^{16} cm^{-3} while passing through the maximum value of 4.58 (±0.001), 4.78 (±0.09), 4.84 (±0.03) and 4.90 (±0.12) ×10^{16} cm^{-3} at 2 mm distance for the incident laser energy of 25, 50, 75 and 100 mJ respectively.

5.2.4 Assessment of optical thin condition in inhomogeneous LIP of molybdenum

In assessing the space-resolved studies, same pairs of MoI lines are used for branching ratio as mention in the section 5.1.4, for the temporal evolution to investigate the optical thin condition of LIP. The experimental results are shown in Fig. 5.20 along with the corresponding theoretical value, equation (2.11) as a solid line.

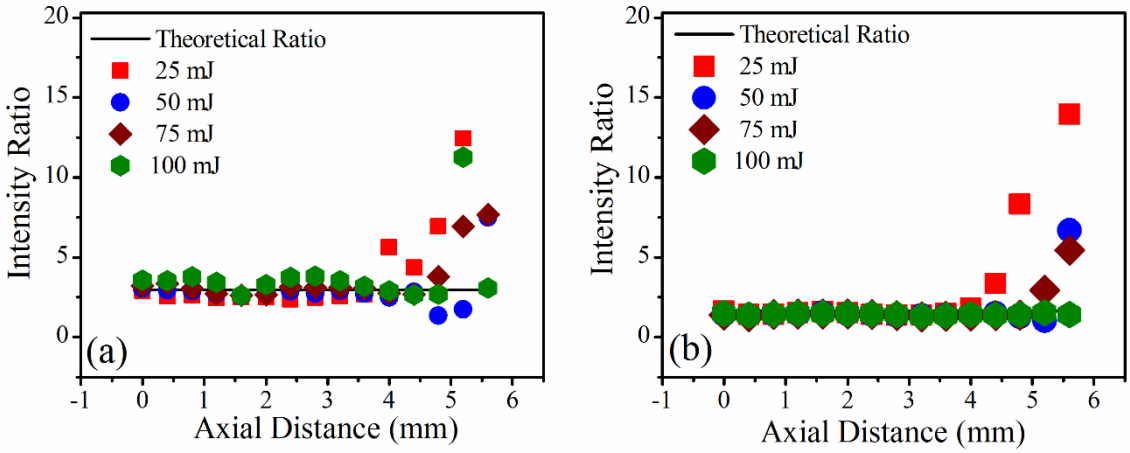

Figure 5.20 Variation of intensity ratio (a) MoI-572.2/585.8 and (b) MoI-568.9/579.1 at different location of plasma along direction of expansion as a function of laser energy.

The experimental intensity ratio for both, MoI-585.8 /MoI-572.2 nm and for MoI-568.9/MoI-579.1 are in the close proximity of the theoretically estimated values equation (2.11), up to a

distance of 4 mm away from the target at all the energies and it deviates beyond this distance from the target. The LIP is found to be optically thin up to a distance of 4 mm from the target at all the four laser energies.

5.2.5 Validity of LTE condition in inhomogeneous LIP of molybdenum

In the spatial evolution studies, the LTE criteria is assessed in LIP of Mo in two situations. In first case, the LIP is considered to be stationary and homogeneous and Mc-Whirter criteria condition, equation (2.4) is employed to estimate the minimum required electron density at different axial location for the validity of LTE. In the second case, the diffusion of LIP is estimated by equation (2.10) at different axial position in LIP during the expansion to take into account the inhomogeneous nature of the LIP. The estimated values of the required minimum electron density and diffusion length at various axial location for different incident laser energies are shown Fig. 5.21 (a) and (b) respectively.

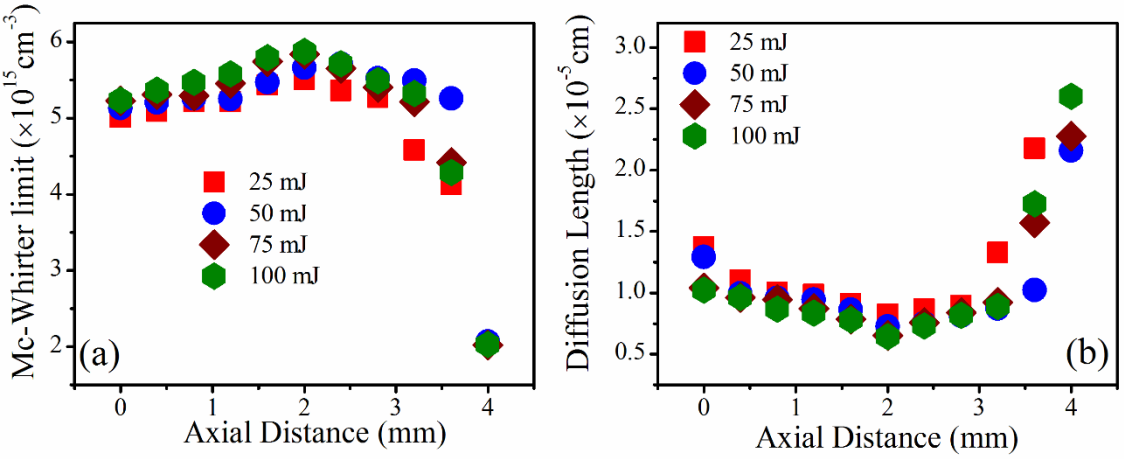

Figure 5.21 (a) Minimum required electron density for LTE (b) diffusion length of the plasma at various axial position at various energies.

It is observed that the minimum electron density at different axial location is of the order of 10^{15} cm^{-3} which is less than the estimated electron density, Fig. 5.19, thus confirming the LTE in case of stationary and homogeneous LIP. To assess the LTE in case of stationary and inhomogeneous LIP, the diffusion length should be at least ten times less than plasma dimension. As shown in Fig.5.21 (b) the order of diffusion length of the 10^{-4} mm is much smaller than dimension of LIP which of the order of few mm, validating the LTE at different locations of LIP. But it is notable from the Fig. 5.21 (b) that the after the 3.6 mm position the diffusion length starts increase which is the indication of departure from LTE in LIP.

5.3 Conclusion

In this chapter the LIBS studies on Mo in air using time and space-resolved as function of incident laser energy to get the optimized time and spatial window where the LTE and optical thin conditions are valid. The LIP emission intensity of atomic and ionic lines, plasma temperature and electron density are studied in both the cases. The value SNR of the spectra increases up to delay time of 3.5 μs and beyond this it falls down. The plasma temperature is estimated from MoI and MoII lines separately acquires nearly the same value in the temporal window of 1.5-4 μs thus affirming the coexistence of thermal equilibrium among atoms and ions. The LTE condition is verified by Mc-Whirter criteria as well as considering the transient nature of plasma. The obtained relaxation time is of 10^{-10} s which is much less than the plasma decay time of the order of 10^{-6} s. Both these observations confirm the validity of LTE in the LIP. The LIP is observed to be optically thin in the temporal window of 1.5-5 μs as is verified via branching ratio. The SNR is also maximum within this range of temporal window. Thus the optimum temporal window for LIBS study satisfying the LTE and optical thin plasma condition lies in the delay range of 1.5-3.5 μs w.r.t to laser pulse. The space-resolved spectra

of the LIP along the axial plasma expansion direction is studied at a fixed delay of 2 μs (optimum temporal window). The maximum attainable value of the plasma emission intensity and temperature are found to be at a certain distance away from the target surface and decrease close to the target as well as towards the plasma edge, away from the target. The maximum intensity for ionic line appears slightly closer to the target as compared to that of the atomic lines. From the axial profile of plasma temperature, it is also observed that its optimum value is around at 2.4 mm from the target surface. From the axial profile of electron density, it is observed that the electron density attains maximum value at a distance of 2 mm away from the target surface but decreases beyond this. The LTE criteria are satisfied in case of inhomogeneous expansion of plasma. The experimentally obtained branching ratios are in good agreement with the theoretical ratios in the space-resolved studies up to the axial distance of 4 mm. Extensive studies on the LIP of Mo using time and space-resolved studies presented in this chapter will be helpful in offering important reference data for the design and optimization of LIBS systems involved in various field of applications.

Chapter 6 Single-Line Calibration Free LIBS Technique on Cu-alloys for Compositional Analyses

Laser induced breakdown spectroscopy (LIBS) is routinely used to determine the elemental concentration of a sample using the calibration technique. In this technique, a calibration curve is drawn between the emission line intensities versus the known composition of the sample [116, 184]. The composition of the unknown elements of some matrix-matched samples is then estimated by comparing the emission line intensity from the calibration curves. This technique requires a matrix-matched reference sample which cannot be found for every situation. To overcome this problem, Cuicii et al. [126] introduced the calibration free LIBS (CF-LIBS) technique. Owing to some of the salient features the CF-LIBS technique, it has applications in various field. The CF-LIBS method has been applied for the analysis of metallic alloys of Al [62], Fe [185], Cu [186] [187]and Au[188] as well as nonmetallic samples such as soils [142], rocks [189], glasses [190], human hair [191], coral skeletons [192], environmental samples[193] etc. The CF-LIBS technique is applied under the assumptions [97] of (i) the plasma composition is exact reflection of the sample composition (i.e. stoichiometric ablation) under investigation, (ii) the plasma should be in LTE, (iii) plasma emission should be optically thin and (iv) the spectra recorded should give the characteristic transitions of all the constituent elements present in the sample. But all these conditions are highly influenced by the transient and inhomogeneous nature of the laser induced plasma (LIP) which in turn dependent on the experimental condition. In order to study the effect of temporal as well as spatial evolution of LIP on the performance of CF-LIBS technique, single line CF-LIBS technique is applied to three copper alloys samples and presented in this chapter [194]. The concentration of the

constituent elements of the copper alloys sample is estimated via LIBS as a function of delay time and axial position at four laser energies of 25, 50, 75 and 100 mJ. From these the optimum temporal and spatial window are assessed for CF-LIBS application for minimum error in the estimation of percentage composition of constituent elements.

6.1 Estimation of percentage composition from single line CF-LIBS technique

In the CF-LIBS technique, introduced by Cuicii et al.[126], the concentration of elements is obtained from the intercept of the Boltzmann plot for all elements present in the sample, both for atomic as well as for ionic lines. The Boltzmann plot requires at least 3–4 optically thin lines which may be difficult to obtain for some of the constituent elements present in the sample, especially for minor or trace elements [195]. Therefore the technique was subsequently modified by Gomba et al. [196] by developing an algorithm to calculate the percentage composition using the theoretical electron density value. But in this, prior knowledge of the number of elements present in the sample is required, which is not possible in an unknown sample (e.g. soils, biological samples etc.). To overcome this situation in the present study, single line transition method is applied in CF-LIBS technique to estimate the elemental concentration [195]. This method utilizes the single transition of each of the constituent elements. All the steps required in this single line CF-LIBS technique is depicted in the flow chart, Fig. 6.1

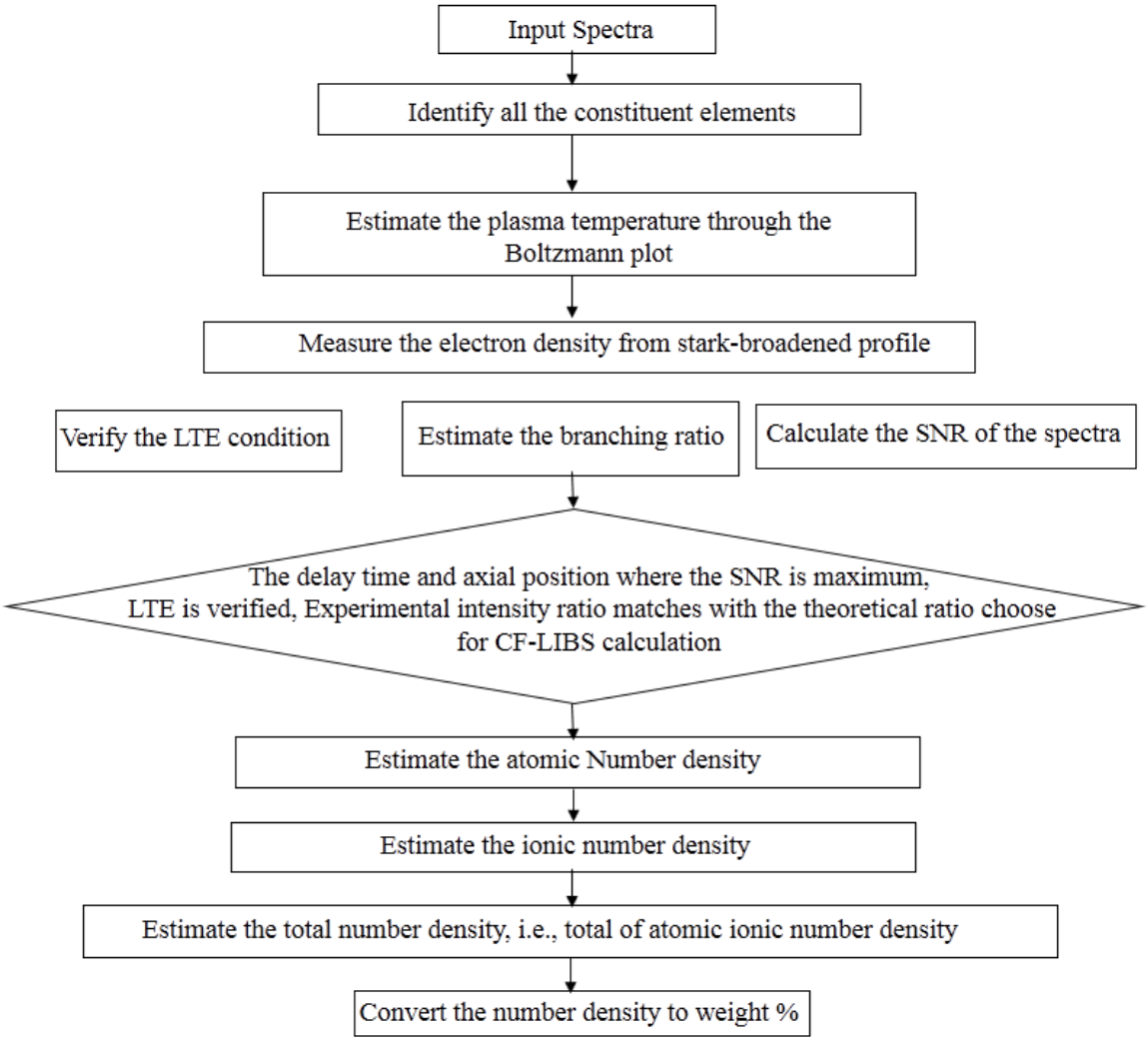

Figure 6.1 Flow chart of the required step in single line CF-LIBS algorithm.

The Boltzmann equation that connect the emission line intensity of the same species, equation (2.12) can be rearranged as

$$FN = \frac{I_{nm}\, U(T_e)}{A_{nm}\, g_n} \exp\left(\frac{E_n}{k_B T_e}\right) \tag{6.1}$$

The ionic number density can be estimated from Saha-Boltzmann equation given by equation following equation,

$$\frac{N_e N^{z+1}}{N^z} = 2\frac{U^{z+1}}{U_Z}\left(\frac{2\pi m_e k_B T_e}{h^2}\right)^{3/2} \exp\left(\frac{-E_z + E_{z+1} - \chi}{k_B T_e}\right) \quad (6.2)$$

The total number density of any element is thus the sum of all the atomic and ionic number density and is given by following equation,

$$N_S^{Total} = \sum_{z=1,2} N_s^z \quad (6.3)$$

The experimental factor F in equation (6.1) can be eliminated by normalizing the sum of the total number density over all elements, m, present in the plasma, given by the following equation,

$$\sum_{s=1}^{m} \sum_{z=1}^{2} FN_s^z = 100\ \% \quad (6.4)$$

In the present case, only atomic and singly ionized transitions are observed therefore, the summation is limited to z=2 in equation (6.3) and (6.4) where z=1 corresponds to neutral atom and z=2 that of the singly ionized ion. For the assessment of percentage composition of constituent elements in copper alloys from the equation (6.1) - (6.4), the intensities of lines are recorded by the experimental set up shown in Fig. 3.1 and Fig. 3.5. The required plasma temperature and electron density are obtained from the Boltzmann plot and stark-broadened profile as discussed in section 2.2. The other atomic parameters required are taken from the NIST database [166].

6.2 Influence of delay time on CF-LIBS measurements

In the following sub-sections, the temporal evolution of the LIP spectra, estimation of plasma temperature, electron density, validity of LTE criteria and condition of optically thin plasma, as a function of delay time with respect to the laser pulse (w.r.t) for various incident laser energies are presented. In the next sub-section the percentage composition of the constituent elements in three of copper alloys are determined as a function of delay time. From the minimum value of the relative error in the CF-LIBS measurement as well as distance function, *dist* (section 6.2.6, equation 6.5) the optimum temporal window for application of CF-LIBS is identified. The results are compared with standard EDX analyses, averaged over four distinct locations on each of the samples. The constituent elements and their corresponding percentage composition obtained via EDX for all the three samples are listed in Table 6.1.

Table 6.1 EDX measurement on three different copper alloys.

Elements	Sample1	Sample2	Sample3
Al	1.17	-	-
Fe	1.50	-	-
Ni	0.50	5.06	7.50
Cu	57.15	75.28	92.50
Zn	34.12	19.65	-
Sn	0.90	-	-
Pb	4.00	-	-

It is observed that sample1 (commercial brass) comprised of Cu and Zn as the major constituent elements and Al, Fe, Pb, Sn and Ni are present as trace elements. Sample 2 contains only three elements with Cu having maximum concentration of 72.58% followed by Zn with 19.65% and

third element being Ni having remaining concentration of 5.06%. The third sample comprised of only 92.5 % of Cu and 7.5% of Ni only.

6.2.1 Temporal evolution of emission spectra of copper alloys

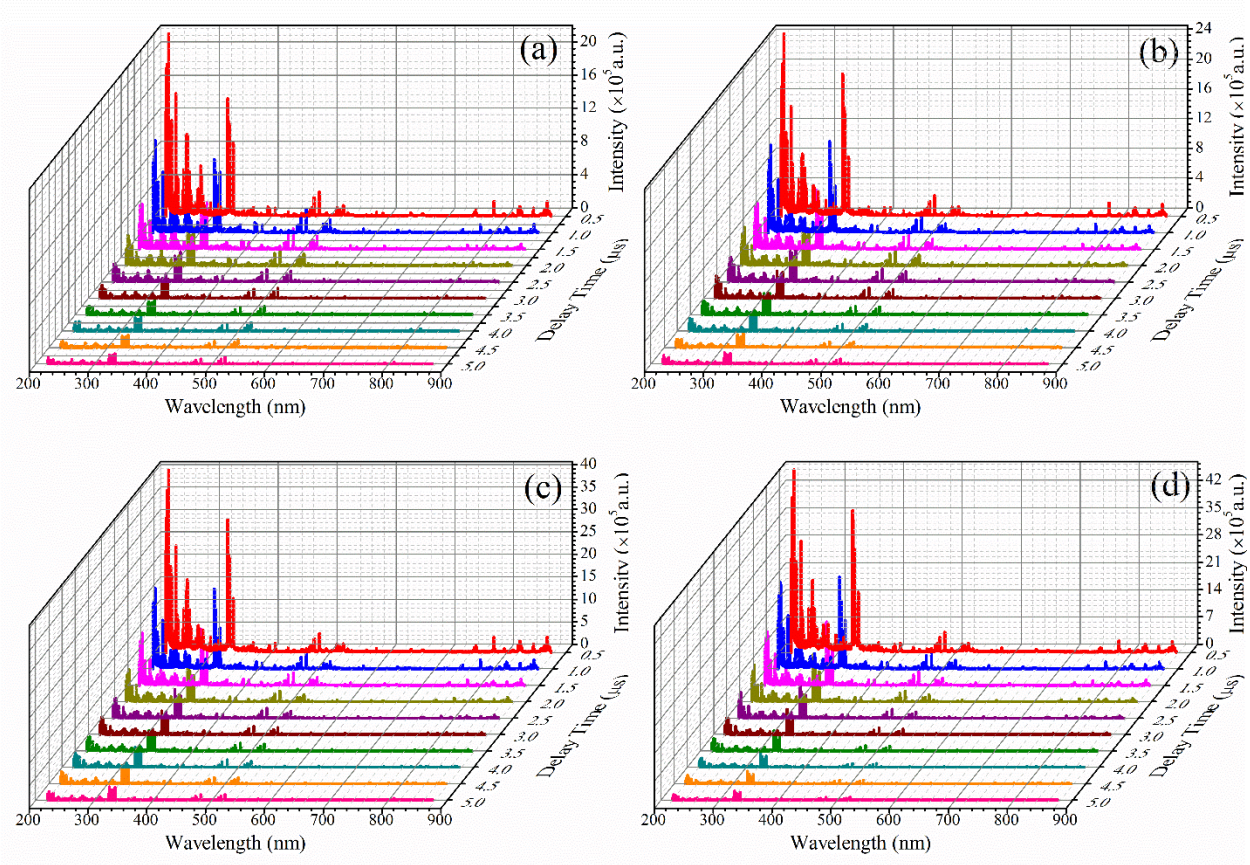

Figure 6.2 Temporal evolution of LIP spectra of sample 1 in air in the time window of 0.5–5 μs for the laser energy (a) 25 mJ. (b) 50 mJ, (c) 75 mJ and (d) 100 mJ.

The laser ablation on sample 1 is performed at four different laser energies 25, 50, 75 and 100 mJ while that of the sample 2 and sample 3 is performed at laser energy of 50 mJ in air. The minimum laser energy of 25 mJ is greater than the breakdown threshold for all the elements present in all three samples [87]. The temporal evolution of emission spectra are recorded from

the LIP all the three samples in delay time range of 0.5-5 μs w.r.t incident laser pulse. The time-resolved spectra of LIP for sample1 at four laser energies are shown in Fig. 6.2 (a)-(d).

From the spectra, various atomic and ionic transitions of Cu, Zn, Al, Fe, Sn, Pb and Ni are identified in this sample1 using NIST database [166]. The expanded view of some of the identified transitions corresponding to various elements present in sample 1 for a delay time of 2 μs along are shown in Fig. 6.3. The temporal variation of intensity of each of the constituent elements of sample 1, AlI-394.2, FeI-438.5, NiI-349.2, CuI-510.5, ZnI-468.0, SnI-326.2 and PbI-405.2 is shown in Fig. 6.4 (i)-(vii) and that of the SNR of the spectra estimated using intensity of CuI-465.0 nm in equation (4.1) is given in Fig. 6.4 (viii).

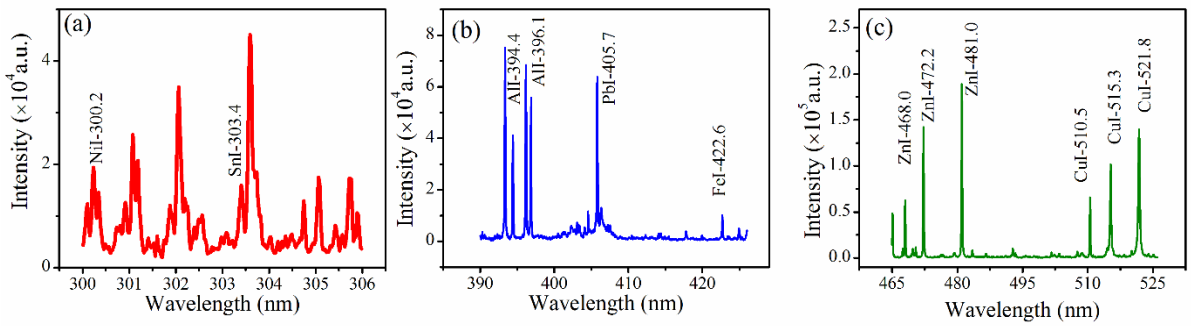

Figure 6.3 Expanded view of the spectra for sample1 in the spectral range of (a) 300-306 nm (b) 390-430 nm and (c) 465-525 nm at a delay of 2 μs.

The temporal evolution of LIP spectra of the sample 2 at 50 mJ of incident laser energy Fig. 6.5(a) and that of the expanded view of some of the identified transitions in sample 2 are shown in Fig. 6.5 (b)-(c) respectively. The temporal variation of the emission intensity of the identified elements in the sample 2 and the SNR of the spectra are shown in Fig. 6.6 (i) - (iii) and (iv) respectively. The temporal evolution of LIP spectra of the sample 3 at 50 mJ of incident laser energy is shown in Fig. 6.7(a) and that of the expanded view of some of the

identified transitions in sample 3 are shown in Fig. 6.7 (b)-(c) respectively. The temporal variation of the emission intensity of the identified elements in the sample 3 and the SNR of the spectra are shown in Fig. 6.8 (i) - (ii) and (iii) respectively

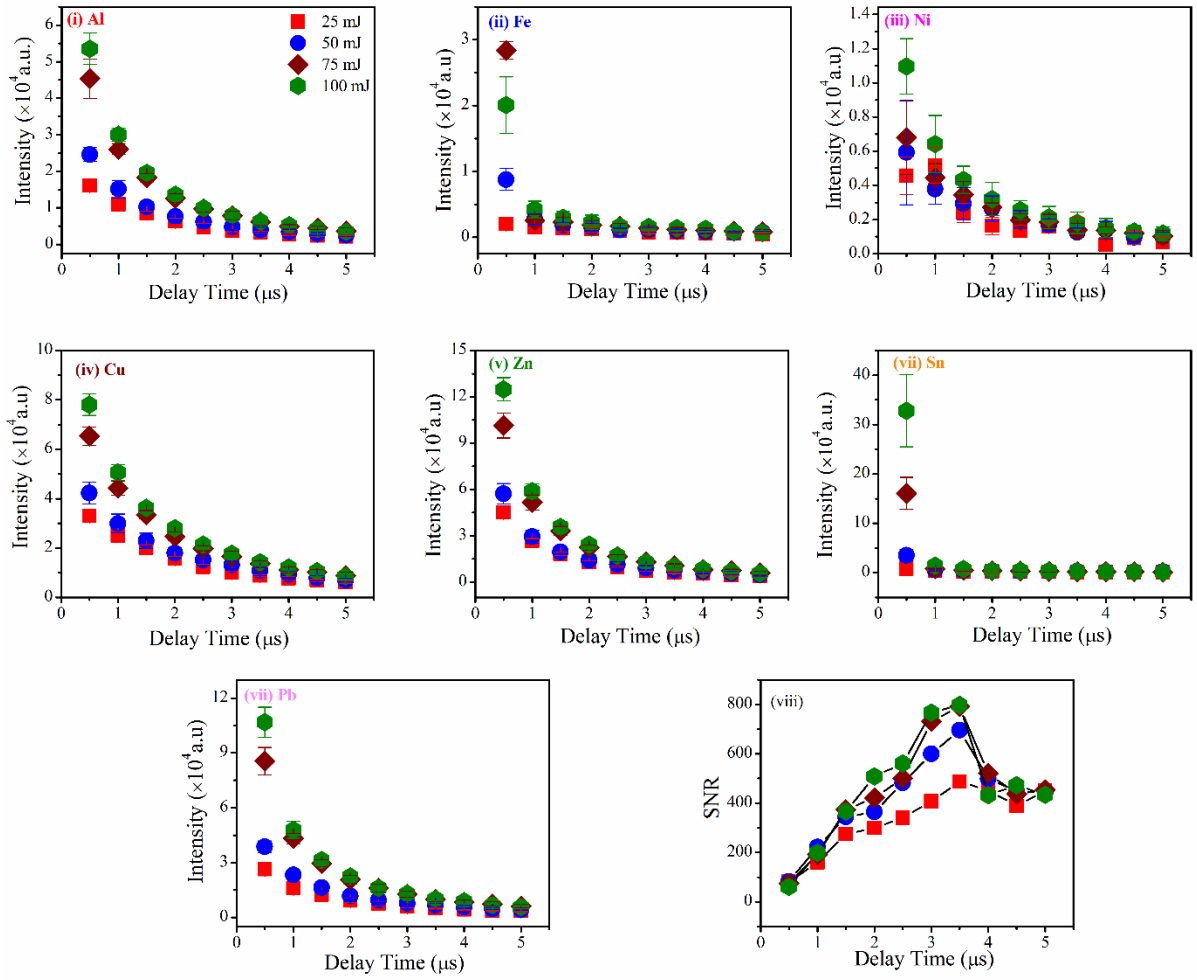

Figure 6.4 Temporal variation of intensity for (i) Al, (ii) Fe, (iii) Ni, (iv) Cu, (v) Zn, (vi) Sn (vii) Pb and (viii) SNR for sample 1 as a function of laser energy.

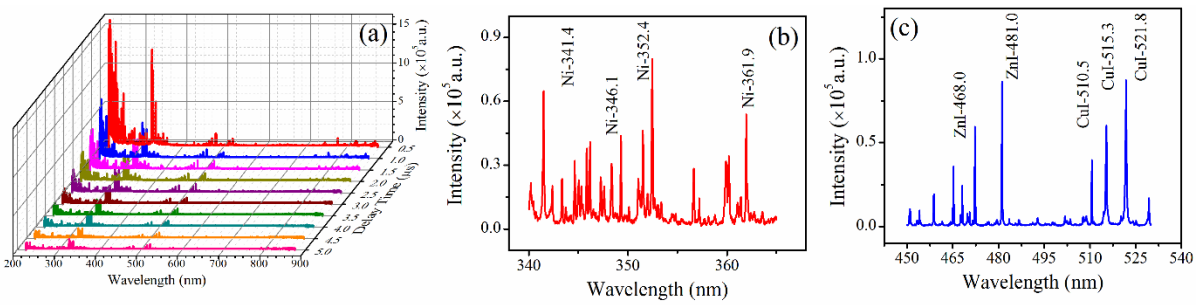

Figure 6.5 (a) Temporal evolution of the spectra and expanded view in the spectral range (b) 340-370 nm and (c) 450-530 nm for sample 2.

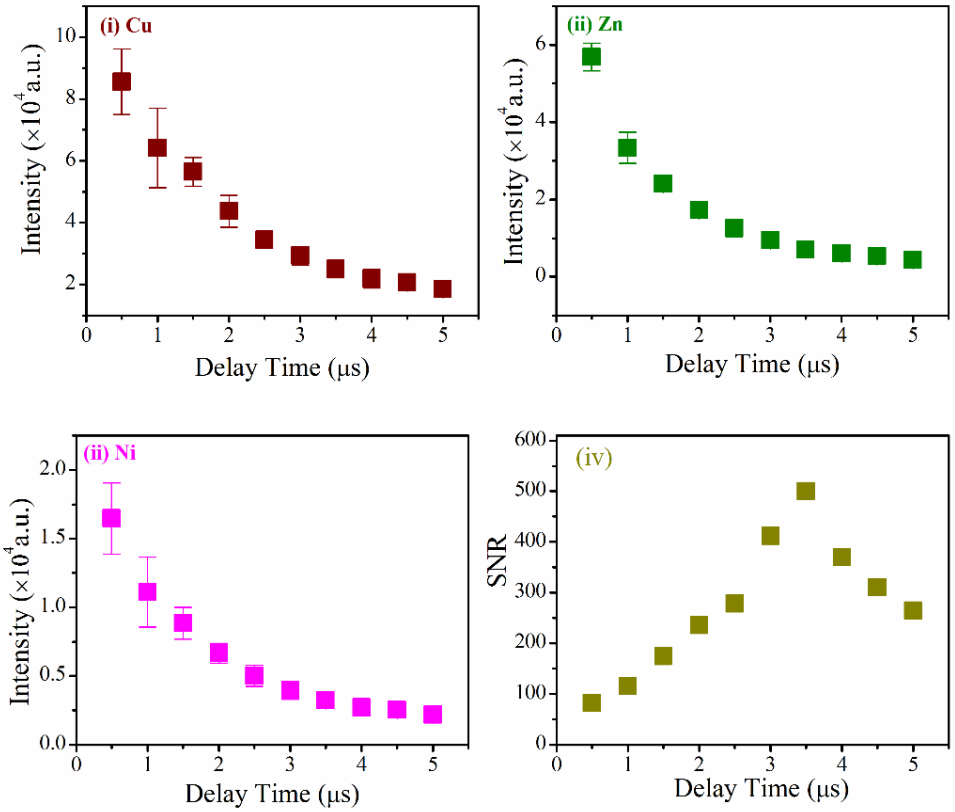

Figure 6.6 Temporal variation of intensity for (i) Cu, (ii) Zn, (iii) Ni, and (iv) SNR for sample 2 at a laser energy of 50 mJ laser energy.

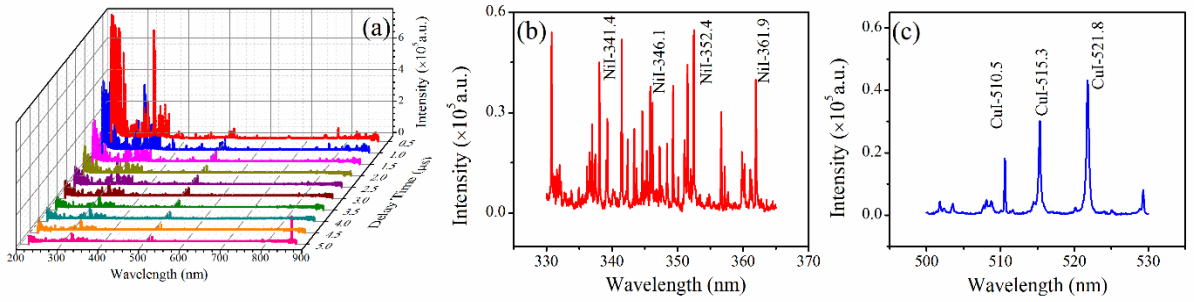

Figure 6.7 (a) Temporal evolution of the spectra and expanded view in the spectral range (b) 330-365 nm and (c) 500-530 nm for sample 3.

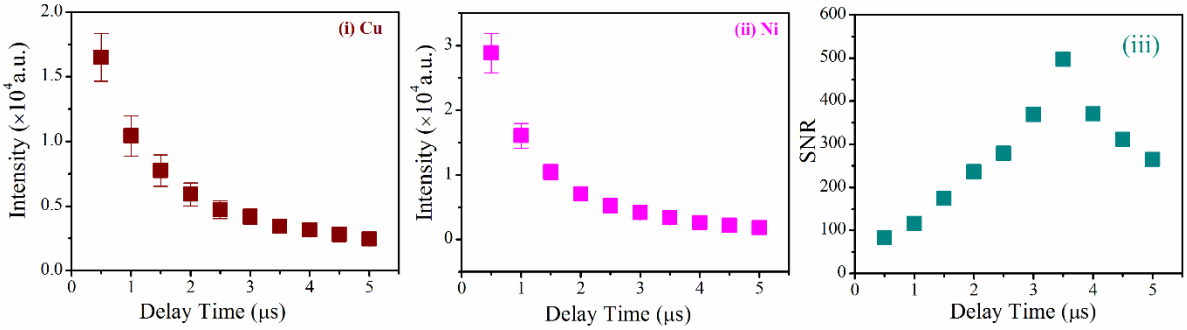

Figure 6.8 Temporal variation of intensity (i) Cu, (ii) Ni and (iii) SNR of sample 3 at laser energy of 50 mJ.

The presence of all these elements for all the three copper alloys sample are also confirmed by the EDX analysis as listed in Table 6.1. It is observed from the temporal evolution of emission intensity, as the delay time increases the emitted intensity from all the elements has fallen down rapidly in the early phase of the plasma evolution within the delay time of 0.5 -1.5 μs at all the incident laser energies compared to that of the later stage beyond 2 μs for all the samples. As soon as the plasma is generated, it starts expanding in the surrounding environment and cools down. During the laser pulse, plasma expands isothermally but after the termination of laser pulse, it begins to expand adiabatically. In the later stage, after the termination of laser pulse, there is no source of energy left for plasma, so it starts losing its energy due thermal conduction

to the ambient and target sample. Due to all the radiative as well as non-radiative processes involved in plasma expansion, it cools down further. Therefore, as the delay time increases due to the loss of energy via various mechanisms the intensity of the emitted lines decrease. While SNR of the spectra increases with the delay time up to 3.5 μs and then its start to fall down. In the initial phase as well as towards the tailing end of LIP, the SNR is very crucial as in the former, there is a large contribution of continuum emission and in the later part the signal intensity goes down drastically.

6.2.2 Temporal evolution of plasma temperature of copper alloys

Assuming the LIP is in LTE, the Boltzmann plot method is employed to find out the plasma temperature (section 2.2.1). The accuracy of temperature measurement from Boltzmann plot method depends on the selection of the lines.

Table 6.2 Spectroscopic data of CuI lines for Boltzmann plot.

λ (nm)	**A_{nm} ($10^7 s^1$)**	**Lower Level Energy E_m (eV)**	**Upper Level Energy E_n (eV)**	**Lower Level Conf.**	**Upper Level Conf.**	**g_m**	**g_n**
465.1	0.38	5.072	7.737	$3d9(^2D)4s4p(3P^0)$	$3d^94s(^3D)s$	10	8
510.5	0.02	1.388	3.816	$3d^94s^2$	$3d^{10}4p$	6	4
515.3	0.60	3.785	6.192	$3d^{10}4p$	$3d^{10}4d$	2	4
521.8	0.75	3.816	6.192	$3d^{10}4p$	$3d^{10}4d$	4	6
570.0	0.0023	1.642	3.816	$3d^94s^2$	$3d^{10}4p$	4	4

The selection criteria are following: (1) the line's transition probability should be low so as neglect self-absorption, (2) the lines should not be a resonant line (terminating to the ground

state) and (3) spread in upper energy level as large as possible. The upper energy levels of all these selected lines for Boltzmann plot are widely apart as well as all these possess low values of transition probability that will discard the possibility of self-absorption. In the present case, the plasma temperature is estimated using five copper atomic transitions at 465.1, 510.5, 515.3, 521.8 and 570.0 nm for all the samples under investigation. The corresponding atomic spectral data for all these five lines is taken from NIST database and are listed in Table 6.2.The Boltzmann plot from CuI lines at a delay time of 0.5, 3.0 and 5.0 μs for the laser energy of 50 mJ is shown in Fig. 6.9 (a), (b), (c) respectively for sample 1as an example. The correlation coefficient for the fitted straight line by equation (2.14), for the measurement of the plasma temperature is found to be in the range of 0.97-0.99. The experimental error in the estimation of plasma temperature is found to be around 3%.

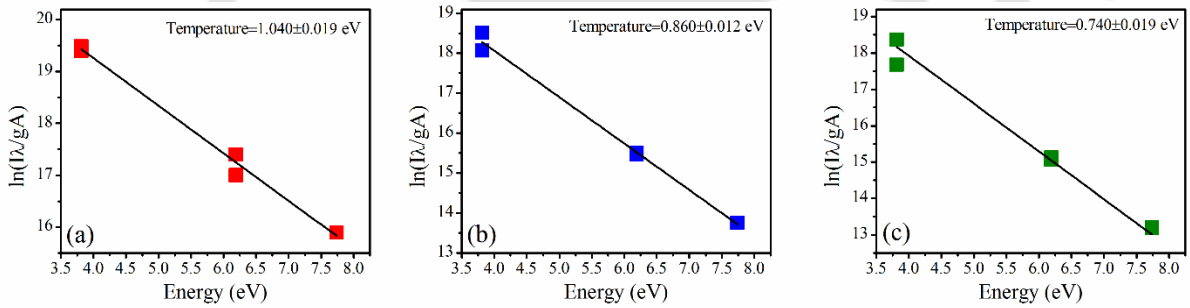

Figure 6.9 Boltzmann plot from CuI line for sample1 at 50 mJ of incident laser energy at delay time of (a) 0.5, (b) 3.0 and (c) 5.0 μs for sample 1.

The temporal evolution of plasma temperature as a function of gate delay in the range of 0.5-5 μs as a function of incident energy from CuI transitions is shown in Fig. 6.10 (a) for the sample1 at all the four laser energies and that of for sample 2 and sample 3 are shown in Fig. 6.10(b) and (c) respectively for the laser energy of 50 mJ only. The temperature falls down with the increase in delay for all the incident laser energies for all the samples. It is observed

that with the increase of incident laser energy for any given delay time, the plasma temperature increases as shown in Fig. 6.10(a).The plasma cools down with the advancing time adiabatically after the termination of laser pulse. The fall in plasma temperature is fast during the initial phase, delay time of 0.5-1.5 μs, while during 2-5 μs the fall in temperature is slow. In the initial stage of the plasma expansion, the temperature decreases predominantly via the collisional processes and at later times due to the recombination of electrons and ions. The released energy due to recombination compensates the cooling due to expansion and hence fall in temperature at later stage is relatively slow.

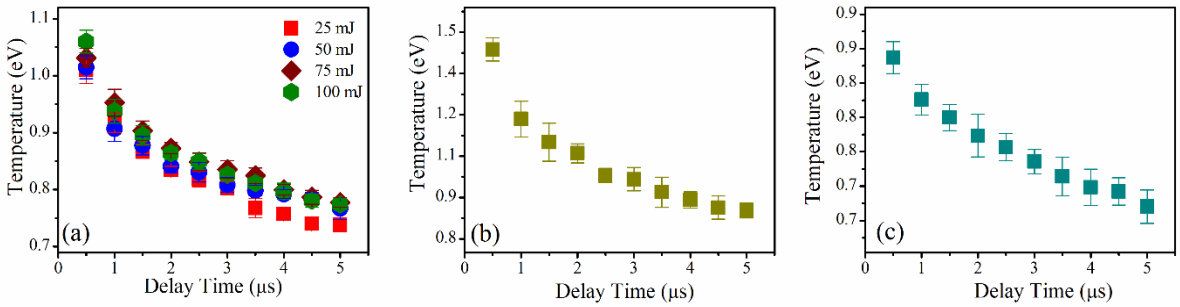

Figure 6.10 Temporal evolution of plasma temperature for (a) sample1 as a function of laser energy, and (b) sample 2 and (c) sample 3 at 50 mJ of incident laser energy.

6.2.3 Temporal evolution of electron density of copper alloys

The electron density in LIP of copper alloys is estimated from the stark-broadened line at CuI-510.5 nm from equation (2.18). In the present experimental conditions the Doppler broadening is estimated from equation (2.15) and found to be of the order of 0.005 nm for CuI- 510.5 nm and hence can be neglected. The required electron impact width parameter *w* in equation (2.18) is a function of temperature and density and is taken from the literature [197]. The temporal variation stark-broadened profile line profile of CuI-510.5 nm and Lorentzian fitted profile at

0.5 μs delay for the incident laser energy of 50 mJ are shown in Fig. 6.11 (a) and (b) respectively for sample 1 as an example. The value of correlation coefficient of the fitting is observed to be within 0.97-0.99 over the range of measurements in the present case.

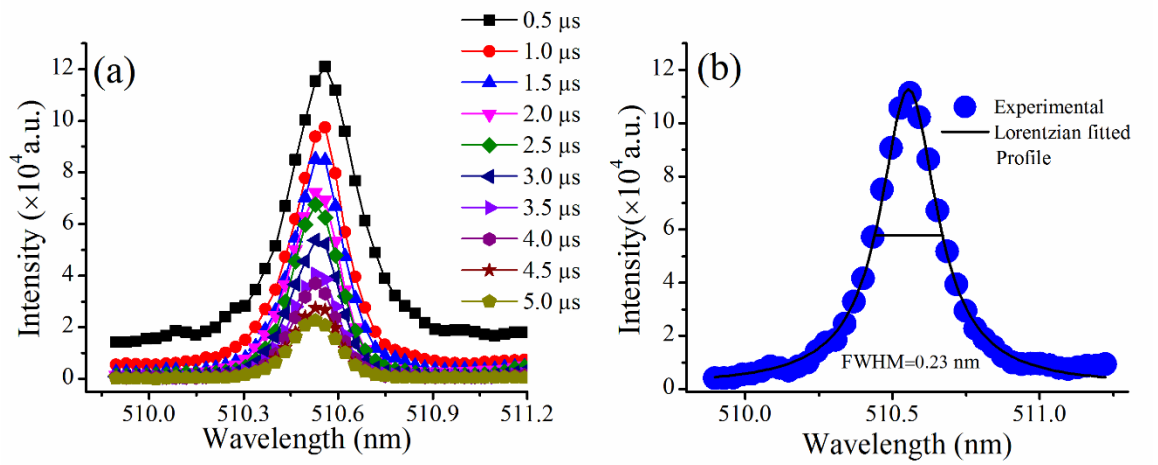

Figure 6.11 (a) Temporal evolution of stark-broadened line profile of CuI-510.5 nm and (b) Lorentzian fitting of CuI-510.5 nm at 0.5 μs delay at 50 mJ of laser energy.

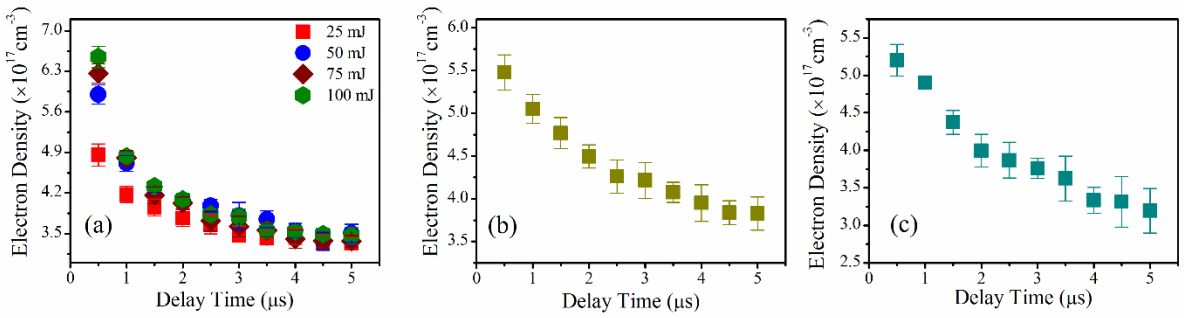

Figure 6.12 Temporal evolution of electron density for (a) sample1 as a function of laser energy and (b) sample 2 and (c) sample 3 at 50 mJ of incident laser energy .

The temporal evolution of electron density at all the four incident laser energies for sample1 is shown in Fig. 6.12 (a) and that of the sample2 and sample3 are given in Fig. 6.12(b) and (c)

respectively at 50 mJ of incident laser energy. The experimental error in the estimation of electron density is found to be less than 5%. It is evident from the temporal evolution of the electron density for all the samples that electron density decreases with the increase in delay time. The fall in the electron density is very rapid from 0.5-1.5 μs while it is slow in the temporal window of 2-4 μs. During the expansion phase, plasma electrons recombine with the ions which reduces the number of electron density at later times.

6.2.4 Validity of optical thin condition of LIP of copper alloys

The validity of optical thin condition is the utmost important requirement for the CF-LIBS application. To check the optical thin condition in the LIP of three copper alloys, the branching ratio method is applied. The CuI lines at 521.8 and 515.3 nm belong to same upper level energy are chosen to estimate the intensity ratio. The theoretical intensity ratio of these two lines $I_{521.8}/I_{515.3}$ is 1.85. The variation of the experimentally obtained intensity ratio for all the samples as a function of different delay time is shown in Fig.6.13. Within the delay window of 2-4 μs, the experimental value is in the range of 1.81-1.73 for all the laser energies for sample 1 and for sample 2 and 3 are 1.71-1.67 and 1.75-1.63 respectively and is close to the theoretical value (shown by straight line) of 1.85 obtained from equation (2.11). Thus in this window the plasma can be treated as optically thin plasma.

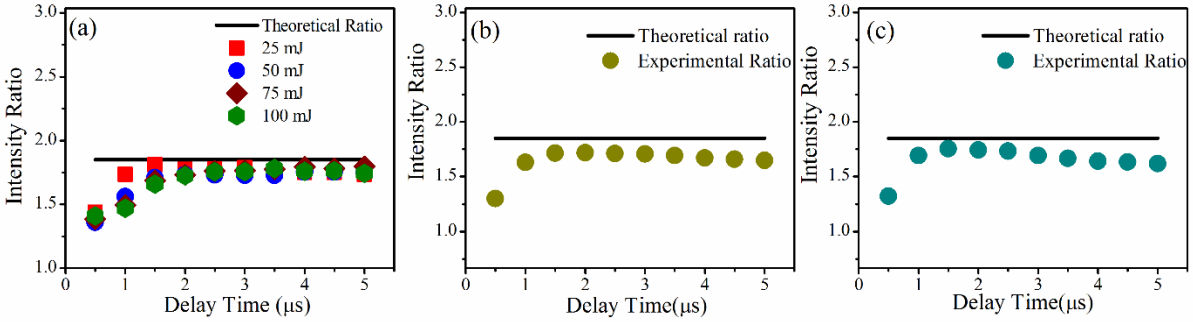

Figure 6.13 Comparison between theoretical and experimental branching ratio for (a) sample 1 at four laser energy, (b) sample 2 and (c) sample 3 at 50 mJ of laser energy as a function of delay time.

6.2.5 Validity of LTE condition of LIP of copper alloys

The validity of the LTE condition is another essential need for the CF-LIBS application. In case of transient evolution of the LIP of copper alloys, firstly the Mc-Whirter criteria, equation (2.4) is employed to determine minimum electron density requires to maintain the LTE inside the LIP. The variation of required minimum electron density at different delay time for three copper alloys plasma are shown in Fig. 6.14. Comparing it with the estimated electron density shown in Fig. 6.12, it is found that experimental electron density is greater than required minimum electron density by two order of magnitude at all the delay time for all the three samples and thus confirming the LTE in LIP.

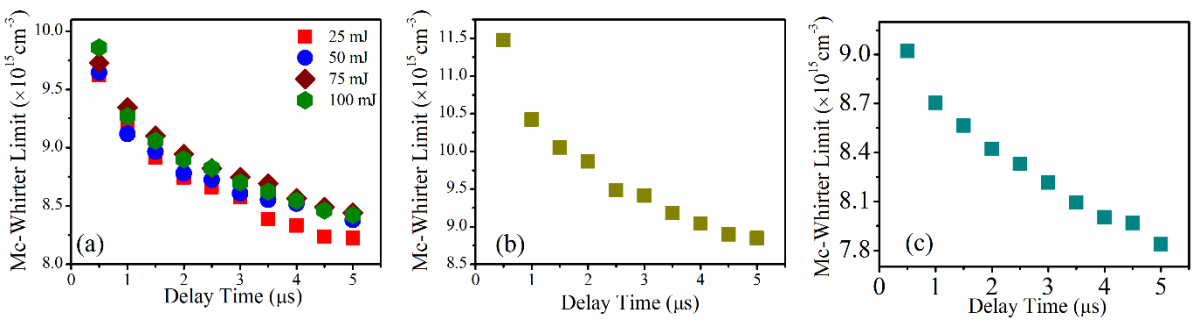

Figure 6.14 Temporal evolution of required minimum electron density from Mc-Whirter criteria for (a) sample 1 at four laser energies and (b) sample 2 and (c) sample 3 at 50 mJ of laser energy.

To take into account the temporal evolution of LIP in the assessment of LTE, the relaxation time is estimated from equation (2.7) using CuI-324.2 nm transition, the transition between ground state and first excited state. The temporal variation of it for all the samples are shown in Fig. 6.15. It is found that at each delay time the relaxation time is of the order of 10^{-10} s that is very small compared to the plasma parameters variation time. This confirms the LTE inside LIP for transient plasma also. But it is worthy to mention at later delay time the difference between experimental electron density and minimum electron density are decreasing and the

value of relaxation time is also increasing which indicates the departure of LTE at later delay time.

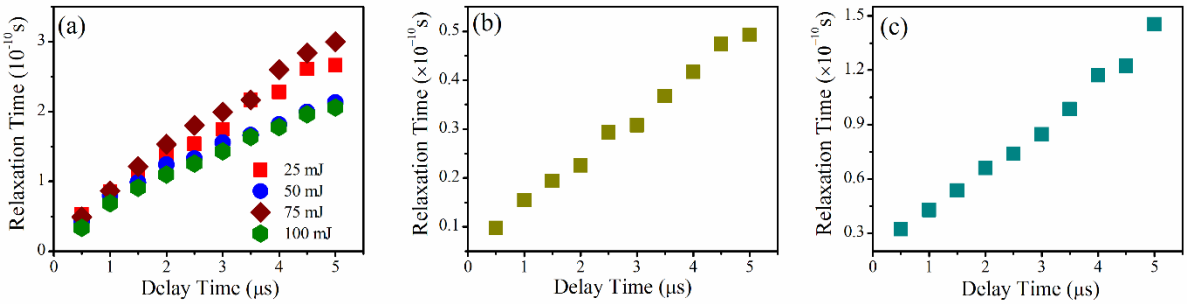

Figure 6.15 Temporal evolution of relaxation time for LTE validity for (a) sample 1 at four laser energies and (b) sample 2 and (c) sample 3 at 50 mJ of laser energy.

6.2.6 Percentage composition of constituent elements via CF-LIBS

The estimated plasma parameters are plugged into the single CF-LIBS algorithm which is described in section 6.2 to determine the elemental concentration in three copper alloys at different delay time. In single line CF-LIBS procedure, any atomic transition line in principle is possible to be used to calculate the number density of the species. But for good accuracy the spectral lines should be detectable within the temporal window, satisfying the LTE, devoid of any overlap with any other neighboring transitions, free form self-absorption and the uncertainty in transition probability should be minimal. Keeping these in view suitable transitions are selected for calculation of total number density of each elements and are listed in Table 6.3 along with their respective atomic parameters. The concentration of all the constituent elements for all these samples are calculated as a function of delay time from equation (6.4).

Table 6.3 The spectral atomic data for relevant line for single line CF-LIBS measurement.

Elements	λ (nm)	$A_{nm}(10^8 s^{-1})$	E_n (eV)	g_n
Cu I	465.1	0.38	7.737	8
Zn I	468.0	0.155	6.654	3
Al I	394.0	0.499	3.142	2
Fe I	438.3	0.500	4.312	11
Sn I	326.2	2.7	4.867	3
Pb I	405.7	0.9	4.375	3
Ni I	349.2	0.98	3.657	3

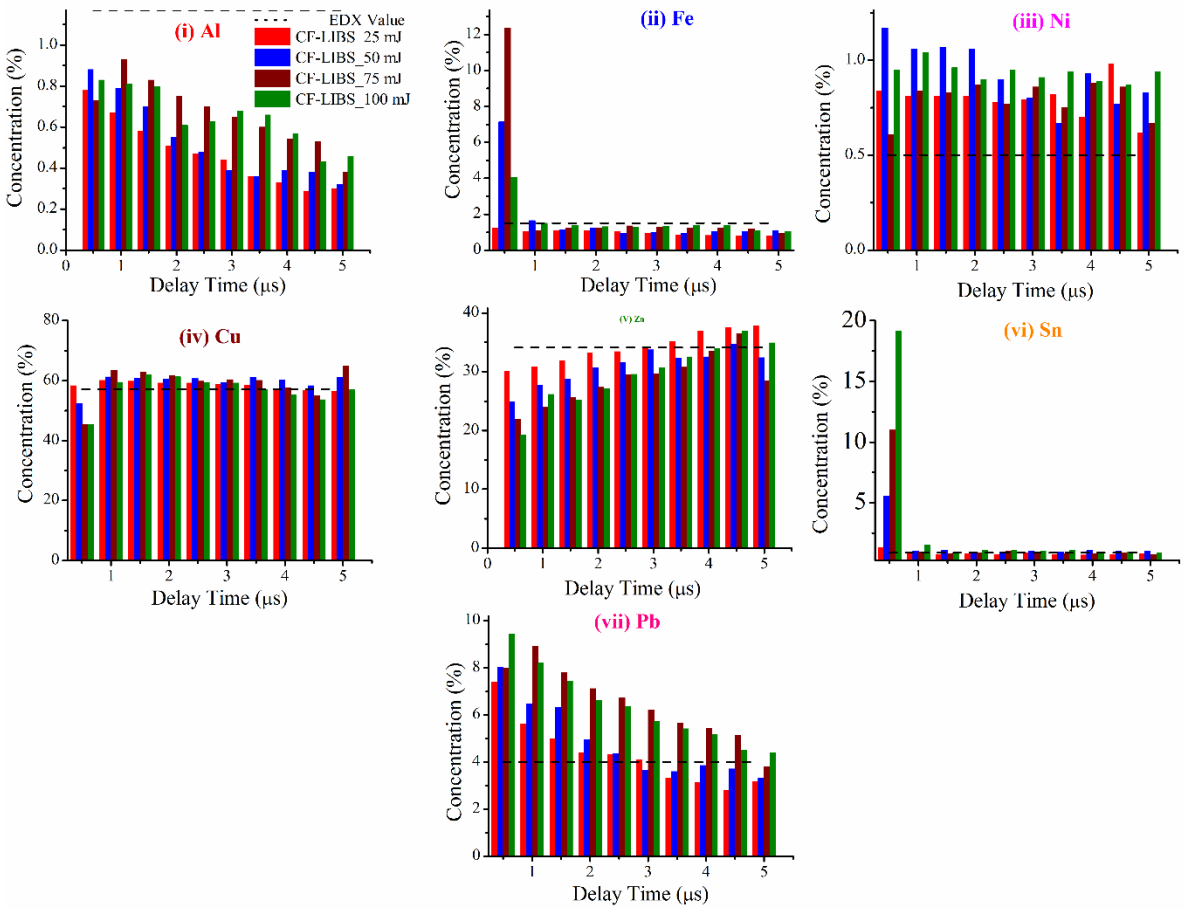

Figure 6.16 Comparison between CF-LIBS results and EDX for sample 1 as a function of delay time and laser energy.

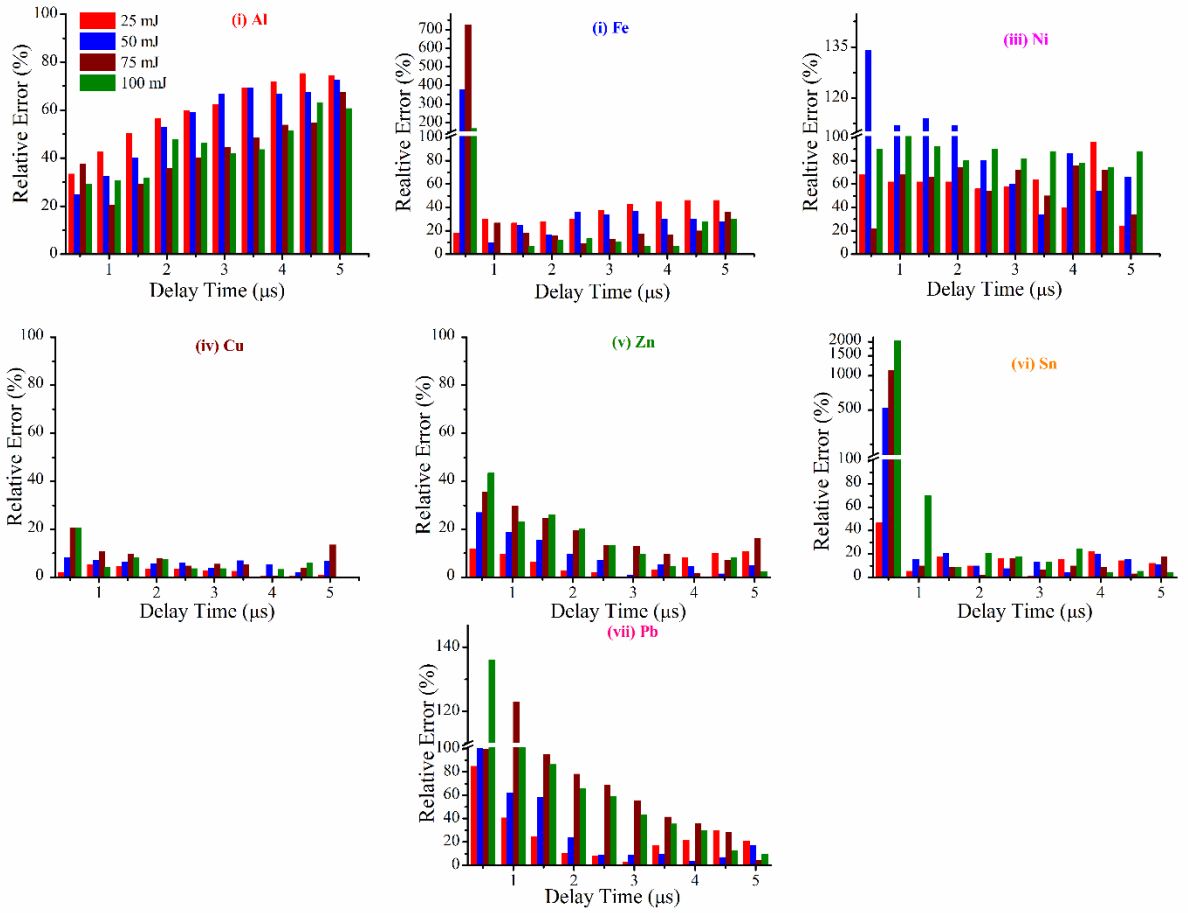

Figure 6.17 Temporal evolution of relative errors in CF-LIBS measurement in each constituent elements of sample1 as a function of laser energy.

The estimated elemental concentration for sample 1 at four incident laser energy in the delay time range of 0.5-5 μs are compared with EDX measurement (broken line) as shown in Fig. 6.16. The relative error in the CF-LIBS measurement for each element as function of energy and delay time are shown Fig. 6.17.

For the sample 2 and sample 3 the CF-LIBS measurement are performed at the incident laser energy of 50 mJ in the same delay time range as in case of sample 1. The estimated concentration for the constituent elements for the sample 2 in the delay time range of 0.5-5 μs

is shown in Fig. 6.18 along with the EDX measurement. The relative error in the CF-LIBS measurement for each of the constituent elements for this sample is shown in Fig. 6.19.

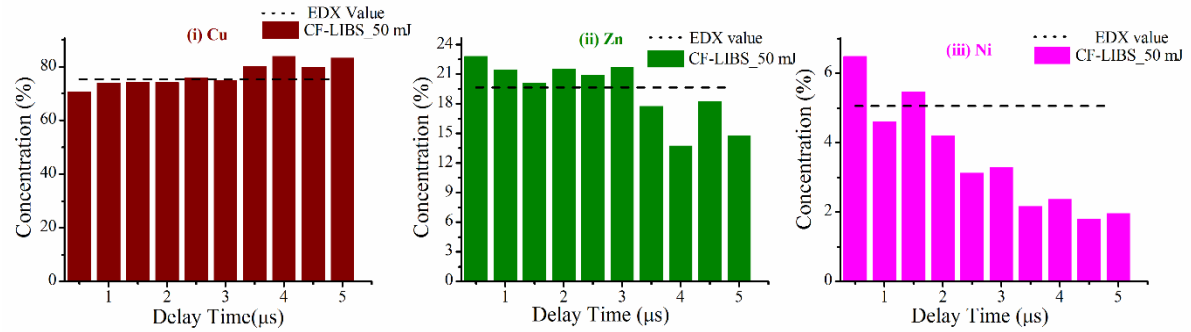

Figure 6.18 Comparison between CF-LIBS results and EDX for sample 2 as a function of delay time for laser energy of 50 mJ.

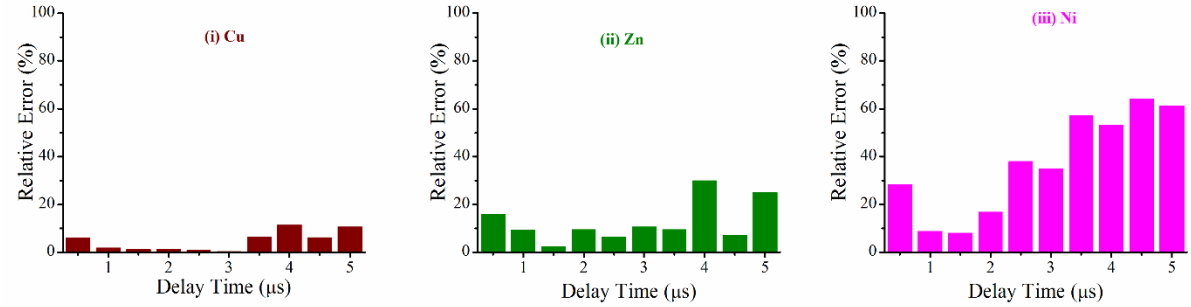

Figure 6.19 Temporal evolution of relative errors in CF-LIBS measurement in each constituent elements of sample 2 for laser energy of 50 mJ.

The estimated concentration for the constituent elements for the sample 3 in the delay time range of 0.5-5 μs is shown in Fig. 6.20 while their corresponding the relative error as a function of delay time is depicted in Fig. 6.21.

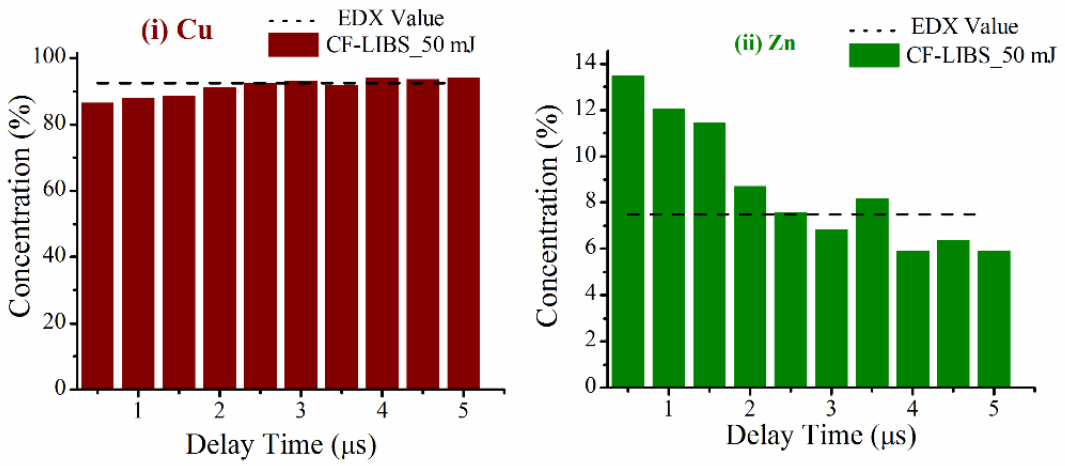

Figure 6.20 Comparison between CF-LIBS results and EDX for sample 3 as a function of delay time and for laser energy of 50 mJ

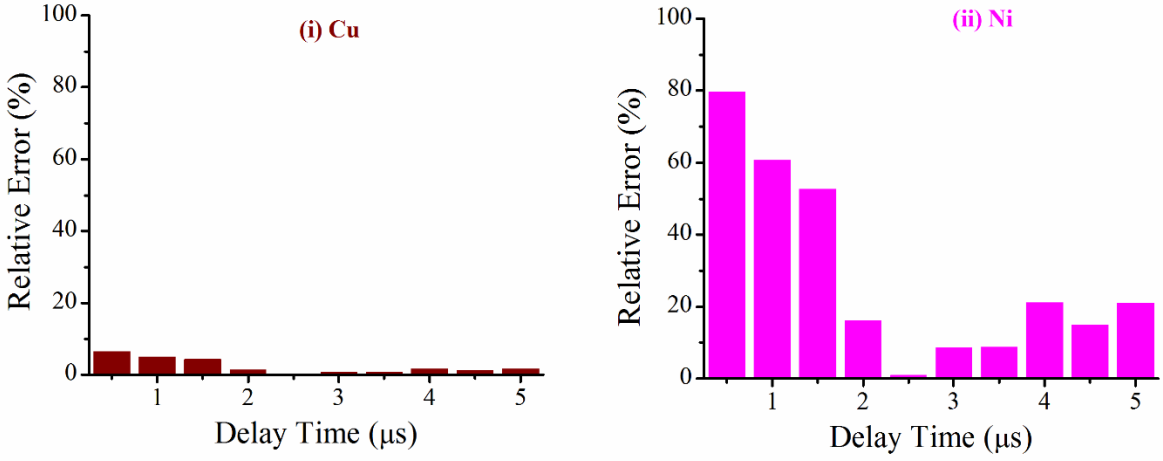

Figure 6.21 Temporal evolution of relative errors in CF-LIBS measurement in each constituent elements of sample1 for laser energy of 50 mJ

The overall accuracy of CF-LIBS technique is defined by the distance function [97], *dist*,

$$dist = \sum_{i=1}^{m} abs \left| M_i - C_i \right| \tag{6.5}$$

where the index *i* runs over all *m* number of constituent elements present in the sample, *M* is the concentration measured by EDX and *C* that of the measured by CF-LIBS. The lower value of *dist* function implies higher accuracy in CF-LIBS. The temporal variation of the *dist* function for all the three sample is shown in Fig. 6.22. The minimum value of relative error and *dist* function, are observed in the temporal window of 2-4 μs for all three samples. The large value of relative error and *dist* function at earlier delay time i.e., from 0.5-1.5 μs and beyond 4 μs could be due to its deviation from LTE as well as optical thin plasma condition [125].

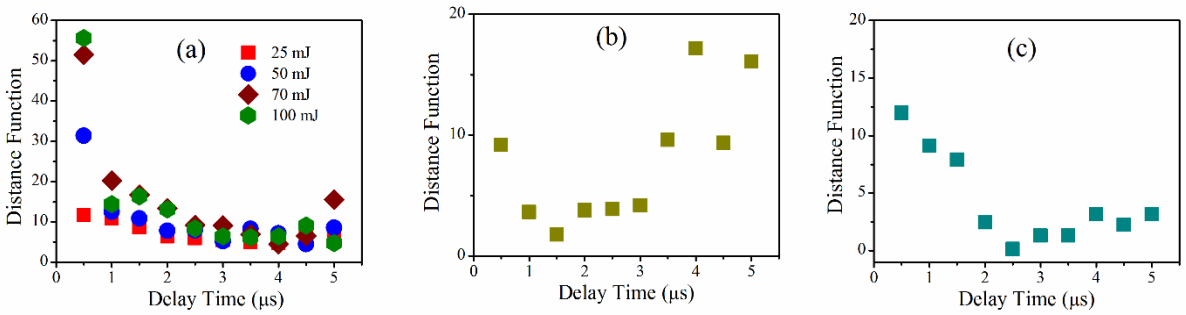

Figure 6.22 Temporal variation of dist function for (a) sample 1 at four laser energies, and (b) sample 2 and (c) sample 3 at 50 mJ of laser energy.

It is observed from the temporal evolution of the intensity, plasma temperature and electron density, that the fall in these parameters are rapid in the initial stage of the plasma evolution but at later time, variation slowdown. The LTE and optically thin condition inside the plasma are also satisfied in the same temporal window of LIP evolution. So 2-4 μs is identified as the optimized temporal window for CF-LIBS technique where all the necessary requirements are fulfilled. For sample1, relative error in the major elements Cu and Zn are 3.93 and 1.08 respectively while that of in the trace elements Al, Fe, Ni, Sn and Pb are 69.23, 36.66, 34, 4.4 and 9.75 % respectively. For sample 2, for Ni, Cu and Zn are 0.17, 2.04 and 7.81% is achieved. For the sample 3 the error is observed to be error 0.96 and 0.08 % for Ni and Cu respectively.

These errors are less for major elements and comparable for the minor elements with those reported earlier in the literature [187, 198].

6.3 Influence of spatial evolution of LIP on CF-LIBS measurements

As soon as LIP is generated on the sample surface it expands into surrounding medium causing the rapid changes in plasma parameters in space. To get the knowledge on how the spatial inhomogeneity of LIP influences the CF-LIBS measurement, the emission from the LIP is recorded at different axial position for the LIP of sample 1 only, in air at four incident laser energy. In the following subsections, spatial evolution of the emission intensity in the temporal window at 2 μs from all the constituent elements of the sample 1, SNR and plasma parameters are studied as a function of incident laser energy. The optical thin condition and LTE, the two essential criteria for CF-LIBS application is also tested in this section. In the next section, single line CF-LIBS algorithm is utilized to estimate the elemental concentration of the sample 1 as a function of axial position at four laser of energies. The relative error is also presented in CF-LIBS measurement for each of the elements and the overall accuracy of this technique is assessed in terms of distance function.

6.3.1 Spatial evolution of plasma emission

In space resolved study, the emission from the LIP of the sample 1, is recorded using the experimental setup described in section 3.2, Fig. 3.5 at incident laser energy of 25, 50, 75 and 100 mJ. The spatial evolution of the plasma emission intensity at four laser energy is shown in Fig. 6.23 (a)-(d).The expanded view of the plasma emission spectra at a distance of 2 mm distance from the target surface with some of the identified lines are shown in Fig. 6.24.

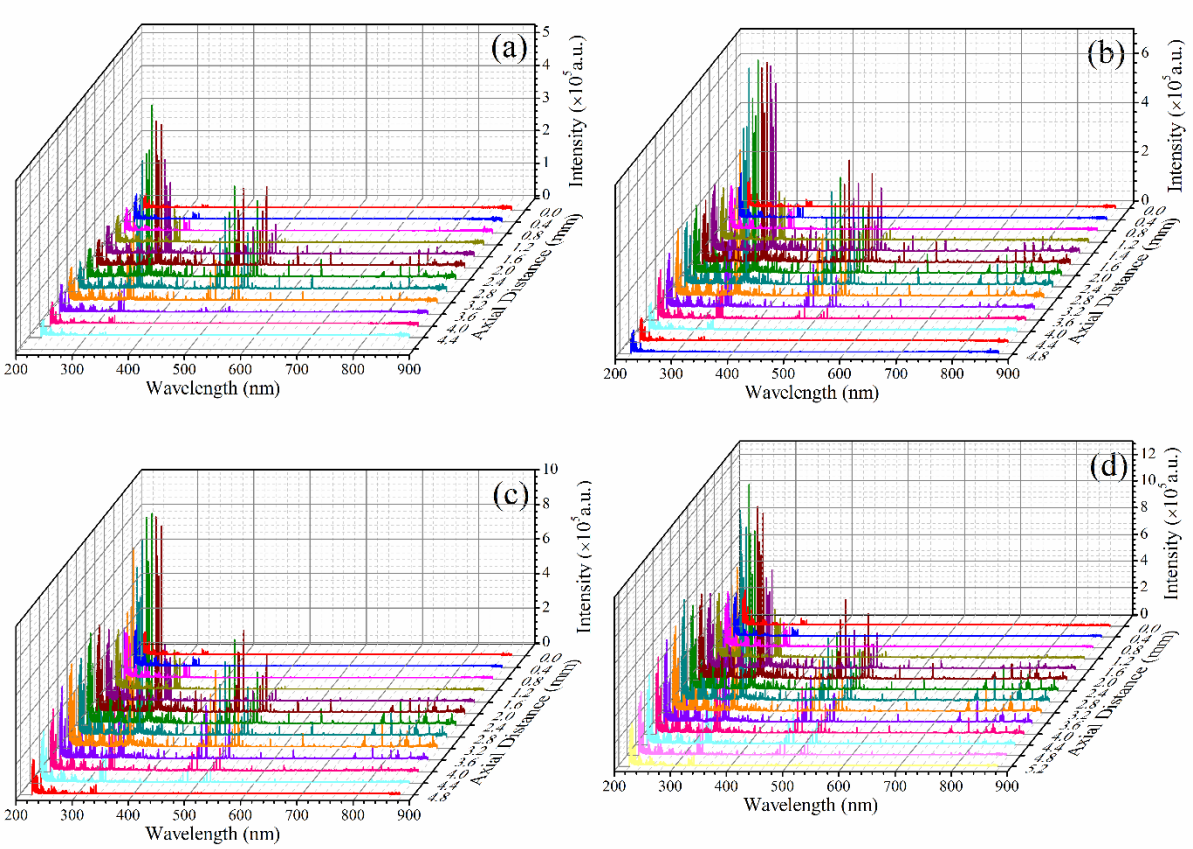

Figure 6.23 Spatial evolution of plasma emission intensity at (a) 25, (b) 50, (c) 75 and (d) 100 mJ of incident laser energy.

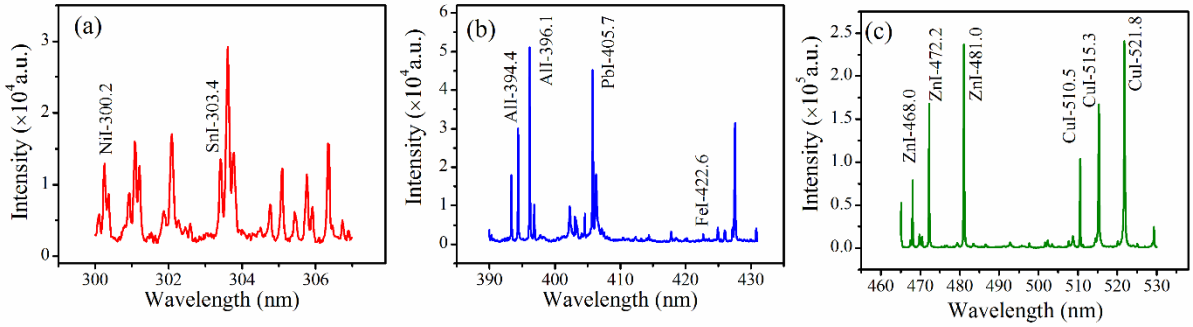

Figure 6.24 Expanded view of the spectrum in the spectral range of (a) 300-306 nm, (b) 390-430 nm and (c) 465-530 nm at 2 mm distance from the target surface at 25 mJ of laser energy.

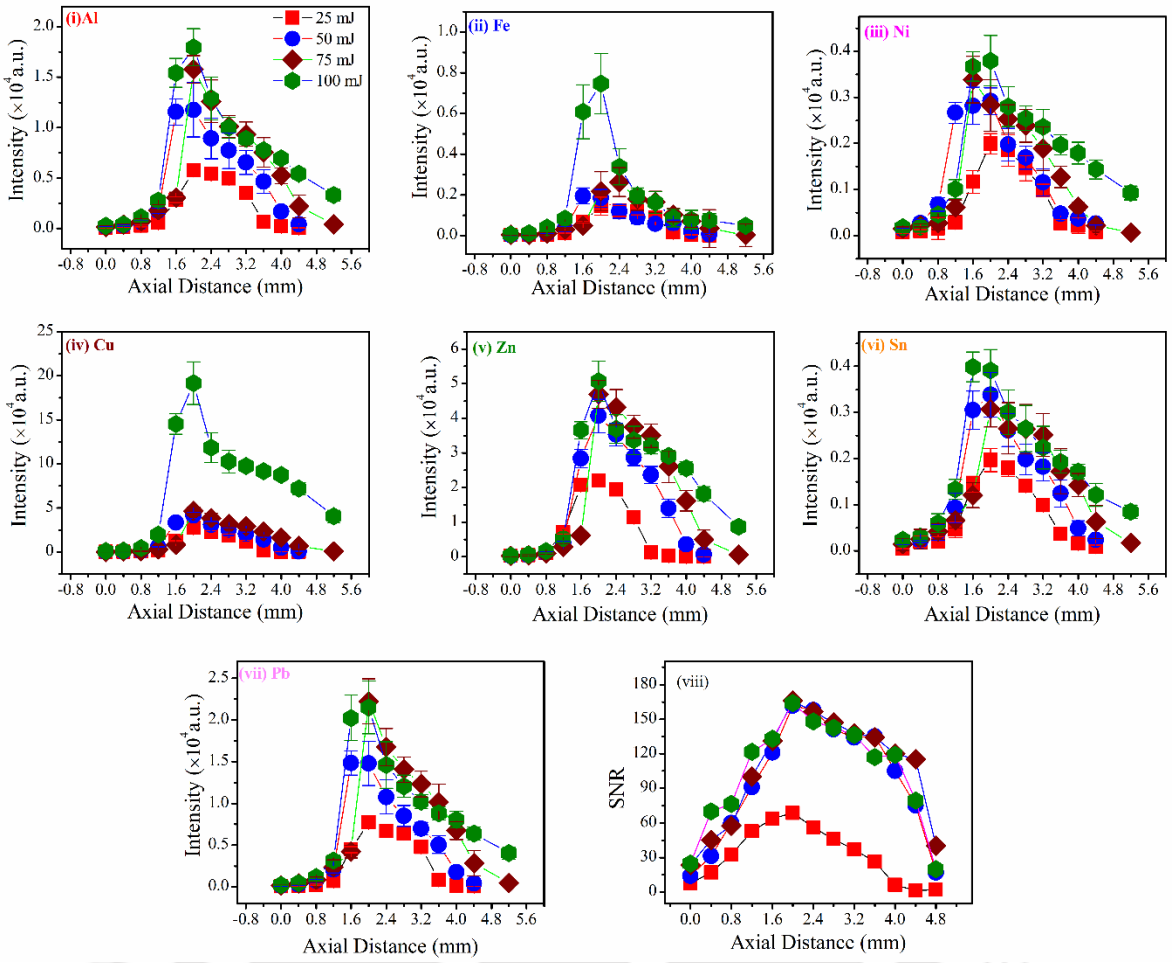

Figure 6.25 Axial variation of intensity for (i) Al, (ii) Fe, (iii) Ni, (iv) Cu, (v) Zn, (vi) Sn (vii) Pb and (viii) SNR for sample 1 as a function of laser energy.

The axial variation of the emitted intensity of these elements at all the four laser energies are shown in Fig. 6.25 (i)-(vii) and that of the SNR is shown in Fig. 6.26 (viii). It is observed that the intensity of each of the elements initially increase on moving away from the target surface up to a distance of 2 mm then start to fall down. The SNR also follows the similar trend as that of the intensity profile. This is due to the fact that the plasma emission is recorded at a delay time of 2 μs, where it has already expanded, and detached from the target. The maximum intensity is going to come from the core of plasma and at its periphery the intensity falls down

on each side, near the target surface and far away from the target. The line intensity from all the elements is enhanced with the increase of laser energy up to 75 mJ but at higher energy of 100 mJ the enhancement is less due to the plasma shielding. Due to the thermal conduction towards the solid target plasma emission intensity decrease close to the target surface.

6.3.2 Axial variation of plasma temperature

The axial variation of the plasma temperature as a function of incident laser energy from the same six of CuI transitions as that of the temporal evolution, section 6.2.2, is shown in Fig. 6.26. From the figure, it is observed that plasma temperature increase w.r.t to distance from the target surface and after attaining the maximum value at a distance of 2 mm and then it start falling down.

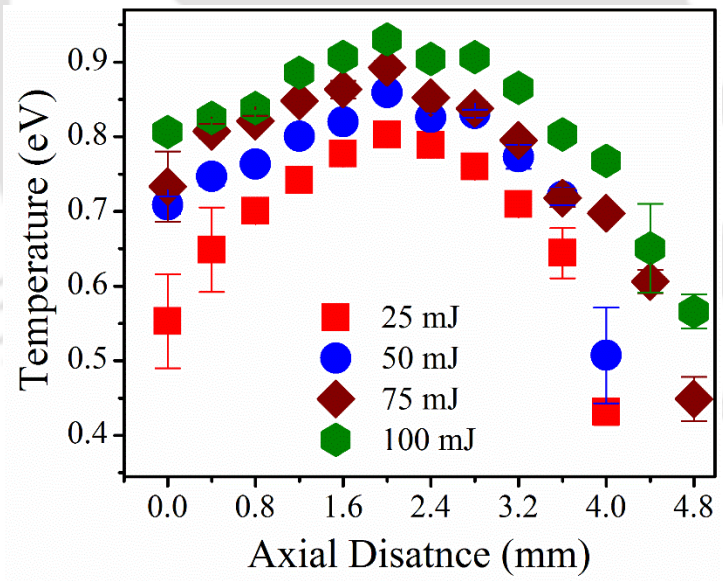

Figure 6.26 Axial variation of plasma temperature as a function of laser energy.

The plasma temperature increases with the increase of the incident laser energy. The fall in the plasma temperature near the surface of the target results from the thermal conduction from the plasma towards the target surface. The increase in plasma temperature in the axial range of

0.8-2 mm in the range of 2 μs window is due to the fact the core of the plasma has move away from the target and this is consistent with the spatial evolution of the emitted line emission from the atomic transitions. At higher energy the increment in temperature is less due to the plasma shielding.

6.3.3 Axial variation of electron density

The estimated electron density, from stark-broadening equation (2.18) from CuI-510.5 nm, at different axial position as a function of incident laser energy is shown in Fig. 6.27. The maximum in the electron density is observed at distance of 1.2 mm from the target surface. In the present study, spatial profile is recorded at a fixed delay of 2 μs, at which the LIP is already detached with target and moving away from the targets and simultaneously expanding and the maxima in the electron density is found to being the core of the plasma which is slightly away from the target at later time.

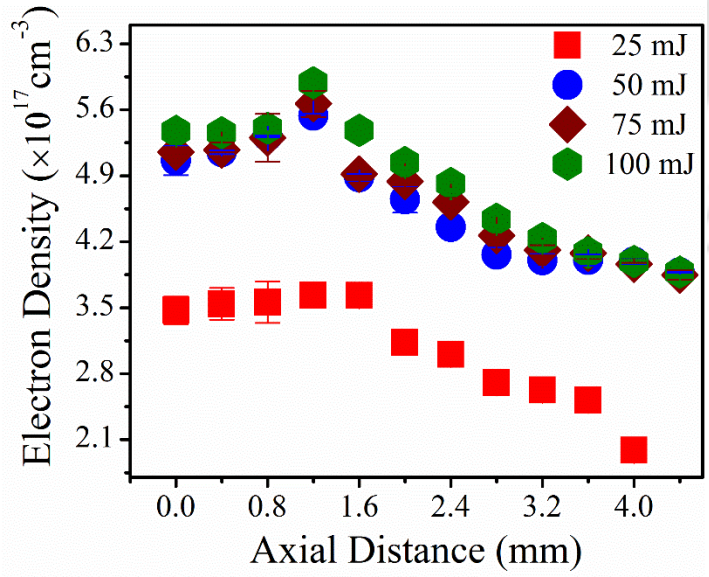

Figure 6.27 Axial distribution of electron density as a function of laser energy.

6.3.4 Assessment of optical thin condition of plasma as a function of separation from the target

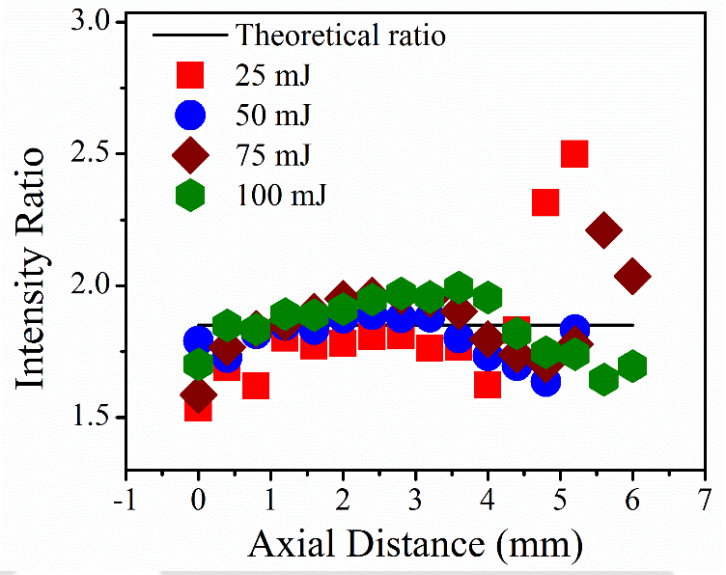

Figure 6.28 Variation of experimental intensity of CuI-521.8/515.3 nm as function of axial position and laser energy.

The same pair CuI lines i.e. 521.8 and 515.3 nm as section in 6.2.4 are used to estimate the intensity ratio and compared with the theoretical branching ratio for the testing the validity of optical thin condition of plasma as is done in temporal study. The variation of the experimental branching ratio along the axis of the plasma at different locations is shown in Fig. 6.28. It is observed that the experimental ratio departs from the theoretical ratio close to the target surface in the range of 0-0.4 mm and beyond the 2.8 mm from the target surface. Thus the spatial window where the optically thin condition of plasma is satisfied lies within the 0.8-2.8 mm distance from the target.

6.3.5 Assessment of LTE Condition of plasma in spatial extension

In Fig. 6.29 (a) shows the Mc-Whirter limit on the electron density as a function of spatial location w.r.t target. On comparing the estimated electron density, Fig. 6.27 with this required minimum electron density, it is found that experimentally obtained electron density is higher by two order of magnitude confirming the LTE in LIP at all the locations. The diffusion length of the LIP of sample 1 is also estimated to take into account the inhomogeneous nature of LIP during spatial evolution via the equation (2.10). The variation in the diffusion length at each axial position at four incident laser energy is shown in Fig. 6.29 (b). From the figure, it is evident that the diffusion length is of the order of 10^{-3} mm which is very small compared to the plasma dimension which of the order of a few mm. Thus it confirms the LTE inside plasma even in inhomogeneous LIP.

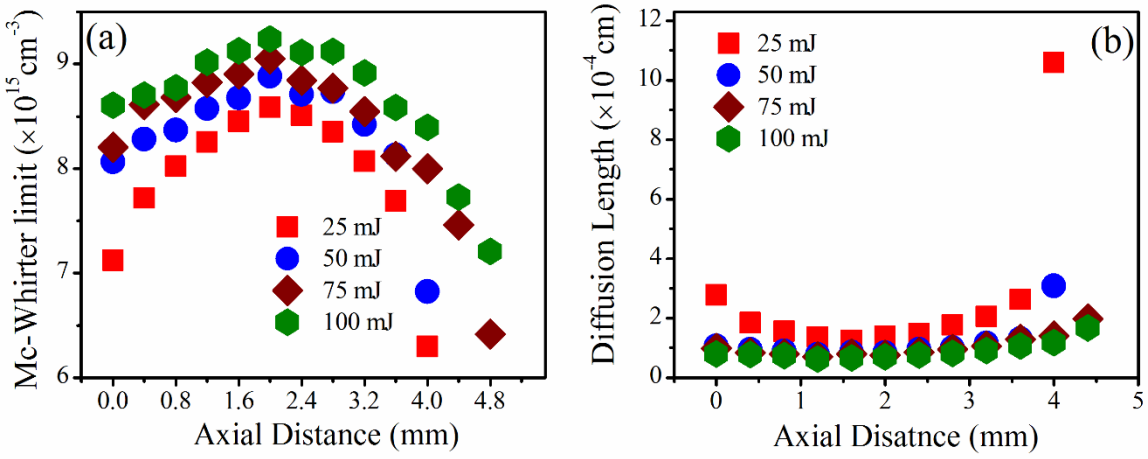

Figure 6.29 (a) Mc-Whirter limiting value of electron density and (b) diffusion length at all the four laser energies.

6.3.6 Optimized spatial window for the measurement of percentage composition via CF-LIBS

The obtained plasma parameters are plugged into the single line CF-LIBS algorithm and elemental composition of the sample 1 is estimated as function of distance from the target at all the four incident laser energies. The obtained percentage composition for each constituent element is compared with the EDX results and shown in Fig. 6.30.

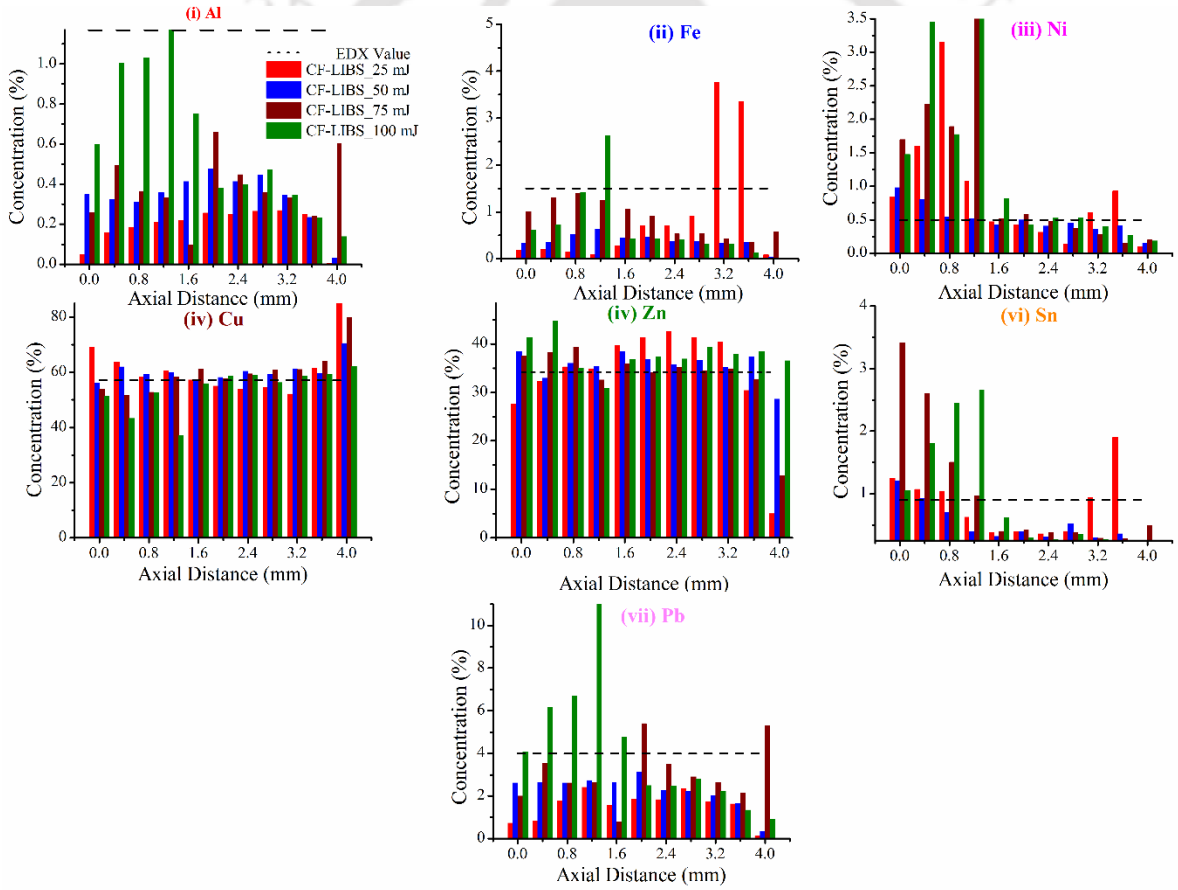

Figure 6.30 Comparison between CF-LIBS results and EDX for sample1 as a function of axial position and laser energy.

From the figure, it is evident that the CF-LIBS results are close to EDX results for the axial position of 0.8-2.8 mm. The departure in CF-LIBS measurement with EDX results are more near to target surface and beyond 2.8 mm distance. The relative errors are also estimated and for each elements are shown in Fig. 6.31 (i)-(vii). The relative error is minimum within the spatial window of 0.8-2.8 mm and higher outside this range. The variation of *dist* function at various axial position is given in Fig. 6.31 (viii). This figure further confirms that error is minimum in the CF-LIBS measurements for this spatial window.

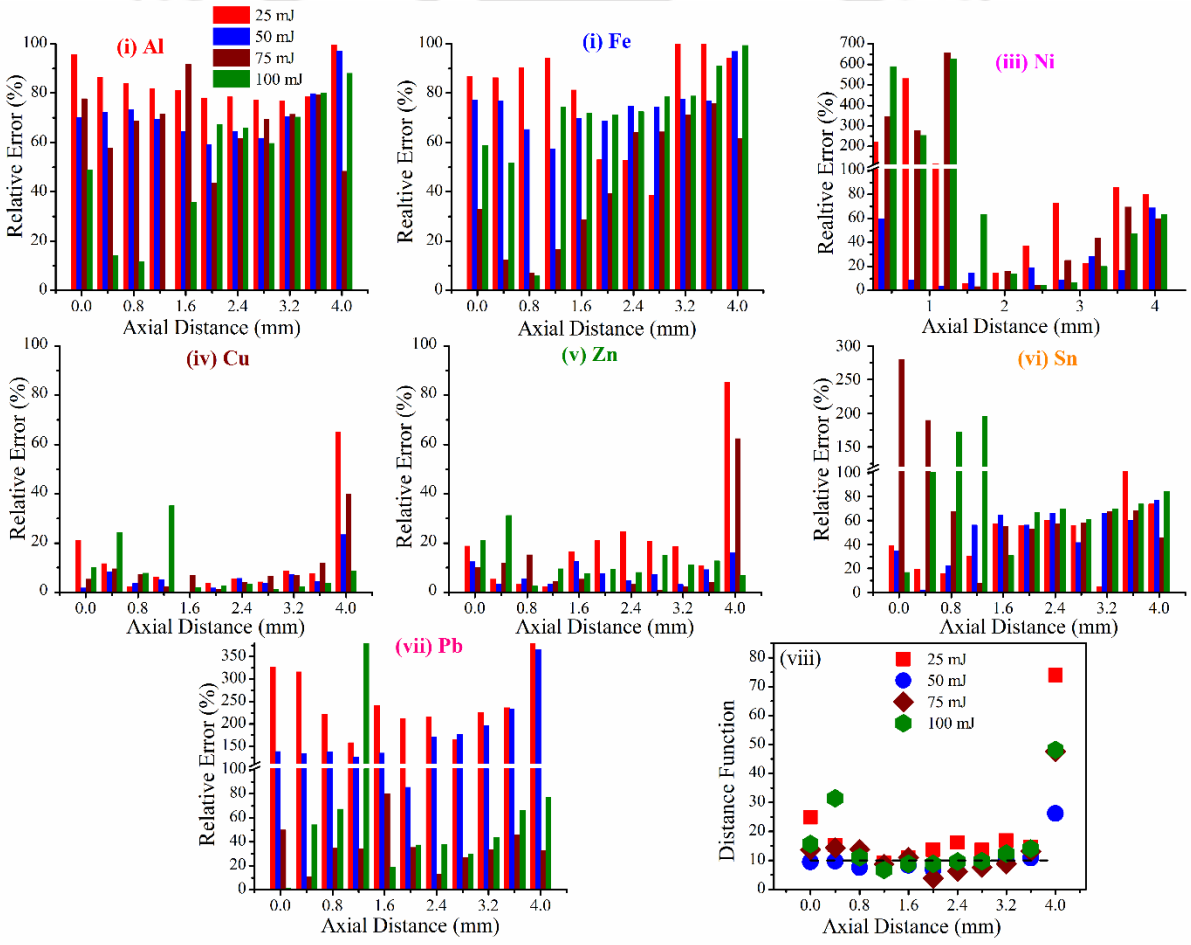

Figure 6.31 Evolution of relative errors in CF-LIBS measurement in each constituent elements of sample1 as a function of axial position and laser energy.

By the observation in the section 6.3.1-6.3.6 it can be concluded that the optimum spatial window for the CF-LIBS for the present experiment is in the range of 0.8-2.8 mm away from the target.

6.4 Conclusion

This chapter is devoted on the application of LIBS via CF-LIBS to measure the percentage composition of the constituent elements in three Cu-alloys. In the first part, temporal evolution of LIP spectra are studied and percentage composition of the constituent elements are measured via CF-LIBS algorithm. The accuracy of the CF-LIBS technique is measured in terms of relative error as well as by *dist* function. It is found that for the temporal window of 2-4 μs where the SNR is high, LTE and optical thin condition plasma are properly maintained, the value relative error and *dist* function minimum indicating the optimum temporal window. In the second part of the experiment the space-resolve spectra from sample 1 (commercial brass) are recorded as function of laser energy at a delay time of 2 μs (in the optimized time window). It is observed that the optimum spatial window lies in the range 0.8-2.8 mm away from the target. From the time and space-resolved studies confirm that for the application CF-LIBS technique with good accuracy, the validity of LTE, optical thin condition of plasma is necessary and there is a requirement of optimization temporal as well as spatial window where all these conditions are valid thus giving the minimum error in the measurement. From the present study the obtained optimized time window is 2-4 μs and that of the spatial window is 0.8-2.8 mm. The implementation of the single line CF-LIBS technique in the optimized time and space window will be useful for practical implementation in the rapid analysis of the composition of any sample.

Chapter 7 Surface Morphological Characterization of Laser Ablated Sample

Laser ablation from solid samples imprints behind the micro-nano structure on the surface. It has remarkable potential to alter electrical, optical, and mechanical and tribological properties of the surface. Such structured surfaces have various applications in the industry [199]. Fabrication of micro/nanostructures of compound element of tungsten (i.e.WO_3, WS_2 etc.) [200] as well as molybdenum (i.e.MoO_3, MoS_2 etc.) are of special interest as a sensor and optoelectronic devices [164, 201, 202]. The laser ablation of copper is of special interest to synthesize the copper oxide nanoparticles, useful in the solar cell, sensor, antifungal activity etc.[203] Controllable surface modification specific to particular application is very much dependent of the laser parameters (energy, pulse duration, wavelength and repetition rate). Among various laser parameters, the laser energy strongly effect the dynamical and plasma properties which in turn modulate surface structure. In the present chapter the surface morphological changes on the tungsten, molybdenum and Cu-alloy (commercial brass) targets as a result of LIP are presented as a function of laser energy.

7.1 Experimental details

In the present study, three samples tungsten, molybdenum and Cu-alloy (commercial brass), same as that of the used in the previous chapters, are ablated by focusing laser pulse using a lens of focal length of 15 cm using 30 consecutive laser shots on to the sample in air. The surface damage visibility appears in form of craters formation in the focal region and re-deposition of plasma ablated material on peripheral region of the focal plane. The pictorial view of the process is shown in Fig. 7.1.

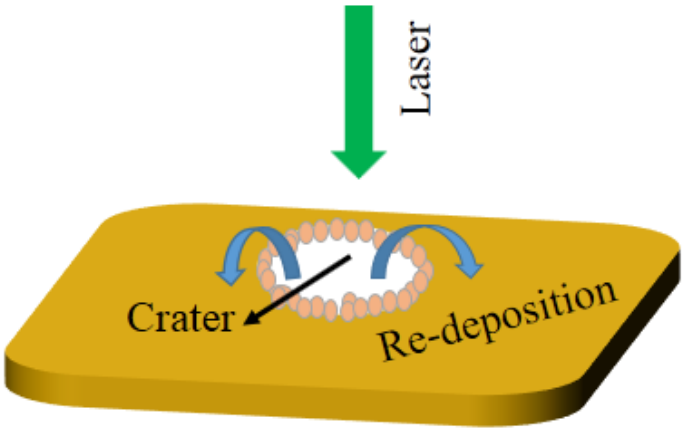

Figure 7.1 Schematic re-deposition of laser ablated material.

The surface of the laser ablated tungsten, molybdenum and Cu-alloy are studied via optical microscope, surface profilometer, Field Emission Scanning Electron Microscope (FESEM) and Raman spectroscopy.

The surface morphology of laser ablated targets are first characterize using optical microscope (OLYMPUS BX51M) to identify the heat effected zone (HAZ).

The depth of the crater is determine by noncontact high resolution surface profilometer having field of view of 0.825 mm×0.825 mm (Taylor Hobson, Taly surface CCI lite).

The changes in the surface morphology and the formation of micro and nano structures are investigated by FESEM (*ZEISS sigma*).

Raman spectra of the laser ablated samples are recorded by the micro Laser Raman spectrometer (Horiba Jobin Yvon, LabRam HR800) using a holographic grating of 1800 groves/mm to identify formation of the oxides of the respective constituent elements of the target. An Ar-ion laser of wavelength 488 nm is used as an excitation source. The laser beam

is focused on the sample, using 100X microscopic objective lens, to a spot size of ~1μm diameter on the film surface. The spatial resolution of the Raman spectrometer is 1 μm and spectral resolution is less than 1 cm^{-1}.

7.2 Surface characterization using optical microscope

The images of laser ablated surface of tungsten, molybdenum and Cu-alloy taken via optical microscope, are given in Fig. 7.2, Fig. 7.3 and Fig. 7.4 at laser energy of 25, 50, 75 and 100 mJ for tungsten, molybdenum and commercial brass target respectively. The three distinct regions are clearly observed in these images.

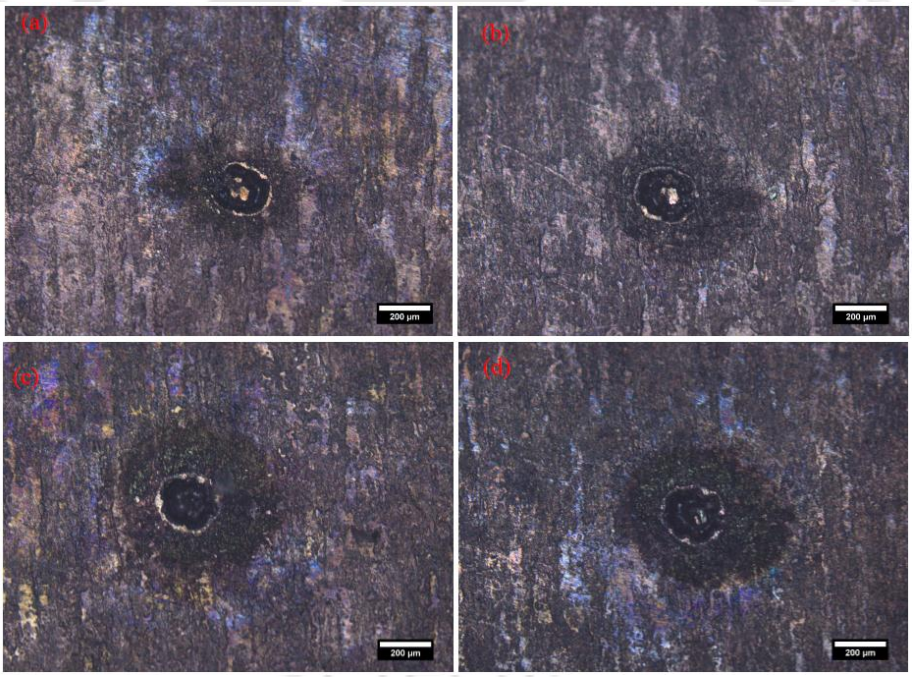

Figure 7.2 Optical microscopic image of laser ablated tungsten surface at four laser energies of (a) 25, (b) 50, (c) 75 and 100 mJ.

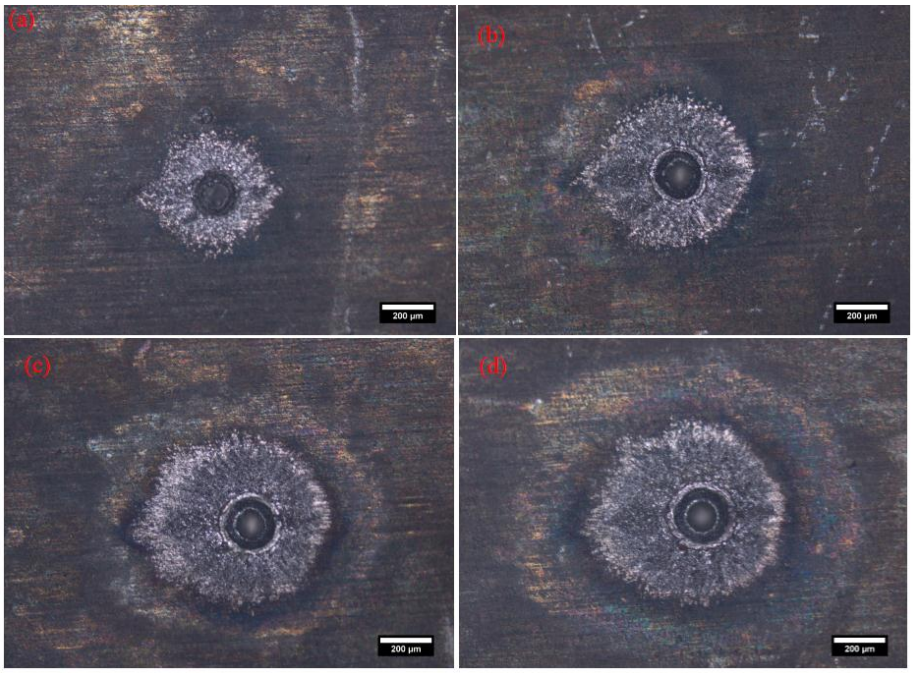

Figure 7.3 Optical microscopic image of laser ablated molybdenum surface at four laser energies of (a) 25, (b) 50, (c) 75 and 100 mJ.

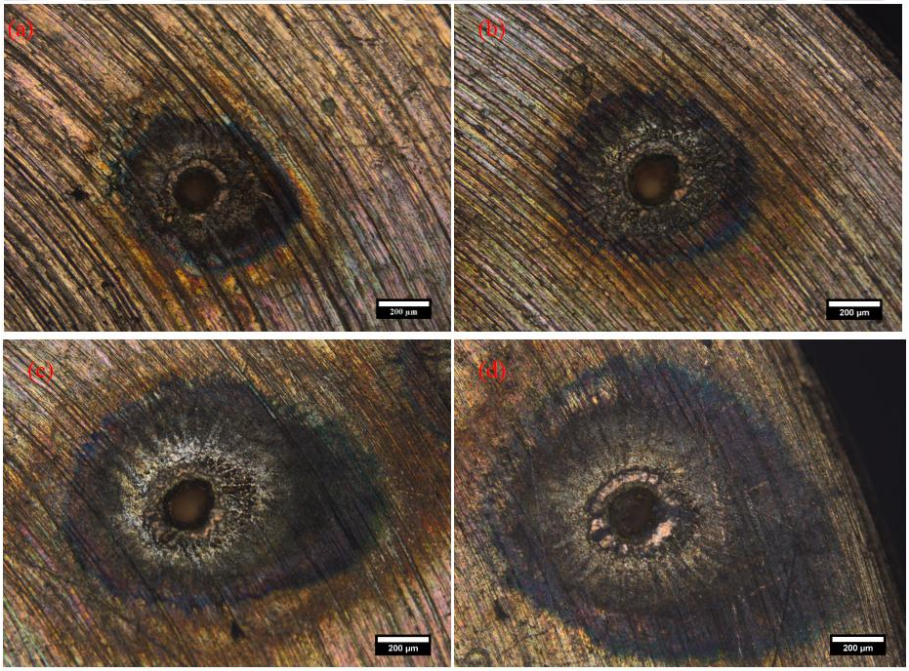

Figure 7.4 Optical microscopic image of laser ablated Cu-alloy surface at four laser energies of (a) 25, (b) 50, (c) 75 and 100 mJ.

These three regions are (i) crater formation in the focused region of the laser, (ii) region of re-deposited material around the crater rim and (iii) heat affected zone depicted. For the clarity all these three regions are marked in Fig. 7.5 (a), Fig. 7.6 (a) and Fig. 7.7 (a) in green, yellow and red circle restively for region (i), (ii) and (ii) on tungsten, molybdenum and Cu-alloy at 25 mJ laser energy respectively. In case of metal, initially laser energy is absorbed by the free electron via IB process. For the nano second laser pulse, the pulse duration is greater than the electron relaxation time and lattice heating time so the absorbed laser energy initially heats the target surface to its melting point and followed by the vaporization temperature [58, 77]. The absorbed laser energy subsequently spread via heat conduction to an area outside the focal region, causing the irradiated target to attain the boiling and evaporation temperature. Boiling and evaporation of the target material leads to the production of an uncontrollable melt layer and is known as HAZ. From these images HAZ are estimated and shown in Fig. 7.5 (b), Fig. 7.5 (b) and Fig. 7.5 (b) for the tungsten, molybdenum and Cu-alloy respectively as a function of laser energy. In all three samples, the diameter of HAZ region increases with the laser energy.

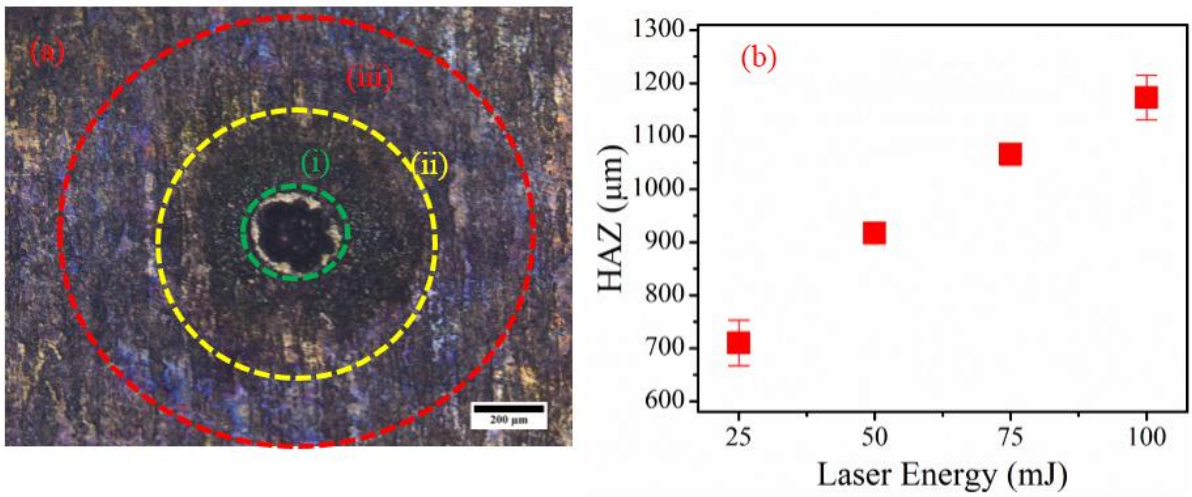

Figure 7.5 (a) Division of crater in three regions and (b) variation HAZ of tungsten as a function energy.

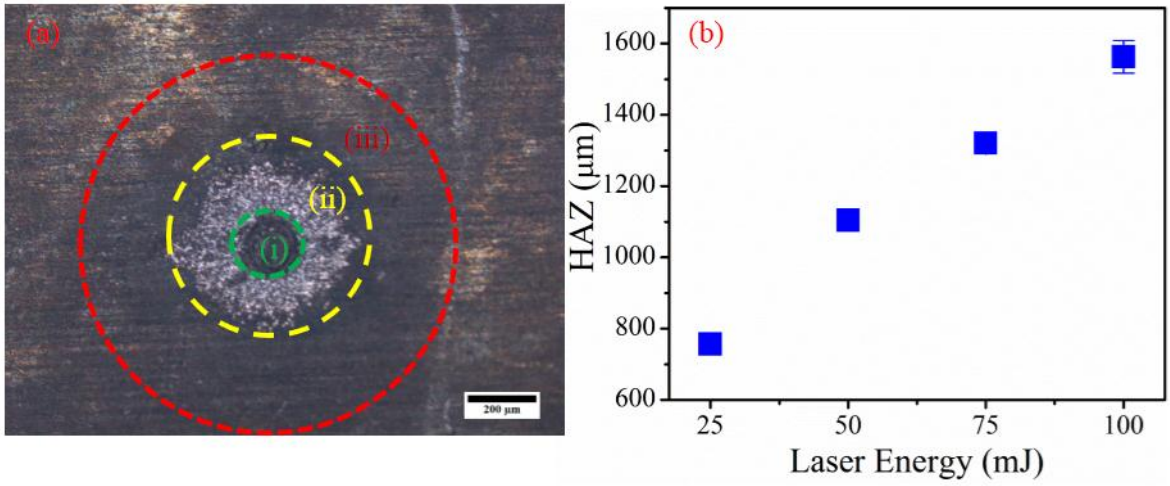

Figure 7.6 (a) Division of crater in three regions and (b) variation HAZ of molybdenum as a function energy.

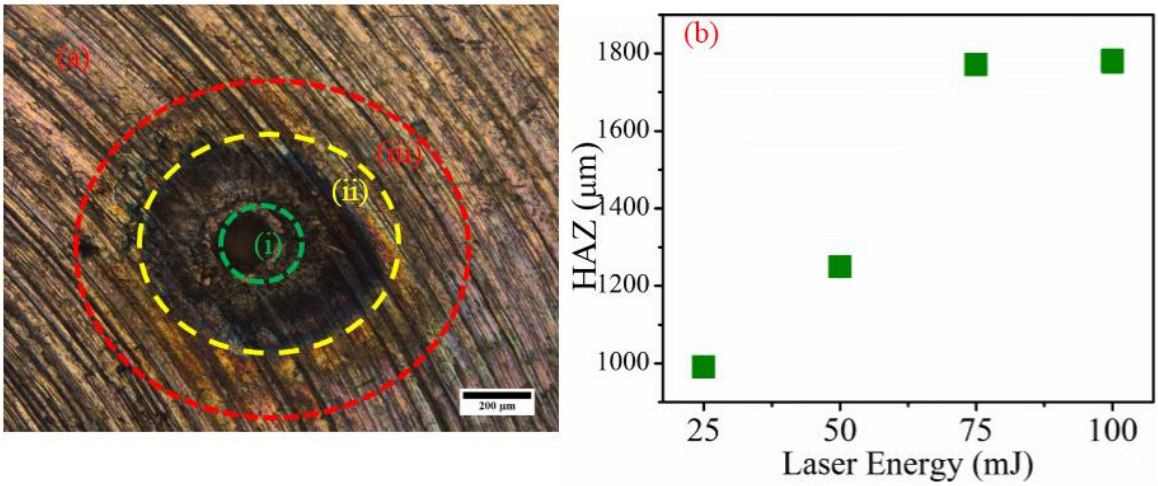

Figure 7.7 (a) Division of crater in three regions and (b) variation HAZ of Cu-alloy as a function energy.

7.3 Depth profile measurement by Surface Profilometer

The depth profile of the laser ablated target at four laser energies is recorded via surface profilometer. From this mass ablation rate is assessed by considering the depth profile to be cone shape, the mass ablation rate estimated in the following manner: the volume of the cone is estimated by the following relation,

$$Volume = \frac{1}{3}\pi r^2 h \quad (7.1)$$

where *r* is the radius of the focused area and *h* is the maximum depth in the crater. The ablated volume is converted to mass by multiplying it by the atomic weight of the corresponding ablated target. As in the present case, the ablation of the target is done by 30 consecutive laser pulse the mass ablation per laser shot is obtained by dividing the total ablated mass by the 30. The depth profile of the laser ablated target of tungsten, molybdenum and Cu-alloy at four laser energies are given in Fig. 7.8, Fig. 7.10, and Fig. 7.12. The corresponding mass ablation rate as a function of energy is given in Fig. 7.9, Fig. 7.11, and Fig. 7.13 respectively.

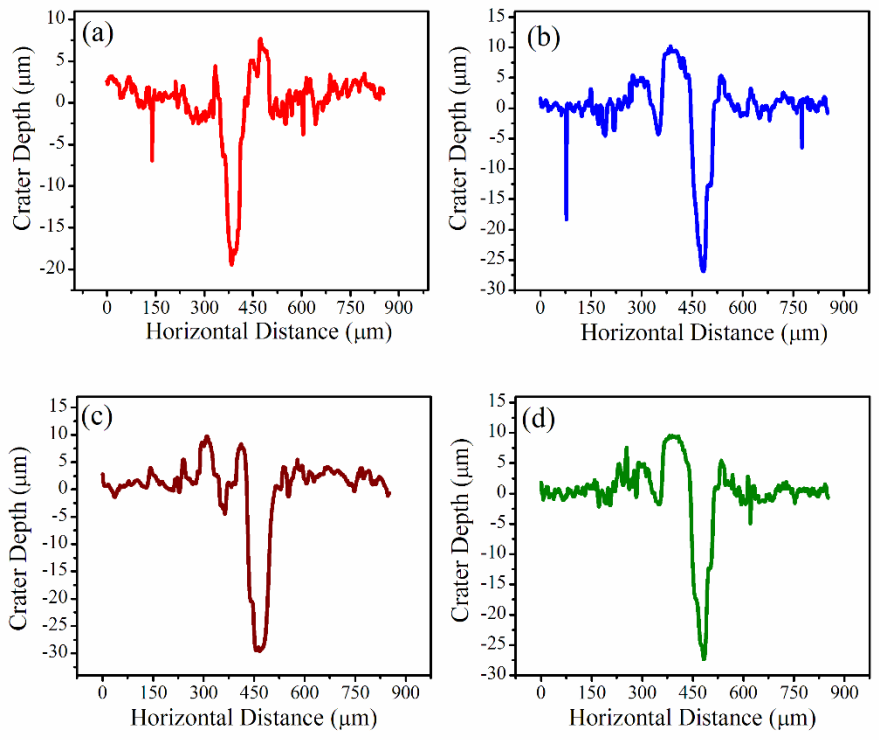

.

Figure 7.8 Laser ablated crater depth profile of tungsten at (a) 25, (b) 50, (c) 75, (d) 100 mJ of laser energy.

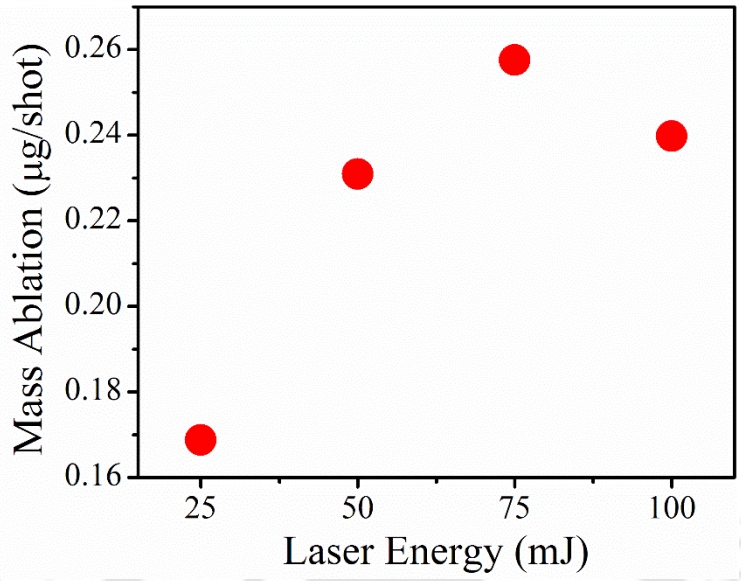

Figure 7.9 Mass ablation rate of laser ablated tungsten in air as a function of laser energy.

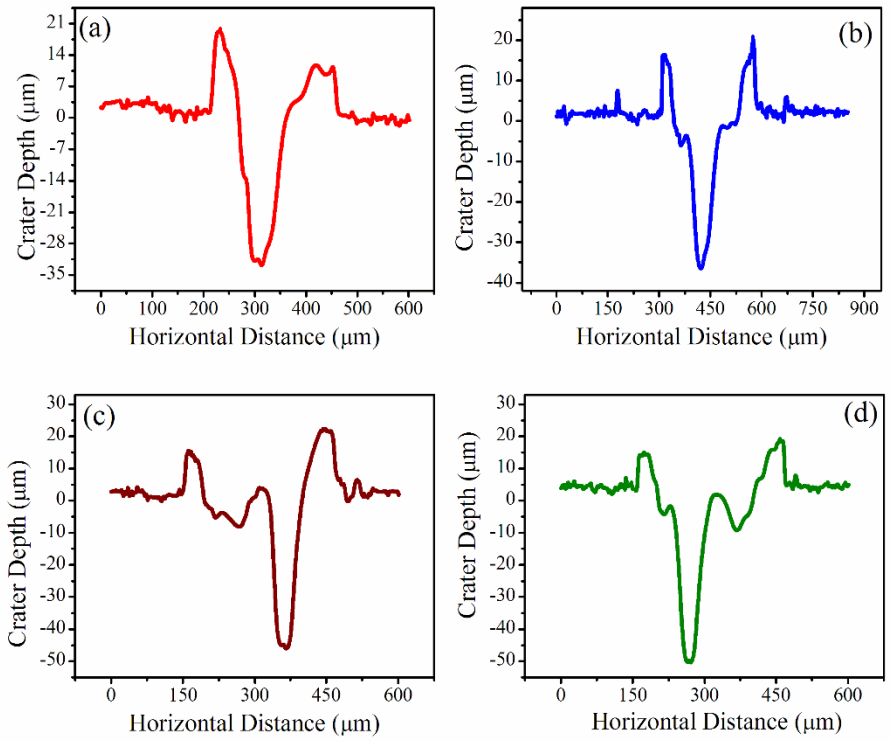

Figure 7.10 Laser ablated crater depth profile of molybdenum at (a) 25, (b) 50, (c) 75, (d) 100 mJ of laser energy.

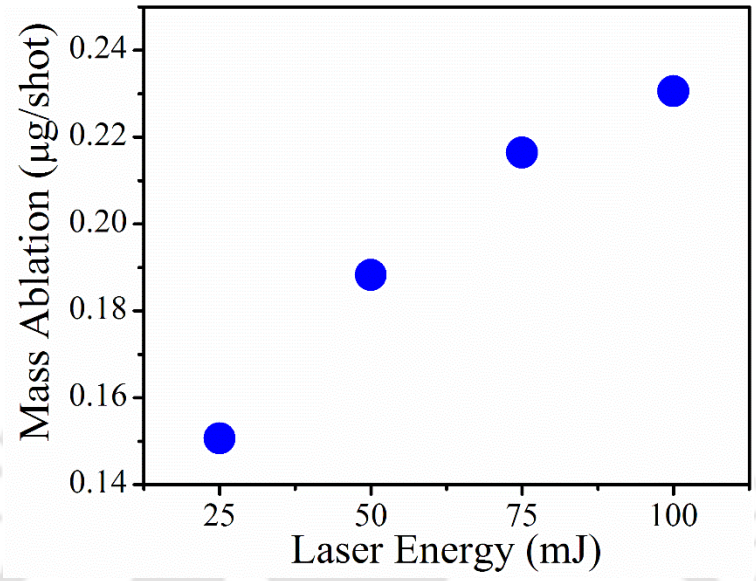

Figure 7.11 Mass ablation rate of laser ablated molybdenum in air as a function of laser energy.

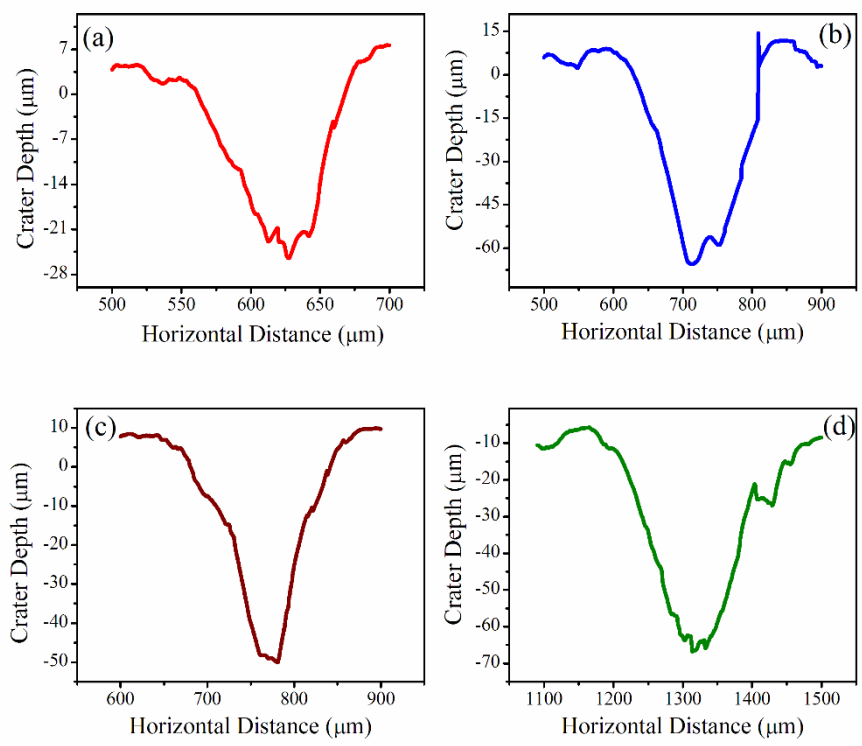

Figure 7.12 Laser ablated crater depth profile of Cu-alloy at (a) 25, (b) 50, (c) 75, (d) 100 mJ of laser energy.

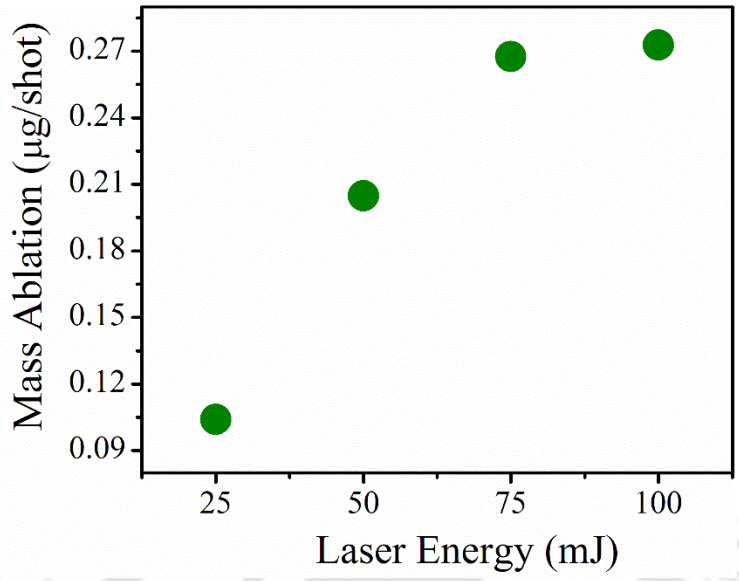

Figure 7.13 Mass ablation rate of laser ablated Cu-alloy in air as a function of laser energy.

It is observed the depth profile as well as mass ablation rate of all the three targets increases as the incident laser energy increases from 25-75 mJ but at 100 mJ of laser energy there is fall in mass ablation rate for tungsten and for molybdenum target where as that of for Cu-alloy, there is hardly any change. This is due to the fact that initially with the increase in laser energy the more energy is deposited on to target surface that results into higher mass ablation but at higher energy due to excessive plasma density the plasma shielding comes in to picture and the laser energy is prevented to reach the target and thus reduces the mass ablation rate. This observation is similar to the LIBS studies (Chapter 4,5 and 6) where increase in line emission intensity and electron density is observed up to 75 mJ and then start to decrease at 100 mJ [110].

7.4 Characterization of re-deposited particulates by FESEM

The surface structure of the laser ablated tungsten, molybdenum and Cu-alloy (brass) in air by 30 laser shots are also examined by FESEM analysis. The FESEM images of the crater formed on the tungsten, molybdenum and copper alloy are shown in Fig. 7.14-7.16 at all the four laser energies. In these images the surface of the laser irradiated target region can be divided in to three regions. The enlarged view of all the three region for tungsten, molybdenum and Cu-alloy at four laser energies are shown in Fig. 7.17-7.20, Fig. 7.21-7.24 and Fig. 7.25-7.29 respectively. In these FESEM images, image (a) corresponds to the central region of the crater, image (b) that of the crater rim, image (c) is crater periphery and image (d) that of the magnified image of the crater periphery.

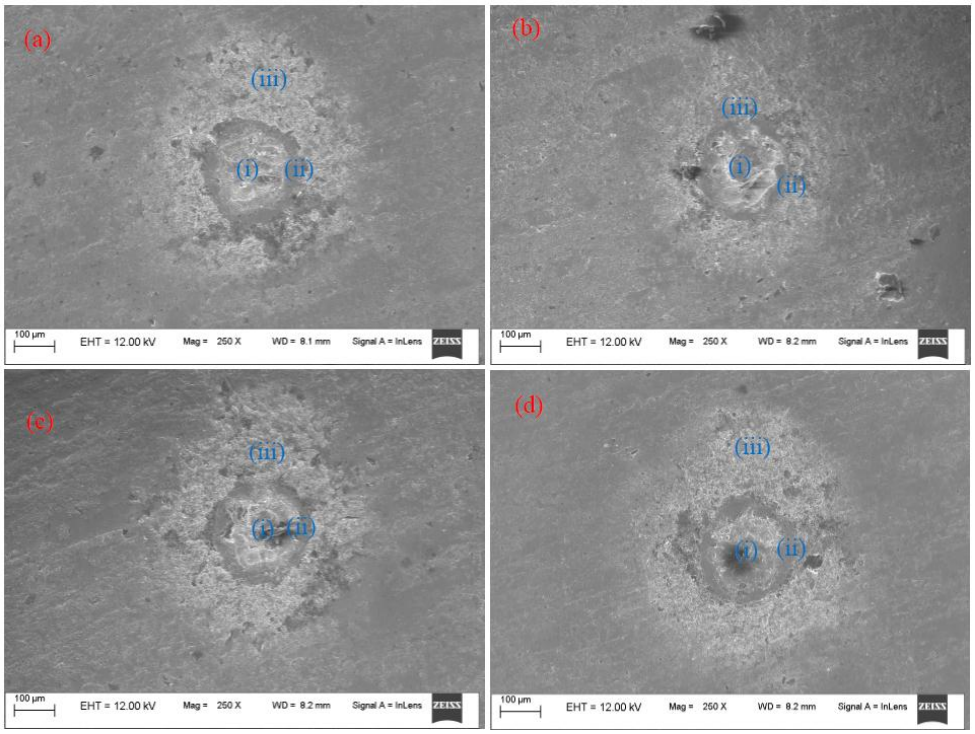

Figure 7.14 FESEM images laser irritated tungsten at four laser energies of (a) 25, (b) 50, (c) 75 and 100 mJ.

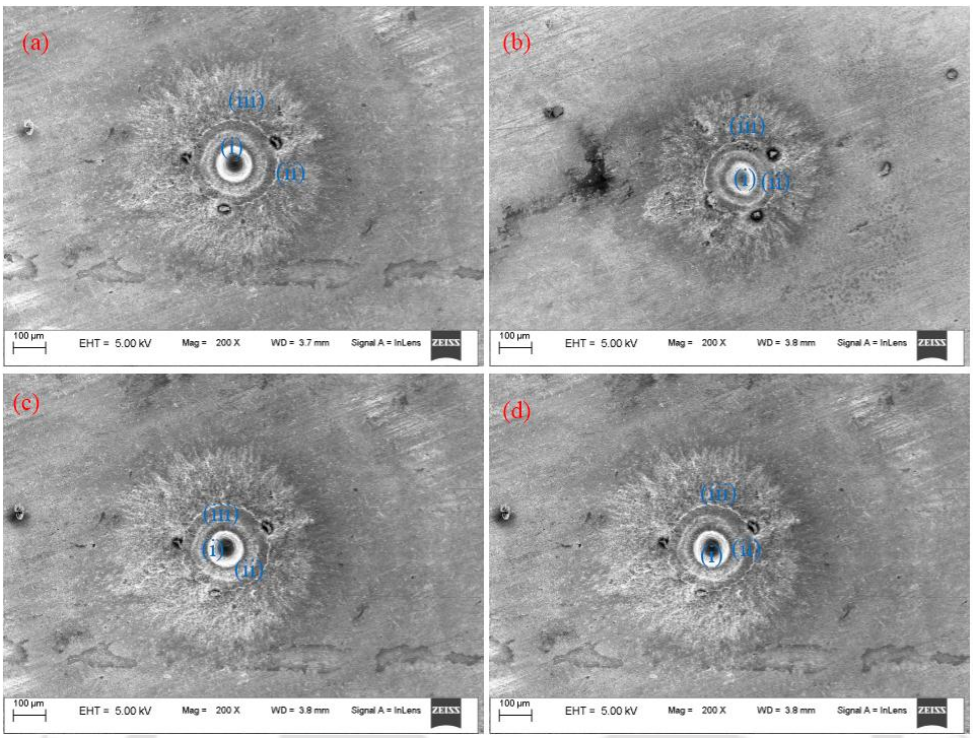

Figure 7.15 FESEM images laser irritated molybdenum at four laser energies of (a) 25, (b) 50, (c) 75 and 100 mJ.

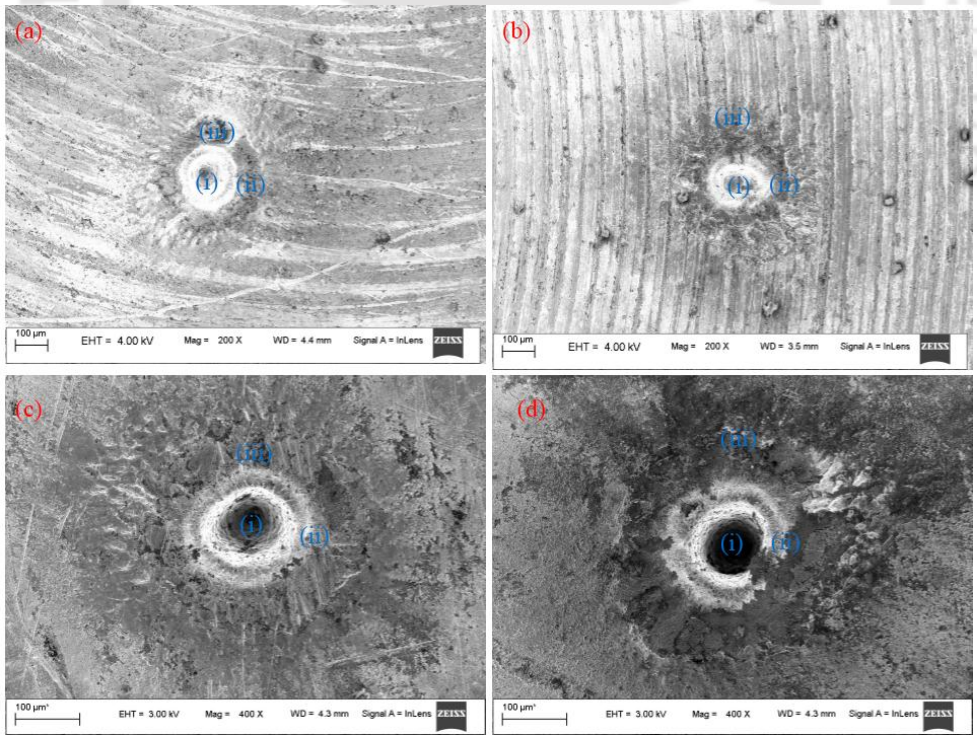

Figure 7.16 FESEM images laser irritated Cu-alloy at four laser energies of (a) 25, (b) 50, (c) 75 and 100 mJ.

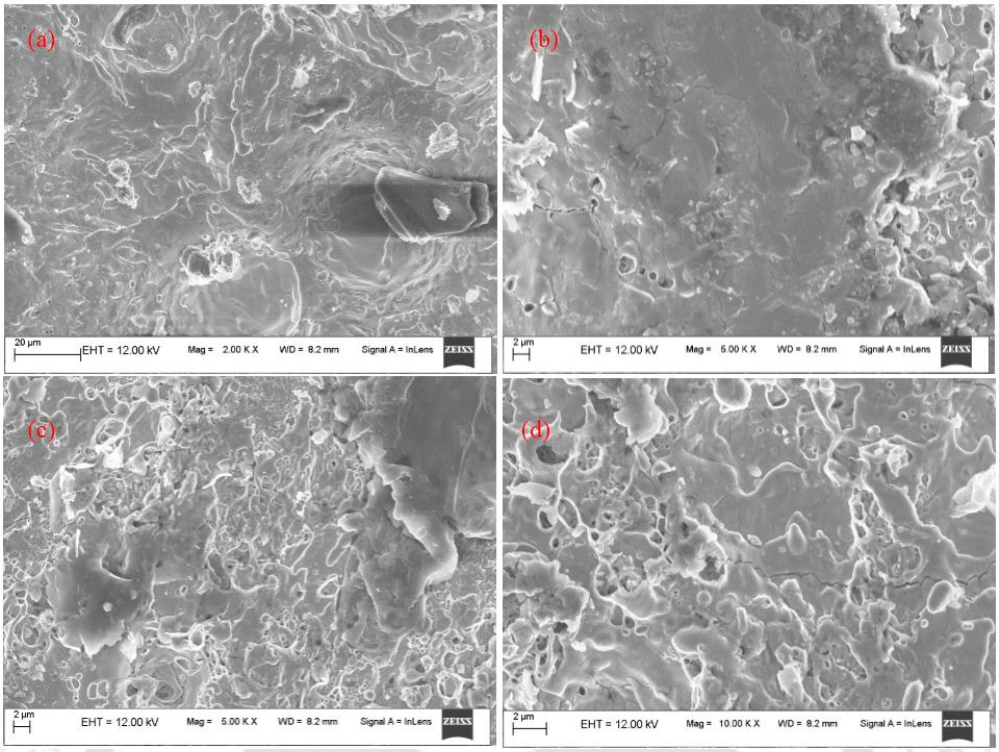

Figure 7.17 FESEM images laser irritated tungsten from different regions at 25 mJ of laser energy.

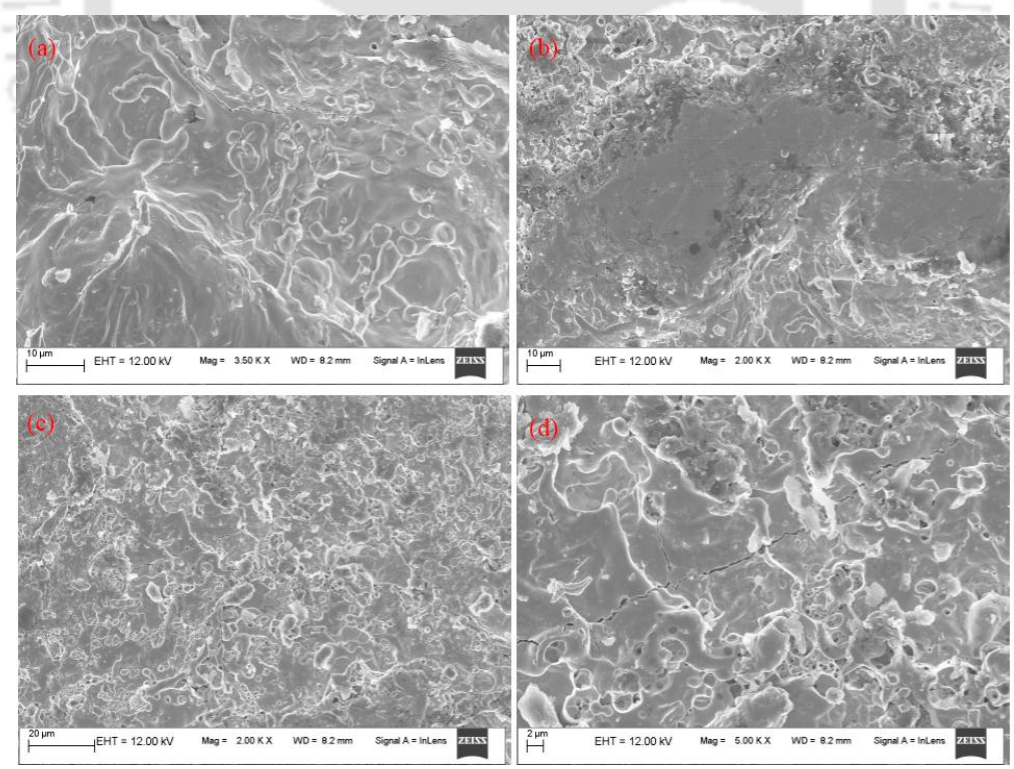

Figure 7.18 FESEM images laser irritated tungsten from different regions at 50 mJ of laser energy.

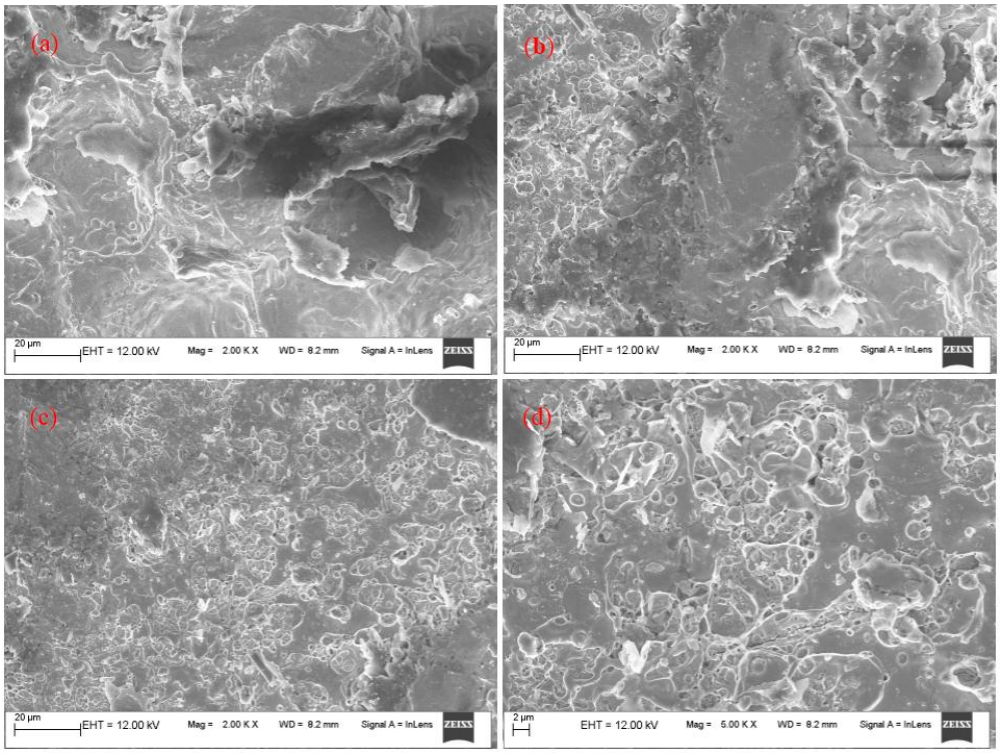

Figure 7.19 FESEM images laser irritated tungsten from different regions at 75 mJ of laser energy.

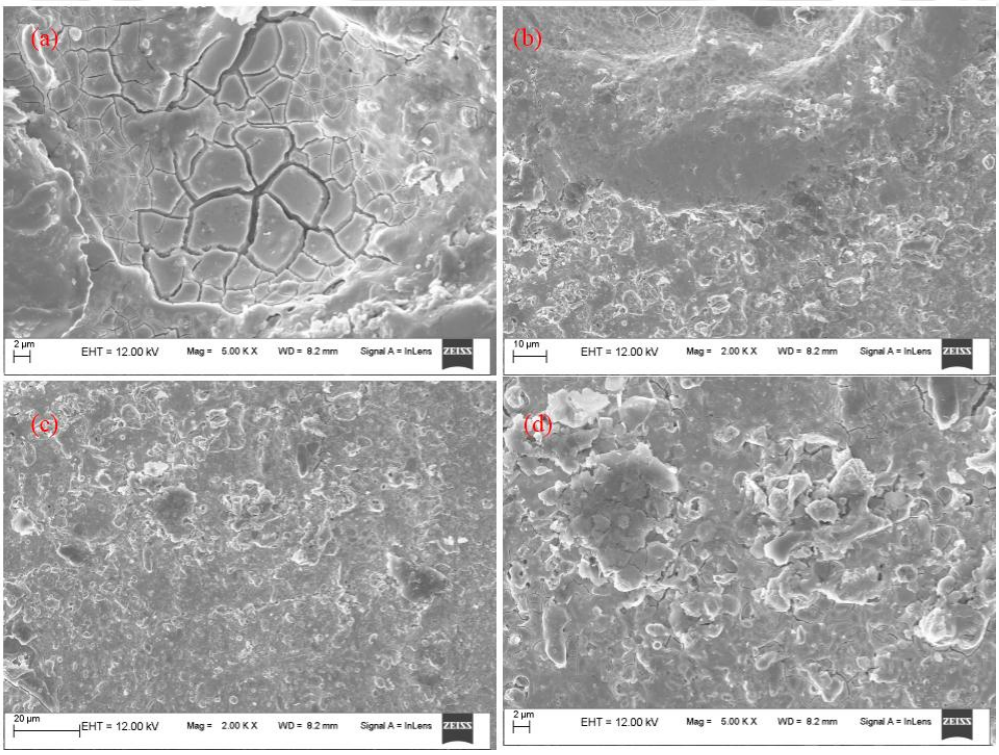

Figure 7.20 FESEM images laser irritated tungsten from different regions at 100 mJ of laser energy.

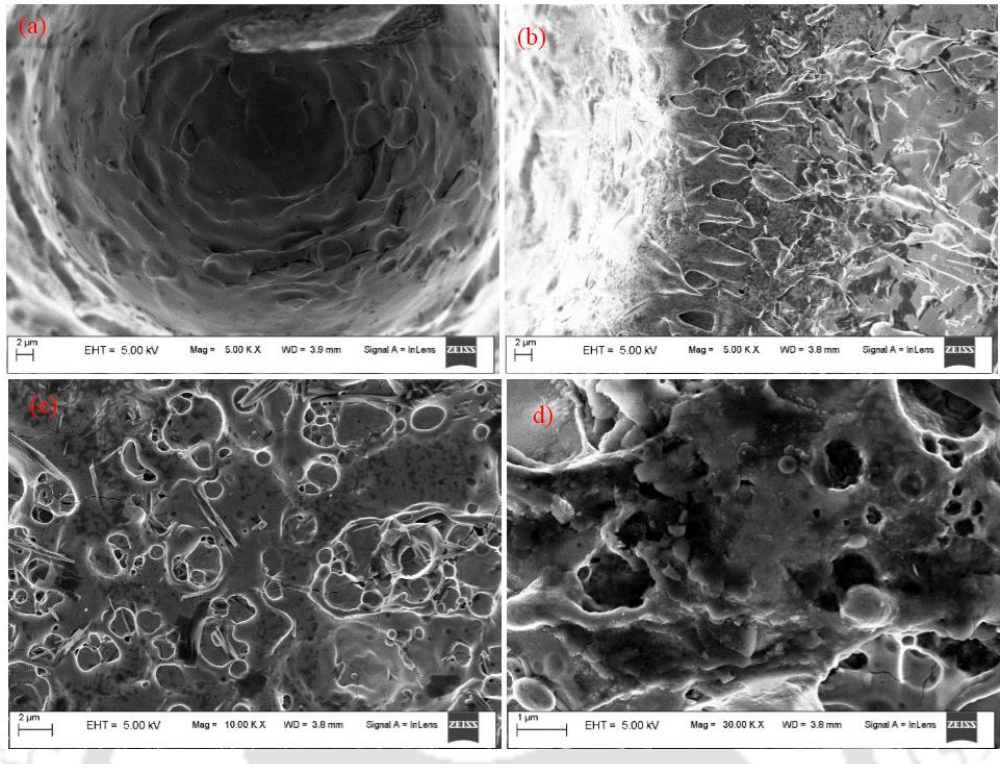

Figure 7.21 FESEM images laser irritated molybdenum from different regions at 25 mJ of laser energy.

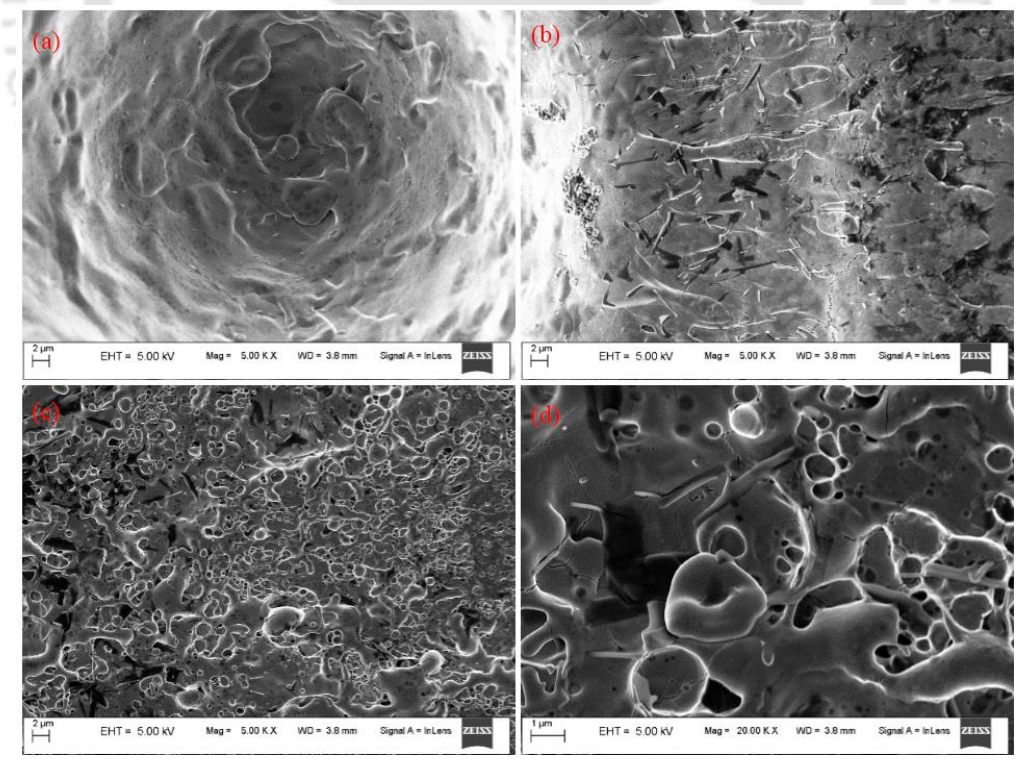

Figure 7.22 FESEM images laser irritated molybdenum from different regions at 50 mJ of laser energy.

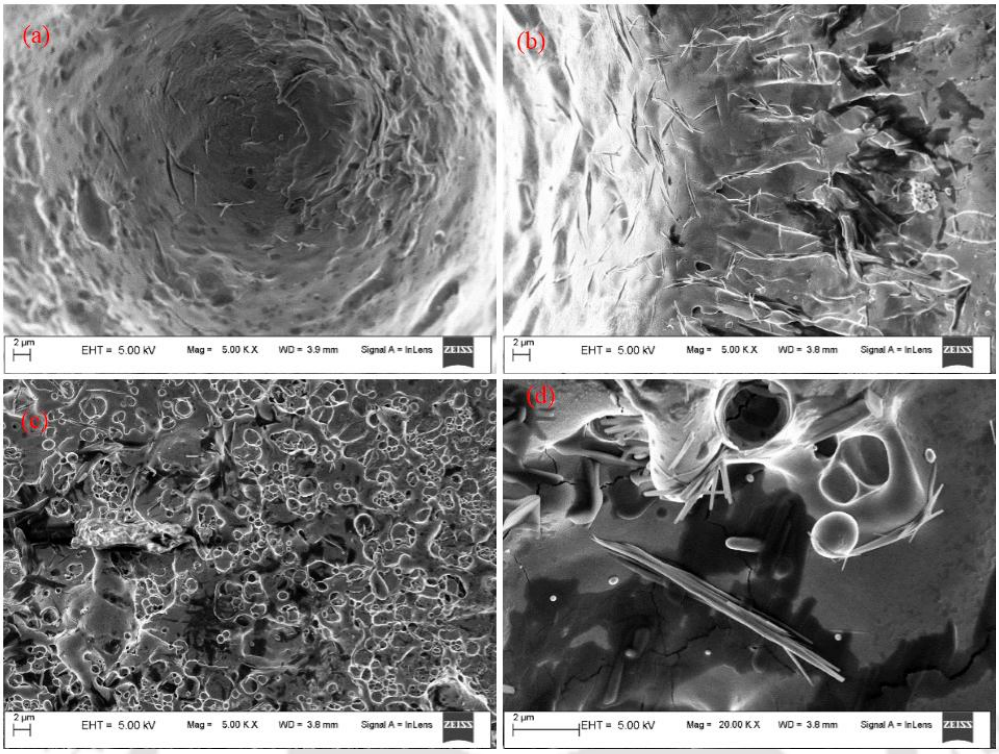

Figure 7.23 FESEM images laser irritated molybdenum from different regions at 75 mJ of laser energy.

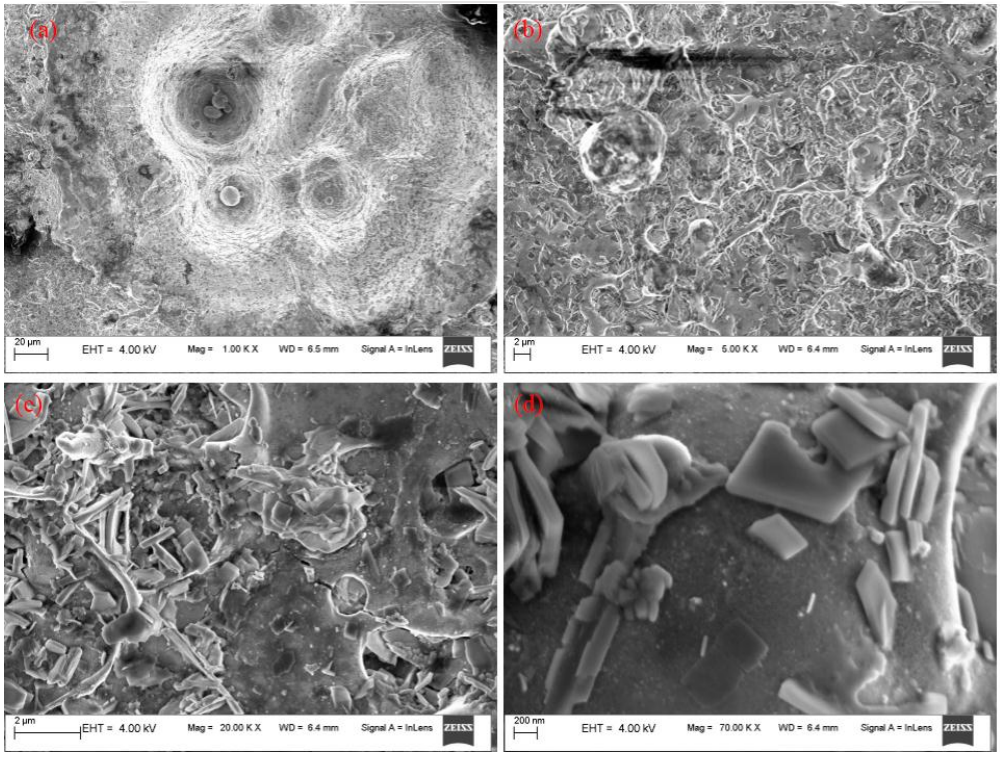

Figure 7.24 FESEM images laser irritated molybdenum from different regions at 100 mJ of laser energy.

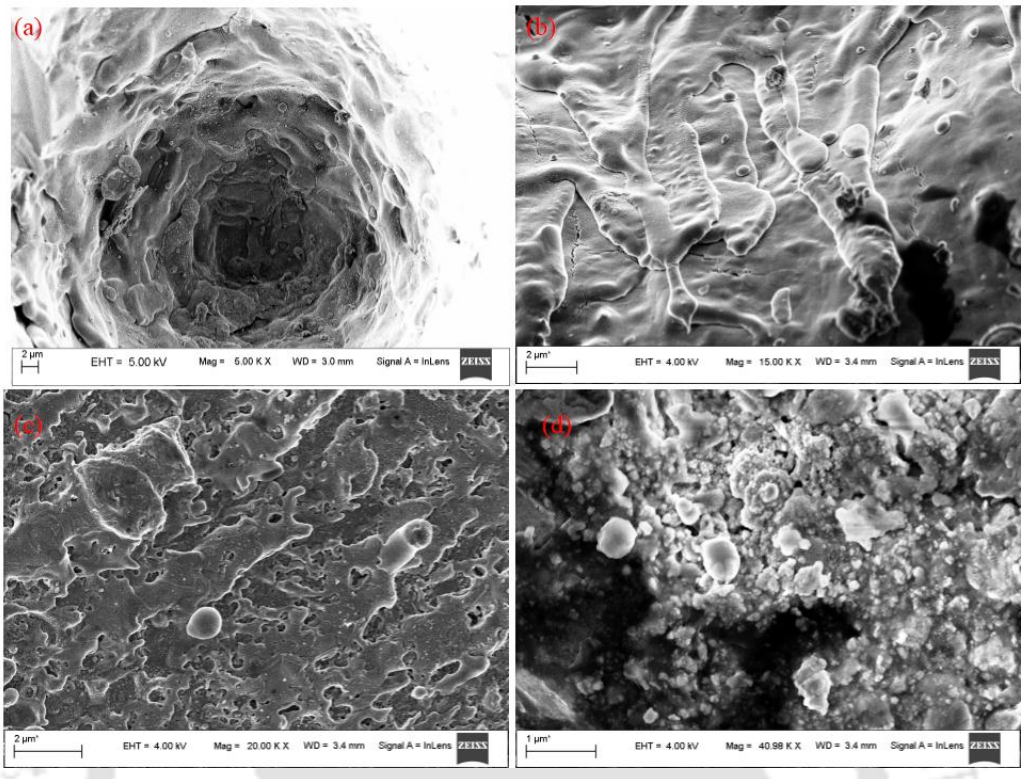

Figure 7.25 FESEM images laser irritated Cu-alloy from different regions at 25 mJ of laser energy.

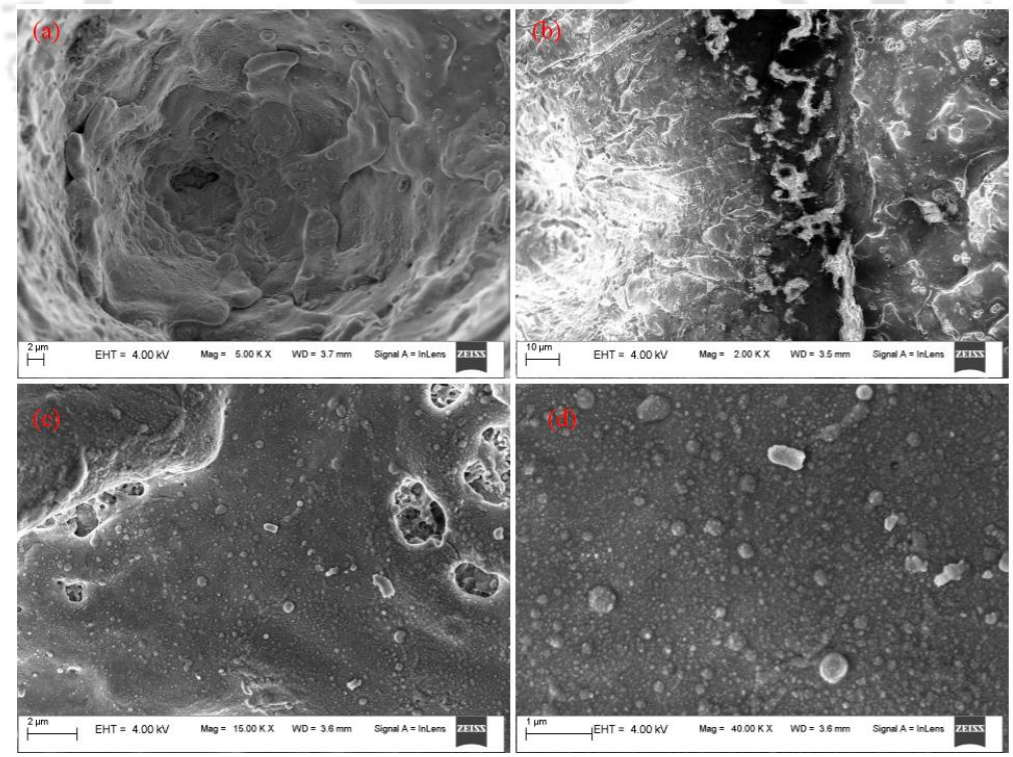

Figure 7.26 ESEM images laser irritated Cu-alloy from different regions at 50 mJ of laser energy.

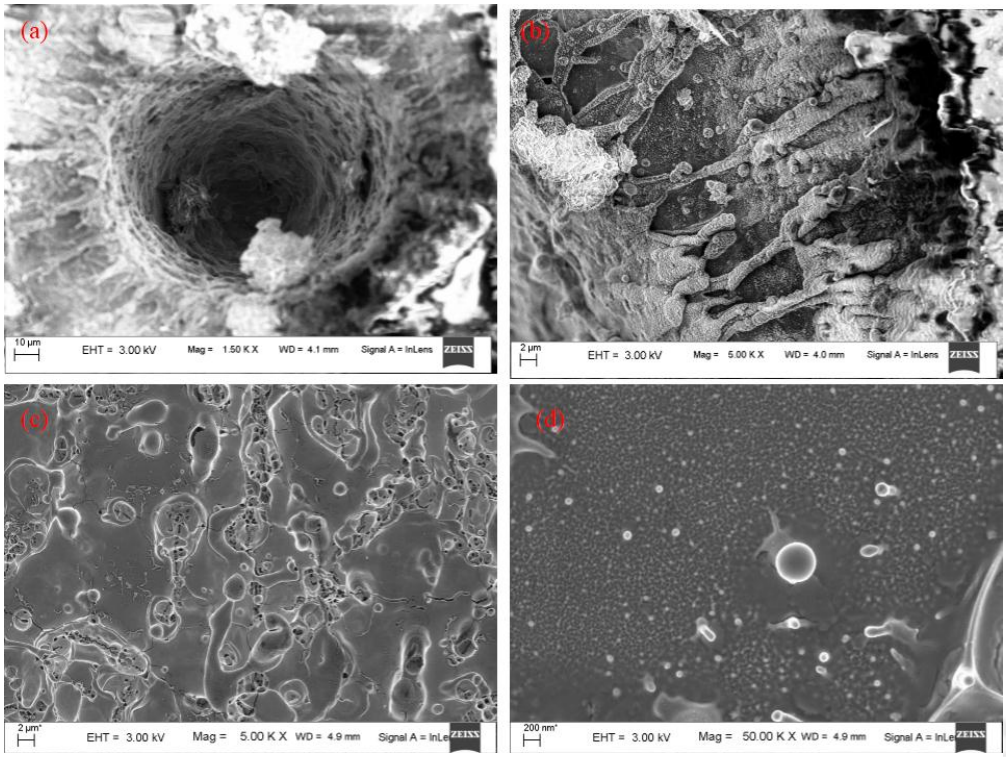

Figure 7.27 FESEM images laser irritated Cu-alloy from different regions at 75 mJ of laser energy.

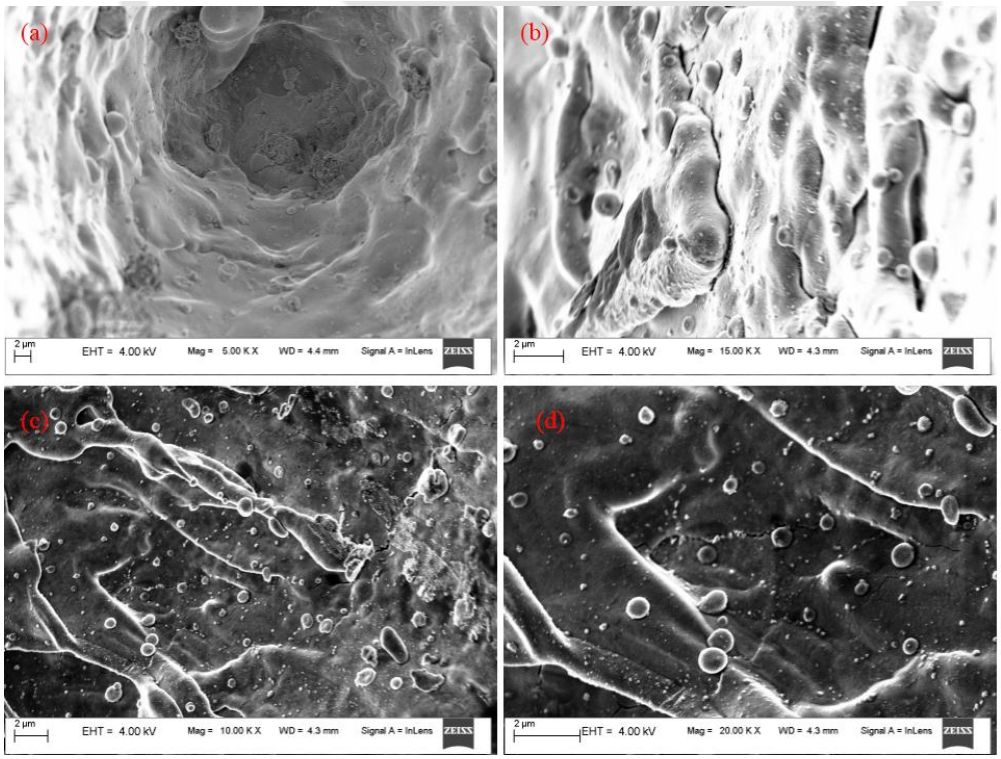

Figure 7.28 FESEM images laser irritated Cu-alloy from different regions at 100 mJ of laser energy.

All these FESEM images clearly reveal the modification on surface due to the localized heating, melting, evaporation and re-solidification. There is formation of cracks, pores and grain at the central region. The crack formation takes place due to the thermal stress, due to the two reasons: (i) there is a temperature gradient between the heated surface and surrounding cold bulk surface that generates the compressive thermal stress, and (ii) when the laser ablated material and plasma cools down, the upper surface of the melted layer condensates faster than inner surface. The difference in the cooling rates of these two layers generates the thermal stress which results in the crack formation [204]. The size of the cracks increases with the increase in laser energy. The images in Fig (b) are corresponding to the crater rim which is grown due to the displacement and re-deposition of the melt layer. This portion is characterized by formation of crack and irregular coarse grain structures. There is a deposition of mass on the crater rim due to the splashing and displacement of molten layer from the crater center. This occurs due to the recoil pressure of the molten layer which results in to the radial outflow of the molten layer towards the crater rim and deposited on the rim due to the cooling via conduction of heat. The ripple kind of structures formed in these area due to the hydrodynamic instability [205]. The crater periphery and magnified images are shown in Fig. (c) and (d) respectively. The different kinds of nano and microstructures formation is clearly visible in these figures. The formation different size and shaped nano and micro particle is attributed to the condensation of laser ablated mass and plasma plume [206].

7.5 Structural studies on the re-deposited material by Raman spectroscopy

Due to the laser ablation, target as well as LIP come in contact with oxygen from air and oxide formation take place. Thus the re-deposited material is a mixture of target material as well as its oxide. To study the phase of the re-deposited materials on to the target surface, the laser irradiate target is investigated under Raman spectrometer. The Raman spectrum from the laser ablated surface is recorded in all three region: (i) center of the crater, (ii) periphery of crater and the (iii) re-deposited material outside the crater periphery. In the first two region no Raman signal is observed, indicating the absence of oxides formation. It is experimentally verified that a strong concoction occurs between the atom and ion in LIP with the air at the interface between the outer sphere plasma and the ambient. At this point atoms or ions able to reach the edge of the crater and get easily oxidized which results in to the formation of oxides in the peripheral region and not in the crater [207].

The Raman spectra of the peripheral region of laser ablated tungsten in air for the incident laser energy of 50 mJ is shown in Fig. 7.29. The observed peaks at 90, 137, 192, 265, 685, 805 and 948 cm^{-1} correspond to WO_3 phase [208, 209] .

The Raman spectra from laser ablated molybdenum in air in the peripheral region for the incident laser energy of 50 mJ is shown in Fig. 7.30. The peaks are observed 114, 126, 149, 198, 215, 239, 284, 339, 380, 469, 667, 823, and 996 cm^{-1} are due to MoO_3 phase [210, 211].

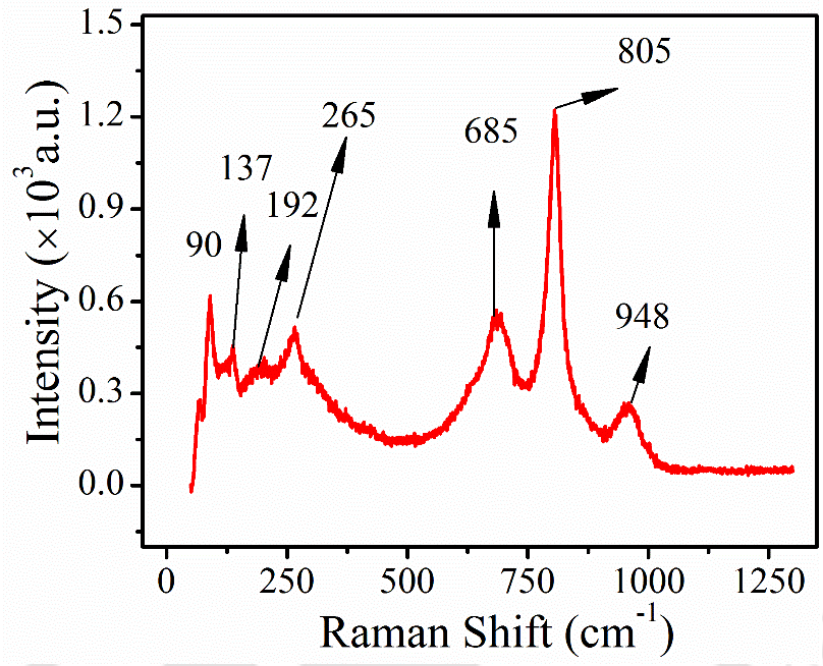

Figure 7.29 Raman spectra from periphery region of crater surface of tungsten at 50 mJ of laser energy.

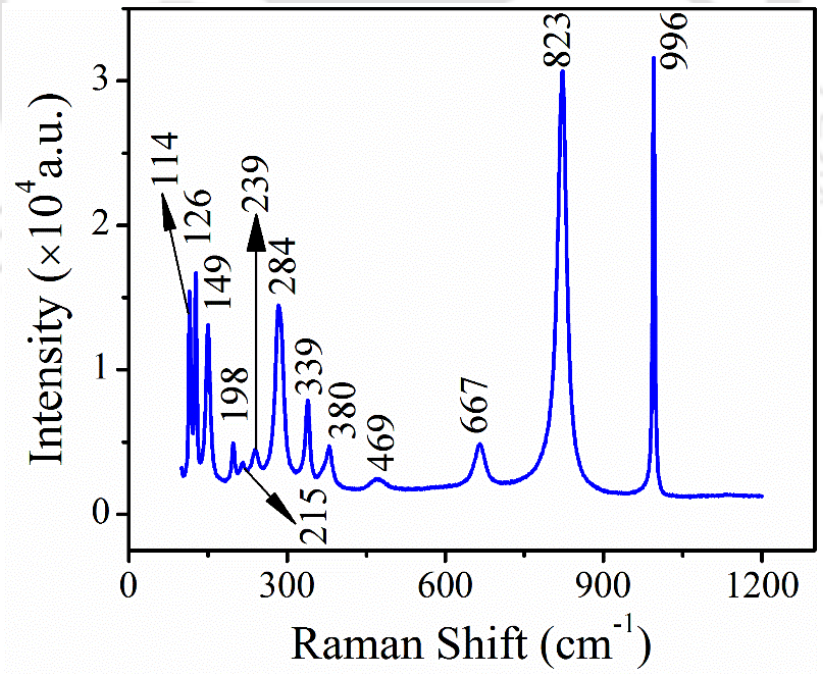

Figure 7.30 Raman spectra from periphery region of crater surface of molybdenum at 50 mJ of laser energy.

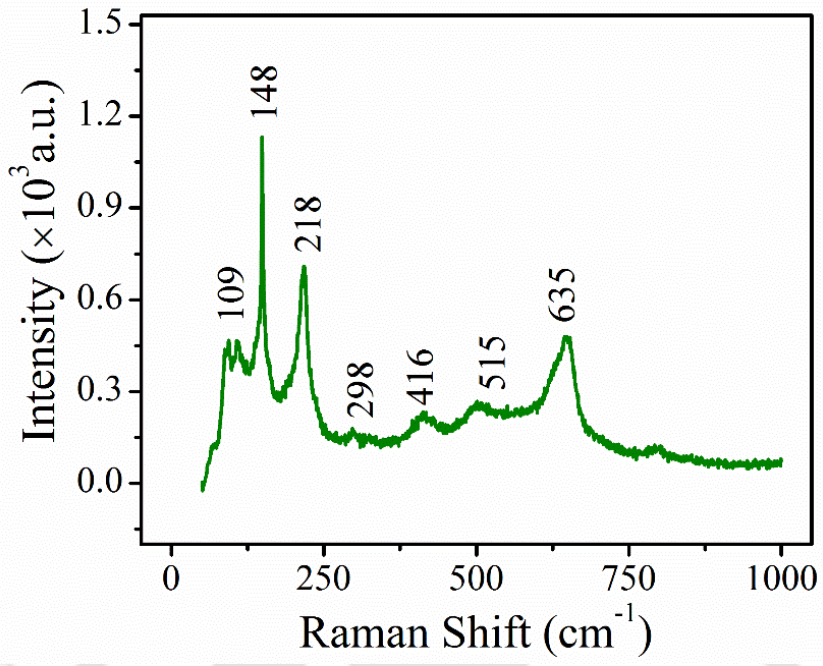

Figure 7.31 Raman spectra from periphery region of crater surface of Cu-alloy at 50 mJ of laser energy.

The Raman spectra from laser ablated Cu-alloy in air (peripheral region) for the incident laser energy of 50 mJ is shown in Fig. 7.31. The peaks are observed at 109, 148, 218, 298, 416, 515, and 635 cm^{-1} which corresponds to different oxidation state of copper [212]. The peak at 109,148, 218, 416, 515 and 635 cm^{-1} is assigned Cu_2O. The characteristic peak of CuO is observed at 298 cm^{-1}. Though this target is made of Al, Fe, Ni, Cu, Zn, Sn, and Pb (chapter 6) but the concentration of Cu being maximum in the target. So only the formation of different phase of Cu is prominent.

7.6 Conclusion

The three target i.e. tungsten, molybdenum, Cu-alloy are ablated by 30 consecutive laser shots in air. The laser irradiated targets are investigated via optical microscope, surface profilometer, FESEM and Raman spectroscopy. From the optical microscopic images three different zones are identified, first one is the crater formed in the focal region of laser, second one is the crater

rim and the third one is crater periphery. From the optical images the HAZ are estimated as a function of laser energy. The crater depth profiles are measured via non-contact surface profilometer at all the laser energies for all the three targets. From the measured crater value the mass ablation rate is estimated. It is observed that HAZ, crater depth and mass ablation rates are increases up to 75 mJ and then start to saturate and decrease. This is due to the plasma shielding effect at higher energies. FESEM images are taken at three regions, for all the three targets. The central region of the crater reveals the formation of grains and crack. The splashing of the molten layer is observed at crater rim with ripple structures. The periphery region is made up of uplifted re-solidified material of different size and shape. The Raman spectra from crater periphery region reveal the formation of respective oxides of the target elements only in the peripheral regions. These studies can be utilized to obtain micro and nano-structures in a controllable manner for various applications as well as laser micro-nano machining.

भारतीय प्रौद्योगिकी संस्थान गुवाहाटी
Indian Institute of Technology Guwahati

Chapter 8 Conclusion and Future Scope

In the present thesis work, time and space evolution of laser induced plasma via laser induced breakdown spectroscopy (LIBS) on Tungsten, Molybdenum and Cu-alloys in air as a function of laser energy are presented. To study the temporal evolution of LIP of W, Mo and Cu-alloys as a function of laser energy, a high power Nd:YAG laser (INNOLAS Split light 1200), is focused on the samples using a lens of focal length 15 cm to generate the LIP on the sample surface. The emitted radiation from LIP is collected through an optical fiber, the outer end of which is connected to echelle spectrometer to disperse the radiation from the LIP in order to record the spectra as a function of time (delay time) with respect to laser pulse. To avoid the high intensity of continuum radiation in the initial stage of plasma formation, the spectrum is recorded in the temporal window (delay) of 0.5 -5.0 μs with respect to laser pulse. In the next part, of the experiment the space evolution of LIP is studied by recording the spectrum at different axial positions away from the target surface. For this, the plasma is imaged in one to one correspondence on the optical fiber, positioned on to a translational stage, moving in a step of 0.4 mm to record space resolved spectra of LIP. As an application of LIBS, the single line CF-LIBS techniques is applied to Cu-alloys to find the percentage composition of the constituent elements. The analytical performance CF-LIBS is highly effected by the temporal and spatial evolution of LIP. So the time and space resolved spectra are recorded from the Cu-alloys and is analyzed to estimate the plasma temperature and electron density. The estimated plasma parameters are plugged into the single line CF-LIBS algorithm to measure elemental concentration. The surface characterization of laser ablated region is also under taken via optical microscope, surface profilometer, FESEM and Raman spectroscopy for W, Mo and

Cu-alloy to understand the surface modification during LIBS studies and its dependence on laser energy.

The temporal studies on the LIP of tungsten and molybdenum reveals that plasma emission comprised of several atomic and ionic lines of tungsten and molybdenum which decay exponentially with the time. The persistence time of ionic lines is smaller than that of atomic lines. The SNR increase in the temporal window of 0.5- 3.5 μs, and beyond this window it starts to fall down. The plasma temperature is estimated using several atomic and ionic transitions of tungsten and molybdenum through the Boltzmann plot method. The ionic lines are offering higher value of plasma temperature in the initial time of 0.5-1 μs as compared to that of the obtained from neutral atomic lines, while at later time both these temperatures possess nearly same values indicating the coexistence of thermodynamic equilibrium among ions and atoms in temporal window of 1.5-4 μs. The stark-broadened profile of WI line and MoI at 430.2 and 313.2 nm are exploited for the estimation of electron densities of LIP of tungsten and molybdenum respectively. The plasma parameters increases with the increase of incident laser energy from 25-75 mJ in both the targets but at higher energy of 100 mJ its start to saturate due the plasma shielding effect. The lower limit of electron densities to maintain the LTE inside the plasma at different delay time as a function of incident laser is estimated using McWhirter criterion and relaxation time is also measured to take into account the transient nature of the plasma. The relaxation time is found to be of the order few nanosecond which is much less than plasma evolution time which is of the order of 10^{-6} s. The matching of theoretical and experimental branching ratio confirm the optical thin condition of plasma in the time range of 1.5-3.5 μs. The experimental studies on the temporal evolution reveals the

optimum time window for characterization of LIP lies in the temporal window of 1-3.5 μs where the optical thin condition as well as LTE conditions are satisfied and the SNR is high.

LIP spectra tungsten and molybdenum are recorded at different locations of the LIP plume along the axial plasma expansion direction at a fixed delay of 2 μs which lies in optimum temporal window. The maximum attainable value of the plasma emission intensity and temperature are found at a certain distance away from the target surface and decrease close to the target as well as towards the plasma edge away from the target. The maximum intensity for ionic line appear slightly closer to the target as compared to that of the atomic lines. The maximum value of plasma temperature is observed in the same spatial window as that of the atomic line intensity. From the axial profile of electron density, it is observed that the electron density attains a maximum value at a distance of 2 mm away from the target surface but decreases beyond this. The LTE criteria are satisfied in case of inhomogeneous expansion of plasma through the Mc-Whirter criteria and diffusion length. The experimentally obtained branching ratios are in good agreement with the theoretical ratios in the space-resolved studies up to the axial distance of 4 mm. From the space resolved study, an optimum spatial window of 0.8-2.8 mm is identified where LTE and optically thin plasma conditions are satisfied for LIBS application.

The analytical performance CF-LIBS is highly effected by the validity of LTE and optical thin condition of LIP which is influence the temporal and spatial evolution of LIP. So the time and space resolved spectra are recorded from the multi-elements Cu-alloys and time and space resolved plasma emission is analyzed to estimate the plasma temperature and electron density. The estimated plasma parameter are plugged into the CF-LIBS algorithm to measure elemental concentration. The CF-LIBS results for all the copper alloys are compared with that of the

EDX measurement. The three different copper alloys are investigated by CF-LIBS. The sample 1, which is a commercial brass piece consists of seven elements of Cu, Zn, Al, Fe, Sn, Pb and N, sample 2 contains three elements: Cu, Zn, and Ni and the sample 3 is made of Cu and Ni only. The estimated relative errors and distance function values in CF-LIBS measurement for sample 1 is minimum at 50 mJ of laser energy. Therefore, the rest of the two Cu-alloys, CF-LIBS is applied for this particular energy only. The CF-LIBS results as a function of delay confirm that within the optimized temporal window of 2-4 μs, where the LTE and optical thin conditions are properly satisfied, the accuracy of the composition of constituent elements is higher and value of distance function as well as relative error are minimum. In case of space resolved study of CF-LIBS, optimum spatial window of 0.8-2.8 mm is identified for the estimation of concentration of constituent elements with good accuracy within the optimum temporal window around 2 μs.

The modification on surface morphology of tungsten, molybdenum and Cu- alloy (commercial bras) due to laser ablation are investigated. The optical microscopic images of the laser irritated target at four laser energies reveal that with the increase in laser energy from 25-75 mJ, HAZ increases but at 100 mJ there is hardly any change in it w.r.t 75 mJ. The laser ablated crater depth is measured using non-contact surface profilometer. Initially with increase of laser energy from 25-75 mJ, the HAZ as well as the crater depth increases due to the enhancement in the ablation with the laser energy. The decrease in HAZ as well as the crater depth at higher energy of 100 mJ is attributed to the shielding effect of the plasma plume which curtails the energy deposition on target surface in the later part of laser pulse. The saturation in HAZ and the crater depth are in agreement with the saturation of the plasma parameter at 100 mJ of laser energy. The FESEM images from the center of the crater, around its rim and its peripheral

region are captured. Surface features formed are due to localized heating, melting, evaporation and re-solidification of molten layer and condensation of plasma particles. FESEM investigations reveal the development of cracks in the central ablated region and the formation of grains. The deposition of splashed molten pool around the crater rim while different shapes of micro and nanostructures are observed at periphery of ablated areas. The Raman spectra confirm the presence of WO_3, MoO_3 in laser ablated tungsten, molybdenum target respectively while CuO and Cu_2O in case of copper alloy (commercial brass).

Future Scope:

This thesis work has been motivated by two basic needs in the improvement of LIBS technique for qualitative and quantitative analyses purposes. The present investigations clearly indicates that there is a need for further detailed study on laser induced plasma as function of other laser parameters to get a complete understanding of laser matter and laser plasma interaction for various applications. The present work on tungsten and molybdenum target can be extended under vacuum for fusion reactor application and deposition of high quality thin film. Moreover LIBs studies can also be extended for estimation of necessary atomic parameters which are not available in the literature. The single line CF-LIBS is to be implemented on other metallic alloys and chemometric techniques can be combined with this technique for various complicated samples. CF-LIBS should also be tested in the presence of external electric and magnetic field to further improve upon the signal to noise ratio and its sensitivity. The ablation using femto second laser pulse will be useful for nano-structuring on the heavy metals for various application.

Bibliography

[1] C. Phipps, Laser ablation and its applications, Springer, 2007.

[2] M. Autin, A. Briand, P. Mauchien, J. Mermet, Characterization by emission spectrometry of a laser-produced plasma from a copper target in air at atmospheric pressure, Spectrochimica Acta Part B: Atomic Spectroscopy, 48 (1993) 851-862.

[3] R.E. Russo, Laser ablation, Applied Spectroscopy, 49 (1995) 14A-28A.

[4] D.A. Cremers, F.Y. Yueh, J.P. Singh, H. Zhang, Laser-induced breakdown spectroscopy, elemental analysis, Encyclopedia of Analytical Chemistry: Applications, Theory and Instrumentation, (2006).

[5] R. Eason, Pulsed laser deposition of thin films: applications-led growth of functional materials, John Wiley & Sons, 2007.

[6] S. Foltyn, DB Chrisey, and GK Hubler: Pulsed Laser Deposition of Thin Films, in, Wiley Interscience, 1994.

[7] J.P. Singh, S.N. Thakur, Laser-induced breakdown spectroscopy, Elsevier, 2007.

[8] C. Liu, X. Mao, S. Mao, X. Zeng, R. Greif, R. Russo, Nanosecond and femtosecond laser ablation of brass: particulate and ICPMS measurements, Analytical chemistry, 76 (2004) 379-383.

[9] T. Donnelly, B. Doggett, J.G. Lunney, Pulsed laser deposition of nanostructured Ag films, Applied Surface Science, 252 (2006) 4445-4448.

[10] W. Gong, Z. Zheng, J. Zheng, X. Hu, W. Gao, Water soluble CdS nanoparticles with controllable size prepared via femtosecond laser ablation, Journal of applied physics, 102 (2007) 064304.

[11] B. Liu, Z. Hu, Y. Che, Y. Chen, X. Pan, Nanoparticle generation in ultrafast pulsed laser ablation of nickel, Applied Physics Letters, 90 (2007) 044103.

[12] P. Dyer, S. Maswadi, C. Walton, M. Ersoz, P. Fletcher, V. Paunov, 157-nm laser micromachining of N-BK7 glass and replication for microcontact printing, Applied Physics A, 77 (2003) 391-394.

[13] A.Y. Vorobyev, C. Guo, Direct femtosecond laser surface nano/microstructuring and its applications, Laser & Photonics Reviews, 7 (2013) 385-407.

[14] T. Kanesue, Y. Fuwa, K. Kondo, M. Okamura, Laser ion source with solenoid field, Applied Physics Letters, 105 (2014) 193506.

[15] P. Yeates, J.T. Costello, E.T. Kennedy, The DCU laser ion source, Review of Scientific Instruments, 81 (2010) 043305.

[16] F. Pegoraro, S. Atzeni, M. Borghesi, S. Bulanov, T. Esirkepov, J. Honrubia, Y. Kato, V. Khoroshkov, K. Nishihara, T. Tajima, Production of ion beams in high-power laser–plasma interactions and their applications, Laser and Particle Beams, 22 (2004) 19-24.

[17] J. Freeman, S. Harilal, A. Hassanein, Enhancements of extreme ultraviolet emission using prepulsed Sn laser-produced plasmas for advanced lithography applications, Journal of applied physics, 110 (2011) 083303.

[18] S. Harilal, T. Sizyuk, A. Hassanein, D. Campos, P. Hough, V. Sizyuk, The effect of excitation wavelength on dynamics of laser-produced tin plasma, Journal of applied physics, 109 (2011) 063306.

[19] J. White, P. Dunne, P. Hayden, F. O'Reilly, G. O'Sullivan, Optimizing 13.5 nm laser-produced tin plasma emission as a function of laser wavelength, Applied Physics Letters, 90 (2007) 181502.

[20] B. Wu, Y.C. Shin, A self-closed thermal model for laser shock peening under the water confinement regime configuration and comparisons to experiments, Journal of applied physics, 97 (2005) 113517.

[21] R. Ganeev, High-order harmonic generation in a laser plasma: a review of recent achievements, Journal of Physics B: Atomic, Molecular and Optical Physics, 40 (2007) R213.

[22] R.A. Ganeev, High-order harmonic generation in laser plasma plumes, World Scientific, 2013.

[23] C. Chenais-Popovics, O. Rancu, P. Renaudin, J. Gauthier, X-ray spectroscopy of laser-produced hot dense plasmas, Physica Scripta, 1996 (1996) 163.

[24] R.A. Smith, J. Lazarus, M. Hohenberger, A. Marocchino, J.S. Robinson, J.P. Chittenden, A.S. Moore, E.T. Gumbrell, M. Dunne, High resolution imaging of colliding blast waves in cluster media, Plasma Physics and Controlled Fusion, 49 (2007) B117.

[25] B.A. Remington, D. Arnett, R. Paul, H. Takabe, Modeling astrophysical phenomena in the laboratory with intense lasers, Science, 284 (1999) 1488-1493.

[26] T.R. Dittrich, S. Haan, M. Marinak, S. Pollaine, D. Hinkel, D. Munro, C. Verdon, G. Strobel, R. McEachern, R. Cook, Review of indirect-drive ignition design options for the National Ignition Facility, Physics of Plasmas, 6 (1999) 2164-2170.

[27] L.J. Radziemski, D.A. Cremers, Handbook of laser induced breakdown spectroscopy, John Wiley & Sons, 1 (2006) 1-4.

[28] F.Y. Yueh, J.P. Singh, H. Zhang, Laser-Induced Breakdown Spectroscopy, Elemental Analysis, Encyclopedia of analytical chemistry, (2000).

[29] F. Breech, L. Cross, Optical microemission stimulated by a ruby maser, Appl. Spectrosc, 16 (1962) 1.

[30] L.J. Radziemski, From LASER to LIBS, the path of technology development, Spectrochimica Acta Part B: Atomic Spectroscopy, 57 (2002) 1109-1113.

[31] D.W. Hahn, N. Omenetto, Laser-induced breakdown spectroscopy (LIBS), part I: review of basic diagnostics and plasma–particle interactions: still-challenging issues within the analytical plasma community, Applied spectroscopy, 64 (2010) 335A-366A.

[32] L. Radziemski, D. Cremers, A brief history of laser-induced breakdown spectroscopy: from the concept of atoms to LIBS 2012, Spectrochimica Acta Part B: Atomic Spectroscopy, 87 (2013) 3-10.
[33] A.J.R. Bauer, S.G. Buckley, Novel Applications of Laser-Induced Breakdown Spectroscopy, Applied spectroscopy, 71 (2017) 553-566.
[34] L.J. Radziemski, Review of selected analytical applications of laser plasmas and laser ablation, 1987-1994, Microchemical Journal, 50 (1994) 218-234.
[35] J.D. Winefordner, I.B. Gornushkin, T. Correll, E. Gibb, B.W. Smith, N. Omenetto, Comparing several atomic spectrometric methods to the super stars: special emphasis on laser induced breakdown spectrometry, LIBS, a future super star, Journal of Analytical Atomic Spectrometry, 19 (2004) 1061-1083.
[36] R.S. Harmon, R.E. Russo, R.R. Hark, Applications of laser-induced breakdown spectroscopy for geochemical and environmental analysis: A comprehensive review, Spectrochimica Acta Part B: Atomic Spectroscopy, 87 (2013) 11-26.
[37] D. Rusak, B. Castle, B. Smith, J. Winefordner, Fundamentals and applications of laser-induced breakdown spectroscopy, Critical Reviews in Analytical Chemistry, 27 (1997) 257-290.
[38] R. Noll, V. Sturm, Ü. Aydin, D. Eilers, C. Gehlen, M. Höhne, A. Lamott, J. Makowe, J. Vrenegor, Laser-induced breakdown spectroscopy—from research to industry, new frontiers for process control, Spectrochimica Acta Part B: Atomic Spectroscopy, 63 (2008) 1159-1166.
[39] G. Lithgow, A. Robinson, S. Buckley, Ambient measurements of metal-containing PM2. 5 in an urban environment using laser-induced breakdown spectroscopy, Atmospheric environment, 38 (2004) 3319-3328.
[40] T. Ctvrtnickova, M.-P. Mateo, A. Yanez, G. Nicolas, Characterization of coal fly ash components by laser-induced breakdown spectroscopy, Spectrochimica Acta Part B: Atomic Spectroscopy, 64 (2009) 1093-1097.
[41] B. Sallé, D.A. Cremers, S. Maurice, R.C. Wiens, P. Fichet, Evaluation of a compact spectrograph for in-situ and stand-off laser-induced breakdown spectroscopy analyses of geological samples on Mars missions, Spectrochimica Acta Part B: Atomic Spectroscopy, 60 (2005) 805-815.
[42] M. Baudelet, J. Yu, M. Bossu, J. Jovelet, J.-P. Wolf, T. Amodeo, E. Fréjafon, P. Laloi, Discrimination of microbiological samples using femtosecond laser-induced breakdown spectroscopy, Applied Physics Letters, 89 (2006) 163903.
[43] A. Kumar, F.-Y. Yueh, J.P. Singh, S. Burgess, Characterization of malignant tissue cells by laser-induced breakdown spectroscopy, Applied optics, 43 (2004) 5399-5403.

[44] L. St-Onge, E. Kwong, M. Sabsabi, E. Vadas, Quantitative analysis of pharmaceutical products by laser-induced breakdown spectroscopy, Spectrochimica Acta Part B: Atomic Spectroscopy, 57 (2002) 1131-1140.

[45] A. De Giacomo, M. Dell'Aglio, O. De Pascale, R. Gaudiuso, A. Santagata, R. Teghil, Laser Induced Breakdown Spectroscopy methodology for the analysis of copper-based-alloys used in ancient artworks, Spectrochimica Acta Part B: Atomic Spectroscopy, 63 (2008) 585-590.

[46] R. Bruder, V. Detalle, C. Coupry, An example of the complementarity of laser-induced breakdown spectroscopy and Raman microscopy for wall painting pigments analysis, Journal of Raman Spectroscopy: An International Journal for Original Work in all Aspects of Raman Spectroscopy, Including Higher Order Processes, and also Brillouin and Rayleigh Scattering, 38 (2007) 909-915.

[47] D. Anglos, Laser-induced breakdown spectroscopy in art and archaeology, Applied spectroscopy, 55 (2001) 186A-205A.

[48] P. Singh, E. Mal, A. Khare, S. Sharma, A study of archaeological pottery of Northeast India using laser induced breakdown spectroscopy (LIBS), Journal of Cultural Heritage, 33 (2018) 71-82.

[49] J.L. Gottfried, F.C. De Lucia, C.A. Munson, A.W. Miziolek, Standoff detection of chemical and biological threats using laser-induced breakdown spectroscopy, Applied spectroscopy, 62 (2008) 353-363.

[50] M. Taschuk, Y. Tsui, R. Fedosejevs, Detection and mapping of latent fingerprints by laser-induced breakdown spectroscopy, Applied spectroscopy, 60 (2006) 1322-1327.

[51] E. Rodriguez-Celis, I. Gornushkin, U. Heitmann, J. Almirall, B. Smith, J. Winefordner, N. Omenetto, Laser induced breakdown spectroscopy as a tool for discrimination of glass for forensic applications, Analytical and bioanalytical chemistry, 391 (2008) 1961.

[52] J. Gottfried, F. De Lucia Jr, C. Munson, A. Miziolek, Laser-induced breakdown spectroscopy for explosive residue detection: a review of the challenges, recent advances, and future prospects, Anal. Bioanal. Chem, 395 (2009) 283-300.

[53] R.C. Chinni, D.A. Cremers, L.J. Radziemski, M. Bostian, C. Navarro-Northrup, Detection of uranium using laser-induced breakdown spectroscopy, Applied spectroscopy, 63 (2009) 1238-1250.

[54] F.C. De Lucia, R.S. Harmon, K.L. McNesby, R.J. Winkel, A.W. Miziolek, Laser-induced breakdown spectroscopy analysis of energetic materials, Applied optics, 42 (2003) 6148-6152.

[55] S. Harilal, B. Brumfield, N. LaHaye, K. Hartig, M. Phillips, Optical spectroscopy of laser-produced plasmas for standoff isotopic analysis, Applied Physics Reviews, 5 (2018) 021301.

[56] M. Sabsabi, P. Cielo, Quantitative analysis of aluminum alloys by laser-induced breakdown spectroscopy and plasma characterization, Applied spectroscopy, 49 (1995) 499-507.

[57] J.J. Chang, B.E. Warner, Laser-plasma interaction during visible-laser ablation of methods, Applied Physics Letters, 69 (1996) 473-475.

[58] D. Patel, P. Pandey, R. Thareja, Stoichiometric investigations of laser-ablated brass plasma, Applied optics, 51 (2012) B192-B200.

[59] V. Margetic, A. Pakulev, A. Stockhaus, M. Bolshov, K. Niemax, R. Hergenröder, A comparison of nanosecond and femtosecond laser-induced plasma spectroscopy of brass samples, Spectrochimica Acta Part B: Atomic Spectroscopy, 55 (2000) 1771-1785.

[60] S. Harilal, C. Bindhu, R.C. Issac, V. Nampoori, C. Vallabhan, Electron density and temperature measurements in a laser produced carbon plasma, Journal of applied physics, 82 (1997) 2140-2146.

[61] J. Yu, Q. Ma, V. Motto-Ros, W. Lei, X. Wang, X. Bai, Generation and expansion of laser-induced plasma as a spectroscopic emission source, Frontiers of Physics, 7 (2012) 649-669.

[62] Q. Ma, V. Motto-Ros, W. Lei, M. Boueri, X. Bai, L. Zheng, H. Zeng, J. Yu, Temporal and spatial dynamics of laser-induced aluminum plasma in argon background at atmospheric pressure: Interplay with the ambient gas, Spectrochimica Acta Part B: Atomic Spectroscopy, 65 (2010) 896-907.

[63] A. Elhassan, A. Giakoumaki, D. Anglos, G. Ingo, L. Robbiola, M. Harith, Nanosecond and femtosecond laser induced breakdown spectroscopic analysis of bronze alloys, Spectrochimica Acta Part B: Atomic Spectroscopy, 63 (2008) 504-511.

[64] X.L. Mao, M.A. Shannon, A.J. Fernandez, R.E. Russo, Temperature and emission spatial profiles of laser-induced plasmas during ablation using time-integrated emission spectroscopy, Applied spectroscopy, 49 (1995) 1054-1062.

[65] W. Marine, L. Patrone, B. Luk'yanchuk, M. Sentis, Strategy of nanocluster and nanostructure synthesis by conventional pulsed laser ablation, Applied surface science, 154 (2000) 345-352.

[66] T. Ohkubo, M. Kuwata, B. Luk'yanchuk, T. Yabe, Numerical analysis of nanocluster formation within ns-laser ablation plume, Applied physics A, 77 (2003) 271-275.

[67] A. Bogaerts, Z. Chen, Effect of laser parameters on laser ablation and laser-induced plasma formation: A numerical modeling investigation, Spectrochimica Acta Part B: Atomic Spectroscopy, 60 (2005) 1280-1307.

[68] M. Polek, S.S. Harilal, A. Hassanein, Two-dimensional mapping of the electron density in laser-produced plasmas, Applied optics, 51 (2012) 498-503.

[69] R. Fabbro, E. Fabre, F. Amiranoff, C. Garban-Labaune, J. Virmont, M. Weinfeld, C. Max, Laser-wavelength dependence of mass-ablation rate and heat-flux inhibition in laser-produced plasmas, Physical Review A, 26 (1982) 2289.

[70] A. Hussein, P. Diwakar, S. Harilal, A. Hassanein, The role of laser wavelength on plasma generation and expansion of ablation plumes in air, Journal of applied physics, 113 (2013) 143305.

[71] N. Farid, C. Li, H. Wang, H. Ding, Laser-induced breakdown spectroscopic characterization of tungsten plasma using the first, second, and third harmonics of an Nd: YAG laser, Journal of nuclear materials, 433 (2013) 80-85.
[72] S. Haq, L. Ahmat, M. Mumtaz, H. Shakeel, S. Mahmood, A. Nadeem, Spectroscopic studies of magnesium plasma produced by fundamental and second harmonics of Nd: YAG laser, Physics of Plasmas, 22 (2015) 083504.
[73] J. Hoffman, T. Moscicki, Z. Szymanski, The effect of laser wavelength on heating of ablated carbon plume, Applied Physics A, 104 (2011) 815-819.
[74] B. Le Drogoff, J. Margot, F. Vidal, S. Laville, M. Chaker, M. Sabsabi, T. Johnston, O. Barthélemy, Influence of the laser pulse duration on laser-produced plasma properties, Plasma Sources Science and Technology, 13 (2004) 223.
[75] K.L. Eland, D.N. Stratis, T. Lai, M.A. Berg, S.R. Goode, S.M. Angel, Some comparisons of LIBS measurements using nanosecond and picosecond laser pulses, Applied spectroscopy, 55 (2001) 279-285.
[76] S. Laville, F. Vidal, T. Johnston, M. Chaker, B. Le Drogoff, O. Barthelemy, J. Margot, M. Sabsabi, Modeling the time evolution of laser-induced plasmas for various pulse durations and fluences, Physics of Plasmas, 11 (2004) 2182-2190.
[77] B.N. Chichkov, C. Momma, S. Nolte, F. Von Alvensleben, A. Tünnermann, Femtosecond, picosecond and nanosecond laser ablation of solids, Applied Physics A, 63 (1996) 109-115.
[78] S. Zhang, X. Wang, M. He, Y. Jiang, B. Zhang, W. Hang, B. Huang, Laser-induced plasma temperature, Spectrochimica Acta Part B: Atomic Spectroscopy, 97 (2014) 13-33.
[79] W. Luo, X. Zhao, Q. Sun, C. Gao, J. Tang, H. Wang, W. Zhao, Characteristics of the aluminum alloy plasma produced by a 1064 nm Nd: YAG laser with different irradiances, Pramana, 74 (2010) 945-959.
[80] S. Harilal, C. Bindhu, V. Nampoori, C. Vallabhan, Temporal and spatial behavior of electron density and temperature in a laser-produced plasma from YBa2Cu3O7, Applied spectroscopy, 52 (1998) 449-455.
[81] S. Harilal, C. Bindhu, V. Nampoori, C. Vallabhan, Time evolution of the electron density and temperature in laser-produced plasmas from YBa2Cu3O7, Applied Physics B, 66 (1998) 633-638.
[82] G.K. Varier, R.C. Issac, S. Harilal, C. Bindhu, V. Nampoori, C. Vallabhan, Investigations on nanosecond laser produced plasma in air from the multi-component material YBa2Cu3O7, Spectrochimica Acta Part B: Atomic Spectroscopy, 52 (1997) 657-666.
[83] S. Harilal, B. O'Shay, Y. Tao, M.S. Tillack, Ambient gas effects on the dynamics of laser-produced tin plume expansion, Journal of Applied Physics, 99 (2006) 083303.

[84] S. Bashir, N. Farid, K. Mahmood, M.S. Rafique, Influence of ambient gas and its pressure on the laser-induced breakdown spectroscopy and the surface morphology of laser-ablated Cd, Applied Physics A, 107 (2012) 203-212.
[85] G. Cristoforetti, S. Legnaioli, V. Palleschi, A. Salvetti, E. Tognoni, Influence of ambient gas pressure on laser-induced breakdown spectroscopy technique in the parallel double-pulse configuration, Spectrochimica Acta Part B: Atomic Spectroscopy, 59 (2004) 1907-1917.
[86] N.M. Shaikh, B. Rashid, S. Hafeez, S. Mahmood, M. Saleem, M. Baig, Diagnostics of cadmium plasma produced by laser ablation, Journal of applied physics, 100 (2006) 073102.
[87] L. Cabalin, J. Laserna, Experimental determination of laser induced breakdown thresholds of metals under nanosecond Q-switched laser operation, Spectrochimica Acta Part B: Atomic Spectroscopy, 53 (1998) 723-730.
[88] D. Bleiner, Z. Chen, D. Autrique, A. Bogaerts, Role of laser-induced melting and vaporization of metals during ICP-MS and LIBS analysis, investigated with computer simulations and experiments, Journal of analytical atomic spectrometry, 21 (2006) 910-921.
[89] J. Cowpe, R. Moorehead, D. Moser, J. Astin, S. Karthikeyan, S. Kilcoyne, G. Crofts, R. Pilkington, Hardness determination of bio-ceramics using Laser-Induced Breakdown Spectroscopy, Spectrochimica Acta Part B: Atomic Spectroscopy, 66 (2011) 290-294.
[90] X. Zeng, S.S. Mao, C. Liu, X. Mao, R. Greif, R.E. Russo, Laser-induced plasmas in micromachined fused silica cavities, Applied Physics Letters, 83 (2003) 240-242.
[91] A.S. Eppler, D.A. Cremers, D.D. Hickmott, M.J. Ferris, A.C. Koskelo, Matrix effects in the detection of Pb and Ba in soils using laser-induced breakdown spectroscopy, Applied spectroscopy, 50 (1996) 1175-1181.
[92] J. Cortez, B.B. Farias Filho, L.M. Fontes, C. Pasquini, I.M. Raimundo Jr, M.F. Pimentel, F. de Souza Lins Borba, A simple device for lens-to-sample distance adjustment in laser-induced breakdown spectroscopy (LIBS), Applied spectroscopy, 71 (2017) 634-639.
[93] R.A. Multari, L.E. Foster, D.A. Cremers, M.J. Ferris, Effect of sampling geometry on elemental emissions in laser-induced breakdown spectroscopy, Applied spectroscopy, 50 (1996) 1483-1499.
[94] J. Aguilera, J. Bengoechea, C. Aragón, Spatial characterization of laser induced plasmas obtained in air and argon with different laser focusing distances, Spectrochimica Acta Part B: Atomic Spectroscopy, 59 (2004) 461-469.
[95] P. Fichet, P. Mauchien, J.-F. Wagner, C. Moulin, Quantitative elemental determination in water and oil by laser induced breakdown spectroscopy, Analytica chimica acta, 429 (2001) 269-278.

[96] C. Aragón, J.A. Aguilera, Characterization of laser induced plasmas by optical emission spectroscopy: A review of experiments and methods, Spectrochimica Acta Part B: Atomic Spectroscopy, 63 (2008) 893-916.
[97] E. Tognoni, G. Cristoforetti, S. Legnaioli, V. Palleschi, Calibration-free laser-induced breakdown spectroscopy: state of the art, Spectrochimica Acta Part B: Atomic Spectroscopy, 65 (2010) 1-14.
[98] H. Bolt, V. Barabash, W. Krauss, J. Linke, R. Neu, S. Suzuki, N. Yoshida, A.U. Team, Materials for the plasma-facing components of fusion reactors, Journal of nuclear materials, 329 (2004) 66-73.
[99] M. Kubkowska, P. Gasior, M. Rosinski, J. Wolowski, M. Sadowski, K. Malinowski, E. Skladnik-Sadowska, Characterisation of laser-produced tungsten plasma using optical spectroscopy method, The European Physical Journal D, 54 (2009) 463-466.
[100] S. Kajita, N. Ohno, S. Takamura, W. Sakaguchi, D. Nishijima, Plasma-assisted laser ablation of tungsten: Reduction in ablation power threshold due to bursting of holes/bubbles, Applied Physics Letters, 91 (2007) 261501.
[101] P. Quinet, P. Palmeri, É. Biémont, Spectroscopic data for atomic tungsten transitions of interest in fusion plasma research, Journal of Physics B: Atomic, Molecular and Optical Physics, 44 (2011) 145005.
[102] R. Neu, Tungsten as a plasma facing material in fusion devices, in, Universität Tübingen, 2003.
[103] B. Ilyas, M. Hussain, A. Dogar, S. Ullah, A. Nadeem, A. Qayyum, Temporal behavior of the tungsten plasma produced by 1064 nm pulsed Nd-YAG laser, Nuclear Instruments and Methods in Physics Research Section B: Beam Interactions with Materials and Atoms, 295 (2013) 81-84.
[104] N. Farid, S. Harilal, O. El-Atwani, H. Ding, A. Hassanein, Experimental simulation of materials degradation of plasma-facing components using lasers, Nuclear Fusion, 54 (2013) 012002.
[105] W. Ding, L. Ping, S. Liying, H. Ran, D. Hongbin, Influence of a static magnetic field on laser induced tungsten plasma in air, Plasma Science and Technology, 18 (2016) 364.
[106] R. Neu, R. Dux, A. Kallenbach, T. Pütterich, M. Balden, J. Fuchs, A. Herrmann, C. Maggi, M. O'Mullane, R. Pugno, Tungsten: an option for divertor and main chamber plasma facing components in future fusion devices, Nuclear Fusion, 45 (2005) 209.
[107] Y. Sun, B. Zhao, Y. Bai, M. He, J. Bai, Linear and Nonlinear Optical Response of Monolayer Two-dimensional Transition Metal Dichalcogenide MoSe2 and WSe2, in: CLEO: Applications and Technology, Optical Society of America, 2018, pp. JTh2A. 92.
[108] P. Tonndorf, R. Schmidt, P. Böttger, X. Zhang, J. Börner, A. Liebig, M. Albrecht, C. Kloc, O. Gordan, D.R. Zahn, Photoluminescence emission and Raman response of monolayer MoS 2, MoSe 2, and WSe 2, Optics express, 21 (2013) 4908-4916.

[109] B. Chen, X. Zhang, K. Wu, H. Wang, J. Wang, J. Chen, Q-switched fiber laser based on transition metal dichalcogenides MoS 2, MoSe 2, WS 2, and WSe 2, Optics express, 23 (2015) 26723-26737.

[110] M. Akram, S. Bashir, M.S. Rafique, A. Hayat, K. Mahmood, A. Dawood, M. Bashir, Morphological and spectroscopic characterization of laser-ablated tungsten at various laser irradiances, Applied Physics A, 119 (2015) 859-870.

[111] D. Nishijima, E. Hollmann, R. Doerner, D. Rudakov, Laser-induced breakdown spectroscopy analyses of tungsten surfaces, Physica Scripta, 2016 (2016) 014032.

[112] L. Mercadier, A. Semerok, P. Kizub, A. Leontyev, J. Hermann, C. Grisolia, P.-Y. Thro, In-depth analysis of ITER-like samples composition using laser-induced breakdown spectroscopy, Journal of nuclear materials, 414 (2011) 485-491.

[113] M. Hanif, M. Salik, Optical Emission Studies of Molybdenum Plasma Produced by an Nd: yag Laser, Journal of Russian Laser Research, 35 (2014) 230-238.

[114] E. Sternberg, N. Rodrigues, J. Amorim, Molybdenum electron impact width parameter measurement by laser-induced breakdown spectroscopy, Applied Physics B, 122 (2016) 21.

[115] N. Farid, H. Wang, C. Li, X. Wu, H.Y. Oderji, H. Ding, G.-N. Luo, Effect of background gases at reduced pressures on the laser treated surface morphology, spectral emission and characteristics parameters of laser produced Mo plasmas, Journal of nuclear materials, 438 (2013) 183-189.

[116] L. Fornarini, F. Colao, R. Fantoni, V. Lazic, V. Spizzicchino, Calibration analysis of bronze samples by nanosecond laser induced breakdown spectroscopy: a theoretical and experimental approach, Spectrochimica Acta Part B: Atomic Spectroscopy, 60 (2005) 1186-1201.

[117] X. Li, W. Wei, J. Wu, S. Jia, A. Qiu, Comparison of nanosecond laser produced brass plasmas under low and moderate pressure air, Journal of Physics D: Applied Physics, 46 (2013) 475207.

[118] M. Achouri, T. Baba-Hamed, S. Beldjilali, A. Belasri, Determination of a brass alloy concentration composition using calibration-free laser-induced breakdown spectroscopy, Plasma Physics Reports, 41 (2015) 758-768.

[119] A. De Giacomo, Experimental characterization of metallic titanium-laser induced plasma by time and space resolved optical emission spectroscopy, Spectrochimica Acta Part B: Atomic Spectroscopy, 58 (2003) 71-83.

[120] S. Kumari, A. Kushwaha, A. Khare, Spatial distribution of electron temperature and ion density in laser induced ruby (Al2O3: Cr3+) plasma using Langmuir probe, Journal of Instrumentation, 7 (2012) C05017.

[121] H. Tang, O. Guilbaud, G. Jamelot, D. Ros, A. Klisnick, D. Joyeux, D. Phalippou, M. Kado, M. Nishikino, M. Kishimoto, Diagnostics of laser-induced plasma with soft X-ray (13.9 nm) bi-mirror interference microscopy, Applied Physics B, 78 (2004) 975-977.

[122] S.H. Glenzer, R. Redmer, X-ray Thomson scattering in high energy density plasmas, Reviews of Modern Physics, 81 (2009) 1625.

[123] S. Harilal, G. Miloshevsky, P. Diwakar, N. LaHaye, A. Hassanein, Experimental and computational study of complex shockwave dynamics in laser ablation plumes in argon atmosphere, Physics of Plasmas, 19 (2012) 083504.

[124] A. Galmed, M. Harith, Temporal follow up of the LTE conditions in aluminum laser induced plasma at different laser energies, Applied Physics B, 91 (2008) 651.

[125] E. Tognoni, G. Cristoforetti, S. Legnaioli, V. Palleschi, A. Salvetti, M. Müller, U. Panne, I. Gornushkin, A numerical study of expected accuracy and precision in calibration-free laser-induced breakdown spectroscopy in the assumption of ideal analytical plasma, Spectrochimica Acta Part B: Atomic Spectroscopy, 62 (2007) 1287-1302.

[126] A. Ciucci, M. Corsi, V. Palleschi, S. Rastelli, A. Salvetti, E. Tognoni, New procedure for quantitative elemental analysis by laser-induced plasma spectroscopy, Applied spectroscopy, 53 (1999) 960-964.

[127] G. Cristoforetti, E. Tognoni, L. Gizzi, Thermodynamic equilibrium states in laser-induced plasmas: from the general case to laser-induced breakdown spectroscopy plasmas, Spectrochimica Acta Part B: Atomic Spectroscopy, 90 (2013) 1-22.

[128] G. Cristoforetti, A. De Giacomo, M. Dell'Aglio, S. Legnaioli, E. Tognoni, V. Palleschi, N. Omenetto, Local thermodynamic equilibrium in laser-induced breakdown spectroscopy: beyond the McWhirter criterion, Spectrochimica Acta Part B: Atomic Spectroscopy, 65 (2010) 86-95.

[129] H.R. Griem, Validity of local thermal equilibrium in plasma spectroscopy, Physical review, 131 (1963) 1170.

[130] P. Kolmhofer, S. Eschlböck-Fuchs, N. Huber, R. Rössler, J. Heitz, J. Pedarnig, Calibration-free analysis of steel slag by laser-induced breakdown spectroscopy with combined UV and VIS spectra, Spectrochimica Acta Part B: Atomic Spectroscopy, 106 (2015) 67-74.

[131] H. Fu, F. Dong, Z. Ni, J. Wang, The Influence of Acquisition Delay for Calibration-Free Laser-Induced Breakdown Spectroscopy, Applied spectroscopy, 70 (2016) 405-415.

[132] W. Karzas, R. Latter, Electron Radiative Transitions in a Coulomb Field, The Astrophysical Journal Supplement Series, 6 (1961) 167.

[133] N.M. Shaikh, S. Hafeez, B. Rashid, S. Mahmood, M. Baig, Optical emission studies of the mercury plasma generated by the fundamental, second and third harmonics of a Nd: YAG laser, Journal of Physics D: Applied Physics, 39 (2006) 4377.

[134] H. Hegazy, H.A. El-Ghany, S. Allam, T.M. El-Sherbini, Spectral evolution of nano-second laser interaction with Ti target in Air, Applied Physics B, 110 (2013) 509-518.

[135] H. Hegazy, Oxygen spectral lines for diagnostics of atmospheric laser-induced plasmas, Applied Physics B, 98 (2010) 601-606.
[136] M. Shah, A. Pulhani, G. Gupta, B. Suri, Quantitative elemental analysis of steel using calibration-free laser-induced breakdown spectroscopy, Applied optics, 51 (2012) 4612-4621.
[137] B. Praher, V. Palleschi, R. Viskup, J. Heitz, J. Pedarnig, Calibration free laser-induced breakdown spectroscopy of oxide materials, Spectrochimica Acta Part B: Atomic Spectroscopy, 65 (2010) 671-679.
[138] M. Horňáčková, J. Plavčan, J. Rakovský, V. Porubčan, D. Ozdín, P. Veis, Calibration-free laser induced breakdown spectroscopy as an alternative method for found meteorite fragments analysis, The European Physical Journal-Applied Physics, 66 (2014).
[139] I. Borgia, L.M. Burgio, M. Corsi, R. Fantoni, V. Palleschi, A. Salvetti, M.C. Squarcialupi, E. Tognoni, Self-calibrated quantitative elemental analysis by laser-induced plasma spectroscopy: application to pigment analysis, Journal of Cultural Heritage, 1 (2000) S281-S286.
[140] D.D. Pace, R.E. Miguel, H.O. Di Rocco, F.A. García, L. Pardini, S. Legnaioli, G. Lorenzetti, V. Palleschi, Quantitative analysis of metals in waste foundry sands by calibration free-laser induced breakdown spectroscopy, Spectrochimica Acta Part B: Atomic Spectroscopy, 131 (2017) 58-65.
[141] X. Shen, J. Sun, H. Ling, Y. Lu, Spectroscopic study of laser-induced Al plasmas with cylindrical confinement, Journal of applied physics, 102 (2007) 093301.
[142] M. Corsi, G. Cristoforetti, M. Hidalgo, S. Legnaioli, V. Palleschi, A. Salvetti, E. Tognoni, C. Vallebona, Double pulse, calibration-free laser-induced breakdown spectroscopy: a new technique for in situ standard-less analysis of polluted soils, Applied Geochemistry, 21 (2006) 748-755.
[143] V.K. Singh, V. Singh, A.K. Rai, S.N. Thakur, P.K. Rai, J.P. Singh, Quantitative analysis of gallstones using laser-induced breakdown spectroscopy, Applied Optics, 47 (2008) G38-G47.
[144] G.P. Bharti, A. Khare, Quenching of visible photoluminescence and observation of two photon absorption-induced photoluminescence in pulsed laser deposited Zn1-x Ti x O (0.000<= x<= 0.050) thin films, Journal of Physics D Applied Physics, 52 (2019).
[145] A. Nath, A. Khare, Effect of focusing conditions on laser-induced shock waves at titanium–water interface, Applied optics, 50 (2011) 3275-3281.
[146] S. Reich, P. Schönfeld, P. Wagener, A. Letzel, S. Ibrahimkutty, B. Gökce, S. Barcikowski, A. Menzel, T. dos Santos Rolo, A. Plech, Pulsed laser ablation in liquids: Impact of the bubble dynamics on particle formation, Journal of colloid and interface science, 489 (2017) 106-113.
[147] P.K. Baruah, A.K. Sharma, A. Khare, Effective control of particle size, surface plasmon resonance and stoichiometry of Cu@ CuxO nanoparticles synthesized by laser ablation of Cu in distilled water, Optics & Laser Technology, 108 (2018) 574-582.

[148] H. Zeng, X.W. Du, S.C. Singh, S.A. Kulinich, S. Yang, J. He, W. Cai, Nanomaterials via laser ablation/irradiation in liquid: a review, Advanced Functional Materials, 22 (2012) 1333-1353.
[149] R. Pitts, S. Bardin, B. Bazylev, M. van den Berg, P. Bunting, S. Carpentier-Chouchana, J. Coenen, Y. Corre, R. Dejarnac, F. Escourbiac, Physics conclusions in support of ITER W divertor monoblock shaping, Nuclear Materials and Energy, 12 (2017) 60-74.
[150] J. Davis, V. Barabash, A. Makhankov, L. Plöchl, K. Slattery, Assessment of tungsten for use in the ITER plasma facing components, Journal of nuclear materials, 258 (1998) 308-312.
[151] V. Philipps, Tungsten as material for plasma-facing components in fusion devices, Journal of nuclear materials, 415 (2011) S2-S9.
[152] S. Brezinsek, T. Loarer, V. Philipps, H. Esser, S. Grünhagen, R. Smith, R. Felton, J. Banks, P. Belo, A. Boboc, Fuel retention studies with the ITER-like wall in JET, Nuclear Fusion, 53 (2013) 083023.
[153] G. Federici, A. Zhitlukhin, N. Arkhipov, R. Giniyatulin, N. Klimov, I. Landman, V. Podkovyrov, V. Safronov, A. Loarte, M. Merola, Effects of ELMs and disruptions on ITER divertor armour materials, Journal of nuclear materials, (2005) 684-690.
[154] M. Fukuda, A. Hasegawa, T. Tanno, S. Nogami, H. Kurishita, Property change of advanced tungsten alloys due to neutron irradiation, Journal of Nuclear Materials, 442 (2013) S273-S276.
[155] A. Suslova, O. El-Atwani, S. Harilal, A. Hassanein, Material ejection and surface morphology changes during transient heat loading of tungsten as plasma-facing component in fusion devices, Nuclear Fusion, 55 (2015) 033007.
[156] R. Neu, S. Brezinsek, M. Beurskens, V. Bobkov, P. de Vries, C. Giroud, E. Joffrin, A. Kallenbach, G. Matthews, M.-L. Mayoral, Tungsten experiences in ASDEX Upgrade and JET, in: 2013 IEEE 25th Symposium on Fusion Engineering (SOFE), IEEE, 2013, pp. 1-8.
[157] S. Almaviva, L. Caneve, F. Colao, R. Fantoni, G. Maddaluno, Laboratory feasibility study of fusion vessel inner wall chemical analysis by Laser Induced Breakdown Spectroscopy, Chemical Physics, 398 (2012) 228-232.
[158] V. Philipps, A. Malaquias, A. Hakola, J. Karhunen, G. Maddaluno, S. Almaviva, L. Caneve, F. Colao, E. Fortuna, P. Gasior, Development of laser-based techniques for in situ characterization of the first wall in ITER and future fusion devices, Nuclear Fusion, 53 (2013) 093002.
[159] L. Mercadier, J. Hermann, C. Grisolia, A. Semerok, Analysis of deposited layers on plasma facing components by laser-induced breakdown spectroscopy: Towards ITER tritium inventory diagnostics, Journal of Nuclear Materials, 415 (2011) S1187-S1190.

[160] K. Piip, G. De Temmerman, H. van der Meiden, A. Lissovski, J. Karhunen, M. Aints, A. Hakola, P. Paris, M. Laan, J. Likonen, LIBS analysis of tungsten coatings exposed to Magnum PSI ELM-like plasma, Journal of Nuclear Materials, 463 (2015) 919-922.

[161] D. Dellasega, G. Merlo, C. Conti, C.E. Bottani, M. Passoni, Nanostructured and amorphous-like tungsten films grown by pulsed laser deposition, Journal of Applied Physics, 112 (2012) 084328.

[162] A. Mostako, C. Rao, A. Khare, Mirrorlike pulsed laser deposited tungsten thin film, Review of Scientific Instruments, 82 (2011) 013101.

[163] Y. Kawakami, E. Ozawa, Tungsten microcone arrays grown using nanosecond pulsed-Nd: YAG laser in a low-pressure He-gas atmosphere, Applied Physics A, 74 (2002) 59-61.

[164] Q.H. Wang, K. Kalantar-Zadeh, A. Kis, J.N. Coleman, M.S. Strano, Electronics and optoelectronics of two-dimensional transition metal dichalcogenides, Nature nanotechnology, 7 (2012) 699.

[165] I. Beigman, A. Pospieszczyk, G. Sergienko, I.Y. Tolstikhina, L. Vainshtein, Tungsten spectroscopy for the measurement of W-fluxes from plasma facing components, Plasma Physics and Controlled Fusion, 49 (2007) 1833.

[166] https://www.nist.gov/pml/atomic-spectra-database.

[167] https://www.cfa.harvard.edu/amp/ampdata/kurucz23/sekur.html.

[168] P.J. Skrodzki, J.R. Becker, P.K. Diwakar, S.S. Harilal, A. Hassanein, A comparative study of single-pulse and double-pulse laser-induced breakdown spectroscopy with uranium-containing samples, Applied spectroscopy, 70 (2016) 467-473.

[169] J. Freeman, P. Diwakar, S. Harilal, A. Hassanein, Improvements in discrimination of bulk and trace elements in long-wavelength double pulse LIBS, Spectrochimica Acta Part B: Atomic Spectroscopy, 102 (2014) 36-41.

[170] J.A. Aguilera, C. Aragón, Characterization of a laser-induced plasma by spatially resolved spectroscopy of neutral atom and ion emissions.: Comparison of local and spatially integrated measurements, Spectrochimica Acta Part B: Atomic Spectroscopy, 59 (2004) 1861-1876.

[171] D. Nishijima, R. Doerner, Stark width measurements and Boltzmann plots of WI in nanosecond laser-induced plasmas, Journal of Physics D: Applied Physics, 48 (2015) 325201.

[172] Y.-I. Lee, S.P. Sawan, T.L. Thiem, Y.-Y. Teng, J. Sneddon, Interaction of a laser beam with metals. Part II: Space-resolved studies of laser-ablated plasma emission, Applied spectroscopy, 46 (1992) 436-441.

[173] Z.-W. Hwang, Y.-Y. Teng, K.-P. Li, J. Sneddon, Interaction of a laser beam with metals. Part I: quantitative studies of plasma emission, Applied spectroscopy, 45 (1991) 435-441.

[174] A. AC00062431, Spectroscopy letters: an international journal for rapid communication, Taylor & Francis, 1968.
[175] O. Barthélemy, J. Margot, M. Chaker, M. Sabsabi, F. Vidal, T. Johnston, S. Laville, B. Le Drogoff, Influence of the laser parameters on the space and time characteristics of an aluminum laser-induced plasma, Spectrochimica Acta Part B: Atomic Spectroscopy, 60 (2005) 905-914.
[176] M. Nazeri, A.E. Majd, R. Massudi, S.H. Tavassoli, A. Mesbahinia, H. Abbasi, Laser-induced breakdown spectroscopy via the spatially resolved technique using non-gated detector, Journal of Russian Laser Research, 37 (2016) 164-171.
[177] M. Hafez, M. Khedr, F. Elaksher, Y. Gamal, Characteristics of Cu plasma produced by a laser interaction with a solid target, Plasma sources science and technology, 12 (2003) 185.
[178] K.J. Grant, G.L. Paul, Electron temperature and density profiles of excimer laser-induced plasmas, Applied spectroscopy, 44 (1990) 1349-1354.
[179] G. Cristoforetti, G. Lorenzetti, S. Legnaioli, V. Palleschi, Investigation on the role of air in the dynamical evolution and thermodynamic state of a laser-induced aluminium plasma by spatial-and time-resolved spectroscopy, Spectrochimica Acta Part B: Atomic Spectroscopy, 65 (2010) 787-796.
[180] A. Mostako, A. Khare, Molybdenum thin films via pulsed laser deposition technique for first mirror application, Laser and Particle Beams, 30 (2012) 559-567.
[181] M. Wisse, L. Marot, A. Widdowson, M. Rubel, D. Ivanova, P. Petersson, R. Doerner, M. Baldwin, J. Likonen, E. Alves, Laser-assisted cleaning of beryllium-containing mirror samples from JET and PISCES-B, Fusion engineering and design, 89 (2014) 122-130.
[182] M. Akram, S. Bashir, M.S. Rafique, A. Hayat, K. Mahmood, Laser induced surface morphology of molybdenum correlated with breakdown spectroscopy, Plasma Chemistry and Plasma Processing, 37 (2017) 287-304.
[183] G. Abdellatif, H. Imam, A study of the laser plasma parameters at different laser wavelengths, Spectrochimica Acta Part B: Atomic Spectroscopy, 57 (2002) 1155-1165.
[184] B. Le Drogoff, J. Margot, M. Chaker, M. Sabsabi, O. Barthelemy, T. Johnston, S. Laville, F. Vidal, Y. Von Kaenel, Temporal characterization of femtosecond laser pulses induced plasma for spectrochemical analysis of aluminum alloys, Spectrochimica Acta Part B: Atomic Spectroscopy, 56 (2001) 987-1002.
[185] D. Bulajic, M. Corsi, G. Cristoforetti, S. Legnaioli, V. Palleschi, A. Salvetti, E. Tognoni, A procedure for correcting self-absorption in calibration free-laser induced breakdown spectroscopy, Spectrochimica Acta Part B: Atomic Spectroscopy, 57 (2002) 339-353.

[186] J.A. Aguilera, C. Aragón, G. Cristoforetti, E. Tognoni, Application of calibration-free laser-induced breakdown spectroscopy to radially resolved spectra from a copper-based alloy laser-induced plasma, Spectrochimica Acta Part B: Atomic Spectroscopy, 64 (2009) 685-689.
[187] F. Colao, R. Fantoni, V. Lazic, L. Caneve, A. Giardini, V. Spizzichino, LIBS as a diagnostic tool during the laser cleaning of copper based alloys: experimental results, Journal of analytical atomic spectrometry, 19 (2004) 502-504.
[188] M. Bel'Kov, V. Burakov, V. Kiris, N. Kozhukh, S. Raikov, Spectral standard-free laser microanalysis of gold alloys, Journal of Applied Spectroscopy, 72 (2005) 376-381.
[189] B. Sallé, J.-L. Lacour, P. Mauchien, P. Fichet, S. Maurice, G. Manhes, Comparative study of different methodologies for quantitative rock analysis by laser-induced breakdown spectroscopy in a simulated Martian atmosphere, Spectrochimica Acta Part B: Atomic Spectroscopy, 61 (2006) 301-313.
[190] V. Burakov, V. Kiris, P. Naumenkov, S. Raikov, Calibration-free laser spectral analysis of glasses and copper alloys, Journal of Applied Spectroscopy, 71 (2004) 740-746.
[191] M. Corsi, G. Cristoforetti, M. Hidalgo, S. Legnaioli, V. Palleschi, A. Salvetti, E. Tognoni, C. Vallebona, Application of laser-induced breakdown spectroscopy technique to hair tissue mineral analysis, Applied optics, 42 (2003) 6133-6137.
[192] S. Pandhija, A. Rai, In situ multielemental monitoring in coral skeleton by CF-LIBS, Applied Physics B, 94 (2009) 545-552.
[193] S. Pandhija, N. Rai, A.K. Rai, S.N. Thakur, Contaminant concentration in environmental samples using LIBS and CF-LIBS, Applied Physics B, 98 (2010) 231-241.
[194] E. Mal, R. Junjuri, M.K. Gundawar, A. Khare, Optimization of temporal window for application of calibration free-laser induced breakdown spectroscopy (CF-LIBS) on copper alloys in air employing a single line, Journal of Analytical Atomic Spectrometry, (2019).
[195] N. Ahmed, R. Ahmed, M. Rafiqe, M. Baig, A comparative study of Cu–Ni alloy using LIBS, LA-TOF, EDX, and XRF, Laser and Particle Beams, 35 (2017) 1-9.
[196] J. Gomba, C. D'Angelo, D. Bertuccelli, G. Bertuccelli, Spectroscopic characterization of laser induced breakdown in aluminium–lithium alloy samples for quantitative determination of traces, Spectrochimica Acta Part B: Atomic Spectroscopy, 56 (2001) 695-705.
[197] B. Zmerli, N.B. Nessib, M. Dimitrijević, S. Sahal-Bréchot, Stark broadening calculations of neutral copper spectral lines and temperature dependence, Physica Scripta, 82 (2010) 055301.
[198] T. Takahashi, B. Thornton, K. Ohki, T. Sakka, Calibration-free analysis of immersed brass alloys using long-ns-duration pulse laser-induced breakdown spectroscopy with and without correction for nonstoichiometric ablation, Spectrochimica Acta Part B: Atomic Spectroscopy, 111 (2015) 8-14.

[199] M. Halbwax, T. Sarnet, P. Delaporte, M. Sentis, H. Etienne, F. Torregrosa, V. Vervisch, I. Perichaud, S. Martinuzzi, Micro and nano-structuration of silicon by femtosecond laser: application to silicon photovoltaic cells fabrication, Thin solid films, 516 (2008) 6791-6795.
[200] P. Tonndorf, R. Schmidt, P. Böttger, X. Zhang, J. Börner, A. Liebig, M. Albrecht, C. Kloc, O. Gordan, D.R. Zahn, Photoluminescence emission and Raman response of MoS2, MoSe2, and WSe2 nanolayers, in: CLEO: QELS_Fundamental Science, Optical Society of America, 2013, pp. QTu1D. 1.
[201] Y. Lang, T. Ouyang, L. Lin, K. Xia, M. Jiang, H. Guan, J. Yu, D. Li, G. Chen, W. Zhu, Side polished fiber coated with molybdenum diselenide (MoSe2) for humidity sensing, in: Optical Sensors, Optical Society of America, 2017, pp. SeW1E. 2.
[202] D. Scorticati, G.-W.R. Römer, D.F. de Lange, Ultra-short-pulsed laser-machined nanogratings of laser-induced periodic surface structures on thin molybdenum layers, Journal of nanophotonics, 6 (2012) 063528.
[203] K. Suzuki, N. Tanaka, A. Ando, H. Takagi, Size-selected copper oxide nanoparticles synthesized by laser ablation, Journal of Nanoparticle Research, 14 (2012) 863.
[204] L. Torrisi, S. Gammino, A. Mezzasalma, C. Gentile, J. Krása, L. Láska, K. Rohlena, J. Badziak, P. Parys, J. Wolowski, Tantalum irradiation by high power pulsed laser at 1315 and 438 nm wavelengths, Applied surface science, 220 (2003) 193-202.
[205] L. Ang, Y. Lau, R. Gilgenbach, H. Spindler, J. Lash, S. Kovaleski, Surface instability of multipulse laser ablation on a metallic target, Journal of Applied Physics, 83 (1998) 4466-4471.
[206] R. Hergenröder, Laser-generated aerosols in laser ablation for inductively coupled plasma spectrometry, Spectrochimica Acta Part B: Atomic Spectroscopy, 61 (2006) 284-300.
[207] A. Misra, A. Mitra, R. Thareja, Diagnostics of laser ablated plasmas using fast photography, Applied physics letters, 74 (1999) 929-931.
[208] J.T. Szymanski, A.C. Roberts, The crystal structure of tungstite, WO 3. H 2 O, The Canadian Mineralogist, 22 (1984) 681-688.
[209] Y. Xiong, Z. Zhu, T. Guo, H. Li, Q. Xue, Synthesis of nanowire bundle-like WO3-W18O49 heterostructures for highly sensitive NH3 sensor application, Journal of hazardous materials, 353 (2018) 290-299.
[210] L. Seguin, M. Figlarz, R. Cavagnat, J.-C. Lassègues, Infrared and Raman spectra of MoO3 molybdenum trioxides and MoO3· xH2O molybdenum trioxide hydrates, Spectrochimica Acta Part A: Molecular and Biomolecular Spectroscopy, 51 (1995) 1323-1344.

[211] M. Dieterle, G. Weinberg, G. Mestl, Raman spectroscopy of molybdenum oxides Part I. Structural characterization of oxygen defects in MoO 3− x by DR UV/VIS, Raman spectroscopy and X-ray diffraction, Physical Chemistry Chemical Physics, 4 (2002) 812-821.

[212] Y. Mao, J. He, X. Sun, W. Li, X. Lu, J. Gan, Z. Liu, L. Gong, J. Chen, P. Liu, Electrochemical synthesis of hierarchical Cu2O stars with enhanced photoelectrochemical properties, Electrochimica Acta, 62 (2012) 1-7.

List of Publications

Peer reviewed Journals

1. **Eshita Mal**, Rajendhar Junjuri, Manoj Kumar Gundawar and Alika Khare, "Temporal characterization of laser-induced plasma of tungsten in air", Laser and Particle Beams, 1-11. doi:10.1017/S0263034619000788

2. **Eshita Mal**, Rajendhar Junjuri, Manoj Kumar Gundawar and Alika Khare, "Optimization of temporal window for application of calibration free-laser induced breakdown spectroscopy (CF-LIBS) on copper alloys in air employing a single line", Journal of Analytical Atomic Spectrometry 2019, 34, 319-330

3. Pankaj Singh, **Eshita Mal** , A. Khare, Sukanya Sharma, "A study of archaeological pottery of Northeast India using laser induced breakdown spectroscopy (LIBS)", Journal of Cultural Heritage, 2018, 33,71-82

4. **Eshita Mal,** Rajendhar Junjuri, Manoj Kumar Gundawar and Alika Khare, "Time and Space-Resolved Laser Induced Breakdown Spectroscopy (LIBS) on Molybdenum in air" (Under review in Applied Spectroscopy).

5. **Eshita Mal**, Rajendhar Junjuri, Manoj Kumar Gundawar and Alika Khare, "Effect of spatial inhomogeneity of laser induced plasma on the accuracy of CF-LIBS technique" (Under preparation).

6. **Eshita Mal**, Rajendhar Junjuri, Manoj Kumar Gundawar and Alika Khare, "Spatial characterization of laser induced Tungsten plasma in air using laser induced breakdown spectroscopy" (Under preparation).

7. **Eshita Mal** and Alika. Khare, "Dependence of laser ablated surface morphology on LIBS parameters" (Under preparation).

Conference proceedings

8. **Eshita Mal** and Alika. Khare, "Studies on Laser Produced Tungsten Plasma using LIBS", "International Conference on Fibre Optics and Photonics", *Optical Society of America*, (2016), paper P1A.6
9. **Eshita Mal** and Alika. Khare, "Measurement of electron density and temperature in laser induced Stainless Steel (SS) plasma" Journal of Atomic Molecular, Condensate and Nano Physics (Accepted)

Conferences/ Symposium Attended

1. **Eshita Mal "**Laser Induced Plasma Studies on W, Mo and alloys of Cu in air via Time and Space Resolved LIBS and application in Single Line Calibration Free –LIBS", DAE–BRNS National Laser Symposium NLS-28, VIT Chennai, 8th -11th January,2020, Thesis presentation.

2. **Eshita Mal** and Alika Khare, "Spectroscopic Characterization of Laser Induced Plasma of Tungsten and Molybdenum in Air", NCRAST2019, Assam Science and Technology University, 15-17th May, 2019, (Poster)
3. **Eshita Mal** and Alika Khare, *"Compositional Analyses of Copper alloys using Single Line Transition via Calibration Free Laser Induced Breakdown Spectroscopy (CF-LIBS) in air"* Research Conclave 2019, IIT Guwahati, 14th -17th March 2019, (Oral).
4. **Eshita Mal**, Rajendhar Junjuri, Manoj Kumar Gundawar, Alika. Khare, *"Quantitative analysis of Brass using Calibration-Free Laser Induced Breakdown Spectroscopy (CF-LIBS) Technique in Air"*, DAE–BRNS National Laser Symposium NLS-27, RRCAT Indore 3th -6th December, 2018 (Poster).
5. **Eshita Mal**, R Junjuri, M K. Gundawar and Alika. Khare *"Spectroscopic characterization of laser produced molybdenum plasma in air"*, MMISLIBS-II 2018, Allahabad University, 2018 (Poster).
6. **Eshita Mal**, R Junjuri, M K. Gundawar and A Khare,*"Characterization of Laser Produced Tungsten Plasma in air using Time-resolved Laser Induced Breakdown Spectroscopy (LIBS)"*, NLS-26, BARC, BARC Mumbai, 20th - 23rd December , 2017, (Poster).
7. **Eshita Mal** and Alika Khare, "Studies on Laser Produced Tungsten Plasma using LIBS", Photonics-2016, IIT Kanpur, 4th -8th December, 2016, (Poster).
8. Prahlad K. Baruah, **Eshita Mal,** Kh. Shantakumar Singh, Ashwini K. Sharma and Alika Khare *"Laser produced plasma and its applications"* Research Conclave 2016, IIT Guwahati, 17th – 20th March, 2016, (Poster).
9. **Eshita Mal** and Alika Khare "Characterization of Laser-Induced Plasma of Tungsten"**,** 30th National Symposium on Plasma Science & Technology (PLASMA-2015), Saha Institute of Nuclear Physics Kolkata, 1st -4th December, 2015, (Poster).
10. **Eshita Mal**, Kh. Shantakumar Singh, Prahlad K.Baruah, Arjun Biswas, Ashwini K. Sharma and Alika Khare, *"Characterization of Copper Plasma using Laser Induced Breakdown Spectroscopy in air"*, 4th PSSI-PLASMA SCHOLARS COLLOQUIUM (PSC-2015), Jadavpur University, Kolkata, 6th -7th August, 2015, (Poster).
11. Prahlad K. Baruah, Kh. Shantakumar Singh, Sumit Goswami, **Eshita Mal,** Ashwini K. Sharma and Alika Khare, *"Application of laser induced breakdown for nanoparticle synthesis and as a powerful spectroscopic technique"*, Research Conclave -15, IIT Guwahati, 23rd -26th March, 2015, (Poster).
12. **Eshita Mal** and Alika Khare *"Measurement of electron density and temperature in laser induced Stainless Steel (SS) plasma"* 4th International Conference on Current Development on Atomic, Molecular, Optical & Nano Physics with Applications, University of Delhi, Delhi, India, 11-14th March, 2015, (Poster).
13. **Eshita Mal** and Alika Khare, *"Laser Induced Breakdown Spectroscopy of Stainless Steel Sample",* 3rd PSSI-PLASMA Scholars Colloquium (PSC-2014) & National workshop on Exploring Plasma Technology on Material Processing, VIT Chennai, 3-5th July 2014 (Poster).

Workshop/School/Exhibition

1. Short Course on *"Laser-matter interaction at the nanoscale" organized by Indian Laser Association (ILA)",* RRCAT Indore 1st -2nd December, 2018.

2. *"One-Day Workshop on Vacuum Technology and Its application In Optical Science"* organized by SPIE IITG student chapter in association with Pfeiffer vacuum, 19th August, 2017.
3. DST-SERB School on "Optical Metrology" organized by Tezpur University, , 1st-21st June 2016.
4. Feel the light-on optics outreach" organized by SPIE IIT Guwahati student chapter, Cotton College, Guwahati, 6th February, 2016.
5. South Asian Workshop on Optics & Photonics "SAWOP-2015"organized by Indian Institute of Technology Guwahati, 17th -18th November, 2015.

Awards

1. **First Prize** in **Oral Presentation** in Research Conclave 2019, 14th -17th March, IIT Guwahati.
2. **Best Poster Award** in DAE – BRNS National Laser Symposium – 26, 20th - 23rd December, 2017, BARC, Mumbai.
3. Selected for the Publication **KIRAN**.